



HAL
open science

Two dimensional electron devices built with large area MAXenes

Athanasios Gkountaras

► **To cite this version:**

Athanasios Gkountaras. Two dimensional electron devices built with large area MAXenes. Mechanical engineering [physics.class-ph]. Université Grenoble Alpes [2020-..], 2022. English. NNT : 2022GRALI034 . tel-03726603

HAL Id: tel-03726603

<https://theses.hal.science/tel-03726603>

Submitted on 18 Jul 2022

HAL is a multi-disciplinary open access archive for the deposit and dissemination of scientific research documents, whether they are published or not. The documents may come from teaching and research institutions in France or abroad, or from public or private research centers.

L'archive ouverte pluridisciplinaire **HAL**, est destinée au dépôt et à la diffusion de documents scientifiques de niveau recherche, publiés ou non, émanant des établissements d'enseignement et de recherche français ou étrangers, des laboratoires publics ou privés.

THÈSE

Pour obtenir le grade de

DOCTEUR DE L'UNIVERSITÉ GRENOBLE ALPES

Spécialité : 2MGE : Matériaux, Mécanique, Génie civil,
Electrochimie

Arrêté ministériel : 25 mai 2016

Présentée par

Athanasios GKOUNTARAS

Thèse dirigée par **Thierry OUISSE**, Professeur, Université
Grenoble Alpes
et co-encadrée par **Johann CORAUX**, Directeur de recherche,
Université Grenoble Alpes

préparée au sein du **Laboratoire Institut Néel**
dans l'**École Doctorale I-MEP2 - Ingénierie - Matériaux,**
Mécanique, Environnement, Energétique, Procédés,
Production

Dispositifs électroniques bi-dimensionnels fabriqués à partir de MAX-enes

Two dimensional electron devices built with large area MAXenes

Thèse soutenue publiquement le **28 mars 2022**,
devant le jury composé de:

Monsieur Thierry OUISSE

PROFESSEUR DES UNIVERSITES, Université Grenoble Alpes,
Directeur de thèse

Monsieur Hubert RENEVIER

PROFESSEUR DES UNIVERSITES, Université Grenoble-Alpes,
Examineur, Président

Monsieur Thierry CABIOCH

PROFESSEUR DES UNIVERSITES, Université de Poitiers, Examineur

Monsieur Benoît HACKENS

PROFESSEUR, Université Catholique de Louvain, Rapporteur

Madame Catherine JOURNET

PROFESSEUR DES UNIVERSITES, Université Lyon 1, Rapporteur

Monsieur Johann CORAUX

DIRECTEUR DE RECHERCHE, Université Grenoble-Alpes, Membre Invité



*Dedicated to my grandfather who inspired me
to constantly improve as a person.*

Acknowledgements

One of the human's basic needs, owing to his social character, is the interaction with other people. That reason forced people to organise the first communities through which they realised that daily issues/problems could be settled efficiently improving thus, their quality of life. The scientific community is a kind of society where every PhD student has to be integrated and learn how to properly cooperate with people that could provide him with all required supplies, which in combination with his personal effort will result in the award of the doctoral degree. In this section of my dissertation I would like to express my sincere gratitude to people I collaborated during my thesis, whose contribution was necessary to successfully complete my doctoral studies.

First of all, I would like to gratefully thank my supervisors for their trust, their patience and their belief in my abilities. Especially, I would like to thank my supervisor Thierry Ouisse and express my gratitude for the opportunity I had all those years to collaborate with such an experienced person in several fields of physics. His guidance in the research and his contribution to the results interpretation were invaluable during my thesis. I am very thankful to my co-supervisor Johann Coraux, whose experience and deeper knowledge of the Scanning Tunneling Microscopy introduced me to an unknown for me world at the nanoscale, where the surface topography of MAX phase samples was observed in atomic resolution images. Also, I had the honor to work with professor Michel Barsoum, the PI of the "Chair of Excellence" program part of which was my PhD project, and who co-supervised my thesis mostly remotely from Drexel university in Philadelphia. The fruitful interaction we had helped me understand aspects of the compound materials. Last but not least, I would also like to thank Vincent Bouchiat as my fourth "unofficial" supervisor for the substantial collaboration we had during the first two years of my thesis as well as for his willingness to show me the implementation of mechanical exfoliation to MAX phases.

Special thanks goes to Youngsoo Kim, postdoc and my colleague at LMGP, for the excellent collaboration we had for a year and a half and his valuable contribution to the experiments and particularly to the chemical etching process. Besides, I also thank Simone Lisi, postdoc and my colleague at Institut Néel, for his help in STM measurements.

As the entire work in my thesis was experimental it could not have been completed without the remarkable help of the engineers/technical staff in the two laboratories I shared my time. In particular, I thank Odette Chaix-Pluchery and Isabelle Gélard at LMGP for their help in Raman and SEM measurements, respectively and Philip David and Valerie Guisset at Institut Néel with their valuable help in STM/UHV issues. I could not have omitted to thank Simon Le-Denmat for our excellent collaboration during my measurements in AFM at Néel, as well as the entire NANOFAB team of Institut Néel and especially, Bruno Fernandez, Latifa Abbassi, Gwénaëlle Julie, Thierry Crozes and Jean-François Motte with whom I shared time both in and out of the lab. Also, I am grateful to Pierre Lachkar, Valerie Reita and Richard Haettel at Néel as well as to Delphine Constantin and Corinne Perret for their assistance in the use of the set-up at the CIME Nanotech clean-room.

My doctoral studies could not have been completed without the financial support of the Nanoscience foundation and specifically Alain Fontaine and Marie-Anne Carré, whom I warmly thank. Special thanks to HR departments of both labs and particularly to Michele San Martin and Annie Ducher at LMGP and Florence Pois, Sabine Gadal and Otmane Benhamed at Néel, for their invaluable help to administrative issues.

In addition, I would like to thank the direction at both laboratories, Franz Bruckert and Carmen Jimenez (LMGP) and Etienne Bustarret and Laurence Magaud (Institut Néel).

I am grateful to the members of the scientific groups part of which I was during my PhD studies, Nanomat (LMGP) and Hybrid (Néel) where that cozy, familial atmosphere among all members, regardless of the professional status (permanents, non-permanents), was very relaxing in the stressful weekly working hours.

Furthermore, I appreciate the contribution of all friends I met during my presence in Grenoble who made pleasant the demanding daily routine in the laboratories and also filled my life with wonderful and unforgettable experiences. Firstly, I would like to thank my colleagues and friends at LMGP and particularly Adria, Antalya, Carlos, Chiara, Damir, Dorina, Eugene, Fidel, Getnet, Jose, Joao, Klaasjan, Lorenzo, Maxime, Morgane, Monica, Raquel and Sara. In addition, many thanks goes to my colleagues and friends at Institut Néel and especially, Alexis, Abishek, Alvaro, Alessandro, Ana, Anike, Aymen, Brice, Corentin, David, Estelle, Farshad, Francesco, Giorgos, Goutham, Guilliam, Hugo, Isabelle, Jesus, Jorge, Julien, Juliette, Kimona, Kazi, Karthik, Laëtitia, Lucas, Maria, Marco, Nedjma, Otavio, Pavel, Priyank, Riadh, Roberto, Stefano, Vadim and perhaps more friends that I still forget but I all thank you for the interaction we had. I also thank my colleague Hérve with whom I shared my office, my mexican friends Tona and Antonio and all my greek friends who helped me keep the greek spirit alive through the participation in festivities organised within the greek community.

Finally, a great share in all my achievements to date has my family, my parents and my sister, who always support my choices and encourage me to never give up.

Abstract

The isolation of graphene using mechanical exfoliation indicated that layered structure bulk materials with weak layer-to-layer bonds can be transformed to their 2D derivatives with such a simple technique. To date, mechanical exfoliation has been successfully applied to various lamellar materials with van der Waals inter-layer bonding, such as hexagonal boron nitride (h-BN) and transition metal dichalcogenides (TMDC).

Another class of lamellar compounds named MAX phases, where “M” is an early transition metal, “A” belongs to group 13-16 of the periodic table and “X” is C or N, has globally aroused interest owing to a particular combination of ceramic and metal properties. Their layered structure displays stronger inter-layer (metallic) bonds than van der Waals and since 2011, when the first 2D counterparts, named MXenes, were produced by chemically etching of the parent MAX phases, no other delamination technique has been applied so far.

In this thesis we introduce a new way to delaminate MAX phases down to the ultimate thinness, via mechanical exfoliation. While such a process has been initially developed for van der Waals layered compounds, the strong inter-layer bonds in MAX phases seems unfavorable *a priori*. Our study was focused on Cr_2AlC , V_2AlC , Ti_2SnC MAX phases and the $\text{Mo}_4\text{Ce}_4\text{Al}_7\text{C}_3$ phase, for which we demonstrated that modifications to the transfer recipe known for graphite/graphene lead to remarkable results: flakes with large lateral dimensions and homogeneous thickness down to monolayer could be isolated. The isolation of few-monolayers thick flakes on SiO_2/Si substrates paved the way for their surface and electrical properties characterization. Besides, Atomic Force Microscopy (AFM), Scanning Tunneling Microscopy (STM) measurements of the surface of cleaved Cr_2AlC single crystals in ultra-high vacuum conditions reveal that clusters of Al atoms remain on the cleaved surface. Electrostatic Force and Kelvin Probe Force Microscopies (EFM and KPFM) provide clear evidence that flakes are

metallic down to monolayer thickness. The same conclusion is deduced both from resistivity measurements as a function of temperature and I-V curves.

Finally, a kinetics study of MAX-to-MXene conversion based on the HF etching of a well-defined structure comprised of square-size V_2AlC pillars indicated that HF penetration takes place at facets perpendicular to the basal planes ab of the single crystal.

Résumé

L'isolation du graphène par exfoliation mécanique a montré que les matériaux massifs nano-lamellaires liés par de faibles liaisons inter-plans peuvent être convertis en leurs dérivés bidimensionnels par une technique simple. À ce jour, l'exfoliation mécanique a été appliquée avec succès à divers matériaux lamellaires avec des interactions inter-plans de type van der Waals, tels que le nitrure de bore hexagonal (h-BN) et les di-chalcogénures de métaux de transition (TMDC).

Une autre classe de composés nano-lamellaires appelés phases MAX, où “M” est un métal de transition des premières colonnes, “A” appartient aux colonnes 13-16 du tableau périodique et “X” est C ou N, a suscité un intérêt général car ils combinent des propriétés intéressantes mais ordinairement rattachées soit aux seules céramiques, soit aux seuls métaux. Leur structure se caractérise néanmoins par des liaisons inter-plans (métalliques) plus fortes que des interactions de type van der Waals. Depuis 2011, date à laquelle les premiers matériaux 2D dérivés, appelés MXenes, ont été produits par gravure chimique à partir des composés MAX précurseurs, aucune autre technique d'exfoliation n'avait été démontrée.

Dans cette thèse, nous présentons une méthode d'exfoliation mécanique des phases MAX, jusqu'à des épaisseurs de quelques couches atomiques. Alors qu'un tel procédé a été initialement développé pour les composés de type van der Waals, les fortes liaisons inter-plans dans les phases MAX sont *a priori* défavorables. Notre étude s'est focalisée sur les phases Cr_2AlC , V_2AlC , Ti_2SnC et la phase $\text{Mo}_4\text{Ce}_4\text{Al}_7\text{C}_3$, pour lesquelles nous avons démontré que des adaptations du procédé développé pour la conversion graphite/graphène conduisent à des résultats remarquables: des feuillets de grandes dimensions latérales et d'épaisseur homogène jusqu'à quelques couches atomiques ont pu être isolés. L'isolation de feuillets épais de quelques monocouches sur des substrats SiO_2/Si a permis la caractérisation de leur surface et de leurs propriétés électriques. En outre, des mesures par microscopie à force atomique (AFM) et par microscopie à effet tunnel

(STM) de la surface de monocristaux de Cr_2AlC clivés dans des conditions d'ultra-
vide révèlent que des groupes d'atomes Al se forment sur la surface clivée. Les
microscopies à force électrostatique et à sonde Kelvin (EFM et KPFM) fournissent
la preuve que les feuillets sont métalliques jusqu'à l'épaisseur d'une demi-maille
de la structure initiale. La même conclusion est tirée de mesures de résistivité en
fonction de la température et des courbes courant–tension.

Enfin, une étude cinétique de la conversion de phase MAX en MXene, basée sur
la gravure par acide fluorhydrique (HF) d'une structure bien définie et composée
de piliers monocristallins de V_2AlC , montre que la pénétration de HF a lieu au
niveau des facettes perpendiculaires aux plans *ab* du monocristal.

Contents

Abstract	ix
Résumé	xi
Preface	xxi
1 Introduction to the structure and synthesis of MAX phases, MXenes and MAXenes	1
1.1 MAX phases	1
1.1.1 History of the MAX phases	1
1.1.2 Structure of MAX phases	4
1.1.3 Synthesis of MAX phases	6
1.1.3.1 Synthesis of MAX phase powders	7
1.1.3.2 Synthesis of bulk MAX phase polycrystals	8
1.1.3.3 Synthesis of MAX phase thin films	9
1.1.3.4 Synthesis of MAX phase single crystals	10
1.1.3.4.1 Description of the reactor's configuration	11
1.1.3.4.2 Growth mechanism description	13
1.1.4 Synthesis of $\text{Mo}_4\text{Ce}_4\text{Al}_7\text{C}_3$ phase	15
1.2 Transformation of 3D bulk materials to their 2D compounds	18
1.2.1 MXenes	18
1.2.1.1 History of the MXenes	18

1.2.1.2	Structure of MXenes	20
1.2.1.3	Synthesis of MXenes	24
1.2.1.3.1	Selectively etching	26
1.2.1.3.2	Intercalation and exfoliation	29
1.2.1.4	Properties and applications of MXenes	30
1.2.2	MAXenes	35
1.2.2.1	Synthesis and structure of MAXenes	35
1.3	Conclusion	36
2	Mechanical exfoliation of MAX phases	38
2.1	Brief overview of 2D materials mechanical exfoliation	38
2.2	Mechanical exfoliation of MAX phase and $\text{Mo}_4\text{Ce}_4\text{Al}_7\text{C}_3$ single crystals	45
2.2.1	Attempts to remove glue residues from the flakes surface	52
2.2.1.1	Thermal annealing in ambient conditions	53
2.2.1.2	Adhesive tapes with different chemical structure: Ultra violet (UV) susceptible tapes	56
2.2.1.3	Thermal annealing in Ar and in high vacuum conditions	61
2.2.1.4	Cleaning with solvents	67
2.2.1.5	Adhesive tapes based on natural rubber	69
2.3	Conclusion	74
3	Characterization techniques and experimental set-up	76
3.1	Introduction to electrical modes of Atomic Force Microscopy (AFM)	76
3.1.1	Brief introduction to Atomic Force Microscopy	77
3.1.2	Electrostatic Force Microscopy (EFM)	81

3.1.2.1	EFM operating methods	81
3.1.2.2	Electrostatic interactions in EFM	83
3.1.3	Kelvin Probe Force Microscopy (KPFM)	88
3.1.3.1	Fundamental principles of KPFM	88
3.1.3.2	Operating methods of KPFM	91
3.1.4	Theoretical approximation of an AFM tip in a metal-air-metal (MAM) and metal-air-dielectric-metal (MADM) configuration	95
3.1.4.1	Models of sphere-plane and sphere-cone configuration	97
3.2	Scanning Tunneling Microscopy (STM)	105
3.2.1	Basic principles of quantum tunneling	105
3.2.2	STM operation modes	108
3.2.3	STM set-up	109
3.3	Physical Properties Measurement System (PPMS)	112
3.3.1	PPMS set-up and the option of resistivity measurements	113
3.4	Conclusion	114
4	Topography of cleaved MAX phase single crystals and MAXenes electrical characterization	117
4.1	STM characterization of mechanically cleaved Cr ₂ AlC single crystals in UHV	117
4.1.1	Preparation of the Cr ₂ AlC samples	117
4.1.2	Cleavage of Cr ₂ AlC crystals in UHV conditions	118
4.1.3	Surface topography characterization of the cleaved Cr ₂ AlC crystals	119
4.2	Probing MAXenes electrical behavior using EFM and KPFM methods	121

4.2.1	EFM and KPFM signal probed on hydrophilic and hydrophobic surfaces	127
4.3	Resistivity measurements on MAXene devices	130
4.3.1	MAXene device fabrication process	130
4.3.2	MAXene resistivity using four-point probes method	133
4.3.2.1	Cr ₂ AlC flake device	134
4.3.2.2	V ₂ AlC flake device	135
4.3.2.3	Ti ₂ SnC flake device	136
4.3.2.4	Mo ₄ Ce ₄ Al ₇ C ₃ flake device	138
4.3.3	MAXene resistivity as a function of temperature	142
4.3.4	MAXene resistivity as a function of flake thickness	143
4.4	Conclusion	145
5	Elementary processes governing V₂AlC chemical etching in HF	147
5.1	Chemical etching and well-defined V ₂ AlC pillar structures	147
5.2	Fabrication of V ₂ AlC pillars	148
5.2.1	Pattern of square size array	149
5.2.2	Formation of V ₂ AlC pillars using Inductively Coupled Plasma (ICP) etching	151
5.3	Hydrofluoric etching of V ₂ AlC pillars and MXene conversion kinetics	153
5.3.1	HF etching of defective V ₂ AlC pillars	154
5.3.2	HF etching of defect-free V ₂ AlC pillars	159
5.3.3	Raman characterization of V ₂ AlC pillars and etching kinetics quantification	164
5.4	Conclusion	175

Conclusions and prospects	177
Bibliography	182
Publications	208

Preface

In 2011, MXenes, a new kind of 2D materials, were produced by chemical exfoliation of their parent bulk ternary compounds named MAX phases. In spite of the efficient production yield of very thin (down to monolayer) MXene flakes derived from the etching process in acid solutions, the lateral size of the produced flakes remains small, as the precursor has to be in powder form while the flakes' surface is terminated by unwanted ions e.g. -F, -Cl, -O, -OH. Additionally, a high density of defects on the flakes structure, resulting from the use of harsh etchants, has probably hindered the measurement of their intrinsic properties, such as resistivity and electronic transport.

The growth of large size MAX phase single crystals ($\sim 1 \text{ cm}^2$) in our lab (LMGP) using the high temperature solution growth technique, motivated us to proceed to the 3D to 2D transformation of the MAX crystals using mechanical exfoliation, an approach that has already been applied to various 2D materials but not to MAX phases. This method is based on an adhesive tape and the mechanical (tensile) stress applied to the surface of the bulk to separate it (cleave) in two parts.

In the present thesis, we explored the surface morphology and detected the electrical properties of mechanically exfoliated flakes, with thickness ranging from a few layers to monolayer, of select MAX phases. Specifically, the objectives of the research carried out during the PhD were focused on the adaptation of the mechanical exfoliation process used for graphene to ternary (Cr_2AlC , V_2AlC , Ti_2SnC) MAX phases and a quaternary ($\text{Mo}_4\text{Ce}_4\text{Al}_7\text{C}_3$) phase, so as to produce monolayer thickness flakes with large lateral dimensions. Emphasis was placed on the development of an appropriate transfer technique of thin and large size flakes on SiO_2/Si substrates in order to obtain insights into the surface topography using Atomic Force and Scanning Tunneling Microscopy (AFM, STM) as well as the electrical properties of the flakes, with the help of Electrostatic Force Microscopy,

Kelvin Probe Force Microscopy (EFM, KPFM) and four-point probes. Last but not least, the kinetics of the MAX-to-MXene transformation was studied for a well-defined structure comprised of square-size V_2AlC pillars that were chemically etched in HF acid, as our research interest was not limited only to mechanical exfoliation.

This dissertation is divided into five chapters. The first chapter presents an overview of the MAX phases and their 2D derivatives, MXenes, and discusses the structure, the methods of synthesis/preparation, the properties and applications of both kinds of material. The synthesis of layered rare earth compounds of MAX phases is also described and the chapter concludes with a brief report on the synthesis and structure of mechanically exfoliated flakes, the MAXenes in which the “A” layer is preserved.

In the second chapter we describe the mechanical exfoliation and flake transfer processes based on the recipe applied for graphene and other 2D materials, such as hexagonal boron nitride (h-BN) and transition metal dichalcogenides (TMDC). Subsequently, the implementation of the exfoliation process to MAX phases and the modified transferring steps for depositing large flakes on SiO_2/Si substrates are presented. The last section describes our efforts and attempts to eliminate the glue residues problem onto MAXene and substrate surfaces after the transfer process, and the analysis of the residues behavior under long time annealing are highlighted.

In the third chapter we discuss the experimental set-ups and working principles of the characterization techniques (AFM, EFM, KPFM, STM) used during our research. A description of the tip-sample interaction in EFM and KPFM measurements is also given based on the sphere-plane and sphere-cone models that provide acceptable approximations of the tip geometry. Notwithstanding the model’s inefficiency at large tip-sample distances, we used a sphere-plane approximation, since it was the only one which could be easily computed for the two configurations of our system, metal-air-metal (MAM) and metal-air-dielectric-metal (MADM). The selection of the model will help us interpret the results derived from EFM and KPFM measurements.

Chapter four reports sample characterizations using several techniques. Firstly, we present the surface topography (for the first time to our knowledge) of a cleaved Cr_2AlC single crystal in the UHV system, using STM, and we thereby put in evidence domains of Al and Cr atoms. In the following, we describe the EFM and KPFM results and demonstrate that MAXenes are metallic and retain their character regardless of the flake thickness. In the last section of this chapter, I-V curves from four-point probe measurements and resistivity versus temperature measurements further confirm the flakes metallic behavior.

Chapter five deals with the MAX-to-MXene conversion kinetics study of well-defined square-size V_2AlC pillars chemically etched in hydrofluoric acid (HF). Our idea to control the size of the chemically exfoliated flakes and besides, to identify several key aspects about MXene chemical etching, such as the facets of HF penetration, the etching rate, the maximum etching distance, led us to produce a recipe that created the desired, aforementioned pillar structure. Raman spectroscopy, scanning electron and optical microscopies were used to assess the MXene conversion kinetics.

The research carried out during this thesis was funded by Nanoscience foundation in the context of a “Chair of Excellence” program that started a collaboration between two laboratories located in Grenoble, Grenoble INP/LMGP (Thierry Ouisse), CNRS/Institut Néel (Johann Coraux, Vincent Bouchiat) and Michel Barsoum from Drexel university in Philadelphia, USA.

The experimental results during the thesis could not have been obtained without the supply of the Cr_2AlC , V_2AlC , Ti_2SnC MAX phases and $\text{Mo}_4\text{Ce}_4\text{Al}_7\text{C}_3$ phase single crystals from LMGP, where they were systematically grown, as well as the characterization methods used at Institut Néel (AFM, SEM, STM, four-point probes, Physical Properties Measurement System/PPMS). Key to the success of the experiments were the clean-room facilities. Especially, the NANOFAB clean-room at Institut Néel, where the mechanical exfoliation trials, the recipe for the fabrication of the well-defined V_2AlC pillar structure and most of the device fabrication steps took place with the valuable help of Jean-François Motte. In addition, the Upstream Technological Platform (PTA) at CEA, where the dry etching set-up was used with the help of Thierry Chevolleau and the

Interuniversity Center of Microelectronics and Nanotechnology (CIME Nanotech) also at CEA, which was used for device processing as well. The contribution of my colleague Youngsoo Kim (postdoc) to the device processing of MAXenes, and particularly to the kinetics study of MAX-to-MXene conversion of chemically etched V_2AlC pillar structure. Finally, the contribution of the engineers/technical staff from both labs and all three clean-room facilities was invaluable to tackle any problem appeared during experimental process.

Chapter 1

Introduction to the structure and synthesis of MAX phases, MXenes and MAXenes

The first chapter is an overview of the MAX phases and their 2D derivatives, MXenes. It refers to the structure, the methods of synthesis/preparation, the properties and applications of both kinds of material. The synthesis of layered rare earth compounds of MAX phases is also described. Lastly, the chapter concludes with a brief report on the synthesis and structure of mechanically exfoliated flakes, the MAXenes in which the “A” layer is preserved.

1.1 MAX phases

1.1.1 History of the MAX phases

In the early 1960s, Nowotny and his group in Vienna discovered a new family of carbides and nitrides, so called Hägg phases or H-phases [1], with the formula of M_2AX , where “M” is an early transition metal, “A” is an A-group element (mainly groups 13 to 16 of the periodic table), “X” is C and/or N and $n = 1, 2$ or 3 . The MAX or $M_{n+1}AX_n$ phases (as they were named later on) are classified according to the n values as 211 (M_2AX), 312 (M_3AX_2) and 413 (M_4AX_3). Apart from many 211 MAX phases, Nowotny’s group discovered the first two 312 phases, Ti_3SiC_2 and Ti_3GeC_2 , with one of Nowotny’s student, Schuster, contributing to this effort by synthesizing

one more 312 phase, Ti_3AlC_2 , in the 1980s [2]. By the late 1990s, those phases were well “hidden” in the literature until Barsoum and El-Raghy from Drexel university brought them back in light, after their publications during 1996 and 1997, proving the remarkable combination of metallic and ceramic properties most of the MAX phases have, which motivated the scientific community to further explore the MAX family.

The discovery of the first 413 phases like Ti_4AlN_3 in 1999 by Barsoum et al. [3] and a few years later (2006) of Ta_4AlC_3 by Manoun et al. [4], Nb_4AlC_3 by Hu et al. in 2007 [5] and Ti_4GaC_3 in 2009 by Etzkorn et al. [6] completed the first seek of the conventional MAX phases family. In addition to the conventional MAX phases, hybrid MAX phases like $Ti_5Si_2C_3$ and $Ti_7Si_2C_5$ were firstly reported in 2004 by Palmquist et al. [7]. Initially, these hybrid phases, which can be described as a combination of half unit cells of the conventional MAX phases, were observed only in thin films. In 2012, the first hybrid $Ti_5Al_2C_3$ bulk sample was produced by Lane et al. [8]. Above 80 ternary MAX phases have been experimentally synthesized to date (Table 1.1).

Table 1.1 List of currently known ternary MAX phases^a

	Al	Si	P	S
Ti_2AlC^b	Hf_3AlC_2 [13]	$Ti_3SiC_2^b$	V_2PC^b	Ti_2SC^b
V_2AlC^b	Ti_4AlN_3 [3]	Ti_4SiC_3 [7]	Nb_2PC^b	Zr_2SC^b
Cr_2AlC^b	Ta_4AlC_3 [4]	$Ti_5Si_2C_3$ [7]		$Nb_2SC_{0.4}^b$
Nb_2AlC^b	Nb_4AlC_3 [5]	$Ti_7Si_2C_5$ [7]		Nb_2SC^b
Ta_2AlC^b	V_4AlC_3 [13]–[15]			Hf_2SC^b
Ti_2AlN^b	$Ti_5Al_2C_3$ [8], [16]			
Zr_2AlC [9]	Ta_6AlC_5 [11]			
Hf_2AlC^b				
Ti_3AlC_2 [10]				
Ta_3AlC_2 [11]				

^a List of MAX phases taken from Ref. [31]. Updated version of previously reported lists in reviews [18], [63], [251] and a book [30].

^b Phases discovered by Nowotny and coworkers in the 1960s.

Zr ₃ AlC ₂ [12]				
Ga	Ge	Sn	As	Zn
Ti ₂ GaC ^b	Ti ₂ GeC ^b	Ti ₂ SnC ^b	V ₂ AsC ^b	Ti ₂ ZnC [24]
V ₂ GaC ^b	V ₂ GeC ^b	Zr ₂ SnC ^b	Nb ₂ AsC ^b	Ti ₃ ZnC ₂ [24]
Cr ₂ GaC ^b	Cr ₂ GeC ^b	Nb ₂ SnC ^b		Ti ₂ ZnN [24]
Nb ₂ GaC ^b	Nb ₂ GeC [20]	Hf ₂ SnC ^b		V ₂ ZnC [24]
Mo ₂ GaC ^b	Ti ₃ GeC ₂ ^b	Lu ₂ SnC [22]		
Ta ₂ GaC ^b	Ti ₄ GeC ₃ [21]	Hf ₂ SnN [23]		
Mn ₂ GaC [17]		Ti ₃ SnC ₂ [24]		
Ti ₂ GaN [18]		Zr ₃ SnC ₂ [25]		
Cr ₂ GaN [18]		Hf ₃ SnC ₂ [25]		
V ₂ GaN [18]		Ti ₇ SnC ₆ [26]		
Ti ₃ GaC ₂ [19]				
Ta ₄ GaC ₃ [19]				
Ti ₄ GaC ₃ [6]				
In	Tl	Pb	Precious Metals	Others
Sc ₂ InC ^b	Ti ₂ TlC ^b	Ti ₂ PbC ^b	Mo ₂ AuC [28]	Ti ₂ CdC ^b
Ti ₂ InC ^b	Zr ₂ TlC ^b	Zr ₂ PbC ^b	Ti ₃ AuC ₂ [29]	
Zr ₂ InC ^b	Hf ₂ TlC ^b	Hf ₂ PbC ^b	Ti ₃ IrC ₂ [29]	
Nb ₂ InC ^b	Zr ₂ TlN ^b			
Hf ₂ InC [27]				
Ti ₂ InN ^b				
Zr ₂ InN ^b				
Ti ₃ InC ₂ [19]				

Our historical overview on the MAX phases family would be incomplete without referring to the recent additions of quaternary phases (2014) which are classified into two distinct groups. The first group comprises the phases that are called out-of-plane ordered MAX phases, abbreviated as *o*-MAX (2014), with the general formula (M',M'')_{n+1}AX_n where M' and M'' refer to two early transition metals and *n* is either 2 or 3. Every second M'' layer is interleaved between two M' layers within each M-X block. The crystal structure is hexagonal. The second group was reported

more recently (2017). Its structure is in-plane ordered and it is thus referred to as *i*-MAX, but due to the different stoichiometry of M' and M'' , its general formula is $(M'_{2/3}M''_{1/3})_2AX$ with index $n = 1$. With each “M” layer, the M' atoms are arranged in hexagons with a M'' atom at their centers. For *i*-MAX phases reported to date, the crystal structure is not hexagonal but monoclinic or orthorhombic.

Altogether, MAX phases that have been synthesized to date, both ternary and quaternary [30], form a family totalling above 150 members with more than 20 different “M” elements and more than 15 different “A” elements (Figure 1.1).

$M_{n+1}AX_n$

Figure 1.1 Periodic table with all chemical elements used to date for MAX phases synthesis. Figure adapted from Ref. [31].

1.1.2 Structure of MAX phases

The $M_{n+1}AX_n$ phases are layered carbides and nitrides with a hexagonal structure (space group $P6_3/mmc$) with two formula units per unit cell (Figure 1.2). Once the “X” element layer is interleaved between two “M” element planes, octahedral units are formed with “X” atoms at their centers, and they are linked to other octahedral units by shared edges. To better accommodate the “A” plane atoms between two “M” element planes, trigonal prisms slightly larger than octahedral sites are formed, with “A” atoms located at their centers.

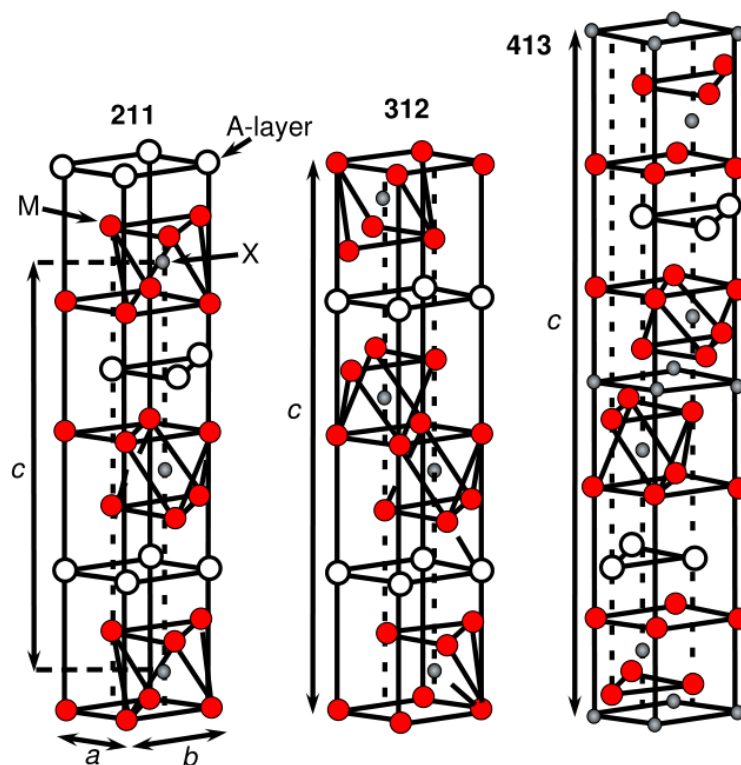


Figure 1.2 Unit cells of 211, 312 and 413 phases. The c parameters define the thickness of the unit cell for each phase. Figure adapted from Ref. [32].

According to the number of “M” layers separating the “A” layers as it is indicated by the index n of the general formula, the MAX phases can be classified in three different groups: i) M_2AX (211) phases when there are two “M” layers, ii) M_3AX_2 (312) phases when there are three “M” layers and iii) M_4AX_3 (413) phases when there are four “M” layers (Figure 1.2). In 211 phases the c axis is 12-13 Å, in 312 phases is 17-18 Å and 22-23 Å in 413 phases.

Depending on the atomic stacking sequence, specifically of adjacent M-X blocks, different polymorphs have been observed for each of the three groups of phases (Figure 1.3). In particular, only one polymorph exists for phase 211 while phase 312 has two polymorphs (α and β), since there are two nonequivalent “M” sites defined as M_I for “M” atoms bonded to “A” atoms and M_{II} for those bonded to “X” atoms. In the same way, phase 413 appears in three polymorphs (α , β and γ), as apart from “M” sites, there are also two nonequivalent “X” sites, with X_I referring to the bonding to M_I atoms and X_{II} to the bonding to M_{II} atoms [30].

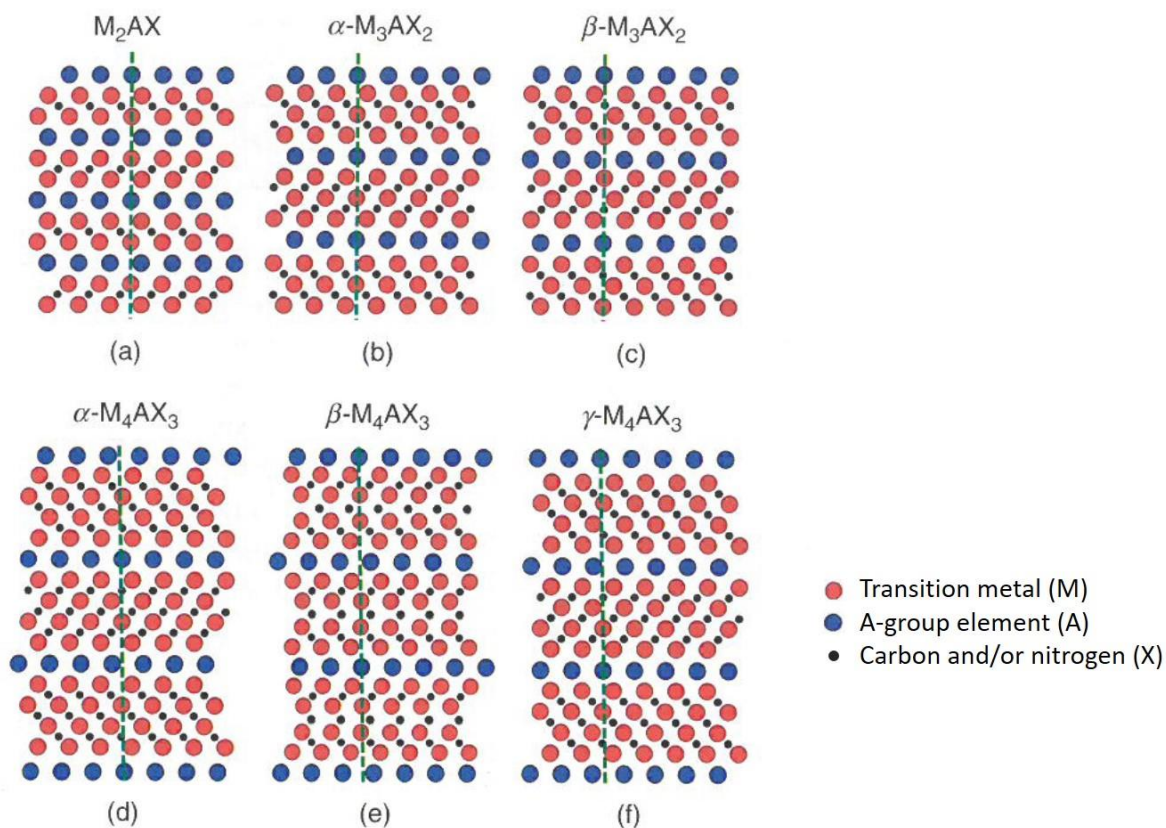


Figure 1.3 Schematics of the $(11\bar{2}0)$ planes in (a) M_2AX , (b) α - M_3AX_2 , (c) β - M_3AX_2 , (d) α - M_4AX_3 , (e) β - M_4AX_3 and (f) γ - M_4AX_3 . The dashed vertical lines are guides to the eyes. Figure adapted from Ref. [30].

A combination of metallic, covalent and ionic chemical bonds constitutes another characteristic of MAX phases with the dominant bond being the strong covalent σ -bond between the $3d$ orbitals of “M” and the $2p$ orbitals of “X” atoms while the bonding of “M” $3d$ and “A” p orbitals is less strong. Due to the existence of the transition metal $3d$ states around the Fermi energy level, MAX phases’ electronic properties show metallic behavior.

In the unit cell (Figure 1.2 - 1.3) the “A” plane is a mirror plane role, and the M-X layers form a herringbone (zig-zag) sequence [30].

1.1.3 Synthesis of MAX phases

Since the 1960s when the MAX phases were discovered by Nowotny and his group, a lot of methods have been used to synthesize MAX phases in different forms

(powders, polycrystals, thin films and single crystals). Some of these methods produce MAX phases with limited purity (50 – 60%) and accompanied with a variety of ancillary phases, while other methods e.g. hot isostatic pressing, yield high purity single phase bulk materials.

A brief summary of the synthesis methods that have been applied to date is presented in the following. This summary also highlights the process used in our lab to grow the single crystal MAX phases which were essential components in the progress of the project.

1.1.3.1 Synthesis of MAX phase powders

Among all the forms MAX phases have been synthesized to date, the easiest way to efficiently produce a large number of solid MAX phases is in powder. Early work has been done on the synthesis of ternary carbides, e.g. Ti-Al-C, by applying combustion synthesis, also called self-propagating high temperature synthesis (SHS). The main advantage of this method is that it relies on direct reactions producing powders with high densification at low temperature. Reactions between elements such as Ti, Al or C are exothermic which results in low purity and small quantities of ternary carbides, as binary carbides are dominant. Nevertheless, this case is reversible once binary powders (TiAl) replace elemental ones (Ti and Al) as a way to decrease the combustion temperature and finally improve the purity of ternary carbides by preventing their decomposition [33], [34].

To increase the purity of ternary compounds in MAX phases powders, solid-liquid reaction processes with elemental powders as the starting materials were used. This alternative fabrication method includes high temperature synthesis at 1200°C – 1250°C and short reaction time. The reaction starts either by adding NaF in the elemental powder mixture for favorising the liquid phase [35] or by forming a binary M-A compound from the “A” element liquid phase in low T and continuing the reaction with graphite as the temperature increases [36]. The small amount of impurities in the as-prepared powders after solution cleaning (HF, HCl) increased the ternary carbides purity to 80 wt% without achieving any further refinement [35], [36].

Pressureless sintering was widely used once the MAX phases synthesis reached high purity ternary powders. As a way to enhance both the ternary phase formation and densification, mechanically alloyed (MA) powder mixture was used during the pressureless sintering process. Elemental powders were milled with steel balls of varying sizes to get fine particles with large grain boundary areas and short diffusion pathway because of the internal strain and the defects formation. Using M-A powders improved the sintering process by decreasing the sintering temperature and time, which finally increased the ternary phase purity (80 wt%) and relative density [37], [38]. A mixture of elemental and binary (M-X) phase powders favored the exothermic reaction under pressureless conditions [39], [40] and increased the ternary phase purity up to 96 wt%. When a small amount (e.g. 1%) of elemental powder, of Si in case of the Ti_3SiC_2 phase, is used as a sintering aid during the pressureless sintering process, it leads to a reduction of the impurity content (M-X powders) in the sintered bodies and further improves the ternary phase purity to nearly 99 wt% [41]. However, it has been reported that ternary MAX phases with purity of almost 99 wt% can also be synthesized by high temperature annealing under vacuum conditions of elemental and binary phase powder mixtures [42]. Generally, pressureless sintering appears to be a widely applied and cost effective technique for high purity MAX phase powders synthesis compared to hot pressing and hot isostatic pressing techniques that are mainly used in the bulk phases synthesis and will be discussed in the following.

1.1.3.2 Synthesis of bulk MAX phase polycrystals

An alternative route to the synthesis of MAX phases is the fabrication of bulk polycrystals using MAX phase powders as components. Many efforts have been done in producing single phase polycrystals, with only few techniques achieving purities above 90%. In particular, hot pressing (HP) technique with solid-liquid reaction synthesis, using either elemental powder mixtures or in combination with binary (M-X, A-X) powders [43], [44], is a simple and very efficient method to produce dense single phases with anisotropic microstructure [45] and purity ranging from 87 wt% [46] to 95 wt% [47]. Another viable process for fabricating

single phase and fully dense polycrystals is the hot isostatic pressing (HIP) technique. In this method, elemental powders or mixtures of elemental and binary (A-X) powders have been synthesized to ternary phases of 92 wt% to 95 wt% purity [48]–[50] and they have different microstructures depending on the time and temperature of the synthesis [51].

Pulse discharge sintering (PDS) process is a technique, that developed in the early 1960s based on the idea of sintering metals and ceramics using pulsed high DC current along with uniaxial mechanical pressure applied to the mold settings [52]. In literature, many references to PDS method have used a different designation so far, that of spark plasma sintering (SPS), due to the dominant view of spark and plasma occurrence during the sintering process. For over forty years period, many studies were conducted to explain the mechanism of SPS, with all of them finally have excluded the presence of spark and plasma at any stage of the sintering procedure [53]. Thus, in the following, any reference to this method will be given by the term PDS. This process has been successfully applied to the reactive sintering synthesis of fully dense and high purity single phases (> 96 wt%) of MAX polycrystals, starting either with elemental or in combination with binary phase powders. Comparing to the above discussed techniques (HP, HIP), PDS method combines low synthesis time (few minutes) with low temperatures for specimens consolidation, whereas the reaction and densification processes can be completed simultaneously, even for materials that are traditionally difficult to be sintered [52], [54]. Nevertheless, the high cost owing to the energy consumption and the restricted volume of synthesized polycrystals remain drawbacks in the implementation of PDS method in industry [52].

1.1.3.3 Synthesis of MAX phase thin films

The fabrication of MAX phases in powder and bulk polycrystalline forms attracted most of the scientific community's interest, however, a few groups e.g. those of Seppänen et al. and Palmquist et al. focused their efforts on the synthesis of MAX phase thin films. The corresponding synthesis techniques can be classified into four main categories based on their working principles.

Chemical vapor deposition (CVD) was early attempted, but without any success as all efforts failed to produce single phase films. Due to phase purity and procedure control problems the interest on the synthesis of MAX phase films using the CVD technique was limited to a few trials focused only on Ti_3SiC_2 phase [55].

Physical vapor deposition (PVD) was considered afterwards. In particular, sputtering and magnetron sputtering techniques using either elemental targets that offer great flexibility through the individually controlled elemental fluxes, or compound targets whose mixed stoichiometries offer great repeatability, were successful in producing many MAX phase thin films [21], [56]–[58]. Additionally to these processes, cathodic arc deposition [59] in which substrate temperature for materials deposition can be lower than in sputtering and pulsed laser deposition [60], where films with higher deposition energy than in sputtering can be synthesized both from elemental and compound targets, has also been used.

Apart from CVD and PVD methods, solid state reactions of two main groups, film/substrate and film/film reactions, are yet another approach of thin film processing in which higher velocity rates of phase transformation have been reported in comparison to other high temperature film synthesis processes [61].

Last but not least, thermal spraying and especially high velocity oxy fuel (HVOF) spraying is a thin film processing method which have seen limited use on MAX phase film synthesis due to insufficiently phase purity coatings. Contrary to the above mentioned techniques, HVOF has been mainly applied in the fabrication of thick MAX phase coatings [62], [63].

1.1.3.4 Synthesis of MAX phase single crystals

The main feature of all the synthesis techniques previously reported is the production of MAX phases in a polycrystalline form that preserves the crystal structure anisotropy only at the microscopic level, apart from a few reported cases dealing with thin single crystalline layers [64] and platelets [65]. The need for experimentally probing the anisotropy of physical properties of MAX phases promoted the efforts to obtain bulk single crystals from liquid phase by growth in solution at high temperature followed by a slow cooling technique, also known as

« flux growth » method. Before getting into details about the growth procedure, a short description (detailed mechanism of the growth technique is given in Ref. [66]) of the reactor, the place where crystal growth takes place, should be given.

1.1.3.4.1 Description of the reactor's configuration

The high melting point of transition metals implies that the growth mechanism is only effective at high temperatures, at which long time operations require crucibles with thermally stable materials. Especially, crucible materials should be resistant to high temperature and thermal shocks and should have high thermal conductivity and optionally great machinability. The best candidate material fulfilling the above criteria is graphite which can be used as a crucible at temperatures up to 2000°C as already shown in previous growth experiments of Ti_3SiC_2 phase [67] or even higher temperatures.

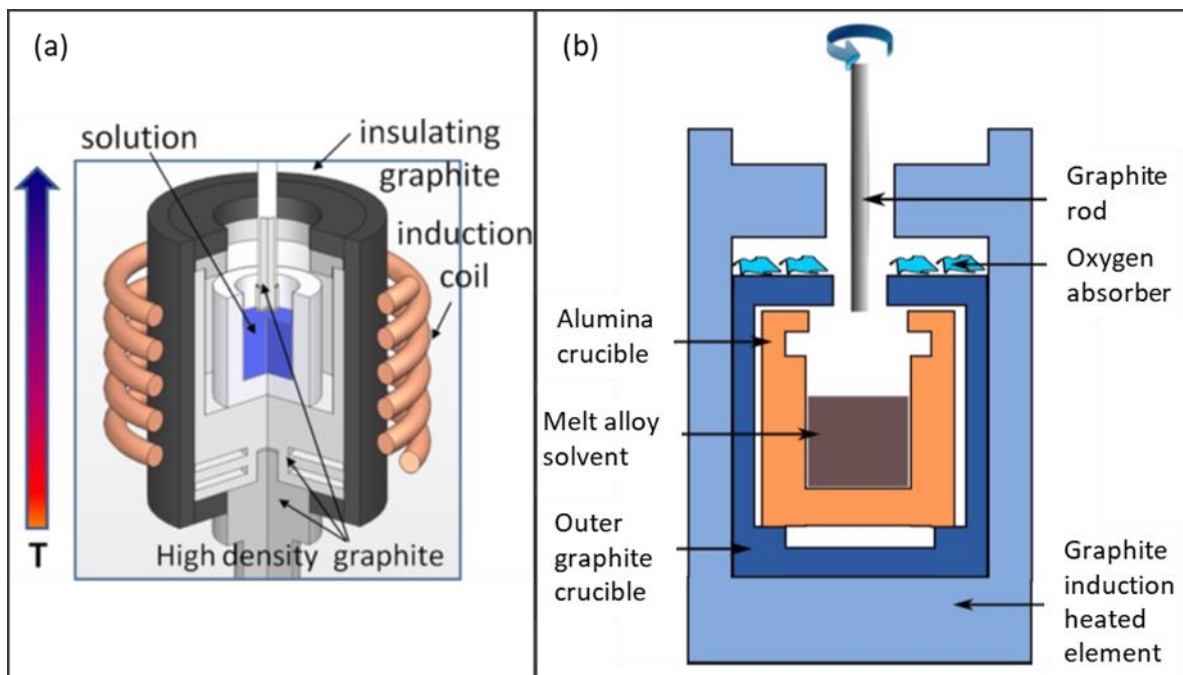


Figure 1.4 Configuration of the experimental set-up used for the high temperature solution growth process of (a) Cr_2AlC and (b) V_2AlC phases. Figures adapted from Ref. [66], [68].

The graphite reactor, as illustrated in Figure 1.4 (a), consists of two main graphite crucibles of different sizes, with graphite surrounding them as insulation

layer. An induction coil is wrapped around the walls of the large crucible and creates an electromagnetic field that inducts current within the crucible and its heating through the Joule effect. Inside the furnace, a smaller size graphite crucible is placed and serves simultaneously as the solvent's container and the carbon source for the growth procedure. Due to a thermal gradient which is applied in the liquid, the bottom part of the liquid is warmer than its upper surface [68], [69].

Nevertheless, the partial dissolution of the graphite walls which determine the carbon content in the liquid phase can negatively influence the phase quality during the growth process. First of all, the graphite incorporation from the crucible walls to the solute cannot be precisely controlled which means that for some Al containing phases and depending on the temperature, the formation of unwanted binary compounds like Al_4C_3 can be unavoidable, even during the initial heating step. Secondly, the critical temperature of $\sim 1400^\circ\text{C}$ in the solute, in combination with the unmelted transition metal owing to its higher melting temperature, can lead to rapid and very violent reactions of Al with the graphite walls in a very short time, resulting in the diminution of the walls' thickness till they finally break [66], [70].

In the Cr-Al-C case, using a graphite crucible for growing Cr_2AlC single crystals is not a problem since Cr melts before reaching 1400°C . However, for phases comprising refractory transition metals such as vanadium in V-Al-C system, with V melting point above 1400°C , the graphite crucible is not appropriate because it can result to Al-graphite violent reactions, as above mentioned. Consequently, the only option to successfully synthesize V_2AlC single crystals was to replace the crucible material with another one, more compatible with V_2AlC growth. For this purpose, Al_2O_3 was chosen and the reactor's configuration was slightly adapted (Figure 1.4 (b)).

Similar to the graphite reactor, the set-up used in V-Al-C case is also composed of two crucibles of different sizes. The outer graphite crucible surrounded by the induction coil and it is heated (and so is the Al_2O_3 crucible that contains the melt) as previously described. Another similarity, in both structures of the reactor which is also a common feature for any configuration and growth, is the use of several pieces of Ti-Zr alloy between the top part of the graphite crucible and the top of the

graphite induction heated element. This alloy acts as a pump of the residual oxygen during the growth procedure owing to Zr de-oxidizing property and the wide range of Ti solubility against oxygen and nitrogen [66].

1.1.3.4.2 Growth mechanism description

A number of melting and cooling steps (Figure 1.5) are involved in full process. They take place under Ar atmosphere with a partial pressure of $p_{Ar} = 1.5$ bar [68].

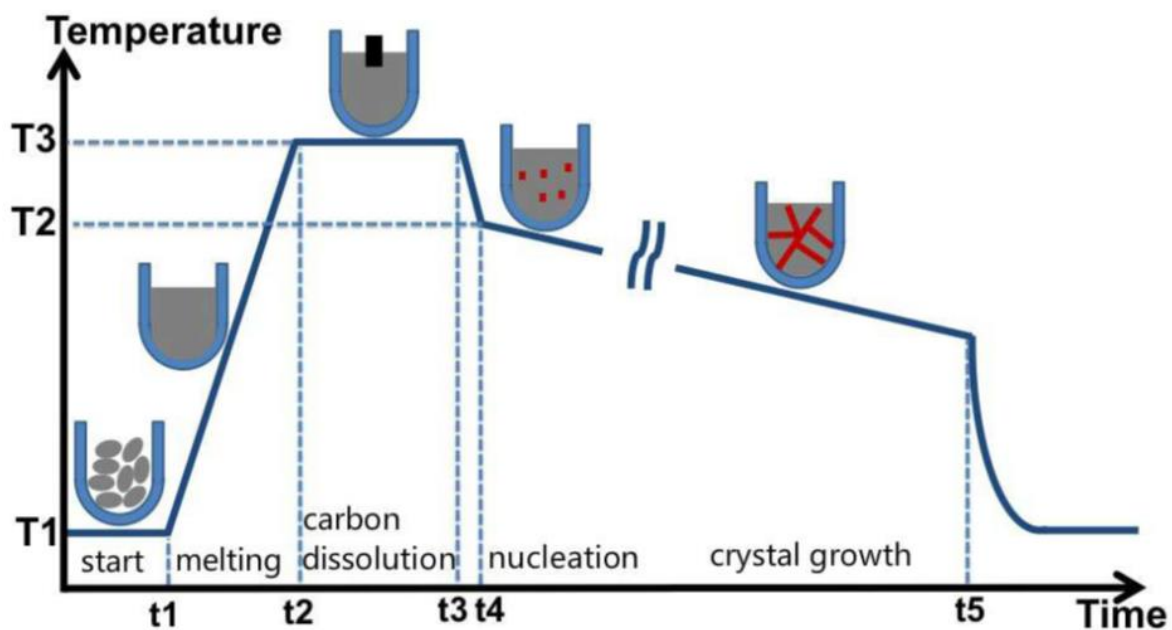


Figure 1.5 Experimental steps in the high temperature solution growth process. Figure adapted from Ref. [66].

Initially, the crucible is heated up to a temperature T_1 , in vacuum, which exceeds 1000°C (temperature controlled with a pyrometer). The temperature range where the metals melt to form the solution corresponds to T_1 - T_3 range with the maximum temperature T_3 changing, according to the binary phase diagram. For the Cr-Al system, T_3 is 1650°C while for V-Al system, the applied temperature overpass 1700°C as long as the alumina crucible can withstand it. Depending on the quantity of raw materials placed in the crucible, the time interval t_1 - t_2 can range from 40 min to 1h. As soon as the melt solvent reaches T_3 , the carbon dissolution starts by dipping a graphite rod which is continuously rotating into the

melt. When the desirable amount of carbon calculated using the ternary phase diagram, has been dissolved in the melt, then the graphite rod is pulled out, at which point the last melting step is completed. Growth continues with the critical cooling procedure where a pre-cooling stage is applied for a small time interval (t_3 - t_4), to decrease the number of nuclei in the melt. A slow cooling step, with total duration ranging from several hours to a few days, follows to complete the crystal nucleation under continuous observation of the temperature decreasing rate. Once the expected low temperature in the system is stabilised, the growth procedure is over and the crucible can be removed from the chamber [66].

One way to release the Cr_2AlC single crystals from the solidified products is to immerse the flux into diluted HCl for 1-2 hours and then clean the remaining crystals in sonication bath either in ethanol or in acetone and propanol. As an alternative, flux can be left for a few weeks in ambient conditions until it turns into powder through hydrolysis. However, in case of V_2AlC and the alumina crucible and once everything has gone well, the solidified flux can be simply taken out from the crucible by turning it upside down. An alternative way to extract the crystals can be either to cut the crucible and so the flux with a saw or to immerse the alumina crucible in concentrated HCl for a few hours. The acid treatment completely dissolves the solidified flux with the single crystals remaining almost unaffected. A sonication bath in the same solvents used in the case of Cr_2AlC is also used for V_2AlC crystals cleaning [68], [70].

At this point, it is worth mentioning the particular difference between, on one hand, high temperature solution growth techniques based on the spontaneous nucleation in the flux, and on the other hand, the seed crystal introduction in the liquid phase for instance in the Czochralski method. Spontaneous nucleation has the advantage of growing crystals from hundred percent liquid phase at high temperature, followed by a slow cooling step for preventing a subsequent nucleation by enhancing Ostwald ripening. As a result, the nuclei density is restricted in the liquid phase, giving rise to an increase of the crystals size.

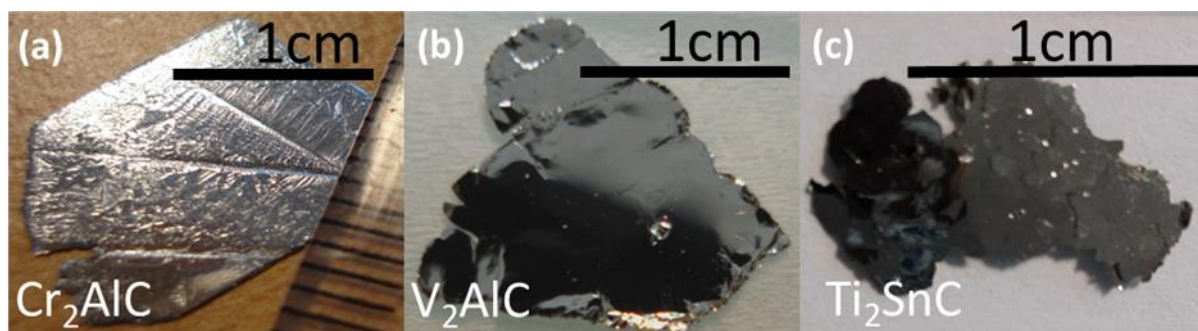


Figure 1.6 Optical microscopy images of different size of MAX phase single crystals. Figures adapted from Ref. [66].

Carbon solubility in the flux is of high importance, as it affects the high temperature solution growth process of many ternary systems, except from Cr-Al-C, by limiting the solution growth. The extremely low amount of dissolved carbon in the solution renders the growth of the Ti₂SnC phase by this technique really difficult, as measuring the carbon solubility in a reliable way at any temperature is not feasible. Consequently, considering a crucible for the solidified flux of a specific size, the final area of the platelet-like form that all single crystals have, depends mainly on carbon solubility. Thus, in our experimental set-up we managed to produce Ti₂SnC crystals at about 1cm², V₂AlC of ~1cm² and Cr₂AlC of several cm² (Figure 1.6). The platelet-like form of all MAX phase single crystals, grown by the present technique, is a consequence of highly anisotropic highly-oriented growth [70].

1.1.4 Synthesis of Mo₄Ce₄Al₇C₃ phase

During the last few years, efforts has been done in the direction of layered rare earth (RE) compounds and particularly in the synthesis of a family of 3D magnetically ordered nanolaminates that can be exfoliated to produce 2D systems by preserving the RE's magnetism. Those phases have been recently discovered in Sweden (Linköping University) [71]–[73] and their stoichiometry is described by the *i*-MAX phases, with the general formula (Mo_{2/3}RE_{1/3})AlC. The phases associated to Ce and Pr, have a different stoichiometry with a modified chemical formula Mo₄RE₄Al₇C₃ that explains the reason why these phases can be also called

4473 phases [74]. Nonetheless, in the following we focus on Ce, which was used for the purpose of the thesis.

Among RE MAX phases, some have ordered in-plane structure and are called RE *i*-MAX [72], [73]. Their structure was described in paragraph 1.1.1. One such phase, the $\text{Mo}_4\text{Ce}_4\text{Al}_7\text{C}_3$ phase, has a triclinic lattice system ($P\bar{1}$ space group) and one formula unit per unit cell (Figure 1.7 (a)). Despite the different stoichiometry, RE *i*-MAX and *i*-MAX phases have the same in-plane chemical ordering for both the Mo and RE elements. The $\text{Mo}_4\text{Ce}_4\text{Al}_7\text{C}_3$ unit cell is composed of a $(\text{Mo}_{2/3}\text{Ce}_{1/3})_2\text{C}$ layer and three Al-Ce layers, with the sequence resembling that of an *i*-MAX phase unit cell with the difference being the replacement of Al layer with a stack of three layers. In particular, the aluminum layers in *i*-MAX structures are replaced by a three layer stacking in $\text{Mo}_4\text{Ce}_4\text{Al}_7\text{C}_3$ phase consisting of (i) one Al layer with a Kagomé lattice (Figure 1.7 (c)) as that in a *i*-MAX phase, (ii) one Ce-Al plane (Figure 1.7 (e)) and (iii) a second Al plane also having Kagomé lattice but shifted with respect to the first one. The insertion of the Ce-Al plane between the two Al layers (Figure 1.7 (b)) is responsible for the shift of the second Al layer with respect to the first one and therefore leads to a triclinic symmetry in the $\text{Mo}_4\text{Ce}_4\text{Al}_7\text{C}_3$ phase.

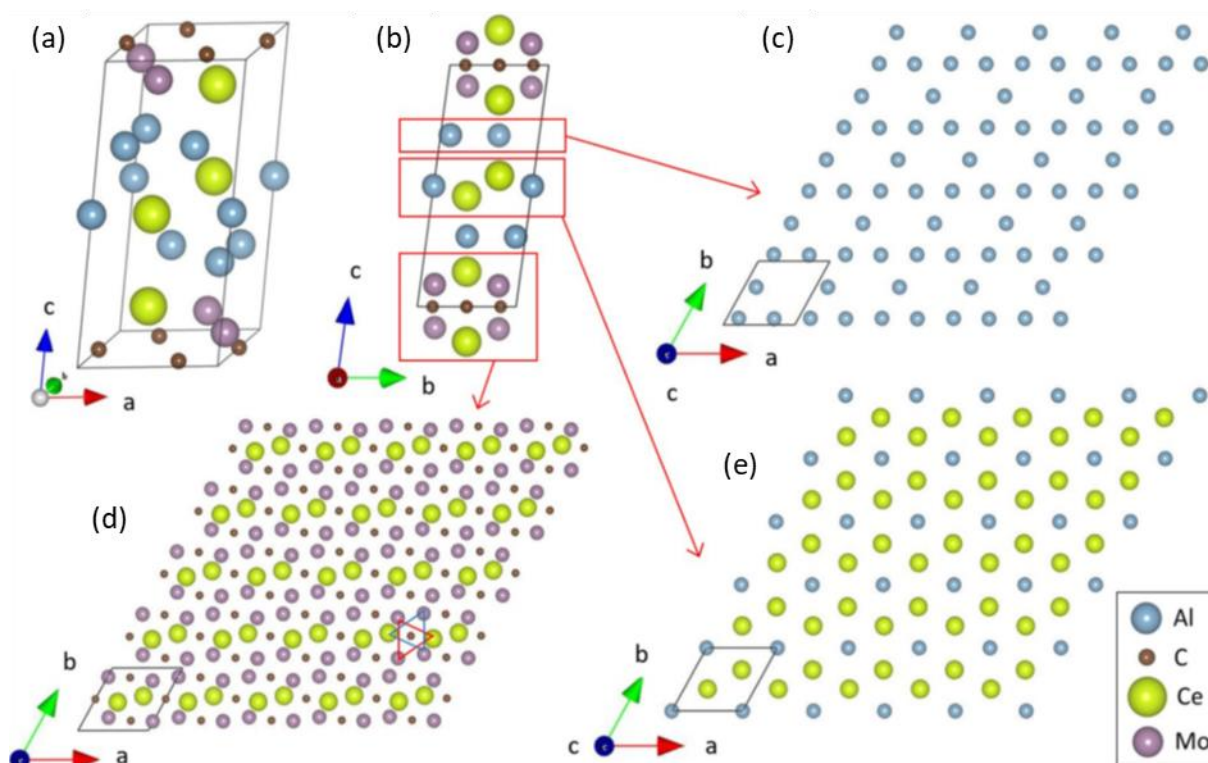


Figure 1.7 (a) $\text{Mo}_4\text{Ce}_4\text{Al}_7\text{C}_3$ crystal's unit cell, (b) crystal view along the [100] zone axis, (c) Al layer's projection in the plane vertical to [001] showing Kagomé-like ordering, (d) projection of Ce-Mo-C-Mo-Ce layers in the plane (001) where blue and red line triangles of Mo and Ce atoms compose a C-centered octahedron, (e) Ce-Al layers after projection in the (001). Figure adapted from Ref. [74].

The $\text{Mo}_4\text{Ce}_4\text{Al}_7\text{C}_3$ phase has been discovered and synthesized in powder form at Linköping University (LiU) and synthesized as relatively large single crystals at our lab in Grenoble.

Concerning the fabrication of powder samples, high purity powders of graphite, Mo, Al and Ce elements were used as the starting material and they were mixed, using the proper stoichiometry, in an agate mortar with the sintering process taking place in an alumina crucible inside a furnace. The mixture was heated up to 1500°C in flowing Ar conditions and it was kept at that temperature for a total duration of 5 hours before cooling down to room temperature. The final step of the synthesis consisted in crushing the sintered body manually until obtaining fine powders for structural characterization [74].

On the contrary, a very similar method to the high temperature solution growth process that we previously described for growing MAX phase single crystals, was used to grow a few mm^2 surface area single crystalline platelets of $\text{Mo}_4\text{Ce}_4\text{Al}_7\text{C}_3$. A sealed graphite crucible with its walls working as a carbon source was used to withstand the high temperature of 1800°C needed for Mo, Ce and Al to melt. The reactor (and thus the crucible) is heated the same way as for MAX phases growth. Once the maximum temperature is reached, it is maintained for a few hours until Mo melts and C from the graphite walls dissolves in the melt. When the melting is completed, the cooling process starts with decreasing the temperature to 1500°C within half an hour, then by slowly linearly cooling the temperature to 800°C within a few days. The latter step is crucial as it determines nucleation and growth starting from the coolest point of the flux which should be near its surface. To select the single crystals from the solidified flux there is no need of acids but only of a simple oxidation step. The flux is placed in a fume hood at room temperature until the excess amount of Ce is oxidised. This procedure normally does not exceed one or two days. The oxidation transforms the flux into a yellow powder that releases

without affecting the shiny and silver-colored single crystals. The lack of linear defects like screw dislocations and the structure anisotropy favored the growth of crystals in a platelet shape with a maximum surface area of 3 mm² and an average thickness around 100 μm. Atomic force microscopy observations indicate several steps with thickness of one unit cell, in most of the cases, separating regular terraces that could be explained by a step flow mechanism during growth [74].

1.2 Transformation of 3D bulk materials to their 2D compounds

1.2.1 MXenes

1.2.1.1 History of the MXenes

The isolation of graphene single layer, almost 16 years ago, clearly proved that transforming a 3D material system in a 2D structure, can reveal a world of novel physical and chemical properties which can establish innovative applications [75]. The dawn of graphene attracted the interest and the enthusiasm of the scientific community with many labs worldwide studying graphene's properties and working on their exploitation either by improving already known applications or by developing new ones.

Nonetheless, the interest around 2D materials was not restricted only to graphene [76] but it was rapidly expanded to other 2D systems, either already known e.g. hexagonal boron nitride (h-BN) [77], transition metal chalcogenides (TMC) or dichalcogenides (TMDC) [78] or newly discovered like oxides [79] and halides [80], with the list being enriched every often and then.

One of the recent addition to the list of 2D materials are transition metal carbides, nitrides and carbonitrides which are called MXenes and derive from their 3D precursors MAX phases after selectively etching of "A" layer during the chemical exfoliation process. MXenes, with the -ene suffix added to make the

connection with graphene, compose a rapidly growing family of 2D materials with more than 750 institutions from 50 countries working on them, counting already up to 30 experimentally studied members and dozens more theoretically predicted in different stoichiometries [81].

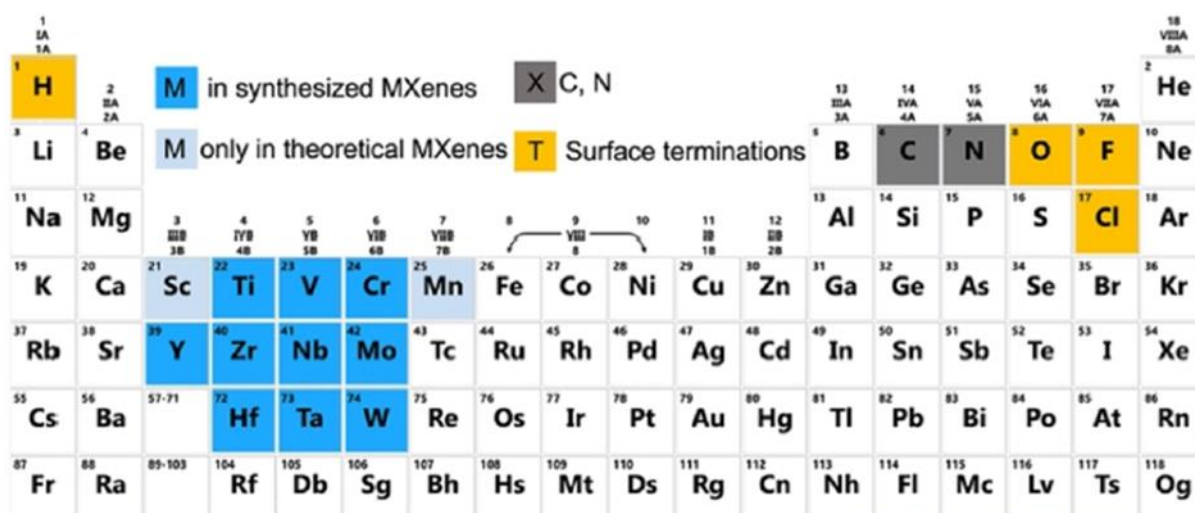


Figure 1.8 Periodic table showing the elements that have been used to date for MXenes synthesis. Elements highlighted with a light blue color have been studied theoretically. Figure adapted from Ref. [81].

The general formula of the 2D family is $M_{n+1}X_nT_z$ ($n = 1, 2$ or 3) or $M_{1.33}XT_z$ where “M” stands for early transition metal, “X” refers to C and/or N and T_z represents various surface termination e.g. -F, -O, -OH, -Cl of the 2D structure owing to the acid treatment used for synthesis.

The first MXene was discovered in 2011 at Drexel university by synthesizing and separating titanium carbide (Ti_3C_2) single layers for the first time [82], a result that paved the way for further research on the production of many new MXenes or their new subfamilies.

Ordered double transition metal MXenes, both in and out of plane, constitute one of the subfamilies that started to be synthesized in 2014 and the search for new compositions is ongoing. The last two years, with the support of computational analyses, efforts have been done on the synthesis of solid solutions either on “M” sites by mixing transition metals and/or on “X” sites by creating carbonitrides.

Last but not least in MXene subfamilies are the 2D borides, a theoretically studied 2D system to date [83], [84], with ongoing synthesis efforts from different

labs around the world and the expectation to expand even more the total number of elements combination. It is worth mentioning that the scientific groups working on MXene field have focused more than 70% of the research on the first discovered MXene, the single and multilayered Ti_3C_2 , owing to the ease of not only synthesizing its MAX phase precursor Ti_3AlC_2 but also in separating its 2D layers with chemical etching [81].

1.2.1.2 Structure of MXenes

MXenes inherit the space group symmetry ($P6_3/mmc$) and their structure from their parent MAX phases and therefore all atomic layers retain their hexagonal closed packed arrangement where “M” atoms remain organised in octahedra whose centers are occupied by “X” atoms. The only difference in the 2D derivatives is the absence of “A” layers that are selectively etched once MAX phases are submitted to the chemical exfoliation process producing the 2D nanosheets of $n+1$ number of “M” layers interleaved by n number of “X” layers ($n = 1 - 3$).

Depending on the integer n , there are three possible packing arrangements for MXenes classification: i) $\text{M}_2\text{X}-\text{M}_2\text{X}$, ii) $\text{M}_3\text{X}_2-\text{M}_3\text{X}_2$ and iii) $\text{M}_4\text{X}_3-\text{M}_4\text{X}_3$ with the “M” atomic layer sequence being different between the three arrangements. A hexagonal closed packed (hcp) stacking (ABABAB) of “M” layers has been observed in the M_2X structure, on the contrary to M_3X_2 and M_4X_3 ones where transition metal layers ordering forms a face centered cubic (fcc) stacking (ABCABC) rendering these structures less stable during MXene synthesis from their 3D precursors [85]. The importance of 2D structures stability is clear in the case of Mo carbides. For instance, DFT calculations on Mo_3C_2 and Mo_4C_3 formation energies indicated lower values comparing to their hexagonal counterpart, Mo_2C . Thus, the synthesis of the fcc structures should not be preferential [86].

A possible way to overpass the low stability problem of some $\text{M}'_{n+1}\text{X}_n\text{T}_z$ nanosheets is to properly choose and incorporate a second transition metal M'' that favors the fcc lattice formation with “X” while in parallel prevents the same structure ordering between M' and “X” atoms [86]. As a consequence, a rearrangement in the composition of the atomic layers occurs leading to the formation of the ordered double transition metal MXenes, a new class of carbides

which derive from their parent *o*-MAX and *i*-MAX phases. In particular, the MXenes obtained from out-of-plane ordered MAX phases are described from the general formula $M'_2M''X_2T_z$ and $M'_2M''X_3T_z$ with the M' transition metal being the outer layer in the 2D stacking while the M'' transition metal is interleaved between the M' atomic layers [86], [87]. In the case of in-plane ordered MAX phases and their 2D derivatives, which can be called *i*-MXenes, during chemical exfoliation of the 3D precursors the etching can be either restricted to the “A” layer removal and so obtained MXenes are described with the $(M'_{2/3}M''_{1/3})_2XT_z$ formula [87], or it can affect both “A” and M'' (e.g. Sc, Y) layers resulting finally to an ordered divacancy 2D structure described by the $M'_{1.33}XT_z$ formula [73], [88], [89].

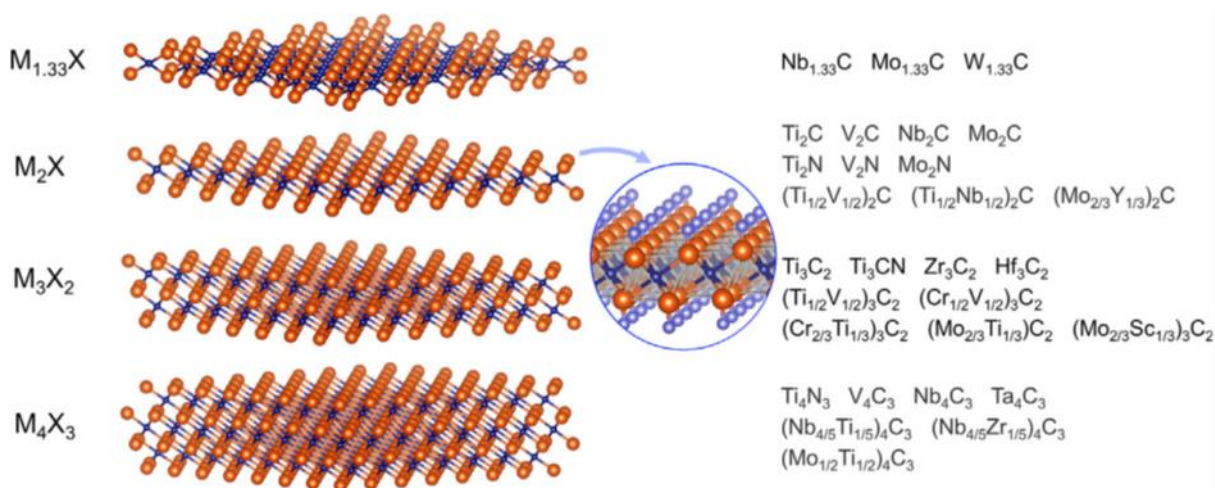


Figure 1.9 Chemical formula and structure of to date experimentally synthesized 2D carbides and nitrides (MXenes). The case of ordered vacancies transition metal layers is presented in $M_{1.33}X$ structure. The inset figure illustrates the surface terminations, T_z (-OH, -O, -F and/or -Cl), in blue, bonded to the “M” atoms. In reality they occupy the hollow sites among “M” atoms. Figure adapted from Ref. [90].

Since the synthesis of non-terminated MXenes has not been reported to date, the only way for obtaining thermodynamically stable 2D nanosheets is to arrange their surface chemistry. Consequently, the role of chemically terminated surfaces is accounted for by the term T_z appearing in MXenes general formula, and which describes the surface terminations that replace the selectively etched “A” layers upon chemical treatment of the 3D counterparts. The surface chemistry of 2D

structures mainly concerns four groups, -F, -O, -OH [91] or -Cl terminations for those MAX phases etched in ZnCl_2 solution [24].

The surface termination groups are strongly bonded to the outer transition metal layers. Strong indication is the large negative values of formation energy [92] that favors MXenes to become fully terminated and thereby to obtain local stability which can be additionally confirmed from all phonon frequencies of their 2D structure [93], [94].

Observations on MXenes' surface confirmed that termination groups are occupying three possible surface sites that are located to either on top of transition metal atoms or in two hollow sites. The hollow site (I) is found under transition metal atoms and between three neighboring "X" atoms while the hollow site (II) is localized on top of the "X" atoms (Figure 1.10 (a), (b)).

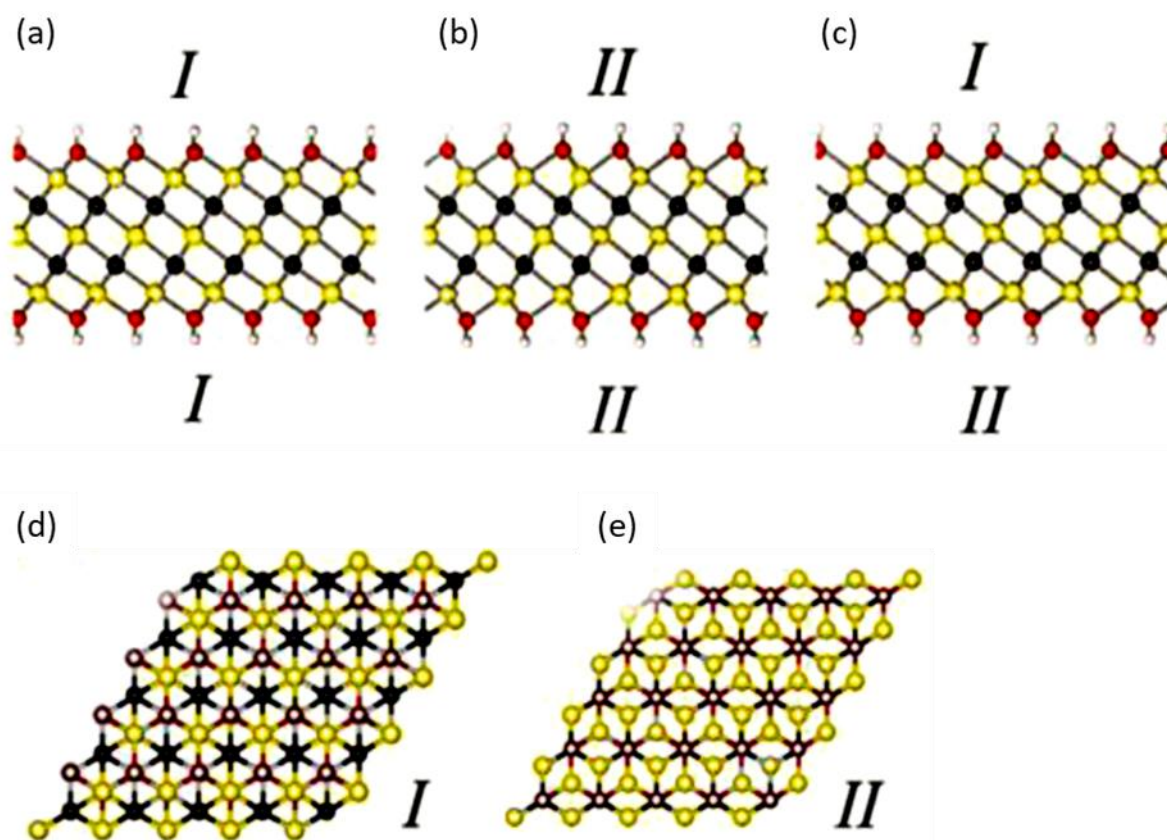


Figure 1.10 Structure and surface termination of $\text{M}_3\text{X}_2(\text{OH})_2$ on side (a)-(c) and top (d), (e) views. The numbering *I* and *II* indicate the cases of hollow sites occupied by the functional groups, -OH in our example. The "M", "X", O and H atoms are illustrated in yellow, black, red and white colored spheres. Figure adapted from Ref. [95].

According to DFT calculations and owing to the steric repulsion [96], extremely stable configuration of MXenes are formed once the surface termination groups occupy the hollow site (I) in both sides of 2D nanosheets. However, the possibility of obtaining chemically stable MXenes with termination groups localized on top of “X” atoms cannot be excluded, since the number of electrons needed to stabilize the termination groups positions is different and cannot be always provided efficiently from neighboring transition metals. Particularly, -F and -OH groups require only one electron while -O needs two from the transition metal and hence -O terminations in MXenes having “M” atoms of low valence electron number, are arranged either on site (II) or mixed site (I) and (II) [95], [92], [97] (Figure 1.10 (c)).

Surface terminations play an important role in the properties of MXenes, with one of the noticeable examples concerning the change in their electrical behavior from metallic, in the parental MAX phases and the non-terminated theoretically predicted 2D derivatives, to semiconducting in surface terminated MXenes [92], [98], [99] [100]. To identify the nature and the relative amount of the termination groups, it is necessary to understand how the etching method, the nature of “M” and “X” elements and the number of MX layers or indicator n , affect the surface chemistry.

Chemical etching of MXenes in different acids can affect the relative number of the terminated groups as well as the interlayer spacing. In the case of $Ti_3C_2T_z$ treated in HF, four times more -F terminations have been reported compared to the flakes obtained by a HCl/LiF treatment. For MXenes treated in a $ZnCl_2$ solution apart from fully chlorinated sides, an increase in the d -spacing has also been reported due to steric repulsion [101]. To date, no method has been reported that exfoliates MXenes solely with -F terminations. On the contrary, the electrochemical and hydrothermal methods can efficiently lead to -F free 2D surfaces.

Generally, after chemical treatment of MXenes, -F terminations occupy most of the space of the 2D system. Nevertheless, studies for a wide range of MXenes (Ti_2CT_z , $Ti_3C_2T_z$, Ti_3CNT_z , Nb_2CT_z , $Nb_4C_3T_z$) illustrated that with time the -F terminations were replaced by -O [91]. An additional way to modify fluorine functional group is postetching with organic bases, like TBAOH, of HF etched MXenes, resulting in a conversion of -F terminations into -O terminations, which

are more stable [102]. Thermal annealing in temperatures above 1000°C [103], [98] or reaction with alkali hydroxides [104] can also replace -F either by -O or -OH terminations. Exception to -F group modification are the factors concerning, the change in the indicator n from 1 to 2 and the change in the nature of “X” element from C to N which, mainly for Ti based MXenes, affect only the -OH to -O termination ratio [102], [90], [105].

1.2.1.3 Synthesis of MXenes

The demand for large-area 2D materials, for both applications and fundamental studies, called for a development of synthesis methods. The fabrication of 2D materials was a breakthrough in materials science field which peaked in by the mechanically exfoliated monolayer of graphene and since then the list of the newly added 2D materials is expanded every so often.

Methods for the synthesis of 2D materials can be divided into two main categories. The first one comprises bottom-up techniques, and particularly for the MXenes case, chemical vapor deposition (CVD) and plasma enhanced pulsed laser deposition (PEPLD). High quality thin films of many materials have been synthesized on top of various substrates by CVD process, however for MXenes, ultra-thin crystals of WC, TaC and at least six layers of Mo₂C [106] have already been reported to literature. However, single MXene layers could not be obtained using CVD so far. Combining the advantages of pulsed laser deposition and plasma enhanced chemical vapor deposition allowed to synthesize large lateral dimensions and ultrathin Mo₂C films with fcc structure on top of sapphire (0001) substrates [107]. By controlling the laser pulse rate, the film thickness can be adjusted from 2-25 nm, with a smooth and uniform surface. Nonetheless, PEPLD usually yields films of lower crystalline quality than those films obtained by CVD [105].

The second category of synthesis methods comprises top-down approaches, with exfoliation of 3D parent compounds being the most widely-used process. Depending on the nature of the driving force, exfoliation can be divided into two essential procedures: mechanical exfoliation, when mechanical stress is applied to delaminate the layered structure, and chemical exfoliation when chemical

reactions are implemented between the solvents' ions and the atoms of lamellar structures. A detailed description of the former will be given in the following subsection about MAXenes and in the second chapter as well. As for the latter, the basic principle of layers separation is to weaken the inter-layer bonding of the 3D structure that is immersed in a solvent, by intercalating the ions/atoms of the proper intercalant. The whole process is taking place in liquid and it is really advantageous as by properly combining the intercalant with the solvent it can lead to really high yields of 2D nanosheets [105].

The liquid exfoliation techniques that have been reported to date can be classified into four main methods. Concerning the first method, an oxidant is used to treat the layered bulk materials that are then dispersed in the proper solvent. The method was applied to the isolation of graphene oxide sheets: a combination of sulphuric acid and permanganate potassium was used as oxidants of the individual graphene sheets of graphite, which weakens the inter-layer interactions and facilitates the sheets dispersion in Ref. [108]. The second method is based on the intercalation of ions and/or molecules in the inter-layer spacing of the layered 3D structures. A tumescence induced by intercalants weakens the inter-layer bonding, resulting finally in the dissociation of the 3D solids into their 2D counterparts. Van der Waals or hydrogen bonds can be formed before 2D sheets get completely dispersed, often with the help of sonication or agitation [109]. The third method of liquid exfoliation relies on the exchange of intrinsic cations with larger size ions accompanied by intense stirring. This method affects the layer-to-layer bonding in the same way as the previous one and is mainly applied in layered systems containing cations in their structure e.g. clays, to counterbalance the charges on their surface [110]. A recently added method and last one in the list of chemical exfoliation, is based on the interaction of the bulk material with a solvent preventing re-aggregation during ultrasonic bath [105]. Such a technique has already been applied to graphite with N-methylpyrrolidone as the solvent resulting to a high yield of monolayer graphene [111].

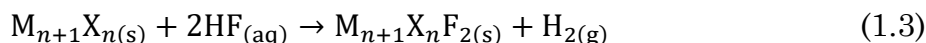
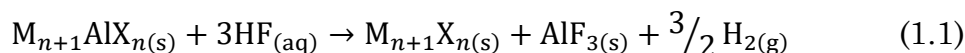
The metallic character of the M-A inter-layer bonding in MAX phases, renders the layer-to-layer attraction stronger than the dominant van der Waals bonds in most of 2D materials and thus classical chemical exfoliation ineffective. An alternative route is selective etching of the "A" layers to produce MXenes, a

mechanism which will be explained in the following, including all the synthesis variants developed so far to obtain MXenes.

1.2.1.3.1 Selectively etching

One of the first etchants used to chemically exfoliate the first synthesized MAX phase, Ti_3AlC_2 , was hydrofluoric acid (HF) which efficiently etched the Al layers producing the 2D derivative $\text{Ti}_3\text{C}_2\text{T}_z$ (Figure 1.11) [82]. Once the amount of Ti_3AlC_2 powder was immersed in an aqueous solution of 50 wt% HF at room temperature (RT), a chemical reaction between Al atoms and F ions took place, showing not only the high selectivity of HF acid but also the different chemical behavior of MAX phase bonds inside HF, with M-A bonds being more active than M-X ones.

The whole selectively etching process can be chemically described as follows [95]:



Equations (1.2) and (1.3) indicate that MXene layers do not have a bare transition metal surface but once they are produced, a spontaneous reaction starts between the surface transition metal and water molecules or F ions until the formation of -F, -O, -OH or mixed terminated surface.

The high yield in the selective “A” layer etching established HF treatment of 3D solids as the most common wet chemical etching process towards the synthesis of a large number of MXenes [112], [113], [114], [115], [86], [73], [116], [117], [118], [119], [120] but no other “A” element than Al and Si [121] could be etched so far. It should not be omitted that chemical etching is a kinetically controlled process whose performance depends on conditions like HF concentration, etching temperature and immersion time of the 3D precursors which are not uniformly

implemented to all MAX phases owing to their different stability and reactivity with the acid. Furthermore, the chemistry and structure of the parental phases affect the etching efficiency as according to experimental observations, $M_{n+1}AX_n$ with small integer n require less etching time and/or lower HF concentration. This is the case of Ti_2AlC which is completely dissolved in 50 wt% HF concentration whereas it is highly converted to Ti_2CT_z when the concentration is decreased to 10 wt% [112]. Depending on HF concentration during *i*-MAX phases etching, 2D layers of different stoichiometries can be obtained. For instance, an aqueous solution of 10 wt% HF favors the Al layers etching of the $(Mo_{2/3}Y_{1/3})_2AlC$ *i*-MAX phase, while immersing the same phase in 50 wt% HF produces the etching of both the Al and the Y layers [117]. It is of great importance to notice that extremely harsh environment during chemical etching e.g. high HF concentration, high temperature, long etching time or use of Cl_2 etchants, are not desirable for MXenes production due to over-etching which can either induce defects formation on “M” sites or totally etch “M” and “A” layers [105], [95].

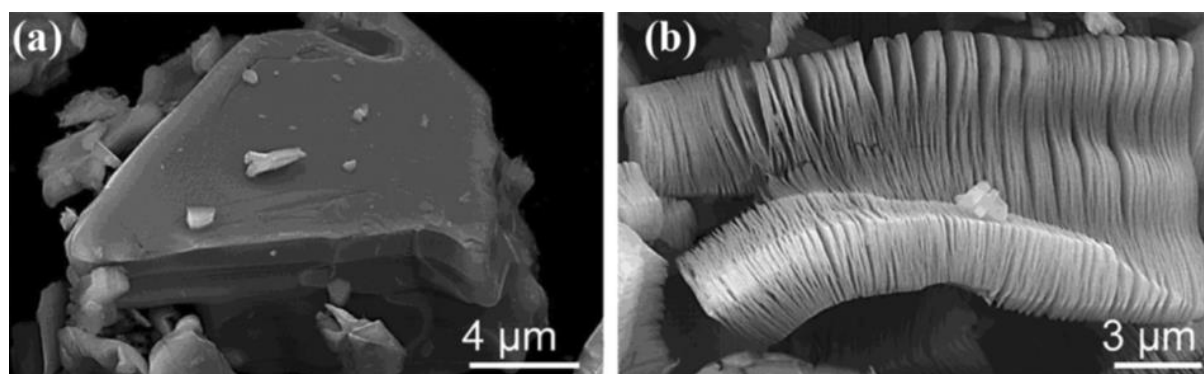


Figure 1.11 SEM images of Ti_3AlC_2 phase before etching (a) and its accordion like structure (b) obtained after selectively etching of Al layers in HF. Figure adapted from Ref. [112].

One of the concerns on the use of hydrofluorine was, from the beginning of its application as etchant for MXenes production, its corrosive behavior especially on human body and consequently its hazardous handling in the lab. Efforts to replace HF acid with lower toxicity etchants but similarly efficient and additionally to avoid -F terminations due to their problematic behavior particularly in biomedical applications, have been made so far. An aqueous solution with a mixture of

hydrochloric acid (HCl) and a fluoride salt that enables *in-situ* formation of HF, has been widely used for wet chemical exfoliation. In particular, the mixture of lithium fluoride (LiF) salt with HCl has become very popular, mainly due to the high yield of etched Ti_3AlC_2 [122]. Alternative fluoride salts like NaF, KF, NH_4F [123], [124] as well as bifluoride ones i.e. NH_4HF_2 [125] have also been successfully used in combination with HCl, without however eliminating HF traces.

Reported HF-free methods for MXene synthesis are alkali assisted (NaOH) hydrothermal etching and electrochemical etching at RT either in diluted HCl or in ammonium chloride/tetramethylammonium hydroxide (TMAOH) electrolytes. The etching conditions at which the hydrothermal procedure is implemented are harsh, rendering etching difficult to escalate, due to the high molarity (27.5 M) NaOH [126] diluted in the aqueous solution at the elevated temperature of 270°C , while HF etching method is applied in a temperature range from RT to 55°C . On the contrary, promising for large scale MXene production seems to be the electrochemical etching method with reported yields up to 90% [127]. Lately added in the list of HF-free synthesis methods, is the chemical etching process based on Lewis acidic melt, such as ZnCl_2 , that was efficiently implemented in the synthesis of both Ti_3C_2 and Ti_2C MXenes [24]. The last approach extends MXenes surface chemistry by adding one more element, -Cl, as “M” side termination and concurrently determines a new synthesis pathway for more MXene compositions.

All the aforementioned methods of wet chemical etching were successfully applied to the synthesis of MXene carbides or carbonitrides but not at all to nitrides, apart from Ti_2NT_z [128], perhaps because of the low formation energy and high cohesive energy of MXene carbides compared to their nitride counterparts [129]. An exception is $\text{Ti}_4\text{N}_3\text{T}_z$, which was produced after heating its parental Ti_4AlN_3 powders in a molten salt mixture of LiF, NaF and KF. The most efficient way to obtain MXene nitrides is the ammoniation process of their corresponding carbides with as recent examples, Mo_2NT_z and V_2NT_z derived from Mo_2CT_z and V_2CT_z carbides, respectively [130].

It is worth mentioning that wet chemical exfoliation has not only been implemented to MXene production from their parental MAX phases, but also from non-MAX precursors. In particular, in the $\text{Mo}_2\text{Ga}_2\text{C}$ phase, the structure resembles the one of 211 MAX phases, but every Mo_2C sheet is separated by two Ga layers.

Their removal leads to Mo_2CT_z MXenes [113]. In another non-MAX phase, $\text{Zr}_3\text{Al}_3\text{C}_5$, a carbon layer separates each metal (Zr, Al) layer. In this case, $\text{Zr}_3\text{C}_2\text{T}_z$ MXenes can be produced by selectively etching Al_3C_3 layers [114]. A different chemical etching approach has been reported in the recent case of $\text{Hf}_3\text{Al}_4\text{C}_6$, a non-MAX phase precursor, that can be efficiently converted into $\text{Hf}_3\text{C}_2\text{T}_z$ by firstly substituting Si on Al site and then by selectively etching the $[\text{Al}(\text{Si})]_4\text{C}_4$ layers [115]. In these few examples, wet chemical etching of non-MAX phases is a viable route to MXenes, which is all the more interesting as the corresponding MAX phase counterpart cannot be synthesized [90], [95], [105].

1.2.1.3.2 Intercalation and exfoliation

Once the step of selective etching is completed, the strong M-A bonding in MAX precursors has been replaced by weaker van der Waals and/or hydrogen bonds, which oppose to the spontaneous production of MXene mono- or few layers. Although the weak bonding in MXene layers is still two to six times stronger than in the case of graphite [131], MXene single layers can be easily exfoliated into aqueous colloidal suspensions using the proper intercalants. The etching conditions and MXenes chemical composition are two factors that affect the exfoliation process and need to be considered with care when choosing the intercalant.

Initial attempts to entirely dissolve salts, such as AlF_3 or alkali fluorides, that remain from the etching procedure and which cannot be thoroughly removed only with water washing, involved pre-washing of MXenes multilayers either in HCl or sulfuric acid (H_2SO_4) [132], [133]. Then multilayers are washed with water several times to remove the aforementioned acids and exfoliation can proceed directly by bath sonication if the etchant used to produce MXene was not HCl/LiF [82].

The poor yield in the production of the resulting colloidal suspensions by sonication [82] was strongly improved by the intercalation of cations and organic molecules in combination with mechanical stirring. Organic intercalants e.g. dimethyl sulfoxide (DMSO), tetraalkylammonium hydroxide (TMAOH), isopropylamine, hydrazine or urea for HF etched MXenes [102], [134] and Li cations for HCl/LiF chemically etched MXenes [122], [135], have been used to

penetrate between MXene sheets. When the molecules or ions of the proper size are hosted among the atomic layers, they expand the inter-layer distance thereby weakening inter-layer bonding, and leading to the delamination of MXene single layers. Additionally, the mechanical agitation either with hand shaking or with bath and probe sonication can further favor single layers exfoliation and dispersion in the solution aiming at either larger flake size (5-15 μm) and better quality (less defects) or at higher concentration of MXene solution, respectively.

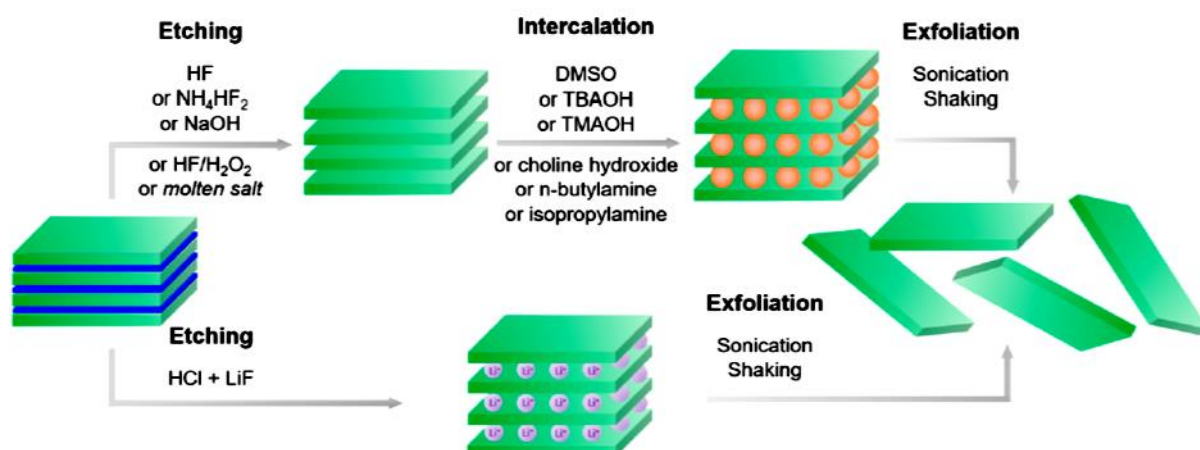


Figure 1.12 Exfoliation process steps of MXene multilayers into 2D nanosheets depending on the etching procedure. Figure adapted from Ref. [105].

The oxidation stability of colloidal suspensions clearly depends on the sensitivity of MXene nanosheets in ambient conditions and particularly in aqueous solutions containing O₂ [136], [137], as they can be instantly oxidized after exfoliation. Consequently, if MXene colloids are not directly used after delamination then to prevent their aggregation they have to be stored in deaerated water or organic solvent to avoid their transformation [95], [105].

1.2.1.4 Properties and applications of MXenes

Properties

An uncharted field of attractive properties arised with the preparation of the first MXene (Ti₃C₂T_z) and it continues to expand when new compositions of

MXenes are formed. Numerous theoretical and experimental studies revealed notable physical and chemical properties, many of which seem promising for a variety of applications.

Early studies were focused on MXenes' electronic properties. Their electrical behavior can be tuned by changing the nature of the transition metals and the surface terminations, the latter ones theoretically creating energy gaps in the flakes' band structure [92]. Density functional theory (DFT) calculations predict metallic to semiconducting band structures, in some case topologically non trivial, especially for flakes containing heavier "M" elements e.g. Mo, W [97], [138]. It is often assumed that bare MXenes behave as metals, which still awaits experimental confirmation, as MXenes synthesis without surface terminations has not been achieved to date. The way the MXenes are obtained can also affect their electrical conductivity, as large lateral dimension flakes with less defective structure (milder etching conditions, hand shaking) exhibit enhanced electronic mobility. Post synthesis treatment like thermal annealing, which can modify surface terminations [98] and/or remove intercalated species such as TBA⁺ [139], [140], can further influence MXenes' electrical behavior. Extensive experimental studies on the electronic properties of MXenes have only been conducted on Ti₂CT_z, Ti₃C₂T_z, Mo_{1.33}CT_z, Mo₂CT_z, Mo₂TiC₂T_z and Mo₂Ti₂C₃T_z so far [98], [113], [139]–[142].

MXenes mechanical properties have also attracted attention with theoretical calculations predicting the superiority of M₂X MXenes owing to their higher toughness and strength compared to their M₃X₂ and M₄X₃ counterparts [143], [144]. Nevertheless, experimental studies have been conducted to Ti₃C₂T_z MXene monolayers highlighting its Young's modulus mean value that exceeds those of graphene oxide and MoS₂ [145]. Furthermore, experiments have been extended to MXene films as well, with measurements showing that a 5 μm thick Ti₃C₂T_z paper folded in cylindrical form can withstand almost 4000 times its own weight. Combining MXenes with small amount of polymers to create composites can further increase the fracture point of the films [146].

In addition to the mechanical properties of MXene thin films, their optical response may be attractive. For very thin films produced by spin casting from MXene colloidal suspensions, light is fully transmitted in the visible region.

Featuring example is the transmittance of $\text{Ti}_3\text{C}_2\text{T}_z$ spin cast thin films that reaches up to 97% per nanometer thickness in visible range [147] and it is almost comparable to that of a graphene monolayer (97,7%) [148]. At the wavelength of 550 nm, $\text{Ti}_3\text{C}_2\text{T}_z$ and Ti_2CT_z thin films show similar transmission [149] half the one corresponding to V_2CT_z films [150]. Another factor affecting films transmittance is the size of intercalants in MXenes structure during delamination that can increase, with e.g. hydrazine, or decrease, with e.g. Na^+ , the absorbance of the films [151]. Another important parameter is, the nature of the etchant, with NH_4HF_2 etched films having lower absorbance compared to HF etched films. In general, in the spectrum ranging from visible to infrared, the light transmittance through ≈ 15 nm thick films is about 90%.

Applications

The structure of MXenes, with diverse elemental compositions and surface terminations, provides endless opportunities to tune their properties that could be the basis of a wide range of applications. The number of MXene applications has recently exploded with some of them such as supercapacitors [122], [152], electrode materials for alkali ion batteries [116], [153], [154], electromagnetic interference (EMI) shielding [155], [156], bio- and gas-sensors [157], [158], electrochemical catalytic surfaces [116], [159], hydrogen storage [160], thermoelectric materials [139], structural composites [146], [161] and photothermal therapy (tumor eradication) [162] have been studied to date. Nevertheless, the energy storage and EMI shielding applications have attracted most of the experimental studies so far.

Energy storage

High electrical conductivity, low diffusion barriers of intercalated ions between the layers and low operating voltage range are the factors that render MXenes competitive candidates to other 2D materials like graphene, for electrodes application in alkali ion (Li^+ [163], Na^+ [164], K^+ [165], Al^+ [166]) batteries. Delaminated single layered flakes are expected to exhibit higher capacity, in

comparison to the multilayered flakes, due to their higher surfaces exposed to the electrolyte [90]. According to theoretical studies, capacity and mobilities for metal ions are also higher in bare flakes as functional groups, mainly -OH and -F, restrict capacity and hinder ion transport [154], [167]. Furthermore, important for partly determining the gravimetric capacity of MXenes electrodes is the formula weight factor for which calculations predict higher gravimetric capacities for M_2X flakes, than for M_3X_2 and M_4X_3 counterparts. Confirming these predictions, experiments conducted on similarly prepared electrodes of Ti_2CT_z and $Ti_3C_2T_z$ revealed a 1.5 times higher Li^+ gravimetric capacity for the former [134], [168].

Other energy storage devices are supercapacitors. They offer smaller charge/discharge time, higher cyclability and longer lifetime than alkali ion batteries. Depending on the charge storage mechanism, supercapacitors can be classified in two main categories: pseudo-capacitors in which the Faradic charge transfer originates from reversible surface redox reactions, and electric double layer capacitors (EDLCs) where an electric double layer is generated in the interface between the capacitor's electrode and the liquid electrolyte. Generally, the Faradic charge transfer effect gives the former a higher capacitance than the EDLC [169].

MXenes are promising candidates for supercapacitors' electrodes, following a pseudo-capacitive mechanism, which, in combination to their high conductivity, leads to volumetric capacitances surpassing the previously reported record values for RuO_2 . MXenes gravimetric capacitance is superior to that of activated carbon [90], [170]. The surface chemistry of MXene flakes can significantly affect their gravimetric and therefore their volumetric capacitance. Measurements on HF etched $Ti_3C_2T_z$ flakes first subjected to functional group modifications in KOH [171], N_2H_4 [172] or DMSO [152], [153] solutions illustrated that, depending on the used electrolyte, the gravimetric capacitance values were increased by a factor of two to seven, with outstanding results coming from the use of acidic electrolytes. Experimental studies have also proved the influence of another factor, the cation's charge-to-size ratio, in the modification of the inter-layer distance between MXene sheets [173]. Especially, studies on 2D $Ti_3C_2T_z$ electrodes showed that large cations holding a low charge modify this distance more strongly than small cations holding a large charge. This cation size dependance of the inter-layer deformation suggests

the fabrication of energy storage devices with longer lifetime and limited energy losses by aiming at zero volume changes upon charging/discharging cycles [85].

Electromagnetic Interference Shielding

Electromagnetic interference (EMI) is an effect deriving from the operation of electronic circuits, associated with the emission of electromagnetic fields disturbing adjacent operating circuits. In the last decades, the technological tension for continuously smaller electronic devices and rapid operational times has increased EMI's relevance, calling for a better shielding. However, except for good shielding properties, candidate materials for such applications are expected to be lightweight and flexible so that they can be easily integrated into electronic devices [174]. The high electrical conductivity of MXenes in combination with their great advantage of being easily produced in a very thin form, led to experimental trials on $\text{Ti}_3\text{C}_2\text{T}_z$, $\text{Mo}_2\text{TiC}_2\text{T}_z$ and $\text{Mo}_2\text{Ti}_2\text{C}_3\text{T}_z$ vacuum-filtered films for EMI shielding applications [156], [175]. The three MXene films exhibited exceptional shielding properties in the gigahertz electromagnetic range, comparable to those of thin Cu layers and superior to synthetic and graphene based composites of the same thickness. Besides MXene films, the experimental study on shielding applications was extended to MXene composite films such as $\text{Ti}_3\text{C}_2\text{T}_z$ / sodium alginate very thin films [156], which showed high conductivity and good flexibility together with record shielding efficiency among all known synthetic materials with similar thickness [90].

1.2.2 MAXenes

1.2.2.1 Synthesis and structure of MAXenes

Since the discovery of MXenes, the dominant procedure for the transformation of bulk MAX phases into their 2D derivatives has been chemical exfoliation while the mechanical exfoliation of MAX phases has been reported only twice in literature so far [98], [176]. Important role in the selection of chemical exfoliation as the main synthesis pathway of MXenes, was at first, the strong metallic inter-layer M-A bond that renders mechanical exfoliation inefficient compared to the weak bonding of other 2D layered systems, like graphite. In addition, the inability of synthesizing large-size MAX phase single crystals, until recently, has further prevented the use of mechanical exfoliation.

After the recent demonstration of large-size single crystal MAX phases in our lab, by Ouisse et al. [68], [70], mechanical exfoliation was attempted again. In the last three years, the process proved successful isolating even single-layer flakes starting from single crystals of Cr_2AlC , V_2AlC , Ti_2SnC MAX phases and the $\text{Mo}_4\text{Ce}_4\text{Al}_7\text{C}_3$ phase. Significant time and efforts were spent for the optimisation of the mechanical exfoliation procedure and we finally achieved to obtain flakes with large lateral dimensions and thickness of even less a fraction of one unit cell of the parent structure. A detailed description of the implemented mechanical exfoliation technique in the MAX phase single crystals is given in the second chapter.

Contrary to the structure of chemically exfoliated flakes that is completely devoid of “A” elements, in mechanically exfoliated flakes the “A” layers are preserved, either in total or partly, even down to one single layer thickness. The general formula M_{n+1}X_n describing the chemically exfoliated MXene flakes does not hold in this case. The mechanically exfoliated flakes are instead referred to as MAXenes. The lack of solvents during mechanical exfoliation limit the surface chemistry of MAXene flakes to -O termination since the process is implemented under ambient conditions. Information about the topography of the exfoliated surface and the way it is arranged are given in the fourth chapter where the experimental results of the flakes electrical characterization are presented.

1.3 Conclusion

Numerous MAX phases have been synthesized in several forms so far and through various methods owing to a vast number of chemical elements that can be properly combined in diverse stoichiometries. To date, the absence of MAX phase single crystals rendered chemical exfoliation of bulk phases the only efficient method to obtain their 2D derivatives, MXenes, in nanosheets with uncontrolled mixing of surface terminations T_z e.g. -F, -O, -OH and -Cl. The synthesis of the single crystal form of MAX phases with the use of the high temperature solution growth technique, which was applied in our lab, paved the way to the generation of MAXenes, another 2D compound of MAX phases where “A” layers are partially or totally retained in the structure. Unlike MXenes, the MAXenes do not derive from chemical but mechanical exfoliation that is a less defective technique based on the process firstly applied to graphene isolation and which leads to larger lateral dimensions nanosheets with controlled surface terminations e.g. -O.

Chapter 2

Mechanical exfoliation of MAX phases

This chapter, deals with the mechanical exfoliation process that was initially developed to produce graphene single-layers and then expanded to other 2D materials. The remarkable contribution of SiO₂/Si substrate in the visual inspection of the exfoliated flakes is also mentioned. Next, it is demonstrated that modifications to the flakes transfer recipe render mechanical exfoliation applicable to MAX phases and the Ce 4473 phase, lamellar compounds with stronger inter-layer bonds. In the chapter's last section, our attempts to tackle the problem of glue residues onto flake and substrate surfaces after the transfer process, using several methods, are presented.

2.1 Brief overview of 2D materials mechanical exfoliation

The isolation of a graphene single-layer by Novoselov et al. in 2004 using mechanical exfoliation [177], showed the way to obtain 2D materials of single- or few-layer thickness with a high crystal quality and large lateral dimensions, compared to chemical exfoliation [178]. Additionally, mechanical exfoliation is easy to handle, and for this reason has been implanted in numerous labs around the world. The last fifteen years, apart from graphene, this method has been applied to a variety of layered materials such as h-BN, TMDC, graphene oxides and black phosphorus.

The process is simply based on an adhesive (or “scotch”) tape, the adhesive strength of which is enough to break the weak bonding of graphene layers. Owing to the “scotch” tape the mechanical exfoliation technique is also known as the “scotch tape” method [177].

One year later, in 2005, Novoselov and his colleagues tried an alternative mechanical exfoliation method. They used a fresh surface of bulk HOPG (highly oriented pyrolytic graphite) and they carefully rubbed it against the surface of another material, like writing with a pencil on the paper. The majority of the flakes remained on the surface were composed of more than ten layers, but among them single-layers of graphene were also found [179].

Among the aforementioned mechanical exfoliation techniques tried by the group of Novoselov, the “scotch tape” method prevailed on the exfoliation of various weak bonding nanolamellar materials, beyond graphite, leading to high yields of large lateral dimensions nanosheets [178], [180]–[183]. With the adhesive tape, tensile stress is applied to separate individual layers of the material while leaving unaffected the intra-layer bonding (preserving the structure of each layer). It is already known, for all layered 2D materials, that strong covalent interactions are dominant between atoms of the same layer while much weaker bonding, mostly van der Waals, is involved in the inter-layer interaction. Consequently, using a simple adhesive tape one can separate the layers producing single- or few-layer thick nanosheets with uniform surfaces.

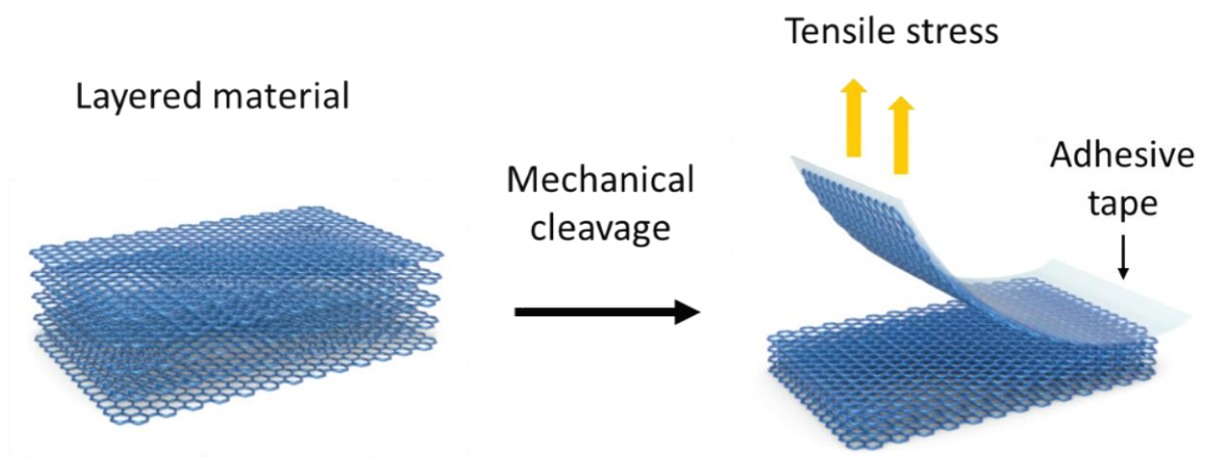


Figure 2.1 Mechanical cleavage of layered material after application of tensile stress. Figure adapted from Ref. [184].

The optimised procedure maximising the yield in few-layers and single-layers, is simply a repetition of exfoliation steps (Figure 2.2). Starting with a piece of a common adhesive tape with an adhesion strength around 2.5 N/m and with a piece of bulk graphite, e.g. HOPG, the tape is applied on the top shiny surface of the bulk. After firmly pressing the tape for a few seconds, using either a tweezer or the finger, and owing to the weaker inter-layer bonding of the structure compared to the tape's adhesion force, the tape is gently pulled apart and it peels off thick layers of graphite. The part of the tape with the graphite layers is refolded on a clear part of the adhesive side of the tape while a firm pressure is applied and keeps together both parts for several seconds. Finally, the tape is again pulled apart, separating the two parts of the tape and thus exfoliating the graphite layers. The exfoliation steps are repeated several times. The process is stopped when the thin shiny layers of exfoliated graphite cover most of the adhesive area of the tape giving it a grey color. Since hardly any bare tape areas remain, very few glue residues from the bare scotch surface are left on the substrate, in the next step of transferring the flakes to a substrate. A p-type or n-type doped silicon substrate with a thermally prepared SiO₂ of around 300 nm on top is used as the substrate. It is firstly washed in acetone and then in isopropanol in ultrasonic bath to remove all surface impurities and increase the adhesion of the substrate so as to improve the yield of the transferred flakes. Using a tweezer, the SiO₂ side of the substrate is brought in contact with part of the graphite/graphene-covered area on the adhesive tape, next it is firmly pressed either by the tweezer or by the finger for a few seconds and then the tape is gently removed with graphite flakes of different thicknesses remaining on the substrate [185].

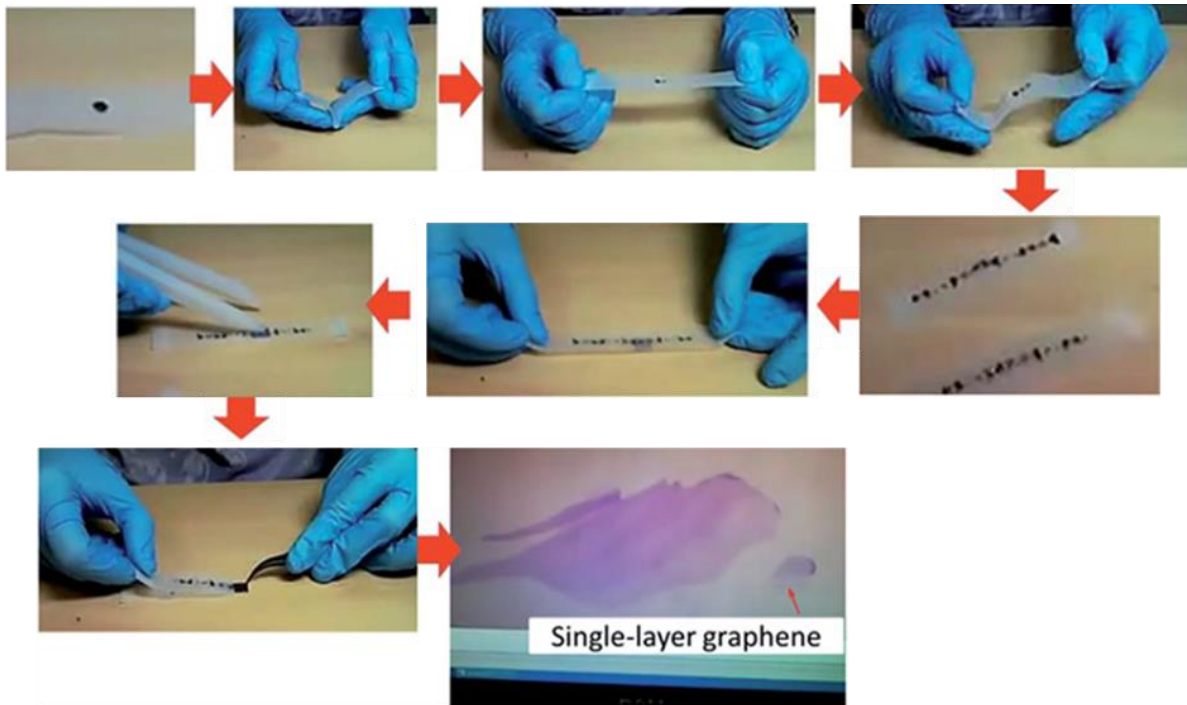
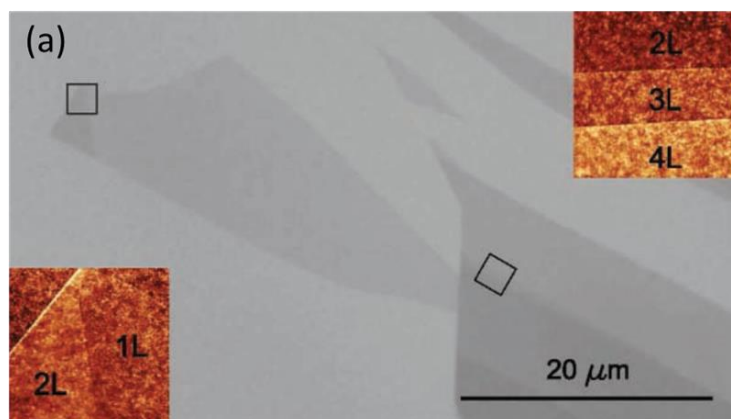


Figure 2.2 Mechanical exfoliation steps of HOPG using the “scotch tape” method. Figure adapted from Ref. [180].

The efficiency of the adhesive tape process in graphene atomic layer isolation is rather low, yet the thinnest layers (including single-layer) are readily detected with standard optical microscopy owing to their characteristic contrast, thanks to a fortunate optical interference effect (see below). This rendered mechanical exfoliation, with the sequence of previously described steps, effective in the preparation of monolayers for various van der Waals structures. Indicative examples are the exfoliated flakes of h-BN [182] and MoS₂ [181] monolayers with large lateral dimensions.



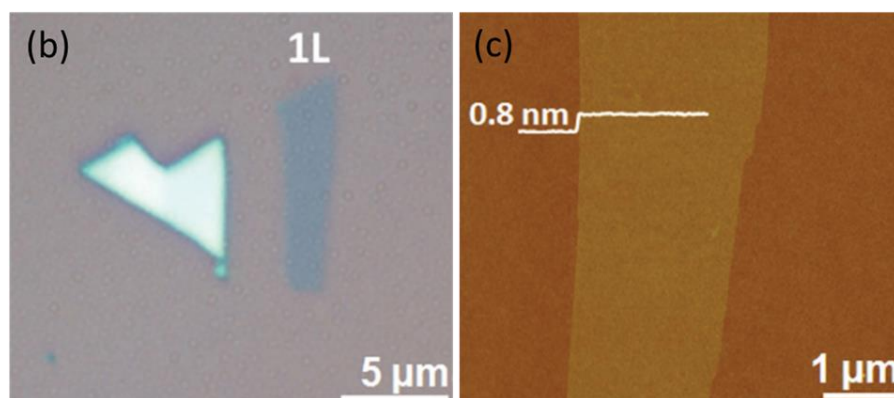


Figure 2.3 (a) Optical microscopy image of single layer (left) and few layers (right) of mechanically exfoliated h-BN crystal on top of 290 nm SiO₂ on a Si substrate. The surface topography of the square (3.5 x 3.5 μm²) regions on top of h-BN sheets, measured by AFM, is illustrated in the insets. Figure adapted from Ref. [182]. Optical microscopy image (b) and the corresponding AFM image (c) of mechanically exfoliated MoS₂ single layer (0.8 nm thickness) on top of 300 nm SiO₂ on a Si substrate. Figure adapted from Ref. [181].

Even if mechanical exfoliation has become extremely popular in numerous labs, it has significant drawbacks, imposed by the use of adhesive tape. Additionally to the low yield in single- or few-layers of the parental exfoliated bulk, the adhesion residues on the flake surface should also be considered after the exfoliation process. Usually, the direct contact of the adhesive tape with the substrate during the flakes transferring procedure releases a critical amount of glue on the surface of both substrate and flakes that can hinder the detection of thin flakes with the optical microscope. To overcome the problem of remaining glue residues, different approaches have been implemented so far, such as chemical solvents (e.g. acetone, isopropanol, ethylbutyl acetate) cleaning [183] and thermal annealing under vacuum or N₂/H₂ conditions [186], [187]. Furthermore, mechanical exfoliation methods of 3D bulk crystals either onto viscoelastic materials like polydimethylsiloxane (PDMS) and subsequent flakes transfer on the substrate (stamping process) [188] or by using stamp-on-tape method (SOTM) [189] have been reported as alternative ways for obtaining pristine thin nanosheets. Each of these approaches come with specific limitations (only partial removal of residues [183], [186], [187], structural defects that can be induced by thermal treatment

[186], etc). The widely applicable procedures to various 2D materials remain so far the chemical cleaning and the thermal annealing.

The detection of single flakes on the substrate is all the easier as the amount of glue is lower. Many characterization techniques such as AFM, SEM, TEM could be used to locate and identify single-layers of 2D materials on Si substrates, but optical imaging remains the simplest, fastest non-destructive method [190]. Single-layer flakes absorb a bit more than 2% of white light, hence their detection is in principle challenging. In the case of a SiO₂/Si substrate however, the visible light reflected at the Si surface and at the graphene flake interfere constructively for an oxide thickness around 300 nm (of the order of visible light wavelength). This greatly improves the contrast of the graphene flakes, which strongly depends on the flake thickness (because thin flakes of different thickness have very different reflectivities) [190], [191].

Detailed analysis using Fresnel equations allowed to determine the thickness of the oxide layer that optimizes the contrast of single-layers. The flake-substrate system that was used in the contrast calculations was described as a layer stacked structure composed of air with refractive index n_0 , the nanolayer with thickness d_1 and refractive index n_1 , the SiO₂ with layer thickness d_2 and refractive index n_2 and the Si substrate with refractive index n_3 (Figure 2.4) [190].

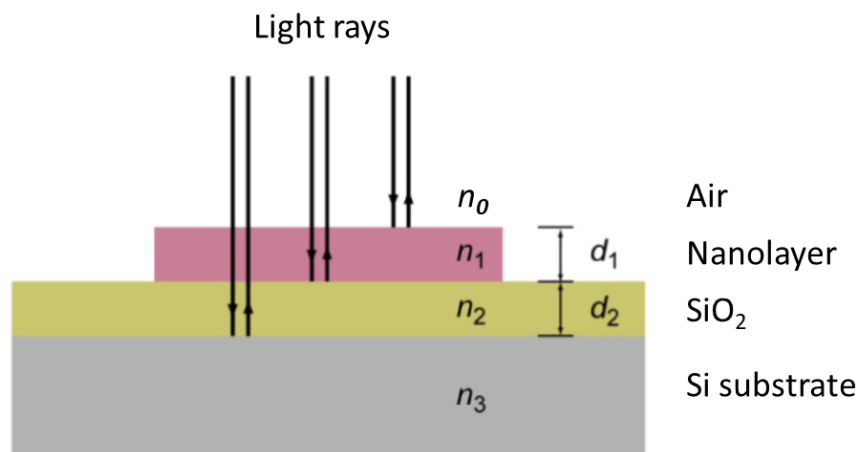


Figure 2.4 Optical reflection and transmission paths of light rays reflected/transmitted at different interfaces of a (TMDC or graphene) nanolayer/SiO₂/Si trilateral. The nanolayer has a thickness d_1 and a refractive index n_1 , the SiO₂ layer has a thickness d_2 and a refractive index n_2 , the Si substrate is

considered infinitely-thick and has a refractive index n_3 . The refractive index of air is n_0 . Figure adapted from Ref. [190].

According to Fresnel theory for normal light incidence, the reflectivity of the nanolayer is described by the following equation:

$$R_{nanolayer} = \left| \frac{r_1 e^{i(\varphi_1 + \varphi_2)} + r_2 e^{-i(\varphi_1 - \varphi_2)} + r_3 e^{-i(\varphi_1 + \varphi_2)} + r_1 r_2 r_3 e^{i(\varphi_1 - \varphi_2)}}{e^{i(\varphi_1 + \varphi_2)} + r_1 r_2 e^{-i(\varphi_1 - \varphi_2)} + r_1 r_3 e^{-i(\varphi_1 + \varphi_2)} + r_2 r_3 e^{i(\varphi_1 - \varphi_2)}} \right|^2 \quad (2.1)$$

with:

$$r_1 = \frac{n_0 - n_1}{n_0 + n_1}, \quad r_2 = \frac{n_1 - n_2}{n_1 + n_2}, \quad r_3 = \frac{n_2 - n_3}{n_2 + n_3} \quad (2.2)$$

being the refractive indices. The factor $\varphi_i = \frac{2\pi n_i d_i}{\lambda}$ refers to the phase shift induced by the refraction of light in different medias [190]. In the absence of flake onto the oxide, the refractive index of the flake is replaced by that of air ($n_0 = n_1 = 1$) and so reflectivity is:

$$R_{SiO_2} = \left| \frac{r'_2 e^{i\varphi_2} + r_3 e^{-i\varphi_2}}{e^{i\varphi_2} + r'_2 r_3 e^{-i\varphi_2}} \right|^2 \quad (2.3)$$

with:

$$r'_2 = \frac{n_0 - n_2}{n_0 + n_2} \quad (2.4)$$

being the refractive index of light at the air-silicon oxide interface [190]. The combination of (2.1) and (2.3) equations defines the absolute value of the optical contrast [190], [191] that is written as follows:

$$Contrast = \left| \frac{R_{SiO_2} - R_{nanolayer}}{R_{SiO_2}} \right| \quad (2.5)$$

Optimal SiO₂ thickness were sought for, as a function of the 2D nanosheets thickness, to obtain optimal optical contrast. High values in excess of 10% were reached for 90 nm and ~280 nm thick oxides [190], [191]. Illumination in the green color range, which is one of the three color channels that are used in a typical color camera, further increased the contrast values to 25% - 30%, in the case of dichalcogenides [190], for the aforementioned thicknesses.

2.2 Mechanical exfoliation of MAX phase and Mo₄Ce₄Al₇C₃ single crystals

As far as we were aware when starting our work, the mechanical exfoliation had never been attempted for materials others than van der Waals-bonded ones. A stronger, than van der Waals, inter-layer bonding on layered bulk materials was thought prohibitive for the isolation of single-layer or even few-layer sheets by the “scotch tape” method. In the case of MAX phases however, the large size of single crystals grown with a well defined composition, (see chapter one) seems to render the standard chemical exfoliation process established for smaller flakes ineffective. To produce high quality thin flakes of phases such as Cr₂AlC and Ti₂SnC, mechanical exfoliation appeared as the only option.

Inspired by the exfoliation recipe for graphite, (Figure 2.2), we attempted exfoliation of millimeter-size bulk MAX single crystals using a piece of adhesive tape with similar adhesive strength (2.5 N/m) as that used for graphite exfoliation. The first repetitive exfoliation steps were encouraging, yet the efficiency lead to crystal splitting, the efficiency of the exfoliation procedure is greatly limited and decreases as the number of exfoliation steps is increased. Due to the strong bonds between transition metal (M) and inter-layer (A) atoms, the MAX phases do not have such a strong cohesive anisotropy as van der Waals solids like graphite, and thus the cleavage within the x-y plane, of a uniform “A” layer from the “M” one is rare. Consequently, cleavage leads to the presence of steps and terraces, with every step height being equal to an integer number of half unit cells ($c/2$) [70]. An

increase in the number of exfoliation steps subsequently increases the crystal roughness, which can be visible under an optical microscope (Figure 2.5 (a)). Roughness eventually prevents good adhesion of the remaining crystals to the tape so that the exfoliation process becomes inefficient after a few steps only.

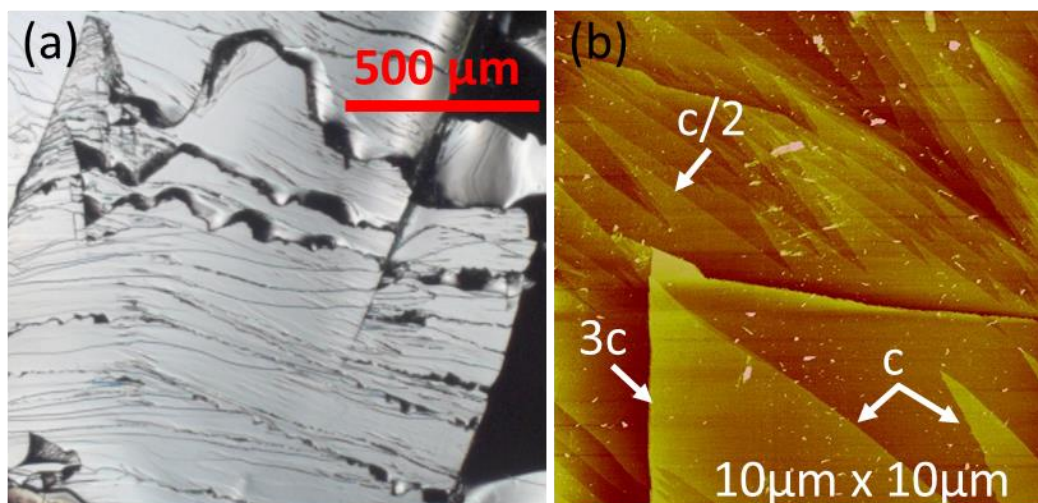


Figure 2.5 Optical microscopy image (a) highlighting the roughness of the cleaved surface of a millimeter size Cr_2AlC crystal. Atomic force microscopy (AFM) image (b) of the crystal's surface topography illustrating the tear shape steps formed after the cleavage. The step thickness is illustrated as an integer number of the Cr_2AlC unit cell c , along z axis. Figure adapted from Ref. [70].

Hence, contrary to our expectations, it turned out that large size single crystals were inappropriate for mechanical exfoliation with an adhesive tape. To overcome this problem, we tested smaller and thinner crystals which require less exfoliation steps until reaching the targeted low thicknesses. In the case of Al-based and Sn-based single crystals, to properly select the desirable small size, we etched the solidified growth flux in HCl and filtered it to retain all crystals. Then, we managed to organise the crystals in categories according to their lateral size, using a sieve shaker. This way, we could use crystals with lateral size below $50\ \mu\text{m}$, from 50 to $100\ \mu\text{m}$, 100 to $200\ \mu\text{m}$, 200 to $300\ \mu\text{m}$, 300 to $500\ \mu\text{m}$ and above $1\ \text{mm}$. Empirically, we found that the optimal lateral size of single crystals for mechanical exfoliation is between $100\ \mu\text{m}$ and $300\ \mu\text{m}$ (Figure 2.6).

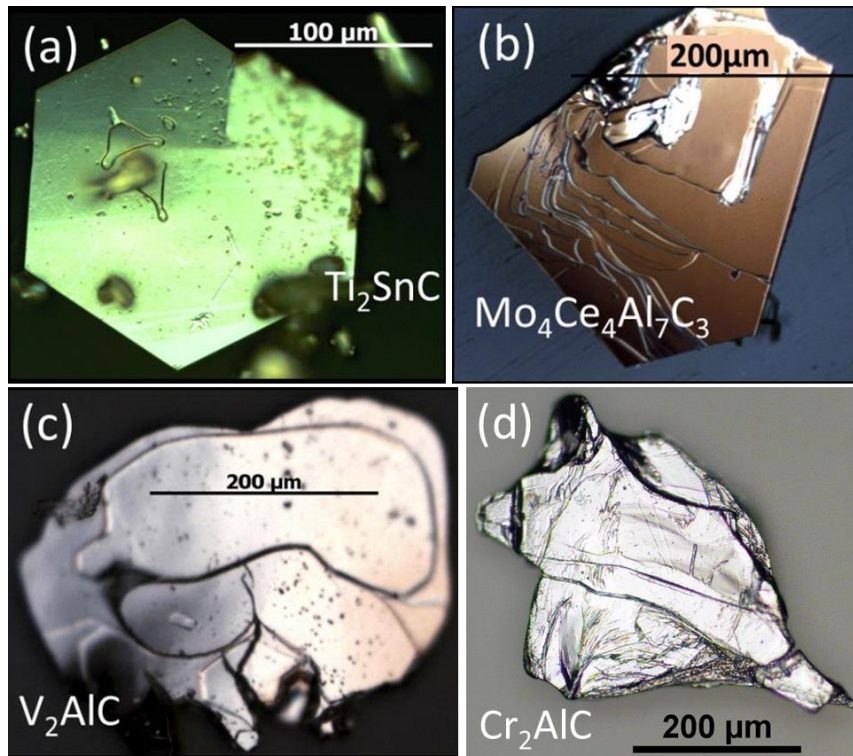


Figure 2.6 Optical microscopy images of MAX phase single crystals with the suitable lateral size for mechanical exfoliation (100 μm to 300 μm).

A few tens of small crystals were initially put on the adhesive part of the same adhesive strength tape used for graphite exfoliation and after ten exfoliation steps by folding and unfolding the tape, as it was described for graphite's exfoliation recipe, we produced flakes. The flakes were transferred on Si substrates on top of which a 285 nm, thermally prepared SiO_2 , had been grown. Prior to flake transfer, the SiO_2/Si wafer-scale substrates were cut in squares of 6 x 6 cm^2 , they were cleaned in a 2 minutes ultrasonic bath firstly in acetone and then in isopropanol and they were dried out under the flow of N_2 gas. It was already reported in literature that similar to all 2D materials, MAX phases flakes of even a single-layer thickness can be detected onto 285 nm SiO_2 layer in visible light, consistent with Fresnel's theory [192]. In particular, after having transferred the flakes on the substrate, in an optical microscope we observed a distribution of nanosheets with different colors that correspond each to different thicknesses. We also observed some glue residues from the adhesive tape. According to Fresnel's theory, under visible light irradiation the flakes with intense light colors are thick flakes while the thinner ones appear as dark color areas (deep blue and purple color). Our

interest was focused on the optical detection of the thin flakes and their position recording through their x, y coordinates.

The tapping mode operation of atomic force microscopy (AFM) was used to measure the surface topography of every thin flake first identified optically. The accuracy of the AFM in the measurement of the flake thickness helped us to establish empirically a correlation between flake thickness and its optical contrast.

After several exfoliation trials, we noticed that the transferred flakes on SiO₂/Si substrates had minimum thickness around 12-15 nm and that their thickness was not homogeneous. Apart from the thick flakes that were distinguished by an intense yellow or light blue color, several colors were observed on the surface of the majority of flakes indicating an inhomogeneous thickness along their surface that can be described as a sequence of various height terraces or steps (Figure 2.7 (a), (b)). Usually, some terraces or steps of the flake surface were observed to have the lowest thickness among the flakes measured on the substrate (parts of flakes with red arrows in Figure 2.7 (a), (b)). Exception to this observation was a restricted number of flakes, which had a uniform surface of the minimum measured thickness (12 – 15 nm) but their lateral dimensions did not exceed 5 μm (bottom right in Figure 2.7 (b)).

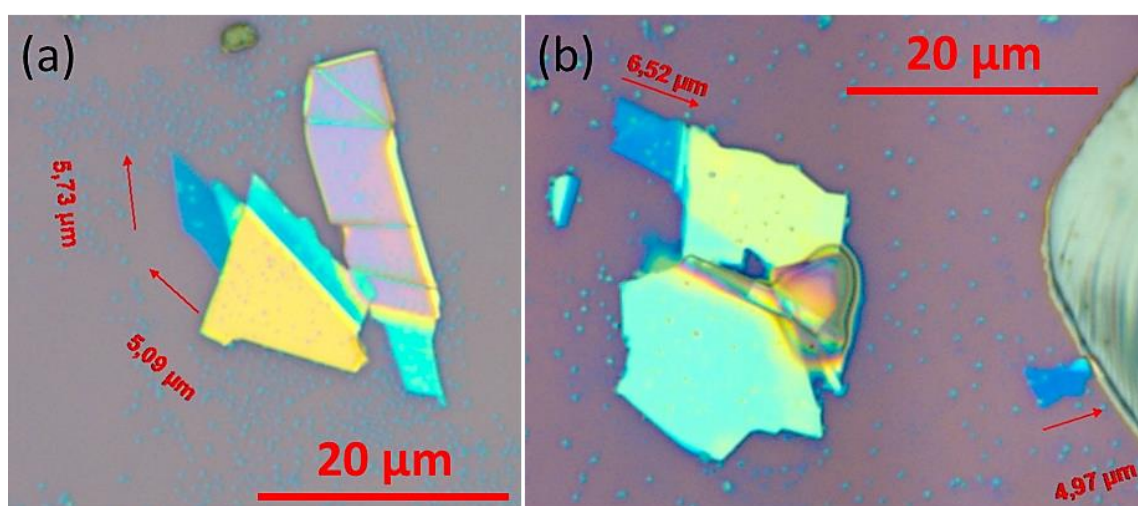


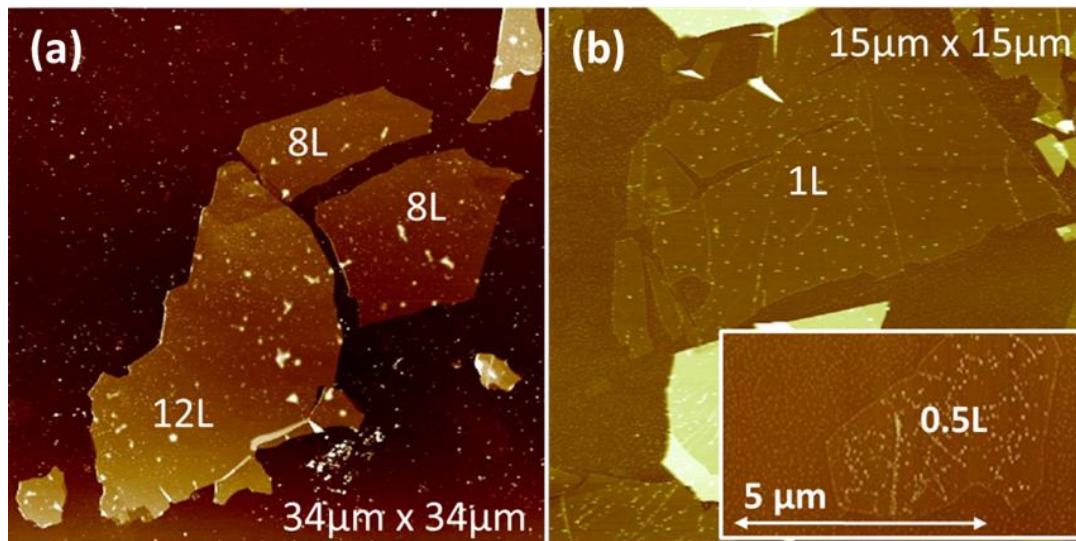
Figure 2.7 Optical microscopy images (a), (b) of Cr₂AlC flakes onto a SiO₂/Si substrate. The color difference indicates different flake thicknesses. The small spots dispersed across the surfaces of the substrate and flakes are glue residues.

Apparently, our exfoliation procedure was not efficient to produce very thin and homogeneously thick flakes, regardless the number of folding/unfolding steps. The adhesive strength of the tape being used was sufficient to exfoliate uniformly the layers of the structures with van der Waals bonds but not strong enough to break the inter-layer (metallic) bonding between the “M” and the “A” layers of the MAX phase. To select the adhesive tape with the proper strength for breaking uniformly the inter-layer metallic bonds, we made numerous exfoliation trials with tapes of different adhesive strength. Our efforts finally indicated that an efficient adhesive tape for producing MAXenes should exhibit an adhesive strength around 4.8 N/m, almost twice the value used for exfoliating 2D materials with weak inter-layer bonding.

The first exfoliation trials with the new adhesive tape led to MAXenes with homogeneous thickness along the flakes surface and a minimum value around 3-4 unit cells but the lateral dimensions were not exceeding 7-8 μm . To solve the problem of these small lateral sizes, we tried to increase the yield of the exfoliated flakes by enhancing the efficiency of the transferring mechanism. Thus, we modified some steps of the standard exfoliation recipe mentioned for graphite and particularly the step of the flakes transfer. Once the substrate was cleaned in acetone and isopropanol as previously mentioned, the tape with the exfoliated flakes was brought in contact with the substrate and it was gently pressed on the substrate for a few seconds. Instead of directly peeling off the tape, we placed the tape-substrate system onto a hot plate to mild anneal it for 2 minutes at 100°C, in ambient conditions. The increase of temperature in the substrate-flakes interface enhances the adhesion of the flakes on the SiO_2 surface, which may be altered by the glue residues that exist onto the flakes surface after the repeatedly folding/unfolding of the tape. Once the mild annealing is completed, the substrate with the adhesive tape is cooled down to room temperature. It could be assumed that a pressure difference between the substrate-flakes interface and the ambient air, owing to the annealing and the cooling step, could promote a more uniform contact of the flakes surface with the substrate. Thus, according to the explanation in reference [178], the flakes transfer yield can be improved.

The exfoliation procedure is completed once the adhesive tape is slowly removed from the substrate after the cooling step. The optical observation revealed flakes with lateral size ranging from a few μm^2 up to a few tens of μm^2 and thickness down to a few unit cells. Nevertheless, concerning the flakes with a few μm^2 lateral size and thickness less than one and a half unit cells, we realised that estimating qualitatively their thickness is often impossible with the optical microscope. The flake-SiO₂ optical contrast is too weak and the flakes are then almost invisible. The use of AFM seems imperative in such cases, as except from measuring the flakes height profiles, it often contributes to the detection of single-layer flakes and particularly those found close to thicker ones, as it happened to our case (Figure 2.8 (b) inset).

Hundreds of flake height AFM measurements revealed a sequence of discrete height values, separated by an integer number of half unit cells. The smallest observed thickness is $0.5L$, where L refers to one unit cell thickness. The flakes with lateral size up to a few μm^2 were found to have thickness close to $1L$, $1.5L$ and $2L$ while flakes with lateral dimension exceeding $11\text{-}12\ \mu\text{m}$ were usually thicker with their thickness ranging from $4L$ to $12L$ (Figure 2.8).



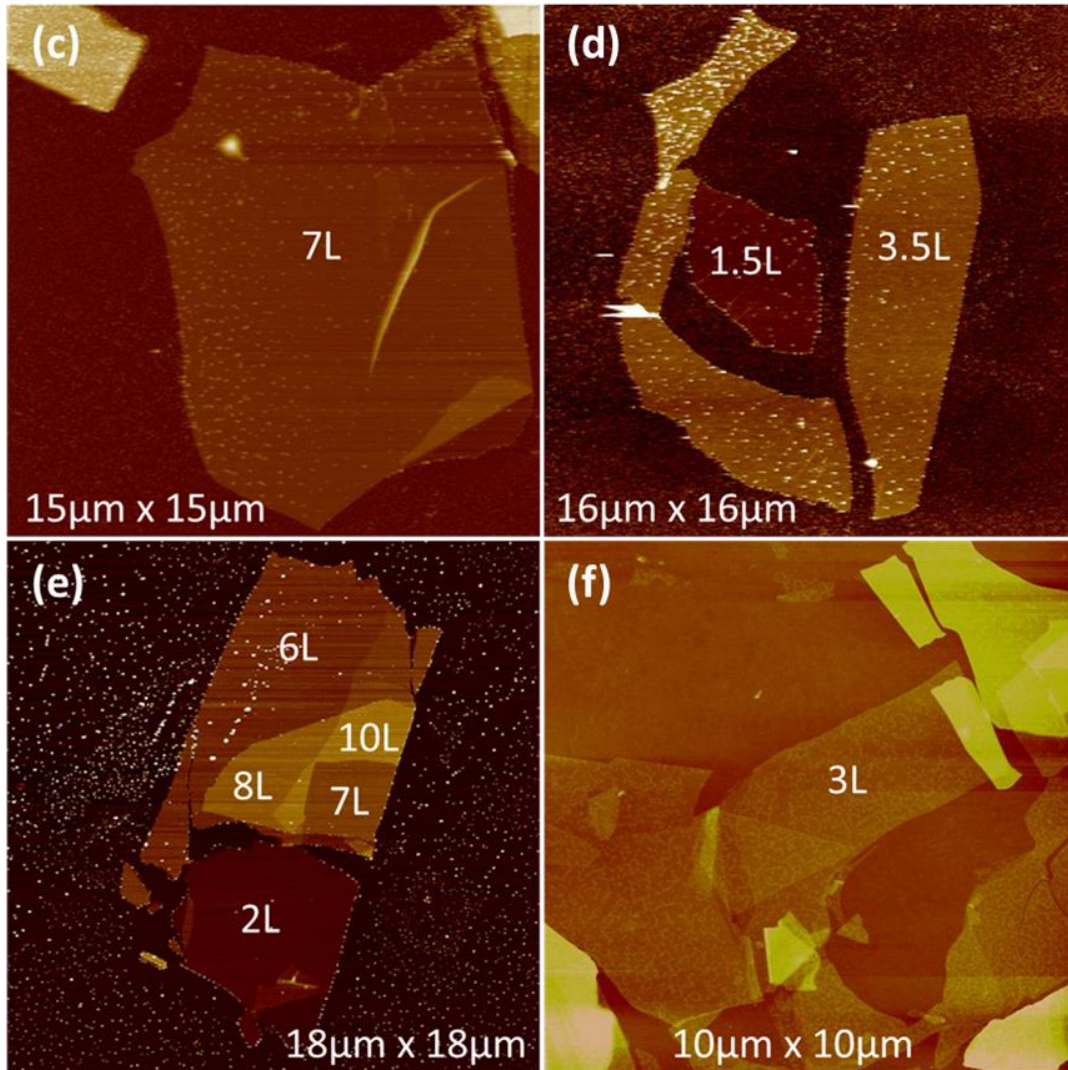


Figure 2.8 AFM topography images of flakes with various thicknesses and lateral sizes, obtained by mechanical exfoliation of MAX and Ce 4473 phases. (a) - (b) V_2AlC flakes with the thinnest one being (0.5L), (c) - (d) Cr_2AlC flakes, (e) Ti_2SnC flake, (f) $Mo_4Ce_4Al_7C_3$ flakes (the thinnest one being 3L).

We are presumably the first to mechanically exfoliate single crystal MAX phase in the form of (half-)monolayer-thick flakes with large lateral size. This is a proof that mechanical exfoliation is not only applicable to van der Waals structures, but also to lamellar structures with stronger (here, metallic) inter-layer bonding. Besides, the large lateral dimensions and the low thickness of the produced MAXenes, as they will be called according to the description in chapter 1, another advantage of the strong adhesion tape that is worth mentioning, is the efficiency in producing flakes with homogeneous thickness (Figure 2.8), as a prerequisite for the device fabrication and the electrical properties measurements.

The accuracy of AFM was valuable for a quantitative estimation of the flakes thickness. However, in all flakes and especially flakes with thickness less than $3L$, the presence of the glue residues atop or below the flakes becomes the limitation factor in the precision of the measurement. Besides, the glue residues hindered the fabrication of good ohmic contacts. Several approaches have been used to remove the glue residues. In the end, they could only be partially removed.

2.2.1 Attempts to remove glue residues from the flakes surface

Contrary to the transfer of graphene flakes on SiO_2/Si substrates, by which the reported flakes are exfoliated during the last pulling tape operation, the transfer of MAXene flakes, as it was said, needs a mild thermal annealing step to release the flake from the stronger adhesive tape that is used in exfoliation. Consequently, in the case of graphene, the overall amount of glue residues is generally limited, while for MAXenes a much larger amount of glue is detected onto both flakes and substrate surfaces. Especially for flakes, a large part of their surfaces is usually covered by glue residues which rendered the optical observation of the flakes as well as their thickness estimation with AFM impossible (Figure 2.9).

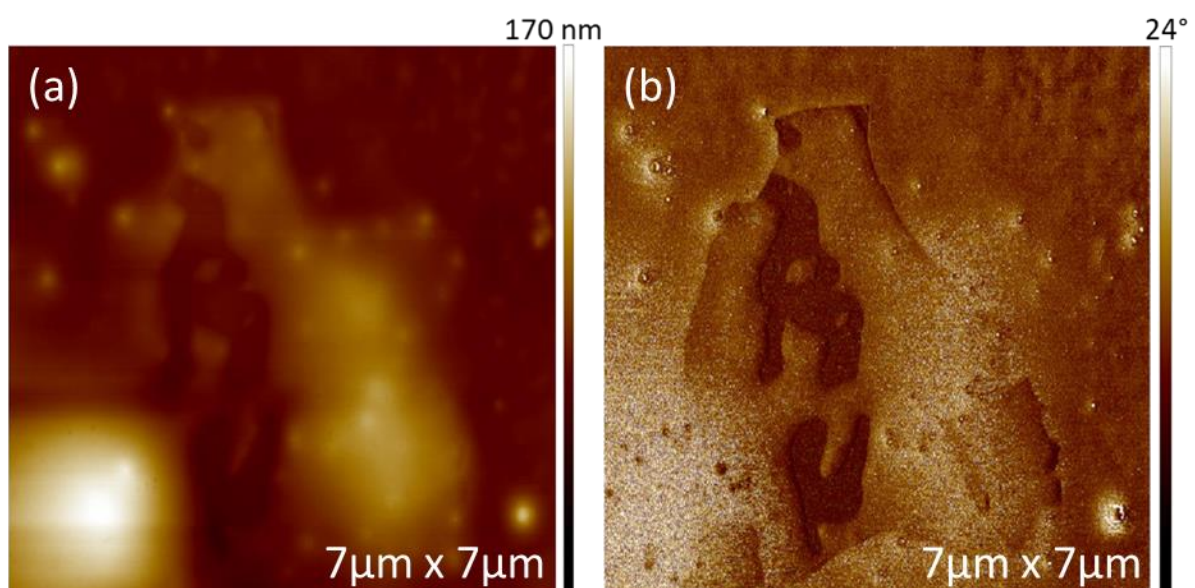
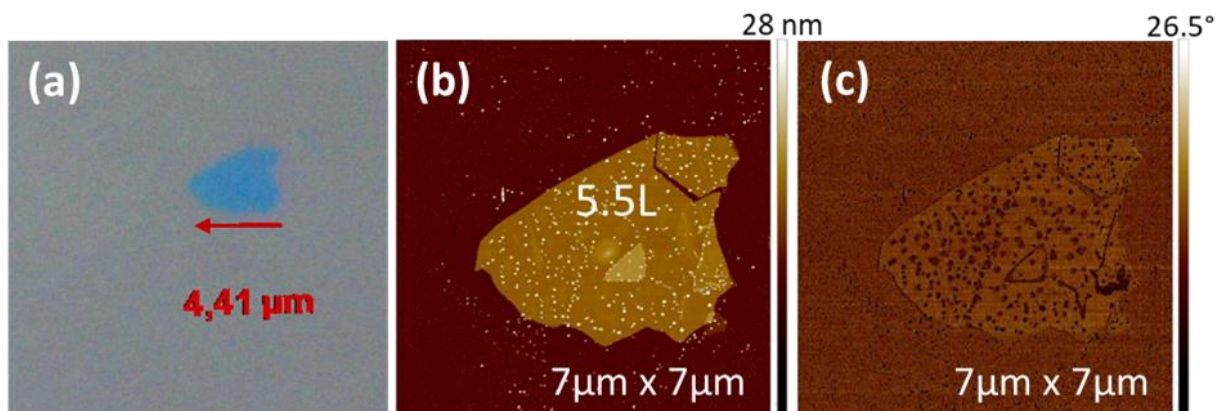


Figure 2.9 AFM topography (a) and phase (b) images illustrating a Cr_2AlC flake directly after the transferring step on a SiO_2/Si substrate. A large amount of glue (yellow color in both images) covers most of the flake surface as it is clearly highlighted by the phase contrast. The phase signal saturation (white color) corresponds to the thickest glue domains.

Although glue residues do not impact all flakes properties, it is of great importance to efficiently remove them in the case of ohmic contacts fabrication.

2.2.1.1 Thermal annealing in ambient conditions

As a first attempt to remove the glue residues, we thermally annealed the samples in ambient conditions, directly after the flakes transfer. We placed the samples onto a hot plate in a fume hood and we annealed them for two hours at 400°C in air. The fast detection of thin flakes was convenient with the optical microscope due to the relatively low amount of glue residues. The topography images obtained during AFM measurements reveal only partial removal of glue residues after annealing, i.e. the glue residues could not be burnt fully this way. As illustrated in Figure 2.9, directly after the tape removal, the residues are spread all over the flake's surface. After the annealing step, it is evidenced that the surviving glue residues have substantially shrunk and agglomerated in clusters (Figure 2.10 (b), (e)).



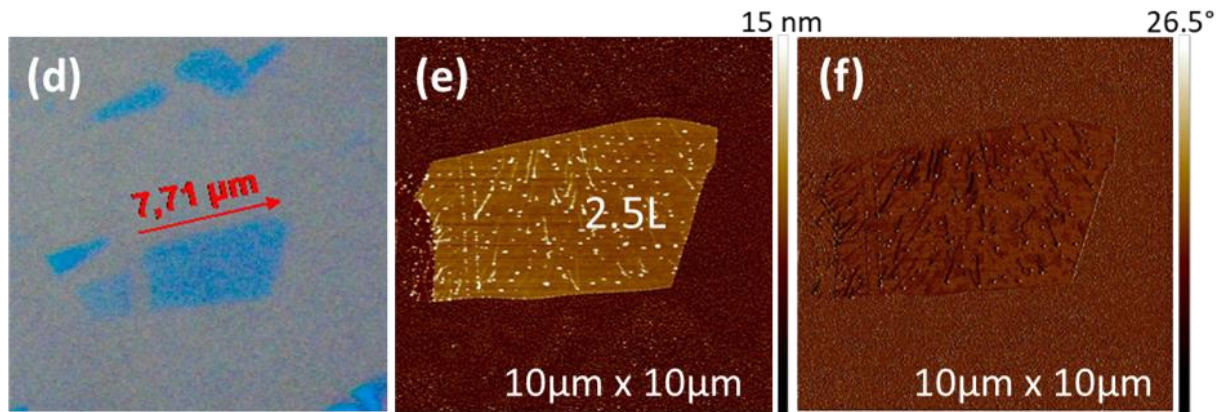


Figure 2.10 (a), (d) Optical microscopy images of Cr_2AlC and V_2AlC flakes and their corresponding AFM topography (b), (e) and phase (c), (f) images after thermal annealing for 2 hours at 400°C in ambient conditions.

AFM topography (Figure 2.10 (b), (e)) reveals diverse size clusters randomly distributed across the surface of the flakes and substrate with a higher density along the flake edges. The phase images in AFM topography generally reveals a contrast, between materials having different hardness/softness, a case that is observed in the flakes phase images (Figure 2.10 (c), (f)) where areas of intense brown or even black color are dispersed onto the different contrast surface of the flakes and correspond to glue residues. Hence, it is proved that MAXene flakes are not fully exempted from the glue residues after annealing in air.

The shrinking of the glue residues and their clustering on the MAXene flakes after the annealing in ambient conditions can be further confirmed by the indentation measurements in a small area of the flakes surface (Figure 2.11 (b)) using the AFM apparatus. The cantilever applies a load on the surface of the tested flake and the resistance of the material to its permanent deformation is recorded. The softer the material, the less resistive it is under the applied load and thus a large deformation is observed.

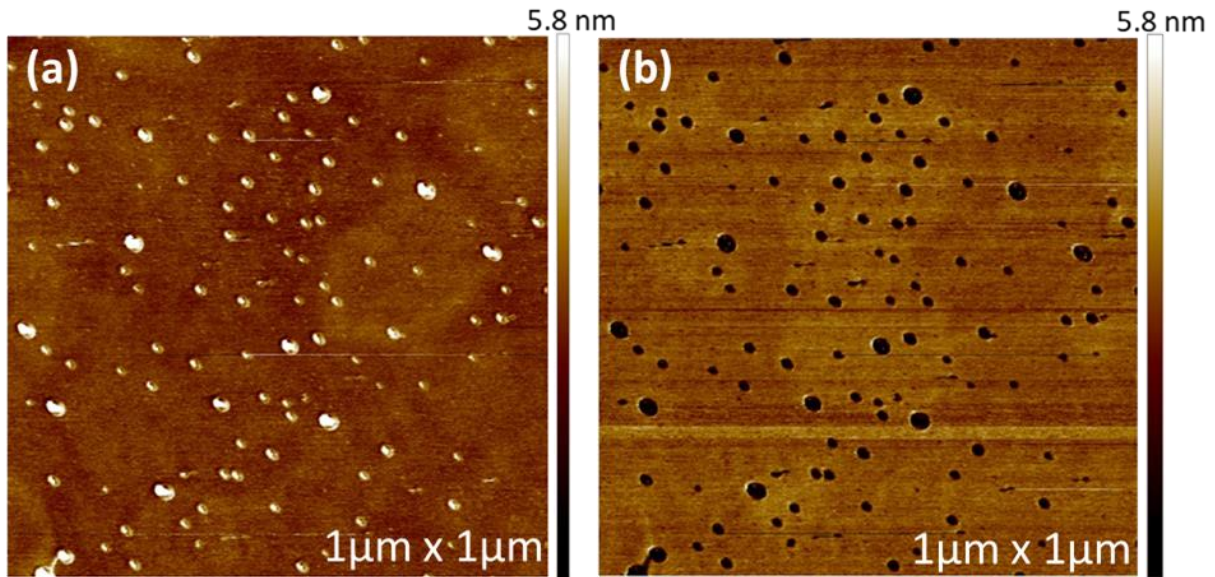


Figure 2.11 AFM topography (a) and indentation (b) images of $1 \times 1 \mu\text{m}^2$ surface of a Cr_2AlC flake after 2 hours of annealing at 400°C in ambient conditions.

A lower scale surface topography of the flakes (Figure 2.11 (a)) confirms the formation of randomly dispersed small spots onto the flakes, after the annealing step in air and these spots can be identified as glue residues considering the indentation image (Figure 2.11 (b)). According to the color scale, the deformation of the material in the spots position is larger compared to that covering the rest of the surface, indicating it less resistive under the applied force (0.255 nN).

Besides limiting the amount of glue residues on the flakes surface, the annealing in ambient conditions favors the oxidation of MAXenes which impedes the fabrication of good ohmic contacts. The annealing induced oxidation was verified by X-ray Photoelectron Spectroscopy (XPS) measurements on the surface of Cr_2AlC crystals in ultra high vacuum (UHV). Some crystals were freshly cleaved in air and others cleaved and annealed in air for 2 hours at 400°C before being introduced in the UHV chamber. Some of the cleaved and annealed surfaces were additionally subjected to 5 minutes Ar^+ etching inside the XPS chamber, to remove the native oxide which seemed to be formed on the cleaved surface upon annealing (Figure 2.12).

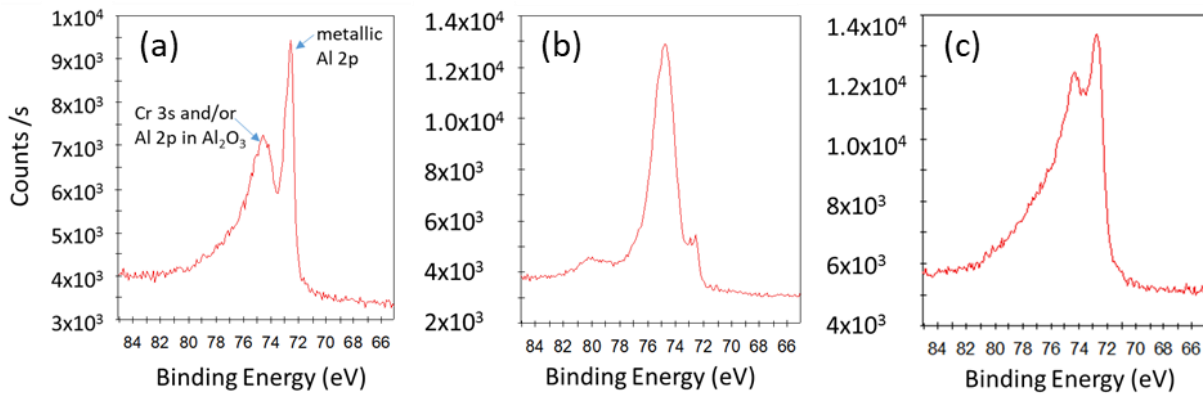


Figure 2.12 Al $2p$ and Cr $3s$ XPS spectra obtained from (a) a freshly cleaved Cr_2AlC single crystal, (b) a crystal cleaved and annealed in air for 2 hours at 400°C and (c) the same crystal as in (b) after 5 minutes Ar^+ etching inside the XPS chamber.

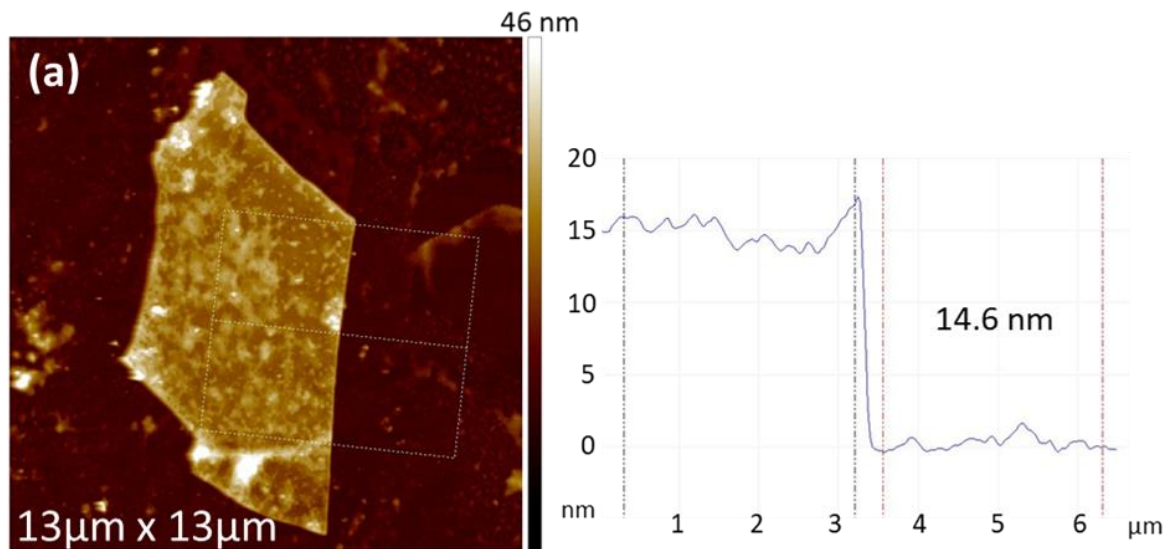
Although the proximity of the Cr $3s$ peak in Cr_2AlC and of Al $2p$ in Al_2O_3 makes it difficult to resolve those two peaks [193] and identify the presence of Al_2O_3 in the freshly cleaved sample, a comparison with the XPS spectrum measured for the annealed samples clearly shows the transformation of the metallic Al $2p$ peak into that of Al in Al_2O_3 (Figure 2.12 (b)). In the same spectrum, a small peak can be also distinguished around 80 meV which seems quite similar to that observed in the case of $(\text{Al}_{1-x}\text{Cr}_x)_2\text{O}_3$ compounds [194].

2.2.1.2 Adhesive tapes with different chemical structure: Ultra violet (UV) susceptible tapes

To avoid the large amount of glue residues left onto the flakes surface after the transferring step of the exfoliation process and the oxidation of the flakes surface induced by the thermal annealing step in air, we tried a tape whose adhesive part has a different chemical structure than the synthetic one previously used. This adhesive tape is sensitive to UV light and is also known as dicing tape since it is regularly used as backing tape in wafer dicing. UV-susceptible tape is widely used owing to its easy removal and the limited amount of residues left on the material's surface. Its main feature is the strong adhesion before UV light irradiation and the ease in which the adhesive bonds breaks during UV exposure.

The exfoliation recipe we followed with the UV tape was the same recipe we used to obtain the thin and large size MAXenes, with the only exception being the replacement of the mild annealing step by UV light irradiation of the tape as an alternative way for the flakes transfer. The samples were placed inside an apparatus containing four UV light bulbs in parallel and they were exposed to UV radiation, in ambient conditions, for 11 minutes. When the exposure to UV light finished the tape was easily removed from the substrates. The time of exposure was chosen as the time needed for a low concentration of glue residues on the MAXenes surface, according to the results of the materials tested in the past, at the lab.

Optical microscopy revealed the low yield of the UV-tape on MAX phases exfoliation, as only three flakes of thickness of 12 nm and above could be found in one of the four $6 \times 6 \text{ mm}^2$ SiO_2/Si substrates used for the flakes transfer. Contrary to our expectations for a low amount of glue residues left onto the flakes, the surface topography images revealed a large concentration of glue that was randomly dispersed all over the flakes and substrate surfaces (Figure 2.13).



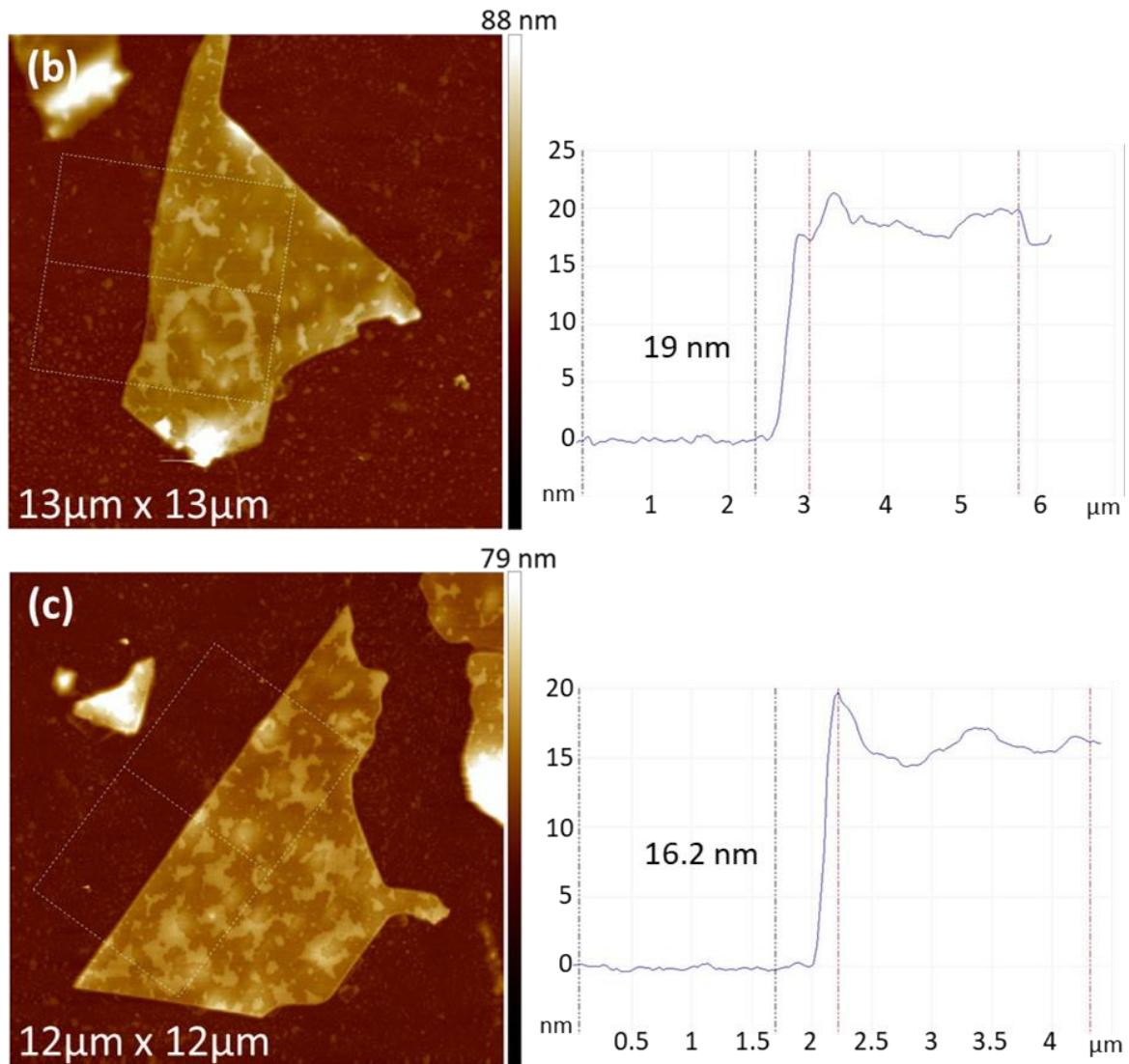


Figure 2.13 AFM topography images of Cr_2AlC flakes illustrating their thickness directly after the transferring step on the SiO_2/Si substrate. The height profile and the measured thickness that are shown on the right of every image derive from the average of the surface encompassed by the dotted rectangle on the corresponding topography image.

To face the glue residues, a thermal annealing process was mandatory, and it allowed to reduce the amount of the glue left on the flakes, as it was shown in section 2.2.1.1. Nevertheless, to avoid the unwanted oxidation that is induced from the annealing in ambient conditions we used a hot plate within an argon (Ar) glove box. There, we annealed the samples for three hours at 400°C . The O_2 and H_2O sensors of the glove box (detection threshold below one part per million (ppm)), confirmed the cleanliness of the atmosphere all along the process. The topography

images of the flakes that were obtained after the annealing process helped us to estimate the flake thickness in a more accurate way (Figure 2.14).

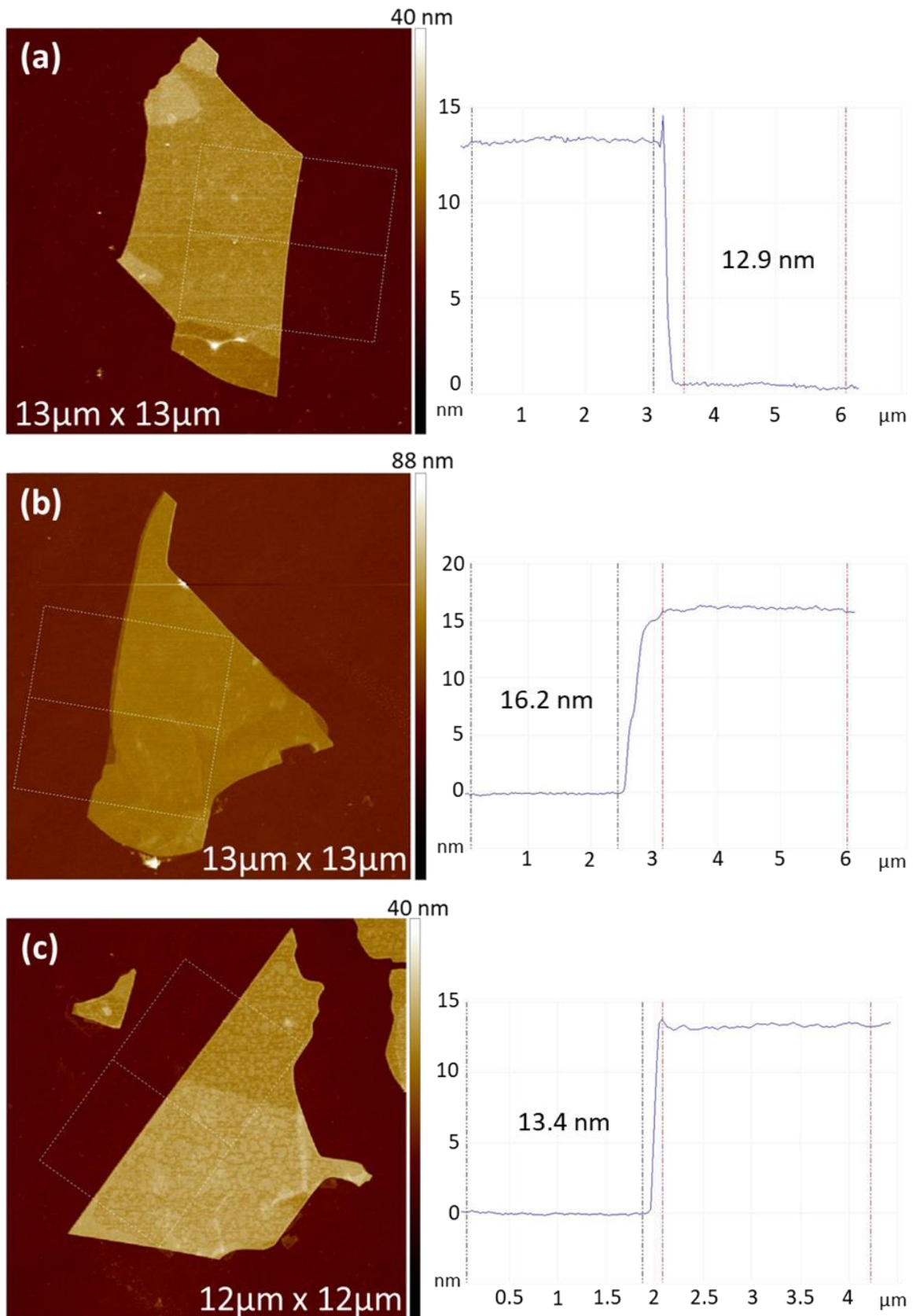


Figure 2.14 AFM topography images of the same Cr_2AlC flakes illustrated in figure 2.13 but after 3 hours of annealing in Ar at 400°C .

Thickness profile measurements on the same side (dotted rectangle) of the Cr_2AlC flakes are done in their topography AFM images before and after the annealing step (Figures 2.13 and 2.14) to detect possible thickness change. A comparison of the thickness profiles between the same flakes indicates a decrease in the average, apparent flake thickness ranging from 1.7 to 2.8 nm after the applied annealing conditions. Therefore, it is deduced that thermal annealing can efficiently reduce the amount of glue residues left onto the flakes surface.

The difference in the surface roughness of both the flake and the substrate due to the glue residues before and after annealing is directly visible in the AFM topography considering the color scale. However, the difference is also seen, with a better contrast, on the phase images (Figure 2.15).

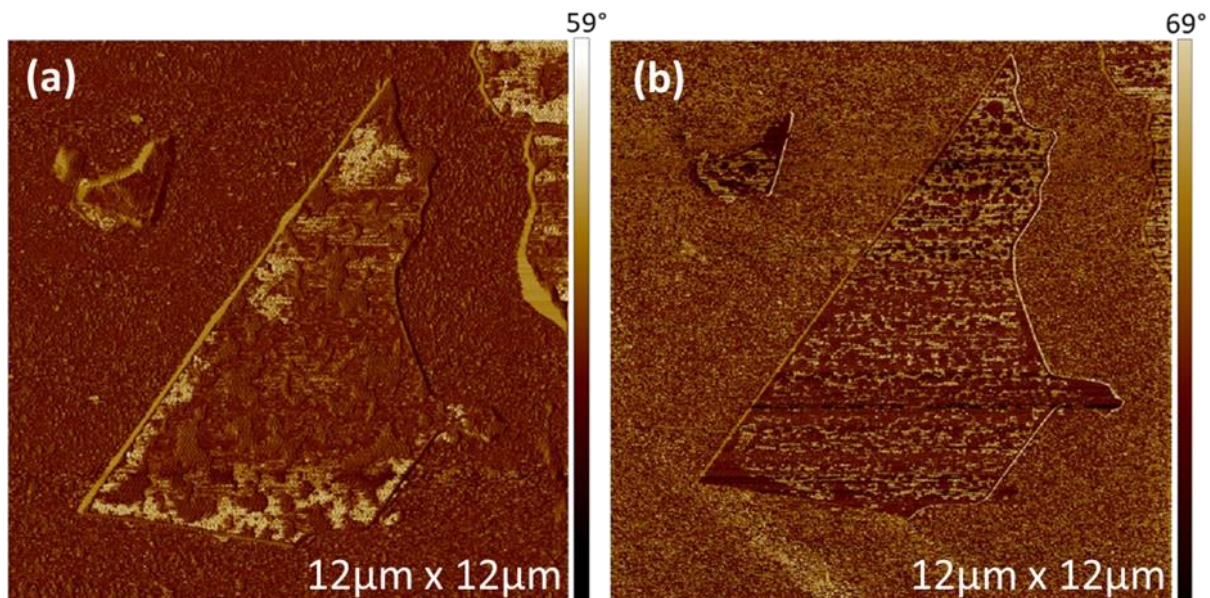


Figure 2.15 AFM phase images before (a) and after (b) thermal annealing in Ar (3 hours at 400°C) of the Cr_2AlC flake that is illustrated in topography Figures 2.13 (c) and 2.14 (c).

Comparing the topographies in Figure 2.14 (c) and Figure 2.13 (c) seem to indicate that the height of the large glue residues substantially decreases, and that the larger scale, inhomogeneously distributed glue agglomerates convert into a

population of smaller ones, more homogeneously distributed and covering a larger part of the flake's surface. This is confirmed by the phase images in Figure 2.15. In association to the decrease of the apparent flake thickness, we can conclude that even if the annealing step removes a substantial part of the glue, residues are not eliminated but they are homogeneously redistributed in a population of smaller agglomerates having a more homogeneous size.

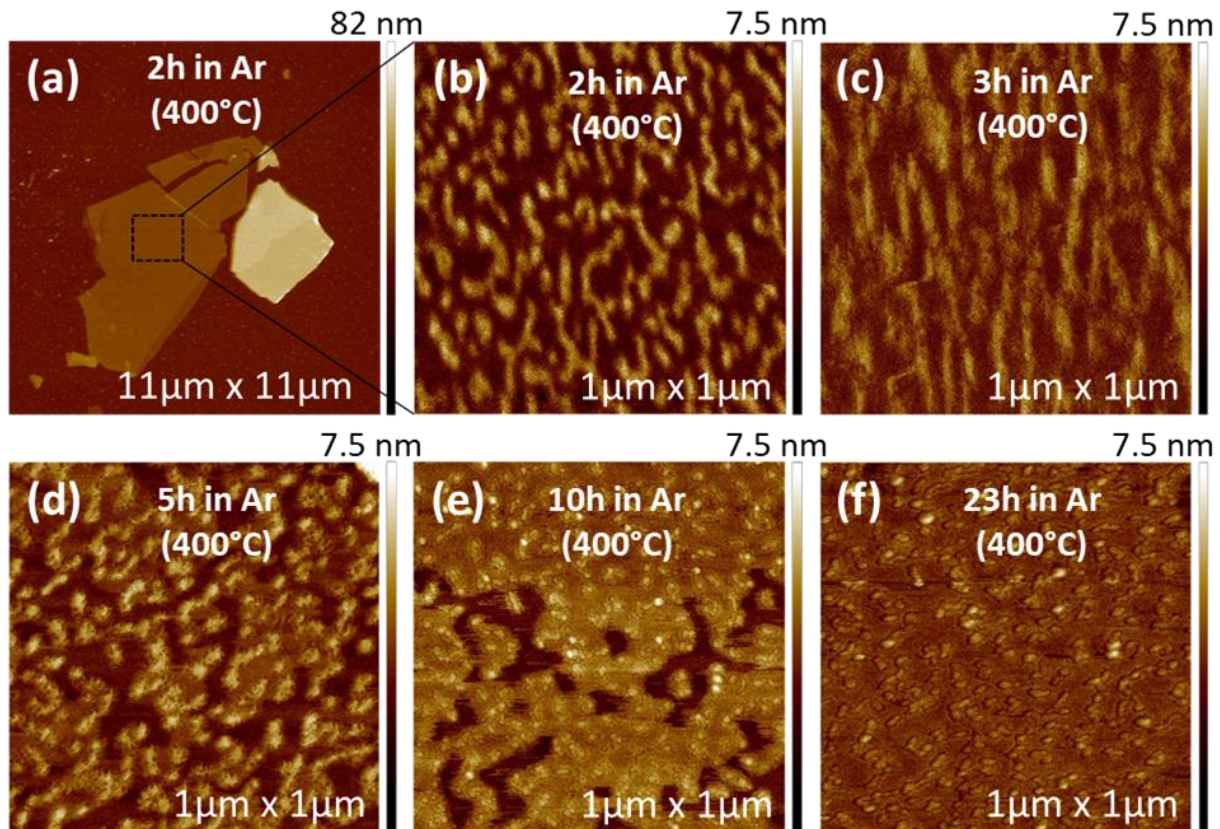
The use of tapes whose adhesion is ensured by bonds susceptible to UV light help to avoid the mild annealing step necessary for normal tape. However they cannot improve the procedure of flakes transfer, as a large quantity of glue is finally transferred on the flakes surface, as well. The UV irradiation seems not enough to reduce the remaining glue. Furthermore, as it was previously mentioned, the yield of this tape in exfoliating thin MAXene flakes was extremely low, proving that its adhesion strength is not enough compared to the inter-layer bonding within MAX crystals. Therefore, the use of the tape susceptible to UV light was abandoned. Henceforth, the mechanical exfoliation of MAXenes relied on the use of a normal (synthetic) adhesive tape with proper adhesive strength.

2.2.1.3 Thermal annealing in Ar and in high vacuum conditions

The promising efficacy of thermal annealing under Ar in eliminating glue residues on the exfoliated flakes motivated us to further investigate the influence of additional annealing steps on the glue residues. For this, we applied various annealing steps on the same exfoliated flakes as a function of time, always using the same annealing temperature (400°C). The annealing process was done in both Ar and high vacuum (HV) conditions to avoid the oxidation of MAXenes.

The impact of the annealing on the glue residues of the flakes' surface was observed at a low scale with topography images of $1 \times 1 \mu\text{m}^2$ lateral dimensions. To detect possible changes in the glue residues after various annealing time intervals, topography images of the exact $1 \times 1 \mu\text{m}^2$ region after each annealing step should be recorded using AFM. We paid special efforts to systematically scan the exact same $1 \times 1 \mu\text{m}^2$ region of the flakes surface after different annealing steps (Figure 2.16 (d)-(f) and (h)-(i)).

Initially, the exfoliated flakes were annealed in Ar conditions at 400°C for 2 hours (Figure 2.16 (a)) directly after the transfer process. As mentioned before, the majority of glue residues, left on the flake and the substrate after the exfoliation, were completely evaporated due to the high temperature of the applied annealing. Nonetheless, some glue residues remained on the flake's surface, as observed in the 1 x 1 μm^2 topography image after the first annealing trial (Figure 2.16 (b)). There, regions of elongated and thicker patches are observed all over the surface. The topography was imaged after each additional annealing step, for a cumulative annealing time 3, 5, 10 and 23 hours in Ar conditions (Figure 2.16 (c)-(f)) and an additional 2, 7 and 12 hours in high vacuum conditions (Figure 2.16 (g)-(i)) after the initial annealing step of 2 hours.



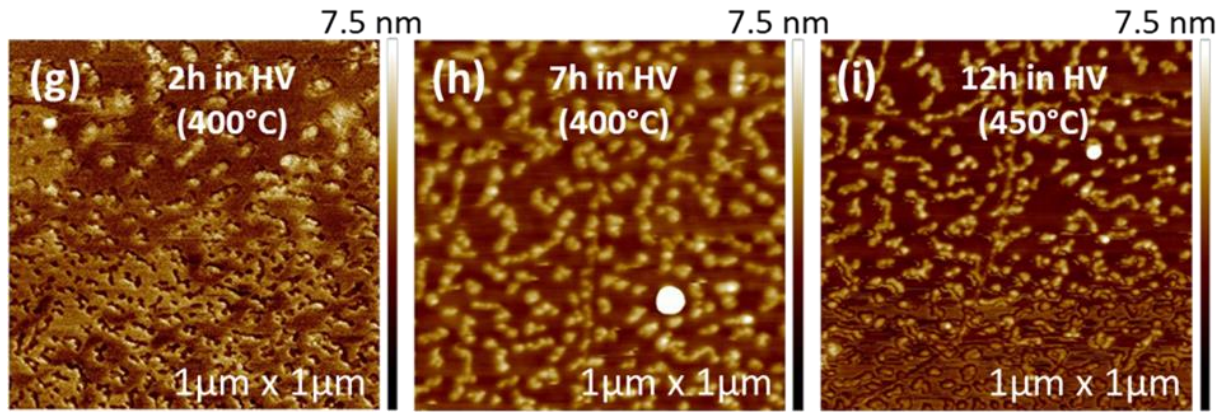


Figure 2.16 AFM topography images of a Cr_2AlC flake (a) and the $1 \times 1 \mu\text{m}^2$ surface on the center of the flake (dotted box) used for the observation of the glue residues under the impact of multiple annealing steps in both Ar and high vacuum conditions (b)-(i). The annealing temperature was kept stable at 400°C during all steps except from the last one where it was increased to 450°C (i). The annealing time is illustrated in cumulative scale in both annealing conditions.

All the aforementioned topography images of the glue residues illustrate after each annealing step two different color regions. The thick elongated patches and the flat regions among these patches. After 23 hours of annealing the entire surface seems to be occupied by one color area indicating a large expansion of the glue residues compared to the previous annealing steps. To explain the effect of multiple annealing steps onto the glue residues we measured the root mean square roughness (R_{rms}) and the percentage of the glue coverage on the $1 \times 1 \mu\text{m}^2$ topography images as a function of the cumulative annealing time (Figure 2.17 (a), (b)). To measure the percentage of the glue coverage at every $1 \times 1 \mu\text{m}^2$ image we initially chose a very flat region that seemed to be devoid of glue (intense brown color) and we locally measured the height mean value. Thereafter we used this value as the threshold height above which the flake's surface was occupied by glue.

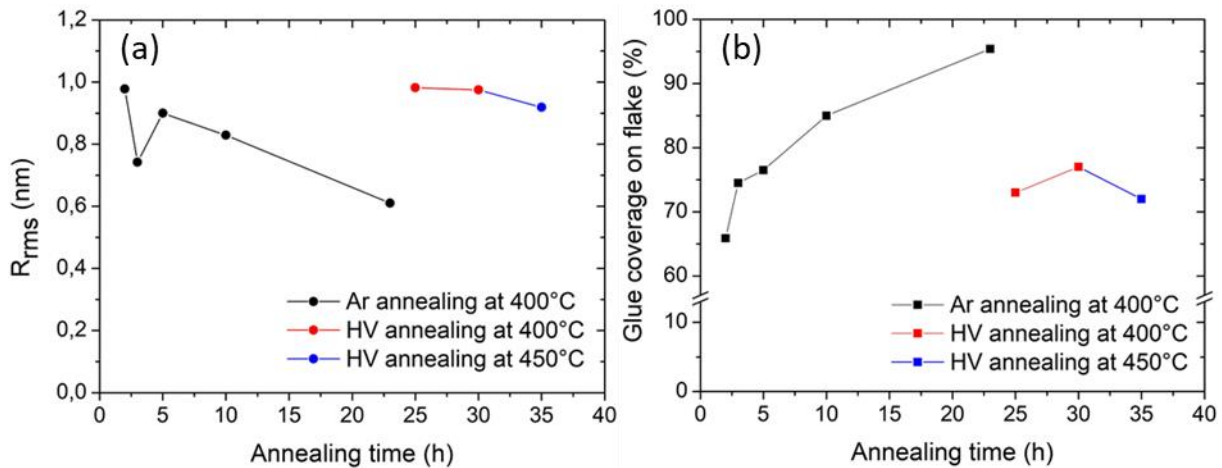


Figure 2.17 Plots of the rms roughness (a) and the percentage of glue coverage (b) on the $1 \times 1 \mu\text{m}^2$ topography images of the Cr₂AlC surface as a function of the cumulative annealing time in Ar and HV conditions.

According to the topography image, after 2 hours of annealing (Figure 2.16 (b)), the amount of glue has been reduced from the flake's surface as it is indicated from the low percentage (~66%) of the glue coverage (Figure 2.17 (b)). The remaining residues are accumulated forming various size agglomerates that are highlighted in yellow color in the topography and thus maintain a high R_{rms} value (0.98 nm). A step by step increase in the annealing time gradually decreases the roughness of the flake's surface until its minimum value (0.61 nm) after 23 hours of annealing. Exception to the approximately linear decrease of the surface roughness is the 3 hours annealing step due to an abrupt decrease of the R_{rms} value (0.74 nm). Additionally, if we consider the corresponding topography image (Figure 2.16 (c)) that shows a low surface resolution compared to the rest images of Ar annealing steps then it can be assumed that a problem during the scan occurred. A possible contamination of the AFM tip with particles attached from the flake's surface owing to the low scanning speed and the repeating scanning of the surface could prevent a proper surface recording and hence to affect the measured roughness. Contrary to the roughness decrease, the percentage of the glue coverage on the flake's surface increases progressively until its maximum value (~95%) as the annealing time increases to 23 hours. Therefore, it can be deduced that any additional annealing step exceeding 2 hours in Ar conditions steadily spreads the glue residues that were initially aggregated in agglomerates on the flake surface.

As a result, a decrease in the surface roughness followed by a simultaneous increase of the surface area covered by glue are observed. The topography images between 5 and 23 hours of annealing in Ar (Figure 2.16 (d)-(f)) illustrate the increase of the surface area that is covered by glue through the expansion of the yellow color regions formed among the glue agglomerates. As a result the glue residues have occupied almost the entire surface after 23 hours of annealing, leaving some tiny regions (~5% of the surface) devoid of glue.

Since additional Ar annealing trials seem to reach a saturation level regarding the reduction of the amount of glue residues onto the flake, as they start to spread the glue all over the flake surface, we decided to continue the annealing steps under different pressure conditions. For that purpose we used a furnace equipped with a system of pumps that could generate high vacuum conditions ($3 \cdot 10^{-8}$ - $9 \cdot 10^{-9}$ mbar) during the annealing process with the hope that glue residues could be further reduced. Thus, the same flakes that were used for annealing tests in Ar, subsequently underwent thermal annealing in high vacuum conditions for various periods of time. We started annealing once the pressure in the vacuum chamber reached $5 \cdot 10^{-8}$ mbar whilst the pressure during each annealing step was ranging between $2 \cdot 10^{-8}$ - $9 \cdot 10^{-9}$ mbar with the pumps working continuously.

According to Figure 2.17 (a) and in contrast with what we found for Ar annealing, a different impact of the HV annealing conditions is observed on the glue residues onto the flake. The R_{rms} abruptly increase to the same value (0.98 nm) as that after the initial annealing step of 2 hours in Ar while a drop in the percent of the surface covered by glue (73%) is recorded after 2 hours of HV annealing (25 hours in total). Further annealing of the flake for 5 hours seems to retain unaltered the roughness (0.975 nm) as well as the amount of surface covered by glue (77%) where the 4% difference compared to previous annealing step probably derives from statistical uncertainties. The last annealing step took place at 450°C for 5 hours (35 hours in total) instead of 400°C in the previous steps and as it is illustrated in the plots above, a small reduction in the surface roughness (0.92 nm) corresponds to a slight increase of the surface area that is devoid of glue residues (72%). As before, the 5% difference between the annealing steps probably derives from statistical uncertainties.

Generally, it is deduced that 2 hours of annealing in HV conditions favor the shrinkage of the glue residues left on the flake's surface leading thus to an increase in the rms roughness while the glue residues coverage decreases accordingly. Any additional HV annealing step either at a stable or slightly increased temperature does not induce any significant variation with time. The contraction of glue residues between the 23 hours of Ar annealing and the 2 hours of HV annealing is confirmed by the topography images (Figure 2.16 (f)-(g)) in combination with their corresponding phase images (Figure 2.18 (e)-(f)) where larger agglomerates have been formed (higher color intensity) and larger areas seem devoid of glue.

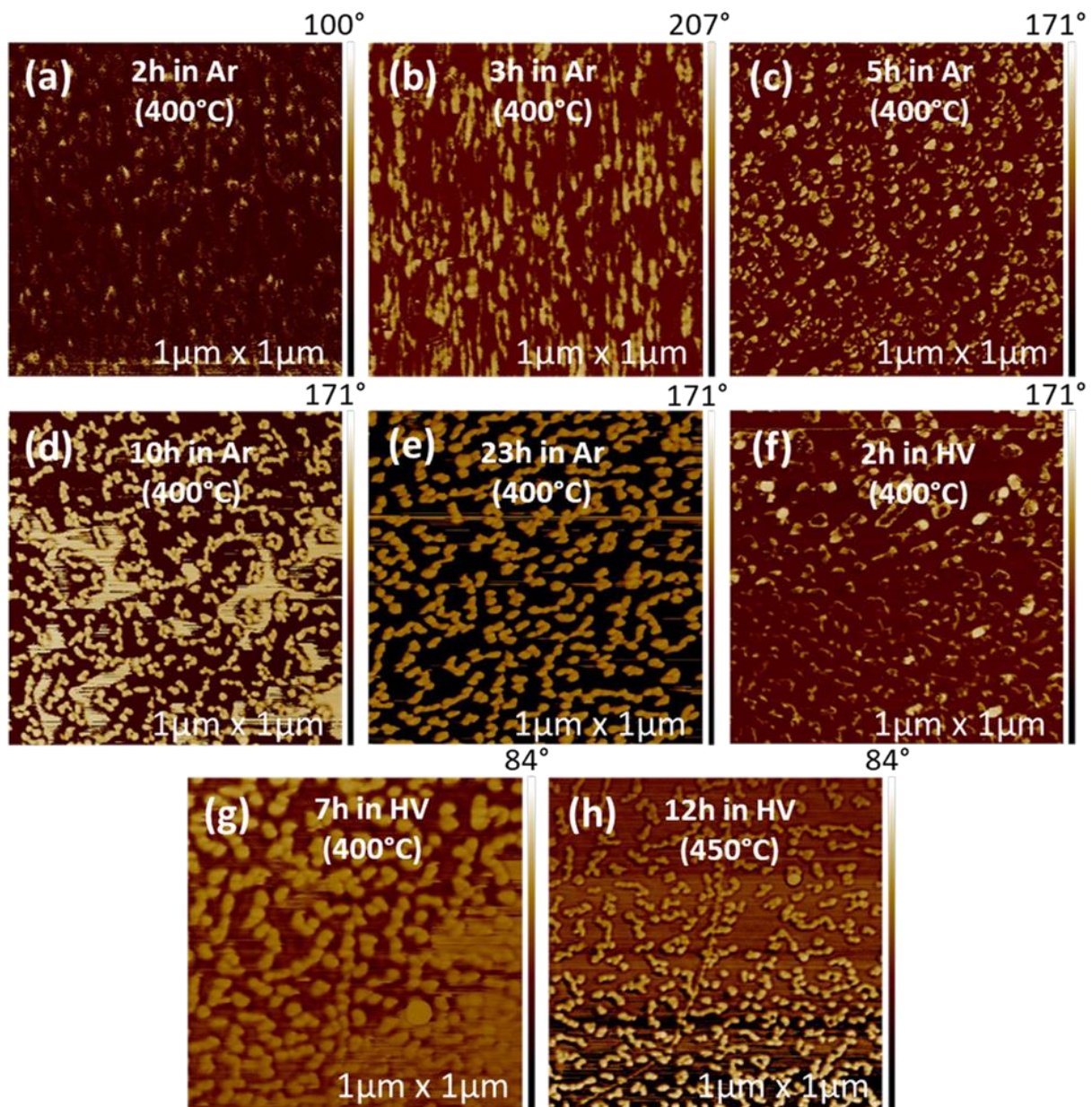


Figure 2.18 AFM phase images of the corresponding $1 \times 1 \mu\text{m}^2$ topography images (Figure 2.16 (b)-(i)) during the annealing steps in Ar and high vacuum conditions.

In addition to the thermal annealing in Ar and high vacuum, few annealing trials were also done in Ar and H_2 flow. In that case samples were placed in a quartz tube in the presence of a gas flow of 100 sccm Ar and 30 sccm H_2 at 400°C for one hour. Nonetheless, the results were not substantially more efficient than in the aforementioned annealing attempts.

The implementation of various annealing steps in different conditions demonstrated the possibility to remove a substantial part of the residues left on the surface of MAXene flakes after exfoliation. Nevertheless, the results remain somewhat unsatisfactory as the studied annealing steps are clearly not sufficient to obtain flakes devoid of glue residues. A brief conclusion of the previous analysis is the importance of the initial annealing step in Ar for 2 hours which reduces drastically the amount of glue on the flakes surface but leaves residues accumulated in agglomerates. Additional annealing steps in Ar favor the spreading of the agglomerates. On the contrary, the annealing in high vacuum conditions favors the agglomerates shrinkage which releases larger areas of the flake's surface, enhancing thus the creation of better ohmic contacts.

2.2.1.4 Cleaning with solvents

The idea of seeking for an adequate solvent to fully remove the glue residues from the surface of the flakes and substrate, seemed promising, since already acetone is commonly used to eliminate residues deriving from adhesive tapes.

Our efforts focused on two polar solvents, acetone and dichloromethane with 10% methanol and non polar solvents such as toluene, xylene and chloroform. After the flakes transfer step, we dipped our samples in laboratory glass beakers filled with the aforementioned solvents for a period of time ranging from a few hours up to three days. The observation of the substrates surface by optical microscopy showed us that only acetone and a combination of acetone and xylene helped reducing, to a small extent only, the amount of glue residues. Especially, we

observed that after leaving the sample in acetone for 36 hours, only part of the residues could be removed from the substrate's surface (Figure 2.19 (b)).

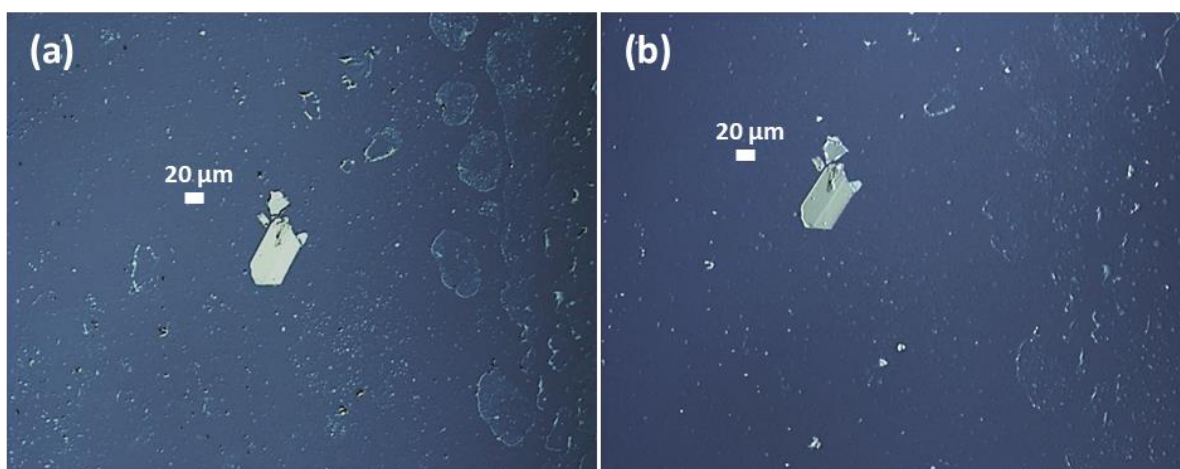
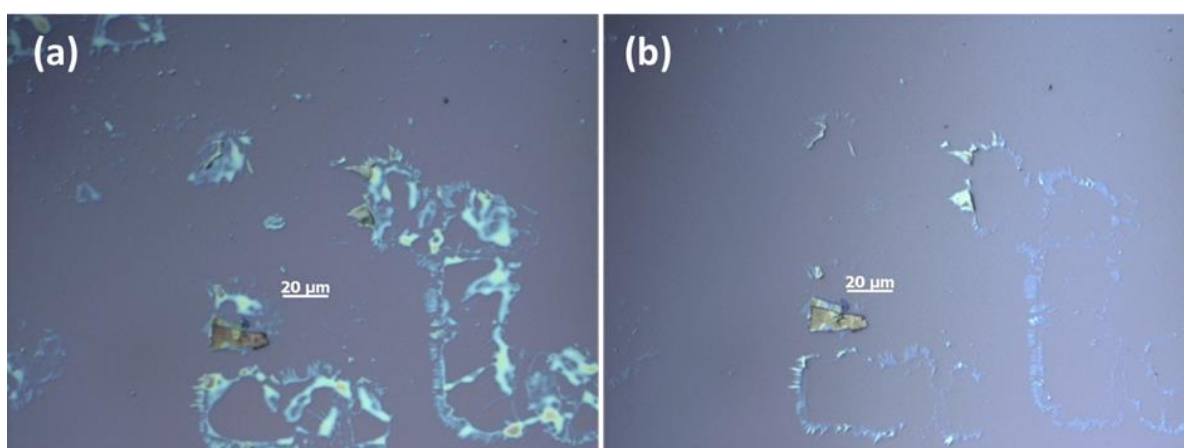


Figure 2.19 Optical microscopy images of the SiO₂/Si surface after transferring the flakes (a) and after having immersed the sample for 36 hours in acetone (b).

A different attempt to dissolve the glue residues, was to immerse the samples in glass beakers filled with acetone and heat them in a temperature range of 40°C - 80°C for various periods of time from a few minutes up to 1.5 hours. We observed that leaving the sample for 90 minutes in warm acetone at 50°C can dissolve larger amounts of glue residues compared to the cases of higher heating temperatures and lower residence time (30 minutes) of the samples in the solvent (Figure 2.20).



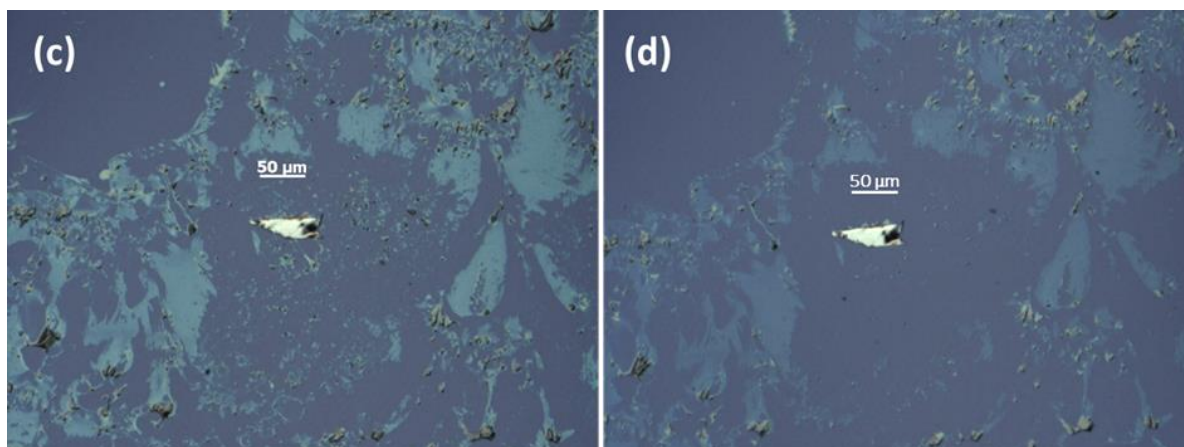


Figure 2.20 Optical microscopy images of the SiO₂/Si surface before (a) and after (b) warm (50°C) acetone cleaning during 90 minutes. Similarly, (c) and (d) images show the glue residues before and after having immersed the sample for 30 minutes in warm (80°C) acetone, respectively.

It is worth mentioning that a prolonged residence time of the sample in warm acetone can lead to the loss of flakes. Especially, we observed that leaving the samples in warm acetone above 60°C for more than 30 minutes usually results in either partial or a complete loss of the flakes from the substrate's surface.

As it can be concluded, the glue residues are too resilient to be fully removed even with solvents. The mild annealing step before peeling off the tape, during the exfoliation process, seems to strengthen the adhesion of the remaining glue to any surface.

2.2.1.5 Adhesive tapes based on natural rubber

The unsuccessful attempts to completely remove the glue residues from the flakes surface using thermal annealing and solvents cleaning steps led us to consider a different kind of tape, based on natural rubber adhesives. With this kind of tape, the residues were expected to be easily removed by dissolving them in acetone, as according to the manufacturers the special chemical structure of the adhesive with the long polymer chains is not very resistant to chemicals and solvents.

All exfoliation trials with the tape of the natural rubber based adhesive followed the same recipe that was implemented in the case of the synthetic adhesive tape. After the flakes transfer, the samples were immersed in warm (50°C) acetone for 36 hours. The 1 x 1 μm^2 topography AFM image, of a region at the center of the flake's surface, represents the effect of the warm acetone to the glue residues aggregation in large agglomerates that are densely distributed on the flakes surface, leaving very small residue-free regions (Figure 2.21 (b), (c)).

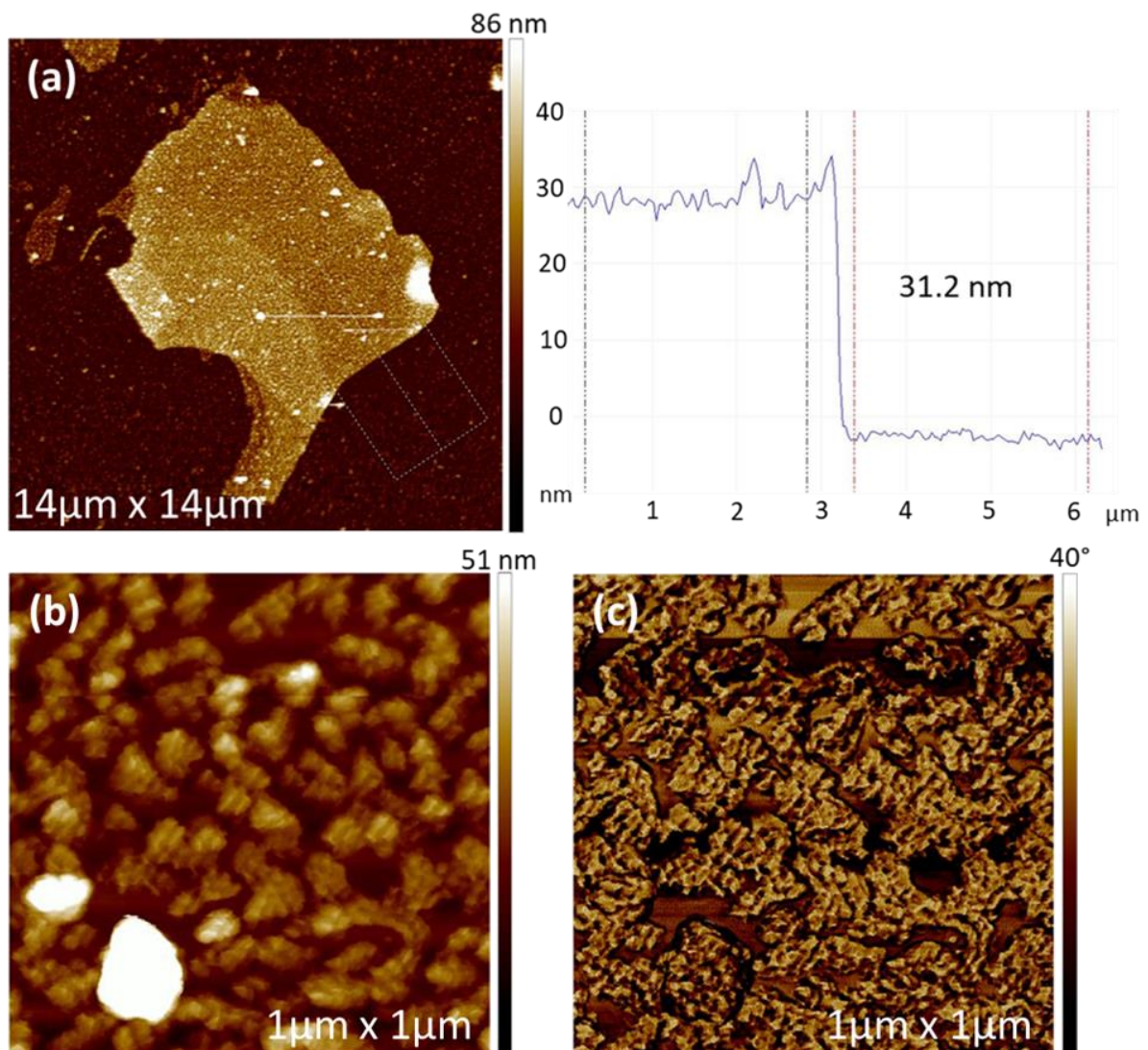


Figure 2.21 AFM topography images of a Cr₂AlC flake (a) and the remaining glue residues on its surface (b) after having immersed in warm acetone at 50°C for 36 hours. The image (c) illustrates the phase difference between the flake and the glue residues.

Notwithstanding the long residence time of the sample in the warm acetone, the solvent was proved insufficient to completely remove the glue residues left on the flake's surface. Once more, the glue residues form agglomerates (Figure 2.21 (b)). Contrary to the previously described Ar annealing treatment, agglomerates have a larger size eliminating thus the areas of the flake's surface that seem devoid of glue.

To reduce the amount of glue residues, as done before with synthetic tape, we annealed the samples. The samples were annealed for 2 hours at 400°C under high vacuum. The surface topography was then characterized with AFM images of the entire flakes and in a $1 \times 1 \mu\text{m}^2$ region (Figure 2.22 (a), (b)). As it was noticed in the acetone cleaning step, all the $1 \times 1 \mu\text{m}^2$ topography AFM images derive from a surface region located in the center of the flake.

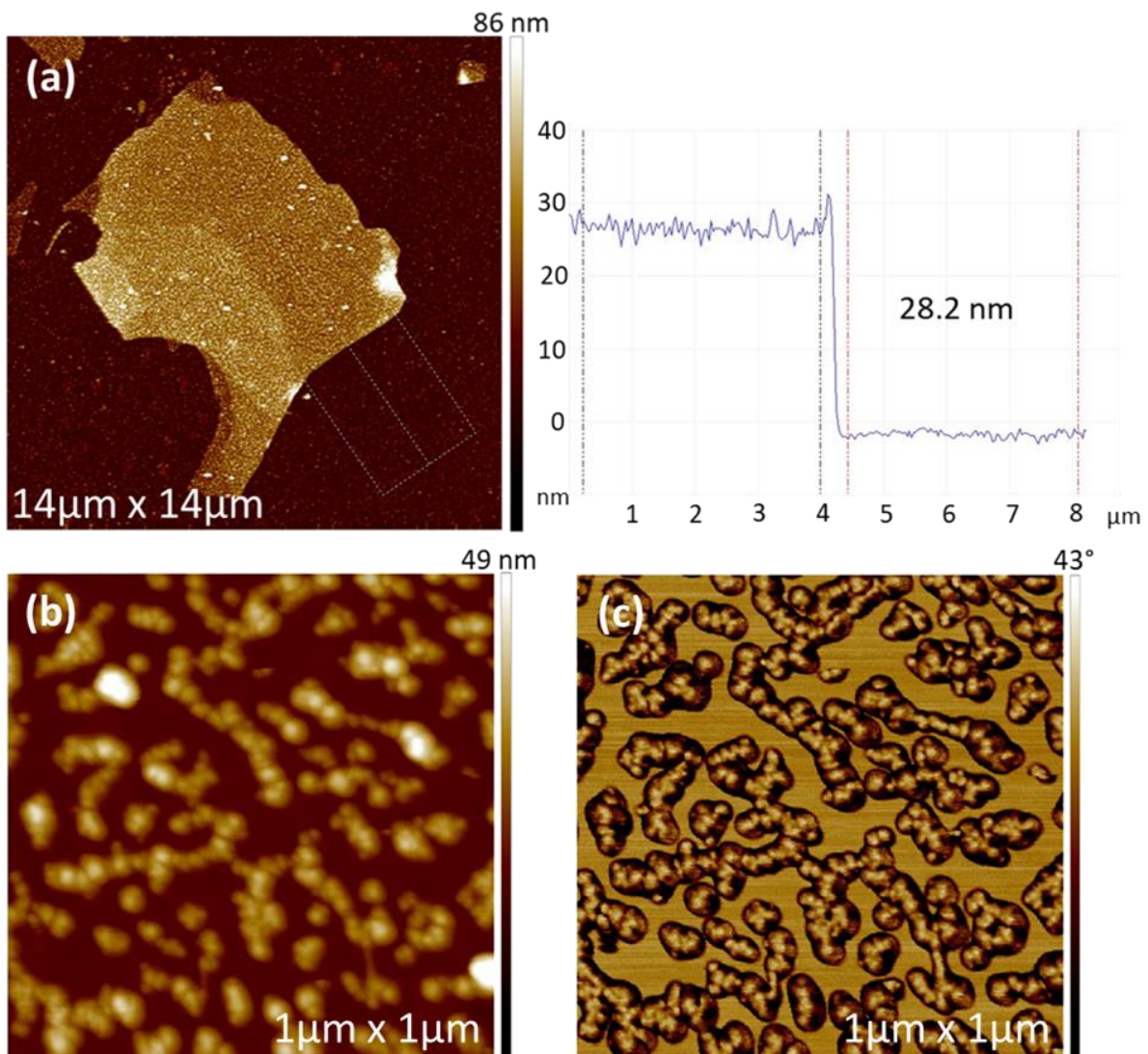
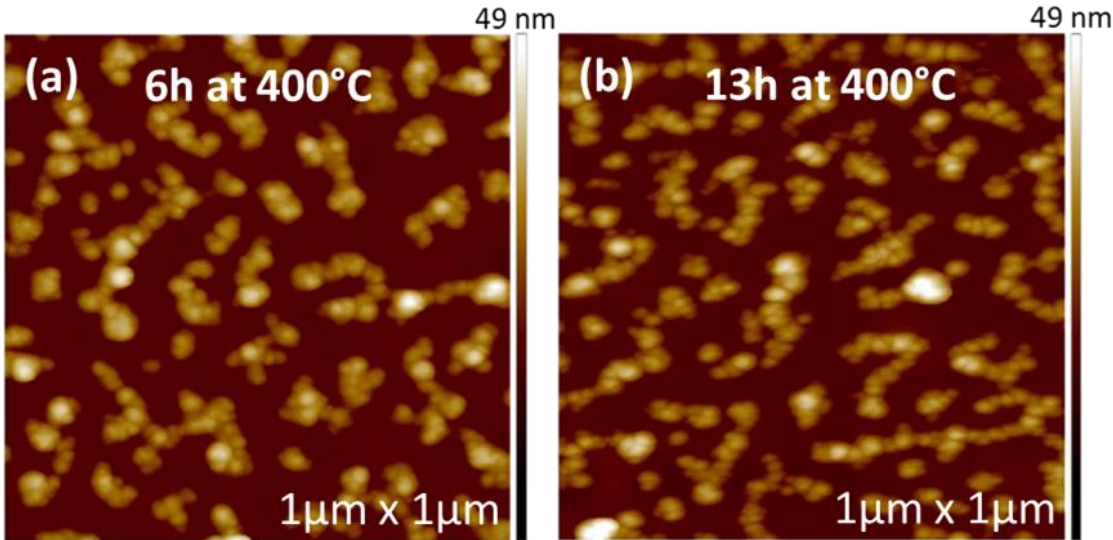


Figure 2.22 AFM topography images of the same Cr₂AlC flake shown in Figure 2.21 (a). The topography image of the flake with its corresponding height profile (a) and the glue residues on its surface (b) after 2 hours of HV annealing at 400°C that followed the warm acetone cleaning. The image (c) shows the phase contrast between the flake and the glue residues.

The thickness profile of the flake topography indicates a difference of 3nm in the average, apparent thickness of the flake after the comparison of the warm acetone cleaning (Figure 2.21 (a)) and the annealing step for 2 hours (Figure 2.22 (a)). This result confirms that annealing treatment remains an efficient process to reduce the adhesive residues onto the flakes, regardless of their chemical composition. Additionally, the 1 x 1 μm² topography image after the annealing step (Figure 2.22 (b)) illustrates a decrease of 29% in the coverage of the flake’s surface by the glue residues, as well as their aggregation in elongated agglomerates.

Increasing the annealing time to 4 hours during the second annealing step (6 hours totally) and to 7 hours in the last annealing trial (13 hours in total) whilst keeping the temperature stable at 400°C does not seem to induce any significant change as seen in both the topography (Figure 2.23 (a), (b)) and phase images (Figure 2.23 (c), (d)). It worths to be mentioned that Figures 2.22 (b) and 2.23 (b) highlight almost the same 1 x 1 μm² surface with the latter one being slightly downshifted to the former in a diagonal direction.



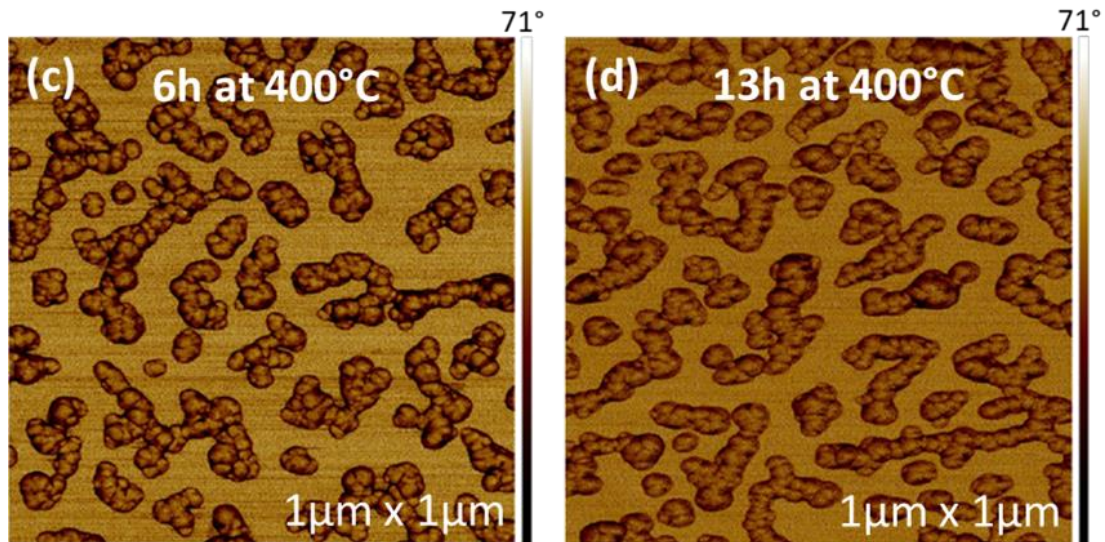


Figure 2.23 AFM topography (a)-(b) and their corresponding phase (c)-(d) images of the glue residues, onto the same Cr_2AlC flake (Figure 2.22), after various annealing steps at 400°C in high vacuum. The images (a) and (c) highlight the glue residues after 6 hours whilst the images (b) and (d) after 13 hours of HV annealing.

A quantitative analysis in the measurements of the roughness and the amount of residues on the flake's surface, as a function of annealing time, provided us with a clearer evidence of the impact of the annealing on the natural rubber based adhesives. Similarly to the previous analysis of the annealing steps in Ar and HV conditions, we measured the rms roughness (R_{rms}) and the surface coverage and we plotted them versus annealing time (Figure 2.24 (a), (b)).

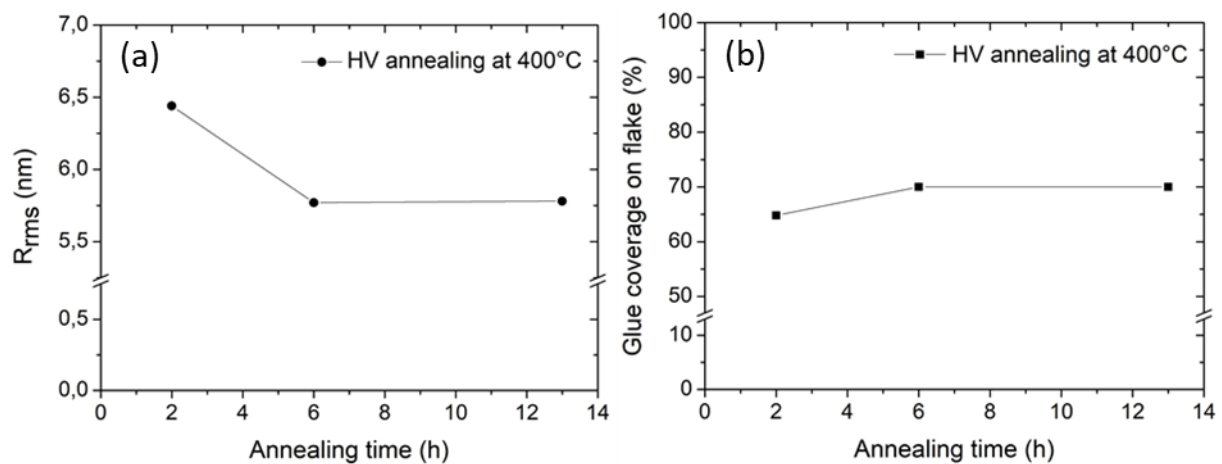


Figure 2.24 Plots of the rms roughness (a) and the percent of glue coverage (b) on the $1 \times 1 \mu\text{m}^2$ topography AFM images of the aforementioned Cr_2AlC flake as a function of annealing time at 400°C in HV conditions.

Similarly to the case of the synthetic tape adhesives annealed under HV conditions (§ 2.2.1.3), the R_{rms} value showed a small decrease from 6.44 nm to 5.77 nm between the 2 hours and 6 hours annealing (Figure 2.24 (a)). Despite the roughness change, the residues coverage apart from some statistical fluctuations in the order of 5% seems to remain unaltered (Figure 2.24 (b)), in accordance to our observations for the synthetic tape residues. An additional increase on the annealing time to 13 hours in total showed a saturation level reached by both the R_{rms} (5.78 nm) and the glue residues coverage (70%).

Consequently, the acetone cleaning proved less efficient than a few hours of HV annealing to the limitation of the natural rubber based adhesive residues left on the flakes' surface, despite the less resilient chemical structure of the residues to the acetone that was expected.

2.3 Conclusion

The transformation of bulk MAX phases to their 2D counterparts MAXenes with obtained flake thickness down to (half-)monolayer demonstrated that mechanical exfoliation can be applied to layered structures where stronger inter-layer bonds than van der Waals prevail. In contrast with weakly-bonded lamellar materials in which the problem of glue residues onto flakes after the transfer process was settled more easily, in the case of MAXenes was a major challenge. Among all the methods we tested to reduce the concentration of glue residues onto the flakes, either by using tapes of different chemical structure adhesives e.g. UV susceptible tapes and natural rubber based adhesive tapes or by applying solvents cleaning or Ar and HV annealing processes, none of them could completely remove the glue residues neither from the flakes nor from the substrates surface. Nevertheless, it was demonstrated that 2 hours of thermal annealing either in Ar or in HV conditions, regardless of the chemical composition of the adhesive residues, can partly act against the residues in an efficient way. In particular, and independently of the kind of the adhesive tape being used, the HV annealing favors the contraction of the glue agglomerates while Ar annealing tends to spread them on the flake's surface.

Chapter 3

Characterization techniques and experimental set-up

In the present chapter, we describe in detail the set-up and working principles of the experimental techniques we used during this thesis, with emphasis to the applied operating modes for the surface and electrical properties characterization of MAXenes. In the case of EFM and KPFM techniques, a description of the tip-sample interaction is given for our system configurations, in the presence and absence of flakes, by two models that provide acceptable approximations of the tip geometry: the sphere-plane and sphere-cone models. Eventually, we explain our selection based on the model's availability to provide computations in both configurations.

3.1 Introduction to electrical modes of Atomic Force Microscopy (AFM)

Atomic force microscopy (AFM) is a non-destructive technique that offers a wide variety of measurement modes. Without any demanding and time consuming preparation of the samples, AFM is indicated for a number of high resolution (nanoscale) measurements of surface topography to mechanical, electrical or magnetic properties of the samples for instance.

Contact modes, dynamic (tapping) modes, advanced imaging modes and electrical modes are some examples of AFM measurement modes. In the present thesis we focused on the electrical modes and particularly on Electrostatic Force

Microscopy (EFM) and on Kelvin Probe Force Microscopy (KPFM) to assess the electrical surface properties of MAXene flakes down to one unit cell thickness. Both EFM and KPFM operation principles are presented in detail in the following. First, the working principle of AFM method is discussed.

3.1.1 Brief introduction to Atomic Force Microscopy

Atomic force microscopy is a type of scanning probe microscopy (SPM) exploiting mechanical interactions between a sample surface and a scanning probe. Before describing the operation principle of the technique it is indispensable to firstly refer to the AFM set-up we used.

A Bruker Nanoscope (model 3100 dimension) V atomic force microscope equipped with EFM and KPFM modules was used for our measurements in ambient conditions. The microscope consists of the AFM head or scanner, a camera with objective lens, an X-Y stage with a vacuum chuck, a cable for transferring the recorded deflection signal to electronics and then to computer and an Invar (Ni-Fe alloy) frame that holds the hybrid head and the camera (Figure 3.1 (a)). The topography signal corresponds to the bias applied to the piezoelectric element which actuates the cantilever along the z axis. A laser beam (Figure 3.1 (b)) is focused by a collimator and by a pair of lenses onto the reflective surface of the cantilever. The reflected beam is guided through a lens to a pair of mirrors, which are arranged opposite to one another, and through the reflection to their surfaces the position of the light beam, which depends directly on the cantilever's deflection, is finally detected by a quadrupole photodiode. Two pairs of knobs exist on top and left side of the AFM head to adjust the laser beam on the cantilever's surface and the position of one of the two mirrors, correspondingly.

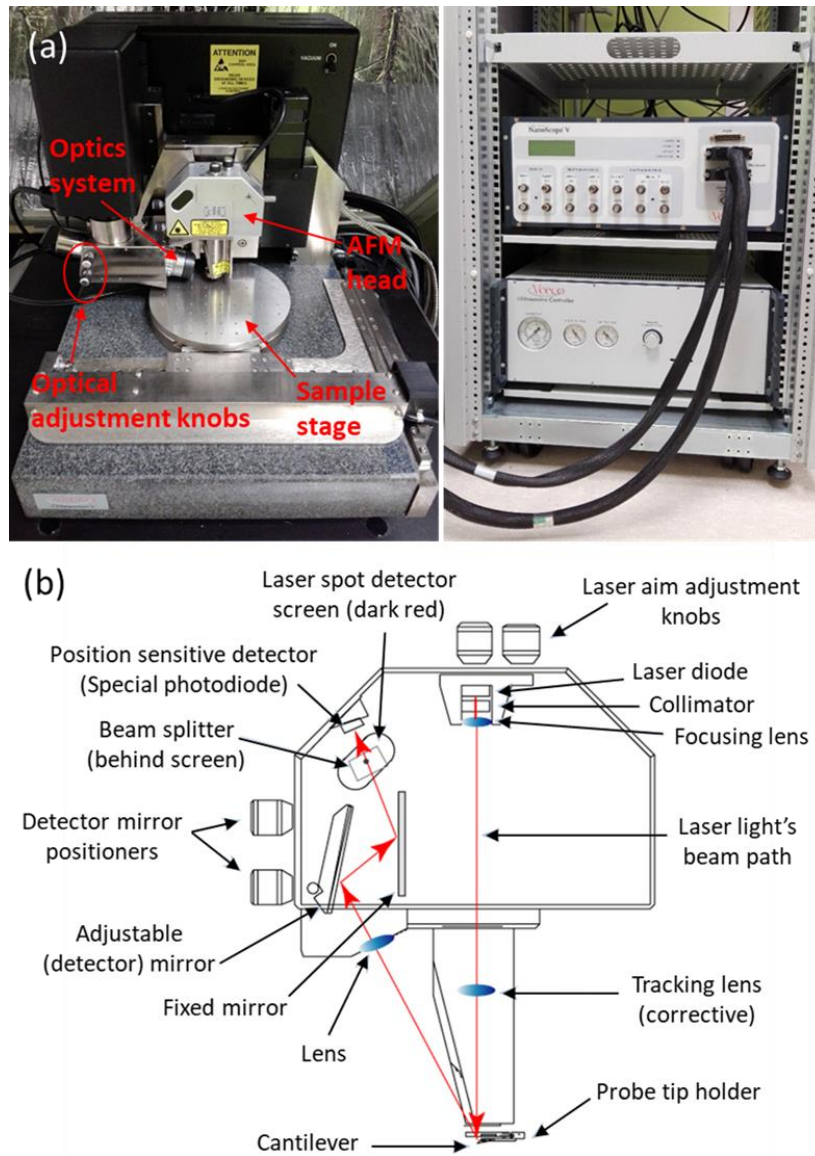


Figure 3.1 AFM set-up with its consisting parts and its corresponding electronics in Néel Institute (Grenoble) (a). Description of the hybrid head configuration (b). Figure (b) adapted from Ref. [195].

The working principle of AFM is based on a cantilever/tip assembly that is usually referred to as probe. An atomically sharp tip, usually made from Si, with a few micrometers height and around 10-20 nm curvature radius, is located at the end of a Si or SiN flexible cantilever with its length ranging from a few tens to a few hundreds of micrometers depending on the type of the cantilever. The probe is mounted on a probe tip holder that is placed on the bottom part of the piezoelectric transducer in the AFM head, which facilitates the probe positioning and the surface scan in X-Y-Z directions with precise movements.

The nature of the sample's surface is usually the criterion which determines the operating mode of the AFM system that can be applied. The contact operating mode can be used for samples with flat surface and high toughness that are not prone to surface damage. On the contrary, dynamic or non-contact AFM modes are indicated in the case of samples with rough surface and less resilient to damage from a tip contact. The dynamic operation modes, also named tapping modes, are divided into two basic methods, the amplitude modulation (AM) or tapping mode and frequency modulation (FM) mode, where changes in oscillation amplitude and resonance frequency are detected. These changes derive from the alteration of the tip-sample interaction because of the distance variations between the tip and sample during the surface scan. The feedback signal used for regulation during scanning is either the amplitude or frequency alteration.

Considering the length scale of the interaction, the frequency shift of the cantilever resonance frequency in FM mode is proportional to the derivative of force in small displacements [196]. This means that the FM-AFM mode detects the force gradient (force derivative) between the tip and the sample, contrary to AM-AFM mode that detects the direct force interaction. This enables the FM mode to reach superior spatial resolution topography images [197]. The AM or tapping mode AFM however remains the most widely implemented imaging process of the surface topography with the probe excitation occurring at or near its resonance frequency [198]. This mode is described in details in the following, as we used it for our measurements.

Once the probe approaches the surface of the sample, various kinds of interactions between the tip and the surface, with van der Waals forces being the dominant ones, lead to the deflection of the cantilever towards the surface. As the probe-sample distance is further decreased down to the point at which the atom of the tip apex almost comes in contact with the atoms of the sample's surface, repulsive forces involving the electrons of the outer orbitals dominate the interactions and cause the cantilever to deflect away from the surface. By scanning the region of interest, the deflection of the cantilever due to the surface topography is monitored by a feedback loop that determines the probe movement in the three dimensions.

As previously mentioned, the reflected light beam on the backside of the cantilever is recorded on a position sensitive photodetector (PSPD), which can track any slight change of the beam position when the cantilever is deflected. Independently of the AFM mode that is used, a setpoint of the beam position on the photodetector is defined prior to the surface scan. A continuous comparison of the reflected beam signal on the photodetector with the setpoint allows, through the feedback loop, the regulation of the probe's position. Any difference in value is sent to the AFM head (scanner) as a voltage input to readjust the probe's position (Figure 3.2) [198].

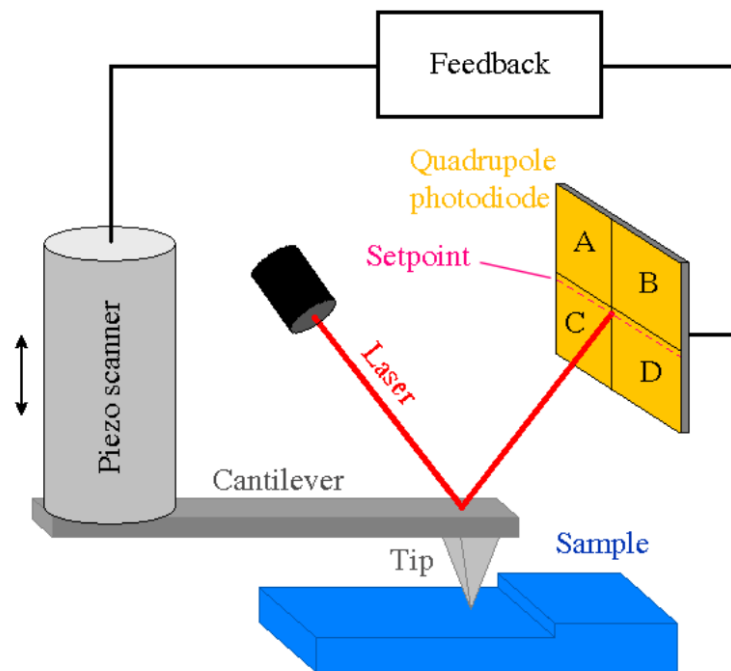


Figure 3.2 Representation of the operating principle of the AFM in the case of contact mode. Figure adapted from Ref. [198].

It is obvious in the figure above that the photodetector (quadrupole photodiode) consists of four adjoint photodiodes, which help to distinguish the deflection signal in lateral and vertical contributions. According to the optical lever mode, the signal difference between the upper and the bottom pairs corresponds to the vertical deflection of the cantilever while the signal difference between the left and the right pair of photodiodes determines the cantilever's lateral deflection. Particularly:

$$\textit{vertical deflection measurement} = \frac{(A + B) - (C + D)}{(A + B + C + D)} \quad (3.1)$$

$$\textit{lateral deflection measurement} = \frac{(A + C) - (B + D)}{(A + B + C + D)} \quad (3.2)$$

These equations include a normalization of the measured signal with the total intensity of the signal detected in the quadrupole photodiode to avoid the perturbations that derive from the intensity variations of the laser diode. Generally, the vertical deflection is mainly used in non-contact and tapping modes whereas the lateral one is mostly used in contact AFM mode for measuring the friction signal [198].

3.1.2 Electrostatic Force Microscopy (EFM)

One of the most common electrical AFM modes, firstly introduced by Y. Martin et al. [199], is Electrostatic Force Microscopy, which records the electrostatic interaction between the sample's surface and the biased tip of the AFM cantilever. EFM provides qualitative information about the surface potential and the charge distribution on the scanned region of the sample, without requiring any time consuming processing of the sample's surface, e.g. contacts fabrication. Exception however, seems to be the preparation of the substrate's surface, hydrophobic or hydrophilic state, as its influence to the recorded electrical signal is not at all trivial (see next chapter).

3.1.2.1 EFM operating methods

EFM uses the same set-up as for the conventional AFM with the only difference between the two microscopies being the probe's material. The necessity of using conducting tips to detect the weak but long range electrostatic forces requires either the metallization of the probes or the use of highly-doped Si tips. In

particular, different kinds of thin metal film coatings, e.g. Cr, Cr-Au, Pt-Ir, Ti-Pt, WC, can be deposited on the cantilever-tip surface, with a thickness in the range of 25 nm, to improve the tip conductivity. These coatings usually deteriorate the lateral resolution in topography as they increase the apex radius [200].

Two operating methods to obtain the electrical information of the sample's surface are available to EFM, the single-pass and the double-pass mode. The former method is used to specific cases only, such as vacuum or high vacuum conditions [201] and hence, only a brief description will be given.

In the single-pass mode, the tip is brought in close proximity to the surface of the sample with their distance being constant during the scanning process, whilst the probe is oscillating at its resonance frequency and a DC bias voltage is applied externally between the tip and the sample. As a result, the amplitude and phase signal of the electrostatic interactions are simultaneously measured with the topography profile. Samples with irregular topography are not suited for this operation mode due to the impossibility to discriminate between the topography and electrostatic force contributions.

In the double-pass method the cantilever scans twice every line of the selected surface region of the sample but in a different mode each time. In the first pass, the piezotube mechanically oscillates the probe along z direction at or close to its resonance frequency and the tip scans the surface in an amplitude modulation tapping mode so as to obtain the topography. Once the first scan is completed, the tip is retracted to a larger distance from the sample surface, where it then retraces the topography variations recorded during the first path, to obtain the electrostatic information of the surface. The lift height, at which the tip is retracted in the second scanning mode (lift mode), is optimized by the user for every image. Normally, the lift height ranges between few tens to few hundreds of nanometers, an interval at which short range forces like van der Waals are no longer dominant. During the second pass, the probe continues to oscillate at its resonance frequency and a DC bias voltage is applied between the tip and the sample, resulting in capacitive electrostatic forces that are exerted on the tip. The electrostatic interaction shifts the resonance frequency and thus the amplitude and the phase signal that are finally recorded in combination with the topography signal [200].

The main drawback of the double-pass mode, compared to the single-pass one, is the limited spatial resolution as a consequence of the increased tip-sample distance in the second scan [201].

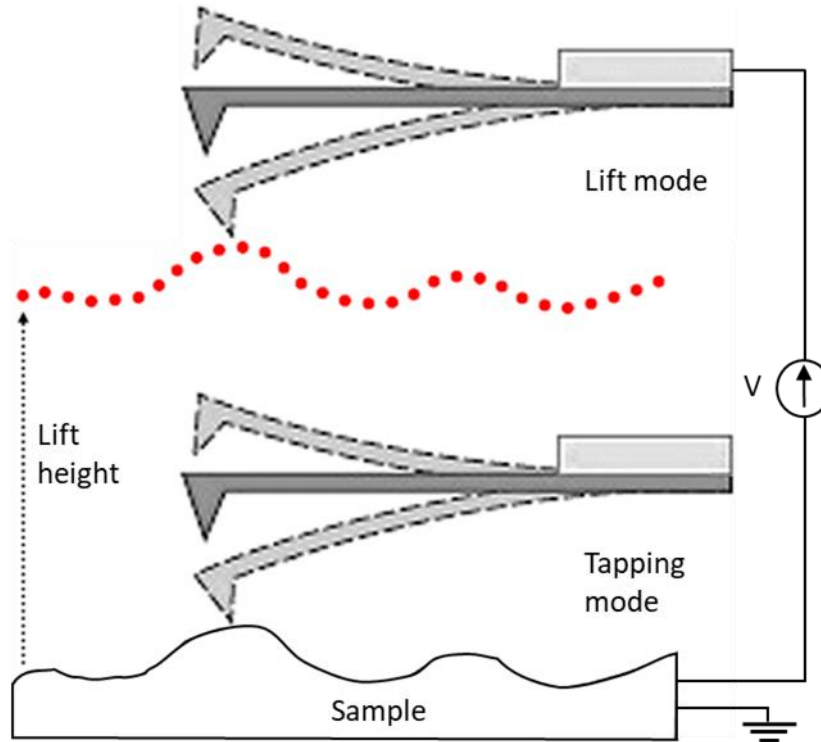


Figure 3.3 Double-pass method of EFM. The cantilever firstly scans the sample's surface in the tapping mode to obtain the surface topography. Then a second scan in the lift mode takes place and following the topography trace detects the electrostatic information. Figure adapted from Ref. [202].

3.1.2.2 Electrostatic interactions in EFM

Independently of the scan mode (single- or double-pass) used in EFM, a voltage source is required to induce the electrostatic interactions between the EFM tip and the sample. For a SiO_2/Si substrate, the DC voltage applied between the metallic tip and the bulk (conductive) Si induces electric charges (q) accumulated at the tip and the SiO_2/Si interface which would be equal to $(-q)$ in the absence of additional parasitic charges in the oxide layer or at its surface. In other words, there is a capacitive coupling between the tip and the Si surface, in serial configuration. Two series plate capacitors are formed with air and the SiO_2 as dielectrics (Figure 3.4).

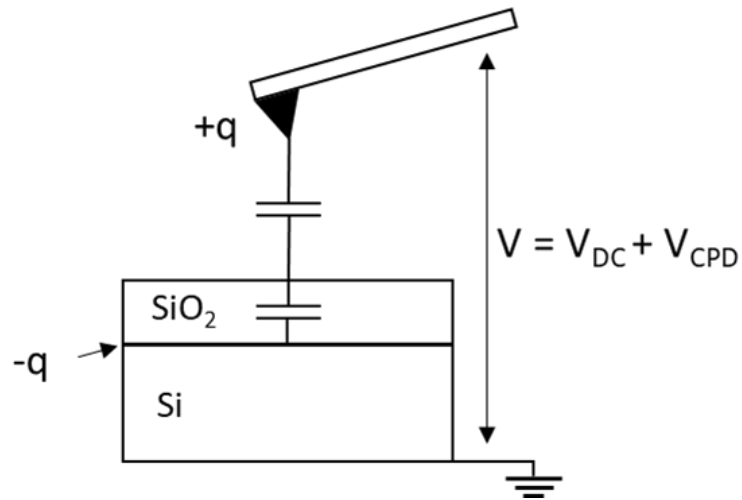


Figure 3.4 Schematics of the electrostatic interaction between the metallic tip of the AFM set-up and the SiO_2/Si sample when a DC voltage is applied externally to the electrodes (tip and Si substrate). Additional parasitic charges can be possibly present in the oxide layer and at its surface however, the total sum of charges in the tip-sample system is always zero.

Attractive coulombic forces (capacitive forces) are exerted between the charges located at the conductor's surfaces. The electrostatic energy of the tip-Si system writes:

$$W = \frac{1}{2} CV^2 \quad (3.3)$$

where C refers to the total capacitance in the serial arrangement and:

$$V = V_{DC} + V_{CPD} \quad (3.4)$$

with V_{DC} the applied DC voltage and V_{CPD} the contact potential difference, which refers to the work function difference between the tip and the Si. V_{CPD} term is measured by KPFM technique, the operation principles of which will be explained in details in the corresponding subsection.

The electrostatic force that describes the tip- SiO_2/Si interaction is the capacitive force which derives from the gradient of the electrostatic energy:

$$F_{el} = -\nabla W = -\frac{1}{2} \frac{\partial C}{\partial z} (V_{DC} + V_{CPD})^2 \quad (3.5)$$

where z is the distance between the tip apex and the surface of the sample that remains constant during the second pass.

The AFM cantilever can be modeled by a harmonic oscillator excited by an externally driven mechanical force $F_p(t)$ resulting from the piezoelectric element and F_{el} . Within this approximation, the equation of the cantilever motion can be written as follows:

$$m \frac{d^2 z}{dt^2} + kz + \frac{\omega_0}{Q} \frac{dz}{dt} = F_p(t) + F_{el}(z) \quad (3.6)$$

where the second and third term on the left part of the above equation refer to the restoring and the friction forces, respectively. For a time-periodic mechanically driven force, $F_p(t) = F_0 e^{i\omega t}$, using the first order development of the F_{el} at any z , the aforementioned formula is modified to:

$$\frac{d^2 z}{dt^2} + \frac{\omega_0}{mQ} \frac{dz}{dt} + \frac{k}{m} z = \frac{F_0}{m} e^{i\omega t} + \frac{F_{el}(0)}{m} + \frac{1}{m} \frac{dF_{el}}{dz} z \quad (3.7)$$

The solution to this differential equation, when the zeroth order term of the electrostatic force is neglected, has the form of $z(t) = z_0 e^{i(\omega t + \varphi)}$ with φ being the phase between the force and the cantilever's deflection and z_0 the oscillation amplitude. Replacing $z(t)$ to the above equation and considering that $\omega_0^2 = k/m$ then:

$$z_0 e^{i\varphi} = \frac{F_0/m}{\left(\omega_0^2 - \omega^2 - \frac{1}{m} \frac{dF_{el}}{dz}\right) - (\omega_0 \omega / mQ) i} \quad (3.8)$$

The oscillation amplitude is eventually written:

$$z_0 = \frac{F_0/m}{\sqrt{\left(\omega_0^2 - \omega^2 - \frac{1}{m} \frac{dF_{el}}{dz}\right)^2 + \left(\frac{\omega_0\omega}{mQ}\right)^2}} \quad (3.9)$$

The driving force of the piezoelectric excites mechanically the cantilever at or close to its resonance frequency in the absence of the electrostatic interaction. The additional contribution of the electrostatic force in cantilever's oscillation shifts the resonance frequency to:

$$\omega_M = \sqrt{\omega_0^2 + \frac{\Delta k}{m}} = \omega_0 \sqrt{1 + \frac{\Delta k}{k}} = \omega_0 \left(1 + \frac{\Delta k}{2k}\right) \quad (3.10)$$

where:

$$\Delta k = k_{eff} - k = -\frac{\partial F_{el}}{\partial z} \quad (3.11)$$

refers to the modification of the probe's spring constant induced by the applied force gradient. The last term in eq. (3.10) derives from the 1st order Taylor development of the square root term. Thus, the difference in the oscillation frequency with and without the electrostatic force contribution is calculated by:

$$\Delta\omega = \omega_M - \omega_0 = \frac{\omega_0}{2} \frac{\Delta k}{k} \quad (3.12)$$

Obviously, any change in the resonance frequency of the cantilever affects the phase which is related to the oscillation frequency:

$$\varphi = \arctan \frac{\omega_0\omega}{Q(\omega_0^2 - \omega^2)} = \frac{\omega_0\omega}{Q(\omega_0^2 - \omega^2)} \quad (3.13)$$

when the only driving force is the mechanical force exerted by the piezoelement. When the electrostatic interaction is added to the cantilever's equation of motion

the above equation of phase is modified by using eq. (3.10). Therefore, the phase difference in the presence and the absence of the electrostatic interaction leads to a phase shift which is defined by:

$$\Delta\varphi = \frac{\omega(\omega_0^2 + \omega^2)}{Q \left((\omega_0^2 - \omega^2)^2 + \left(\frac{\omega_0\omega}{Q} \right)^2 \right)} \Delta\omega \approx \frac{2Q}{\omega_0} \Delta\omega \quad (3.14)$$

Replacing (3.12) to (3.14) and considering that the only effect of the electrostatic tip-SiO₂/Si interaction is the modification of the probe's spring constant k , eq. (3.11), the phase shift can be written:

$$\Delta\varphi = -\frac{Q}{k} \frac{\partial F_{el}}{\partial z} \quad (3.15)$$

The phase shift signal that derives from the frequency shift ($\Delta\omega$) of the cantilever owing to the tip-sample electrostatic interaction is finally measured by the lock-in amplifier of an EFM system (Figure 3.5).

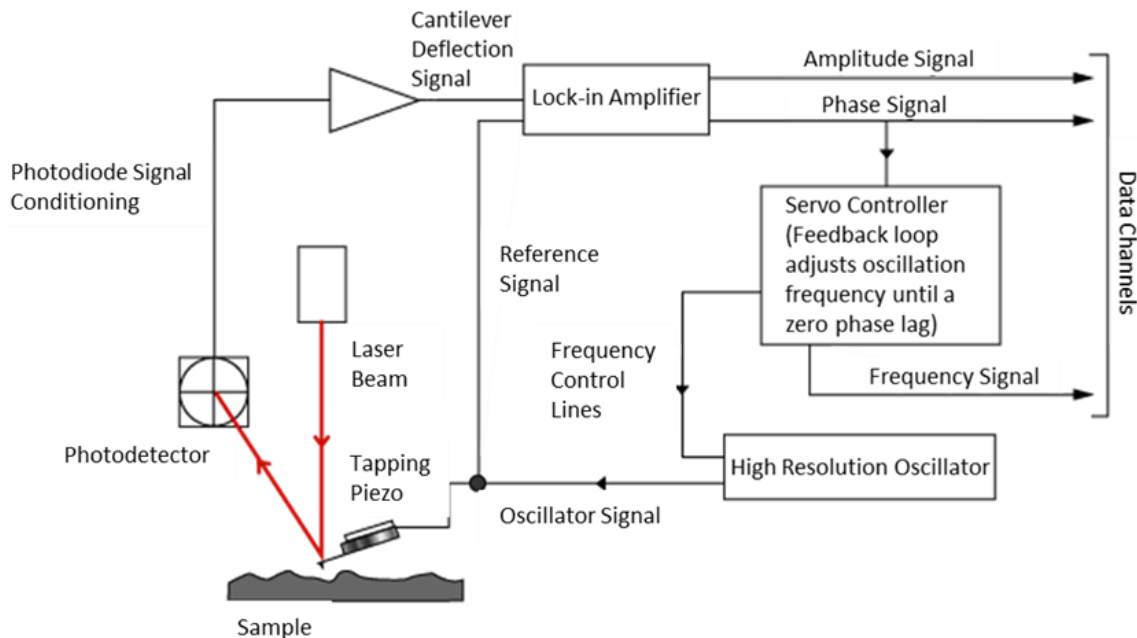


Figure 3.5 Schematics of an EFM circuit. The pre-amplified deflection signal of the cantilever serves as input signal in the lock-in amplifier which measures the amplitude or frequency shift. Figure adapted from Ref. [203].

The capacitance contrast and the surface potential contrast serve as the output signal of the lock-in amplifier that are finally recorded to an EFM image. A detailed analysis of these two kinds of contrast is presented in the following subsections as well as in the fourth chapter.

3.1.3 Kelvin Probe Force Microscopy (KPFM)

This microscopy technique was named “Kelvin” as a tribute to Lord Kelvin, who developed a similar macroscopic method of contact potential difference detection, back in 1898 [204]. The last and now most-common version of KPFM, was introduced in 1991 by Nonnenmacher and colleagues [205], as well as by Weaver and Abraham [206]. KPFM is a surface sensitive method which can provide information about the contact potential difference or work function of the sample surface by probing the contrast related to the sample’s electrical properties at the nanoscale [207].

3.1.3.1 Fundamental principles of KPFM

Based on the AFM set-up and the Kelvin probe principle [204] KPFM is an essential technique to map the surface potential difference between the AFM metallic tip and the sample, at any point of the sample’s surface. Once the tip approaches the sample to a close distance (Figure 3.6 (a)), their different work functions, related to their different Fermi energy (E_f) levels, induce an electrical interaction. Electrons flow from the material with the lower work function to that of higher work function, resulting finally to an equilibrium state of the tip-sample system with the alignment of their energy Fermi levels (Figure 3.6 (b)). This equilibrium state is formed by connecting electrically the tip and sample or even by electron tunneling effect [208], if the tip comes close enough to the sample’s surface, almost touching it, which is however not usually the case. Despite the aligned Fermi levels at a steady state, the energy vacuum levels of the tip-sample

system are no longer in the same line due to the surface charges found at the surface of the tip and of the sample. Those charges lead to a surface potential difference $\Delta\phi$ (or CPD) between the tip and the sample, given by the formula:

$$V_{CPD} = \Delta\phi = \frac{\phi_{tip} - \phi_{sample}}{e} \quad (3.16)$$

with ϕ_{tip} and ϕ_{sample} the work functions of the tip and sample, respectively and e the elementary electron charge. Owing to the existence of the surface charges an electrostatic (capacitance) force is generated between the tip and the sample which is proportional to the contact potential difference and the tip-sample capacitance, as it is described in the following:

$$F = \frac{1}{2} \frac{\partial C}{\partial z} (V_{CPD})^2 \quad (3.17)$$

where z is the tip-sample distance. The surface charges and thus the V_{CPD} signal affect the aforementioned capacitance force and hinders the detection of the sample's surface potential by the tip. This can be circumvented by applying an external bias voltage (V_{DC}) of the same magnitude to V_{CPD} but acting in the opposite direction and which counteracts the tip-sample surface charges, with the purpose of nullifying the capacitance force [208] (Figure 3.6 (c)).

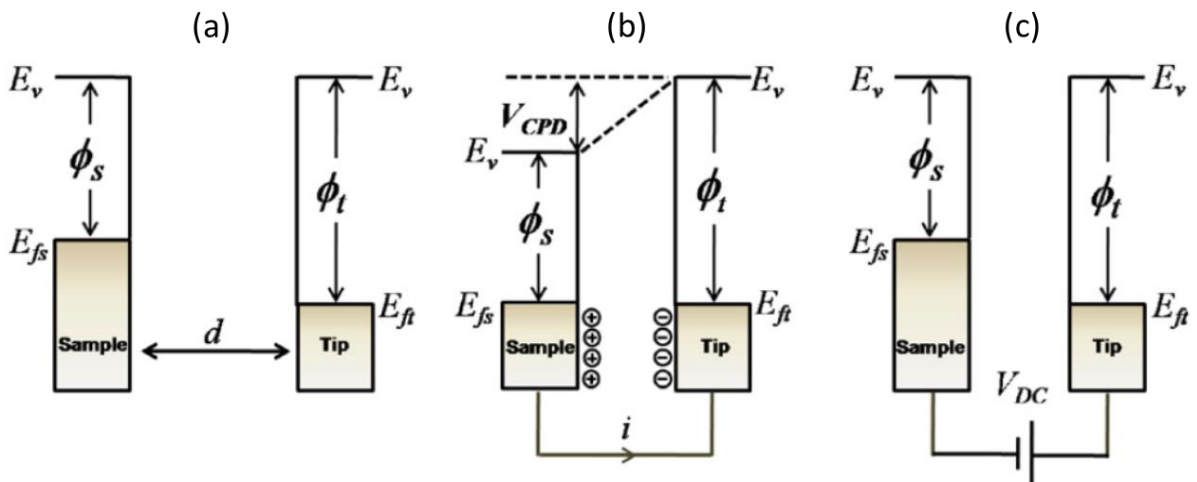


Figure 3.6 Modulation of the electronic energy levels in an AFM tip-sample system for three different cases: (a) the tip approaches to a very close distance d the sample's surface without being electrically connected, (b) electrical contact between the tip and the sample, and (c) application of external DC bias voltage to tip-sample system to compensate the V_{CPD} signal. E_{fs} and E_{ft} refer to the sample and tip Fermi energy levels, respectively while E_v corresponds to the vacuum energy levels. Figure adapted from Ref. [208].

The AFM tip can record the surface contact potential difference in KPFM when it interacts electrostatically with the surface of the sample. The forces acting between the tip and the sample, contrary to what was mentioned regarding the EFM method, derive from the external DC and an additional AC bias voltage that are both applied to the tip-sample system. The AC signal drives the cantilever to an electrical oscillation while the DC signal is adjusted in order to compensate the V_{CPD} voltage that originates from the tip-sample interaction. The total electrostatic force acting between the tip and the sample surface depends on the capacitance term, similarly to EFM principle analysis but with the modified voltage signal:

$$F_{el} = -\frac{1}{2} \frac{\partial C}{\partial Z} (V_{DC} + V_{AC} \sin(\omega t) + V_{CPD})^2 \quad (3.18)$$

Developing further the right part of eq. (3.18) and considering $\sin^2 \omega t = \frac{1 - \cos(2\omega t)}{2}$, one gets the analytical formula of the total electrostatic force which can be divided into three basic force components, each of which contributes differently to the KPFM image [208]. A frequency-independent term, F_{DC} , given by the formula:

$$F_{DC} = -\frac{\partial C}{\partial Z} \left[\frac{1}{2} (V_{DC} + V_{CPD})^2 + \frac{1}{4} V_{AC}^2 \right] \quad (3.19)$$

deflects continuously the cantilever along the vertical axis, additionally contributing to the final topography signal. The first harmonic term, F_{ω} :

$$F_{\omega} = -\frac{\partial C}{\partial Z}(V_{DC} - V_{CPD})V_{AC} \sin(\omega t) \quad (3.20)$$

excites the cantilever at ω_{AC} frequency and is the only term that contributes to the sample's surface potential measurements. The V_{DC} voltage is modified at each point of the sample's surface to compensate the difference of the tip-sample work functions and thus to nullify the F_{ω} force component. The third component force is entirely a second-harmonic one, independent of CPD, it is defined by:

$$F_{2\omega} = \frac{1}{4} \frac{\partial C}{\partial Z} V_{AC}^2 \cos(2\omega t) \quad (3.21)$$

and it mainly contributes to capacitance spectroscopy and imaging [209].

3.1.3.2 Operating methods of KPFM

A probe with a thin conductive coating is required for KPFM technique as well so that tip can interact electrostatically with the surface of the sample which, like EFM, does not require any demanding processing.

Similar to EFM (see previous section), both single- or double-pass measurement modes can be used. The single-pass method is rarely implemented in KPFM and we will address it only briefly here.

In the single-pass mode, the metallic tip of the AFM set-up passes over the sample surface at a constant distance while an AC bias voltage is applied between the cantilever and the sample generating an electrostatic interaction that prompts the cantilever to an electrically driven oscillation. In parallel, an external DC signal is applied in the tip-sample system to compensate the contact potential difference (V_{CPD}) which arises from the electrostatic force exerted between the tip and the sample, due to their work function difference, when the tip approaches very close to the sample's surface. What is finally recorded at each point of the surface is the DC signal that has the same magnitude as V_{CPD} but opposite direction, so as to fulfill the $V_{DC} = V_{CPD}$ condition.

In the double-pass method, the cantilever scans twice the surface of the sample, in a different mode each time. A tapping mode can be applied during the first scan allowing the cantilever to obtain the sample's topography without damaging the tip or the surface. Once the first scan is completed, the tip is lifted over the sample at a height prescribed by the user, with the value ranging between a few nanometers to a few tens of nanometers. During the second pass (lift mode), the tip retraces the profile acquired at the first time at a constant distance from the surface (Figure 3.3).

An essential factor for the second scan is the low tip-sample distance needed to avoid the stray capacitance of the cantilever without damaging the tip if it would touch the surface.

Generally, in the second scan the operating method looks similar to that of the aforementioned single-pass mode, having however, a substantial difference owing to the elimination of the topography contribution. Another difference, regarding the measurement of the surface potential, is that now it can be recorded by both amplitude (AM) and frequency modulation (FM) modes. In the second scan the feedback loop that controls the mechanical oscillation of the cantilever is opened and an external AC voltage is applied between the tip and the sample at a frequency ω_{AC} , either equal or close to the cantilever's resonance frequency ω_0 . The AC voltage excites the cantilever electrically resulting in a deflection of the laser beam on the photodiode. The deflection is the input signal of a lock-in amplifier tuned at ω_{AC} frequency. Depending on the mode used in KPFM, AM or FM, the lock-in treats a signal corresponding to the oscillation amplitude or the frequency, respectively.

In AM-KPFM mode, that was used in our measurements, the first harmonic (F_ω) is directly measured by the amplitude difference (Δz) between the mechanical and electrical oscillation of the cantilever that occur at the same frequency ω_{AC} which derives from the V_{AC} signal. The frequency ω_{AC} is close to the cantilever's resonance frequency ω_0 (Figure 3.7).

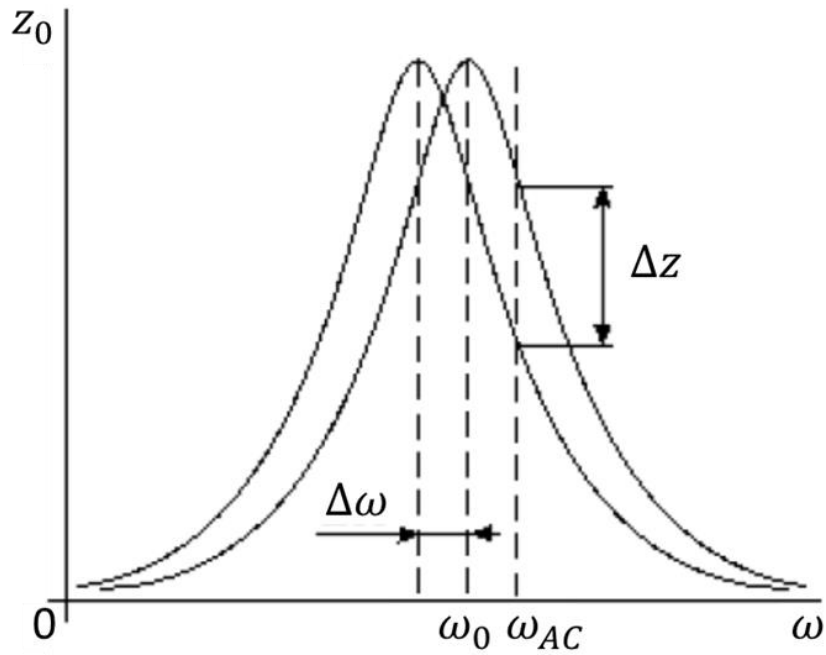


Figure 3.7 Variation of the oscillation amplitude versus frequency during a tip-sample interaction in an AFM set-up. Figure adapted from Ref. [210].

The oscillation amplitude of the cantilever is proportional to the electrostatic force in the tip-sample interaction and it is recorded by a lock-in amplifier (Figure 3.8). The additional DC signal applied to the tip to nullify the oscillation amplitude is regulated by a controller to minimize the first harmonic by matching the DC and the CPD voltage ($V_{DC} = V_{CPD}$) [207].

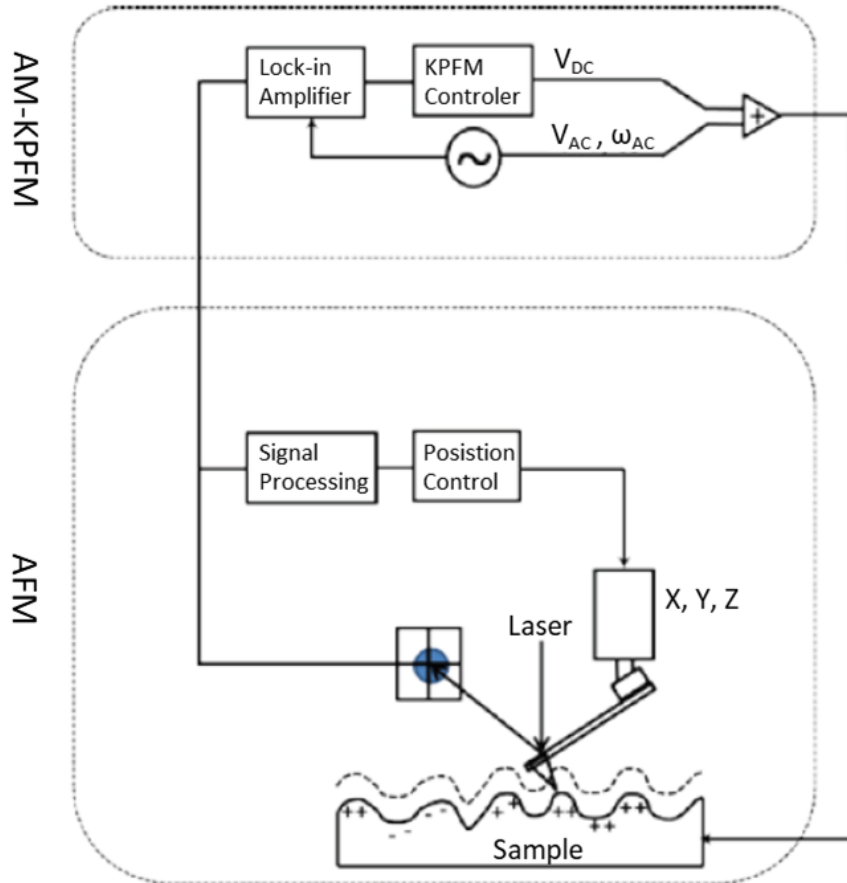


Figure 3.8 Schematic diagram of AM-KPFM method based on the AFM set-up. The lock-in amplifier detects the signal amplitude of the applied AC voltage between the tip and the sample while the KPFM controller regulates the DC voltage to compensate the CPD signal. Figure adapted from Ref. [211].

In the FM-KPFM mode, the direct electrostatic force is not detected, but the electrostatic force gradient, a less straightforward electrical property. In such a case, the cantilever is similarly oscillated by the electrical force induced by the applied sinusoidal voltage between the tip and the sample with the frequency ω_{AC} much lower than the probe's resonance frequency ω_0 . Any change in the electrostatic force gradient affects the effective spring constant of the cantilever, (eq. 3.11 in EFM section), and changes accordingly the resonance frequency, ω_{eff} , which is written:

$$\omega_{eff} = \left[\left(k - \frac{\partial F_{el}}{\partial z} \right) / m_e \right]^{1/2} = \omega_0 \left(1 - \frac{1}{k} \frac{\partial F_{el}}{\partial z} \right)^{1/2} \quad (3.22)$$

with $\omega_0^2 = k/m_e$, and m_e being the effective mass of the cantilever. As a consequence, the force gradient modulates the cantilever's resonance frequency by inducing a frequency shift, $\Delta\omega$ (Figure 3.7) which is described by eq. (3.12) [212] and can be equivalently written:

$$\Delta f = -\frac{f_0}{2k} \frac{\partial F_{el}}{\partial z} \quad (3.23)$$

Therefore, in the FM-KPFM mode any beam deflection detected on the photodiode derives from a force gradient modulation during the tip-sample interaction, owing to the externally applied AC bias. That beam deflection is recorded as a resonance frequency shift, $\Delta\omega$, by a lock-in amplifier, which is tuned at the probe's resonance frequency and whose role is to modulate the phase of the signal. The phase output acts as the input signal of a second lock-in amplifier that is tuned at ω_{AC} and measures the amplitude of the signal at the frequency shift, $\Delta\omega$. Finally, the signal is fed into a KPFM controller whose feedback loop controls the applied DC bias voltage to the tip-sample system so as to compensate the V_{CPD} signal ($V_{DC} = V_{CPD}$) [208], [211].

3.1.4 Theoretical approximation of an AFM tip in a metal-air-metal (MAM) and metal-air-dielectric-metal (MADM) configuration

In a configuration such as ours, a conducting MAXene flake is deposited onto the silicon oxide surface presented in Figure 3.4. The equations derived in the previous sections for bare SiO_2/Si need to be modified. Considering for simplicity the flake as a conducting layer that interacts with the tip and the Si through SiO_2 , the modified configuration will be referred to as metal-air-metal (MAM) and metal-air-dielectric-metal (MADM) in the presence and absence of any flakes, respectively (Figure 3.9 (a), (b)).

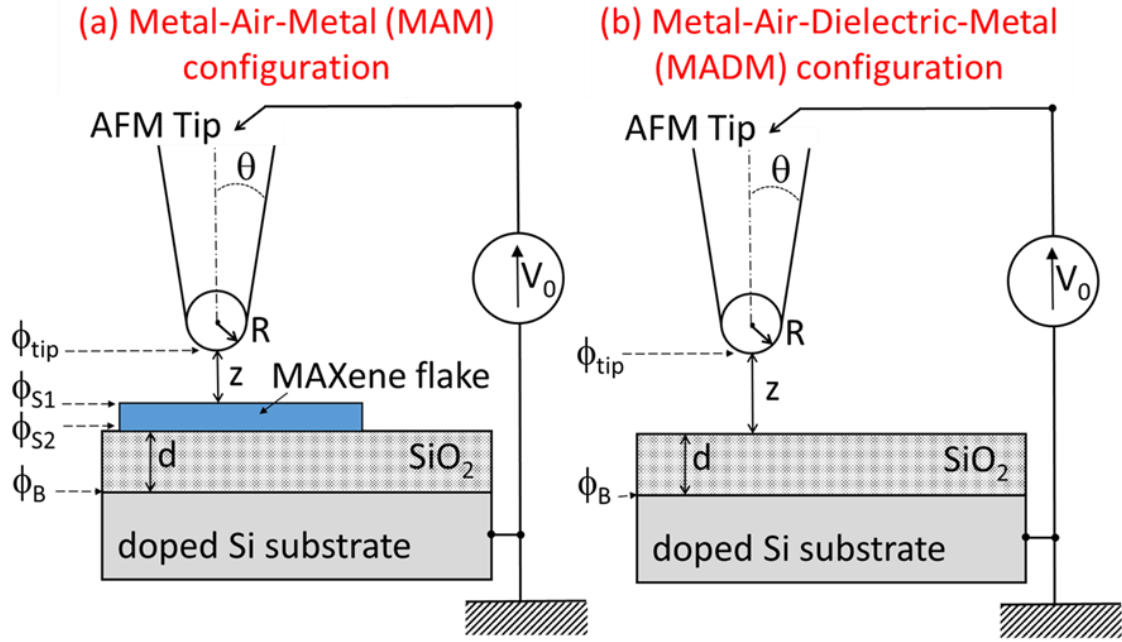


Figure 3.9 Schematics of the EFM and KPFM configurations when (a) the AFM tip is positioned above the MAXene flake (MAM) and (b) when it is positioned above the silicon oxide layer (MADM).

We consider a bias voltage V_0 applied between the metallic AFM tip and the Si substrate. Assuming the flake is metallic, the electrostatic energy generated by the voltage and given by eq. (3.3) is modified as follows:

$$W = \frac{1}{2} \frac{C_M C_0}{C_M + C_0} (V_0 - \phi_{tip} + \Delta\phi_S + \phi_B)^2 \quad (3.24)$$

with C_M and C_0 being the tip-flake and flake-Si substrate capacitances, respectively. The latter can be approximated by $C_0 = \epsilon_{SiO_2} A/d$, where d is the oxide thickness (300 nm in our case) and A the flake area. The terms ϕ_{tip} , ϕ_B and $\Delta\phi_S = \phi_{S1} - \phi_{S2}$ refer to the tip surface potential, the Si substrate surface potential at the Si-SiO₂ interface and the difference of surface potentials between the top and the bottom of a given flake (Figure 3.9 (a)), respectively. It is worth mentioning that the influence of adsorbed surface charges or dipoles (e.g. charges due to triboelectrification of the glue residues at the peeling point [213], charges in the SiO₂ layer [214], adsorbed water molecules [215], [216], etc.) can be incorporated into the form of additional shifts of the above surface potential values. Since force

is the gradient of the energy (3.5) and provided that the surface of MAXene flake is large enough and C_0 does not depend on the tip-sample distance z , the electrostatic force accounting for the tip-sample interaction becomes:

$$F = \frac{1}{2} \left(\frac{C_0}{C_M + C_0} \right)^2 \frac{\partial C_M}{\partial z} (V_0 - \phi_{tip} + \Delta\phi_S + \phi_B)^2$$

$$\cong \frac{1}{2} \frac{\partial C_M}{\partial z} (V_0 - \phi_{tip} + \phi_B + \Delta\phi_S)^2 \quad (3.25)$$

As it was described in the EFM section, during the lift mode and maintaining a constant tip-sample distance z , the gradient of the previously mentioned electrostatic force is simply added to the cantilever's effective spring constant k_{eff} . This modifies the cantilever's resonance frequency leading to the well-known phase dependence of the mechanically excited oscillation of the cantilever (3.15) [217]:

$$\Delta\Phi = -\frac{Q}{2k_{eff}} \frac{\partial^2 C}{\partial z^2} (V_0 - \phi_{tip} + \phi_B + \Delta\phi_S)^2 \quad (3.26)$$

where Q is the quality factor of the cantilever. The capacitance C is replaced by the tip-flake capacitance C_M or the tip-Si substrate capacitance C_{SiO_2} , in the presence of our conducting MAXene flakes or in the presence of a bare SiO₂ layer, respectively.

3.1.4.1 Models of sphere-plane and sphere-cone configuration

The interpretation of both topographic and local electrical properties of the sample's surface, apart from the sample itself, additionally depend on the geometry and dimensions of the tip. A detailed description of the force acting on a nonplanar AFM tip is needed and this is so far done numerically in the general case. Nevertheless, the sphere-plane configuration of Sadeghi et al. [218] and the sphere-cone configuration of Hudlet et al. [219] can be treated analytically. These

models provide acceptable approximations of the geometry of the AFM tip with a rounded apex of radius R .

In the absence of flake (MADM) the system configuration can be modeled by the sphere-dielectric plane geometry proposed by Sadeghi et al. [218] that uses the polarization effect of the initial point charges located at the biased sphere and their corresponding image charges below the dielectric surface (Figure 3.10). According to the model, a point charge $q_1 = 4\pi\epsilon_0RV$ placed in the center of the sphere, at a distance $z_1 = R + s$ from the dielectric, renders its surface equipotential. An image charge $-\beta q_1$ is then induced below the dielectric surface at a distance $-z_1$, distorting the equipotential surface of the sphere, with $\beta = (\epsilon - \epsilon_0)/(\epsilon + \epsilon_0)$ and ϵ , ϵ_0 being the permittivities of the dielectric and air, respectively. This in turn generates a second charge q_2 at a distance z_2 into the sphere and this is repeated, leading eventually to the appearance of a series of point charges $\{q_n, z_n\}$ into the sphere and their corresponding images $\{-\beta q_n, -z_n\}$ below the dielectric's surface [218]. Each point charge located in the sphere at a distance [218]:

$$z_{n+1} = z_1 - \frac{R^2}{z_1 + z_n}, \quad n \geq 1 \quad (3.27)$$

it is described by the formula [218]:

$$q_{n+1} = \frac{\beta q_n R}{z_1 + z_n}, \quad n \geq 1 \quad (3.28)$$

This formula can be written as a second order difference equation (see paragraph 5.08 from Ref. [220]) whose general solution after simplifications determines every point charge q_n [218]:

$$q_n = q_1 \sinh \alpha (\beta^{n-1} / \sinh n\alpha) \quad (3.29)$$

at a distance [218]:

$$z_n = R \sinh \alpha \coth n\alpha, \quad n \geq 1 \quad (3.30)$$

with $\sinh \alpha = z_\infty/R$, as indicated in the following figure.

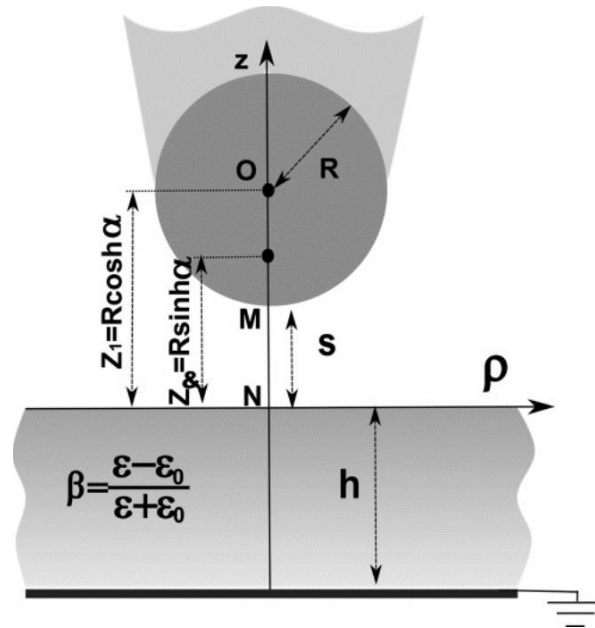


Figure 3.10 The configuration proposed by Sadeghi et al. which consists of a conducting spherical tip apex of radius R separated by a distance s from a dielectric plane of thickness h on top of a grounded bottom electrode. z_1 and z_∞ are the range of the positions where initial point charges are located on the sphere. Figure adapted from Ref. [218].

Within this model the capacitance of the sphere-plane model is calculated by the sum of the “nested” series of image charges (eq. 3.29) [218]:

$$C = \frac{1}{V} \sum_{n=1}^{\infty} q_n = 4\pi\epsilon_0 R \sinh \alpha \sum_{n=1}^{\infty} \frac{\beta^{n-1}}{\sinh n\alpha} \quad (3.31)$$

and the attractive electrostatic force, which is proportional to the derivative of the capacitance is given by the formula [218]:

$$F = \frac{dC}{ds} \frac{V^2}{2} = 2\pi\epsilon_0 V^2 \sum_{n=2}^{\infty} \frac{\beta^{n-1}}{\sinh n\alpha} (\coth \alpha - n \coth n\alpha) \quad (3.32)$$

Using the sphere radius of our tip ($R = 20 \text{ nm}$) as input to (3.31) we calculated the capacitance values as a function of the tip-sample distance z (Figure 3.11 (a)) for the cases where tip is positioned above a metallic flake ($\beta = 1$, MAM configuration), a “naked” SiO_2 layer and when the dielectric is replaced by an air layer ($\beta = 0$) with the same thickness. The capacitance values calculated for these different conditions converge for long distances ($z \gg R$). On the contrary an increasing difference in the values is observed as the tip approaches the sample surface, except for the case of air, where the capacitance remains constant independently of the tip-sample distance. When the SiO_2 layer is used as dielectric, a divergence of capacitance is observed at moderate distances ($R \ll z \ll d$) that is further increased in lower distances ($z < R$). Similar behavior is encountered in the absence of a dielectric layer (MAM), where an additional increase in capacitance is predicted both from air and SiO_2 dielectric at low distances, indicating a capacitance contrast that will be discussed in the following chapter.

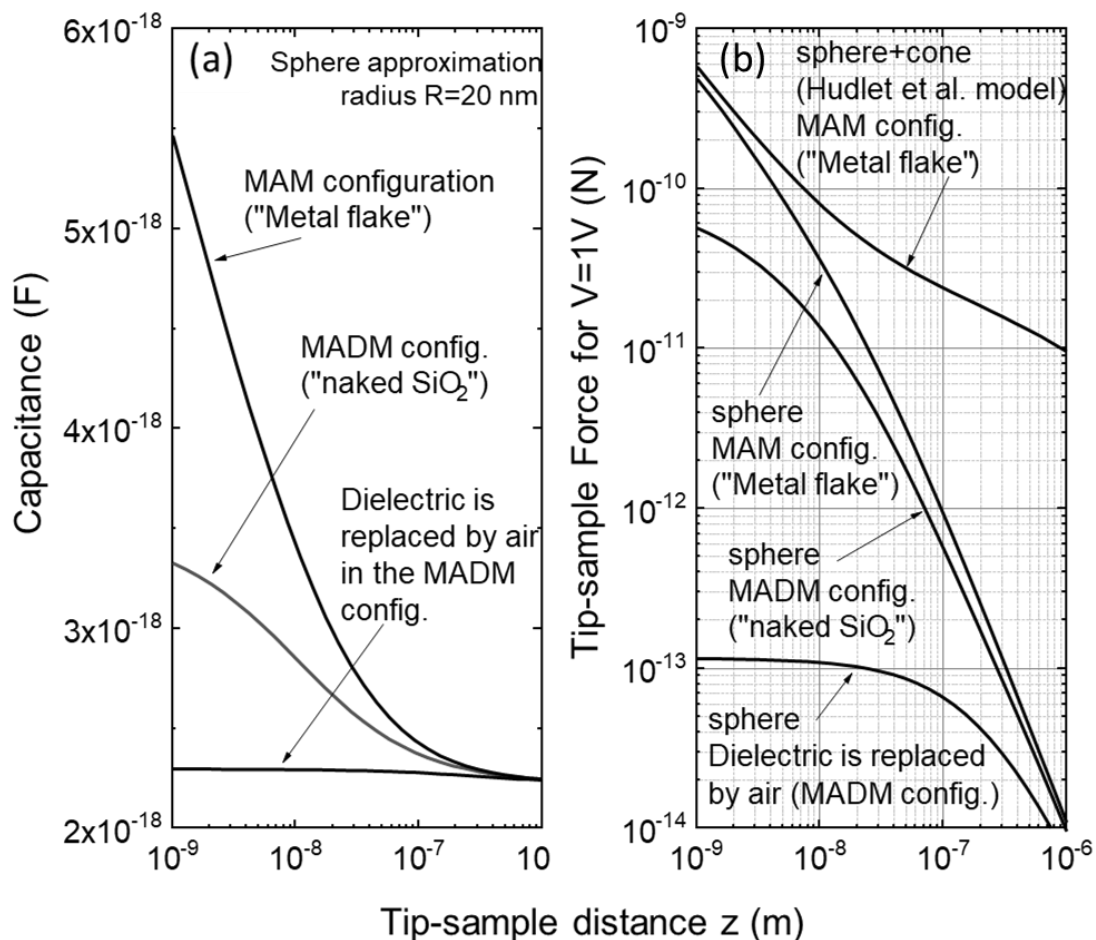


Figure 3.11 (a) Theoretical values of the capacitance vs tip-sample distance calculated using the image charge model [218] and sphere-plane approximation, showing the difference between the configuration where the tip is positioned above a metallic flake, the SiO₂ dielectric or if the dielectric layer is replaced by an air layer with the same thickness. (b) Variation of the electrostatic force with tip-sample distance for a voltage difference of 1V, calculated in the same cases as in (a) as well as in the case where the tip is positioned above a metallic flake using the analytical formula of the sphere-cone approximation [219].

The electrostatic force calculated as a function of the tip-sample distance (Figure 3.11 (b)) shows that the sphere-plane model of Sadeghi converges for both MAM and MADM configurations when $z \gg R$. However, as for capacitance, a small divergence in the electrostatic force values appears between the two configurations at moderate distances that further increases at short distances. The quantitative inaccuracy of the sphere-plane model for $z \gg R$ (the dielectric layer plays no role in the flake case in Figure 3.11 (b)) due to the absence of a model for computing the cone contribution in the case of MADM configuration renders the “stray” capacitance that is generated by the cone of the tip, the prevailing contribution to the overall capacitance value (Figure 3.11 (a), (b)).

The inaccuracy of sphere approximation was corrected by Hudlet and his coworkers after using an analytical approximation of the sphere and cone configuration that they developed in Ref. [219] (Figure 3.12). They considered the AFM tip as a truncated cone that ends to a spherical apex (Figure 3.9).

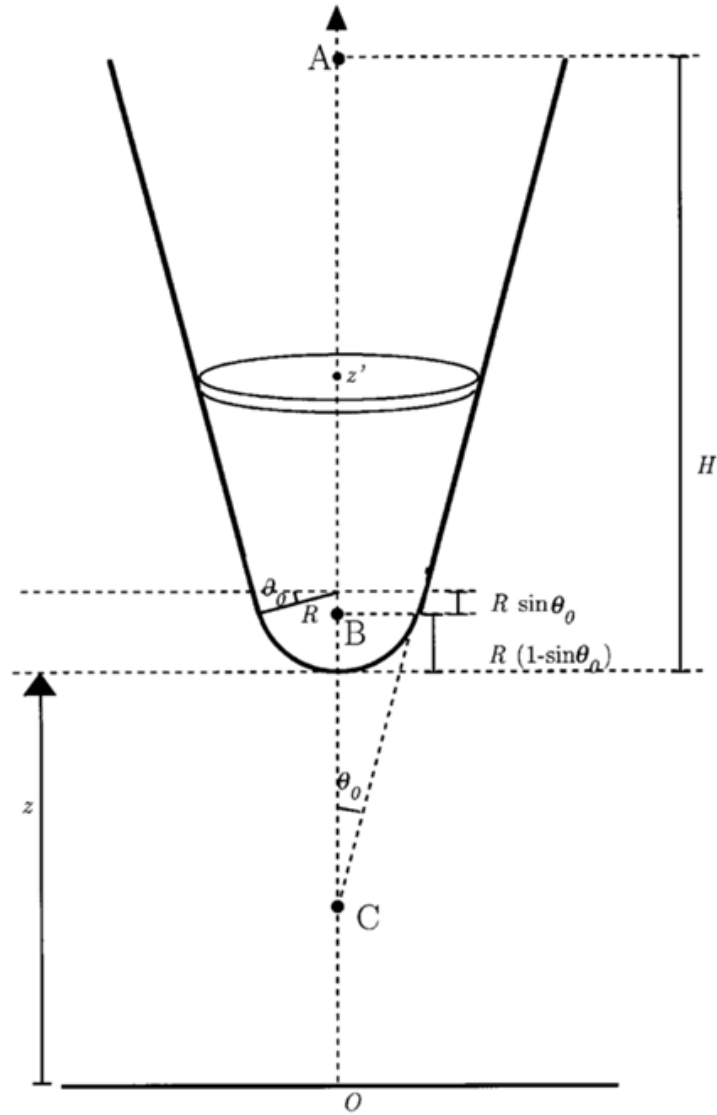


Figure 3.12 The geometry of the sphere-cone model for the tip-sample configuration proposed by Hudlet et al. Figure adapted from Ref. [219].

Their model was based on the division of the surface of the tip apex into infinitesimally faceted surfaces, and on the assumption that the electrostatic interaction between each infinitesimal surface of the tip and the plane generates an electric field similar to that created between a capacitor's parallel metal plates [219]. The sphere-plane capacitance in the sphere-cone configuration is given by the formula [219]:

$$C = 2\pi\epsilon_0 R K \ln\left(1 + \frac{R}{z}\right) \quad (3.33)$$

The electrostatic force in the tip-sample interaction was calculated by Hudlet et al. as the sum of the contribution derived from the spherical tip apex and that of the conical part. The total electrostatic force is [219]:

$$\begin{aligned}
 F &= F_{apex} + F_{cone} \\
 &= \pi \varepsilon_0 V^2 \frac{R^2(1 - \sin \theta_0)}{z[z + R(1 - \sin \theta_0)]} \\
 &\quad + \pi \varepsilon_0 V^2 k^2 \left(\ln \frac{z + R(1 - \sin \theta_0)}{H} - 1 + \frac{R \cos^2 \theta_0 / \sin \theta_0}{z + R(1 - \sin \theta_0)} \right) \quad (3.34)
 \end{aligned}$$

where θ_0 is the angular aperture and R the apex radius. A noticeable difference of 2-3 orders of magnitude in the electrostatic force between the sphere model and the sphere-cone model is found for $z \gg R$ that subsequently decreases for $z > R$ leading finally to a convergence of the two models only when tip approaches very close ($z < R$) the sample's surface (Figure 3.11 (b)).

The capacitance values derived from the sphere-cone model agree reasonably well with experimental data. Assuming the capacitance variation is similar to that of the tip-metal plane in the MADM configuration, we can use the analytical formula proposed by Hudlet et al. [219]. The second derivative of the capacitance is a complicated but fully analytical expression of z , quality factor Q , spring constant k , cone angle θ and apex radius R [219]. Figure 3.13 shows the numerical estimate of the model, for $R = 20$ nm, $\theta = 10^\circ$, $k = 2.8$ N/m (spring constant value provided by the manufacturer) a quality factor $Q = 205$, corresponding to our system [219]. The dashed line is generated by averaging the values computed with the same model over a moving interval equal to the tip oscillation amplitude. An excellent agreement with the measured values is evident, especially when the averaging technique is used.

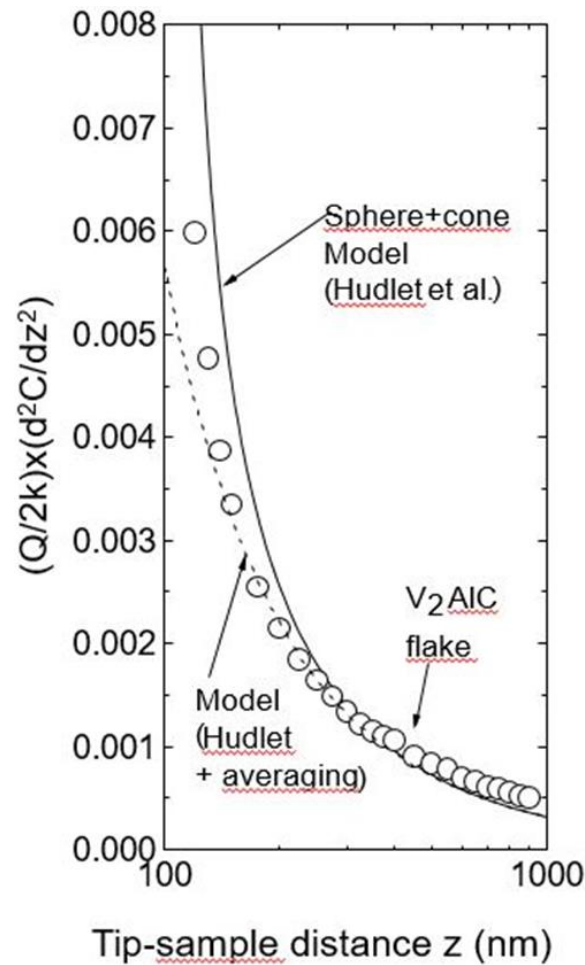


Figure 3.13 Variation of the second derivative of the capacitance vs tip-sample distance, where experimental points (circles) are compared to the analytical model [219] (solid line) and an average of the values computed with the same model over a moving interval equal to the tip oscillation amplitude (dotted line).

The excellent agreement of the Hudlet's model with the above experimental values at all distances, in the case of the flake configuration, cannot counterbalance the fact that this model cannot be used in the MADM configuration. Since we needed to compare the two configurations so as to prove the capacitance contrast, the only option was to use the sphere-plane model of Sadeghi et al. Notwithstanding the model's inefficiency at large distances, it is the only one permitting to compute values in both configurations and to apply well at short tip-sample distances, as compared with the sphere-cone model in the flake configuration. The reasonable agreement between Hudlet's model and sphere-plane model at short distances in the MAM configuration is also a good indication that predicting a contrast between the MAM and MADM configurations, using the

sphere-plane model, must be translated into a measurable contrast experimentally.

3.2 Scanning Tunneling Microscopy (STM)

In 1981, the first scanning probe microscope was invented by Gerd Binnig and Heinrich Rohrer, at IBM in Zürich, whose operation was based on the measurement of the electron tunneling current – the quantum mechanics effect occurring between two biased electrodes separated at a subnanometer distance [221]. Few years later, Binnig and Rohrer were honored with the nobel prize in 1986 for the development of this scanning tunneling microscope (STM). STM probes electronic densities of individual atoms and molecules and images individual atoms and molecules with outstanding spatial resolution. Since the two ends of the tunnel junction are in strong interaction, the STM can also be used to manipulate and design the probed surface with the atomic apex of the scanning tip, by controllably moving individual atoms [222].

On a broader perspective, the invention of STM triggered the development of yet other scanning probe techniques, especially AFM, EFM, MFM and it contributed to the exploration of materials surface at the atomic scale [223].

3.2.1 Basic principles of quantum tunneling

In classical physics the current flows among conductive/semiconducting materials when they are in contact and once a potential is applied to their edges. However, according to quantum mechanics, electric current can additionally flow between two electrodes even if they are not touching. In STM, a sharp metallic tip and a sample's surface play the role of the two electrodes that start to interact when the tip apex approaches the surface, through a system of piezoelectric actuators (x, y, z), at very close distances in the order of one nanometer and below, along the z axis. Then, and provided that a bias voltage, V_b , is applied between the tip and the sample, electrons start to penetrate the medium (vacuum or air) that

separates the tip and the sample surface through the tunneling effect, generating a tunneling current, I_t (Figure 3.15). Hence, the tip-vacuum/air-sample system forms a tunneling junction [223].

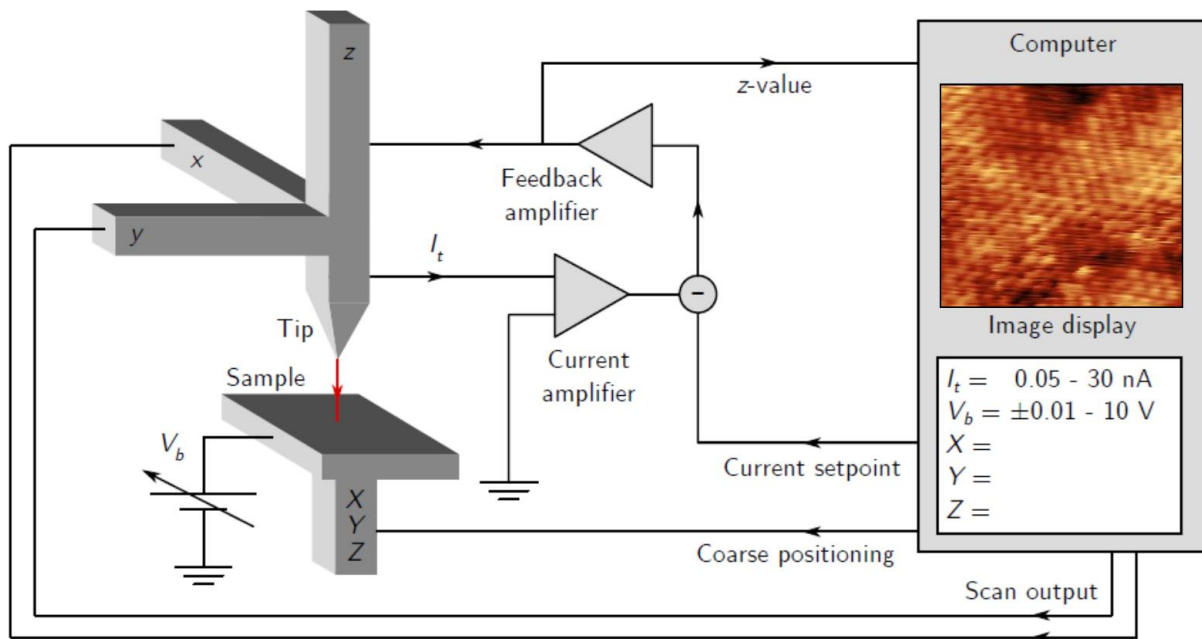


Figure 3.15 Schematic diagram of the STM operation principle. A bias voltage V_b , is applied between the tip and the sample generating a tunneling current, I_t . The probed current is compared to a setpoint value by a feedback loop and it adjusts the tip position along z axis by applying a voltage. This feedback signal is recorded to create the STM image. In the absence of a feedback loop the tunneling current is directly recorded and processed to generate the STM images. Figure adapted from Ref. [224].

Tunneling depends on the different work functions of the tip, ϕ_T and sample, ϕ_S . In conditions of zero potential, the materials of both tip and sample are in equilibrium having a common Fermi energy level but different vacuum levels, which produces an electric field within the gap, based only to the tip-sample work function difference, $\phi_T - \phi_S$ (Figure 3.16 (a)). In this case, electrons can be transmitted from sample to tip and vice versa but no tunneling current is probed.

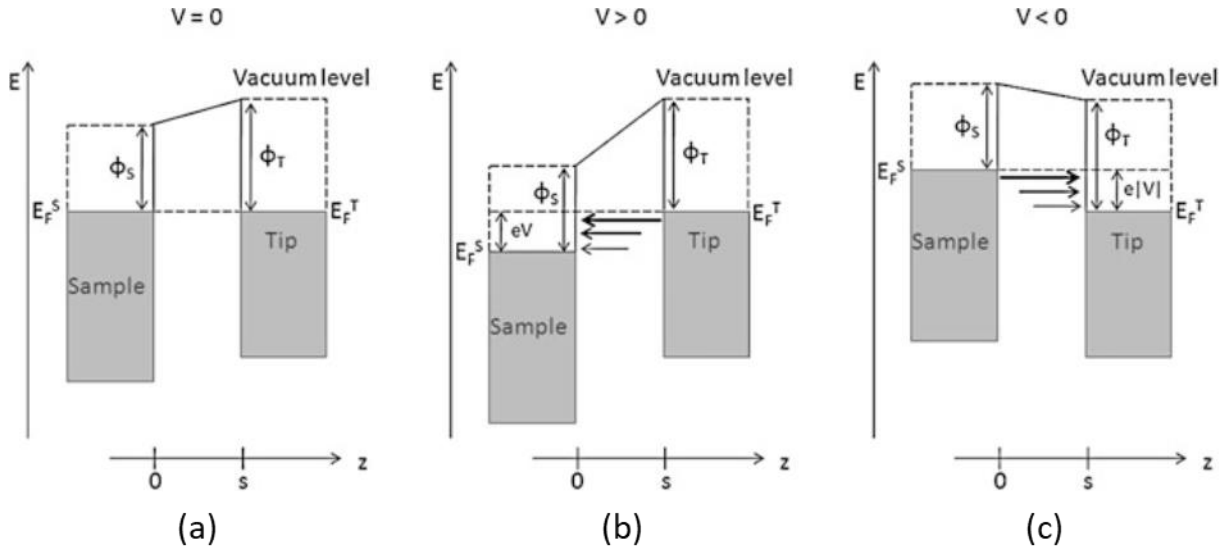


Figure 3.16 Representation of the energy potential for the electrons in a tip-vacuum-sample tunnel junction, along a vertical direction to the tip-sample separation s (z axis), in different potential. E_F^S, E_F^T and ϕ_S, ϕ_T denote the Fermi energy level and the work functions of the surface and tip, respectively. (a) Electrical equilibrium is obtained between tip and sample for zero voltage. When $V \neq 0$, the E_F^S, E_F^T differ by $e|V|$ indicating thus the energy range for the electrons transmittance. For $E > eV$ no electron can tunnel (b) while there are not any empty states for electrons at $E < -eV$ (c). Figure adapted from Ref. [223].

Considering that the electric field energy in the gap region is appreciably higher than the total energy of an electron located in a state of either the tip or the sample, the potential associated with the electric field acts as a barrier to electron transmission since a negative kinetic energy would be required in classical physics. Quantum mechanics however predicts that electrons have delocalised wave functions that can penetrate the gap [223]. Once a voltage V is applied to a tip-vacuum/air-sample tunnel junction, all electrons with energy in the range of $\pm eV$ above or below the Fermi level can tunnel through the gap leading to the appearance of a net tunneling current whose direction is defined by the sign of the applied potential V (Figure 3.16 (b), (c)).

Based on a perturbation theory (a detailed analysis is given in reference [223]) the tunneling current is expressed as:

$$I = \frac{4\pi e}{\hbar} \int_0^{eV} \rho_T(E_F^T - eV + \epsilon) \rho_S(E_F^S + \epsilon) e^{-2ks} d\epsilon \quad (3.35)$$

Hence, the potential V , the density of states in both tip and sample (ρ_T, ρ_S) and the separation s between the tip and the sample determine the electrons flow. The terms ρ_T, ρ_S are the local electronic densities of states of the outer atom of the sharp tip apex and of sample's surface directly beneath the tip apex [223].

3.2.2 STM operation modes

The electrons flow between the tip and sample is probed by two STM operation modes that are mainly used:

- i. *Constant height mode*, in which the tunneling current is recorded point by point with the tip at a fixed position along the z axis, which requires very stable imaging conditions, usually only available at low temperatures (Figure 3.17 (a)).
- ii. *Constant current mode*, where a feedback loop adjusts the tip position in z direction during the scan by applying a voltage signal in the piezoelectric tube to maintain the tunneling current at a predetermined setpoint (Figure 3.17 (b)). Thus, the STM images are generated by recording the feedback signal at each point of the scanned surface.

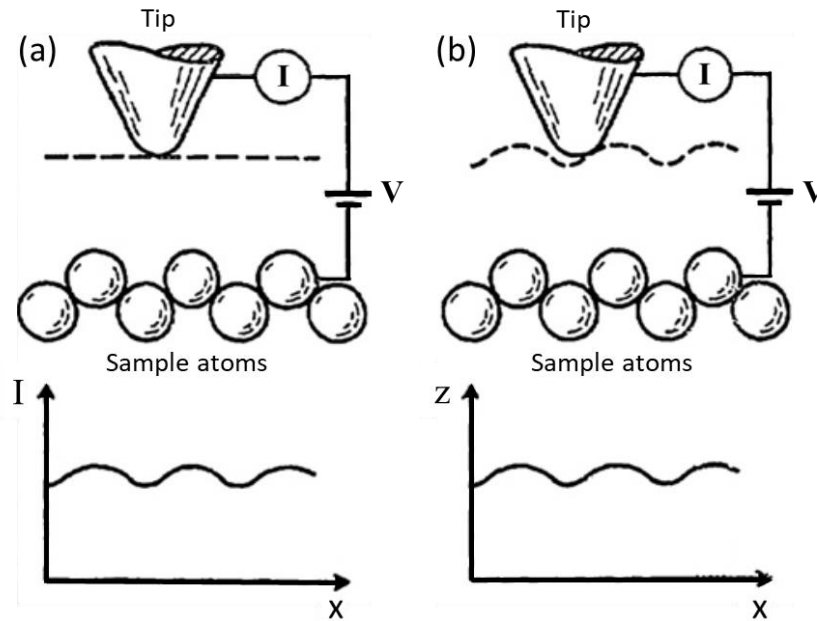


Figure 3.17 Schematics of the STM imaging modes with the corresponding plots where the varying term is recorded along the scan direction. (a) Constant height mode and (b) Constant current mode. Figure adapted from Ref. [225].

The constant height mode can be only applied to atomically flat surfaces, as any corrugated surface raise the risk of a tip crash, while for the constant current mode there are less roughness restrictions. Regarding the latter mode, in the case of flat surfaces the recorded voltage signal represents variations in the local density of states (LDOS) while for non uniform surfaces the recorded signal contains both topographic and electronic structure information [223].

3.2.3 STM set-up

All the STM measurements in the present thesis were performed at room temperature in ultra high vacuum (UHV) conditions ($p < 10^{-11}$ mbar) using an OMICRON STM-1 system, which is placed inside a chamber connected to a multipurpose UHV set-up in Néel Institute (Figure 3.18). The UHV set-up mainly consists of a long tube called “tunnel” in which the pressure does not exceed 10^{-10} mbar. One of the chambers connected to the “tunnel” is a load-lock chamber (SAS) and is used to introduce the samples from air to UHV. The pressure inside load-lock chamber goes down to about 10^{-8} mbar. The second chamber is a growth

chamber where RHEED measurements can be performed, the next chamber is used for samples preparation i.e. deposition, annealing and sputtering is taking place. Almost opposite to this chamber is a last growth chamber in which temperatures can exceed 1500 K. The UHV set-up, in total, is maintained under ultra high vacuum with a system of pumps and particularly a primary, an ionic and a turbo pump.

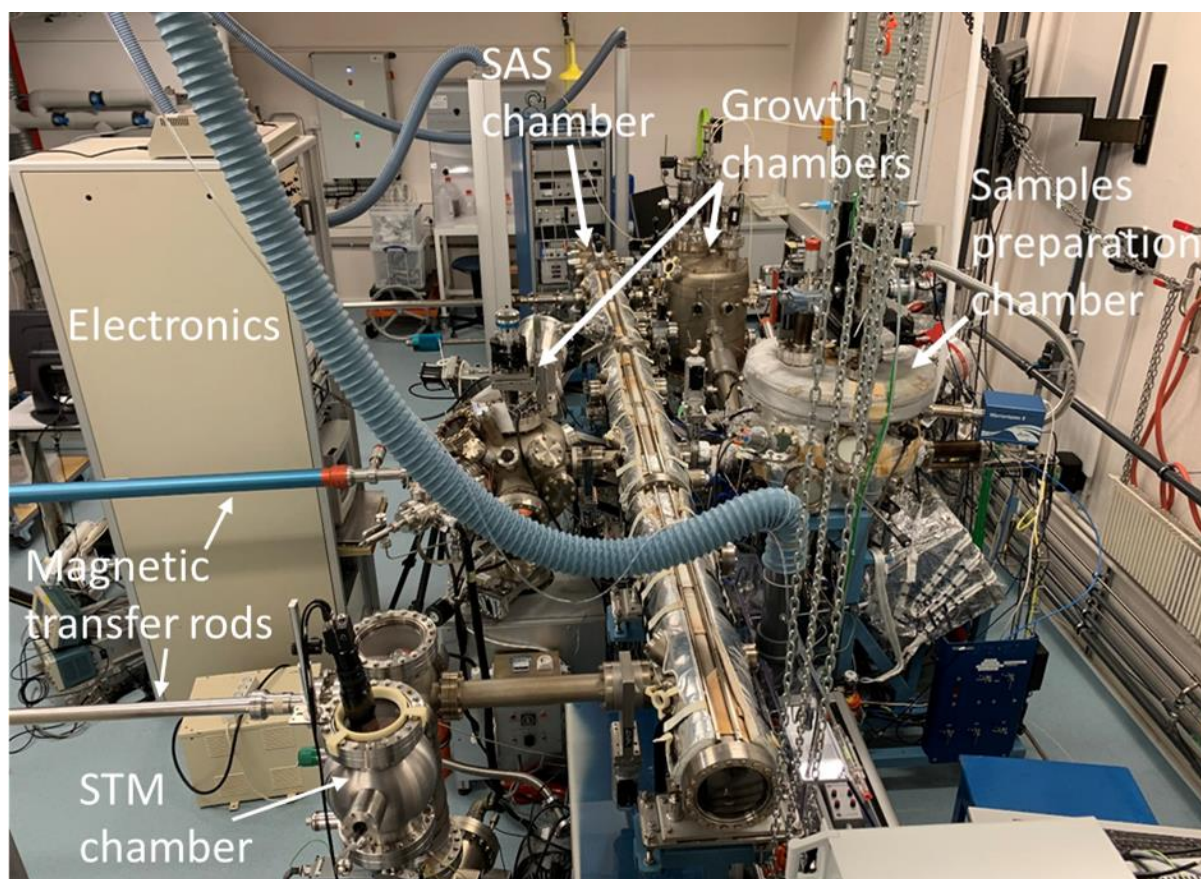


Figure 3.18 The multipurpose UHV system at room temperature in Néel Institute (Grenoble).

HOLDERS of rectangular shape plates made from stainless steel (Figure 3.19 (a)) are used for mounting the MAX samples and then are adapted onto 1 inch Mo supporters called molyblocks (Figure 3.19 (b)). The specific geometry of both plates and molyblocks facilitates the introduction of the samples in the load-lock chamber. The transfer of the samples placed on a trolley is performed by the use of magnetic rods (Figure 3.19 (c)).

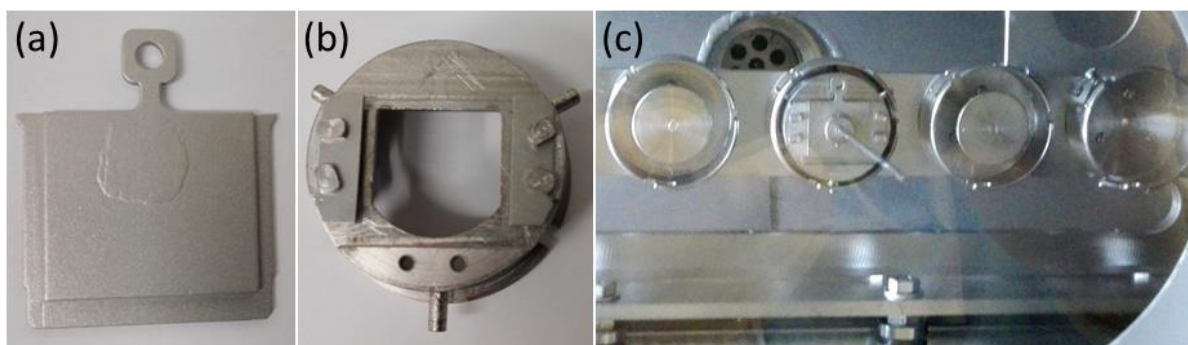


Figure 3.19 (a) Stainless steel plate for mounting the samples. The thickness difference between the sides and the rest part of the plate simplify its adaptation onto the molyblock (b). Two pairs of small screws (at the left and the right of the molyblock) hold two molybdenum rectangular plates which retain the steel plate firmly in place during the sample processing. (c) The magnetic rod (trolley) in the load-lock chamber with one of its slots occupied by a sample mounted on a molyblock.

To limit mechanical vibrations four vertical springs support the STM supporting cradle, whose motion in the x-y plane is damped with the help of magnets via Eddy currents. The STM is composed of the piezoscanners, the holder of the sample plate and the metal frame where the holder of the sample is located (Figure 3.20 (a), (b)). A system of springs both in the x-y plane and along z axis allow short displacements of the ring in x-y-z directions and concomitantly isolates the STM from any mechanical vibration of the surroundings.

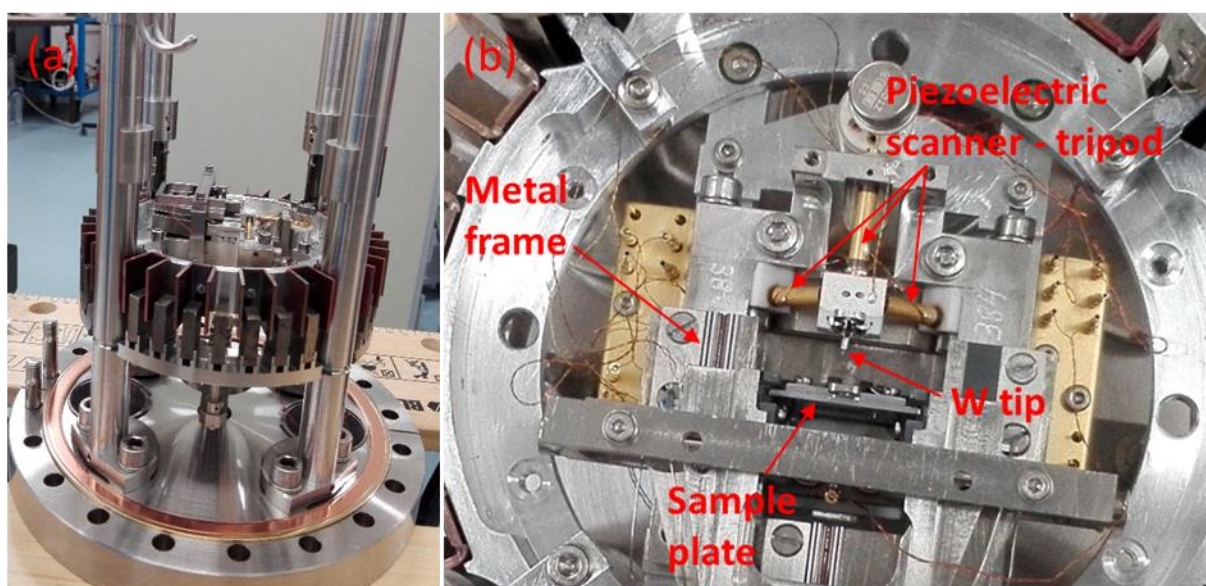


Figure 3.20 The STM set-up in Néel Institute. (a) Side view of the set-up as it is hosted inside the chamber. (b) Top view of the STM illustrating its basic components.

The piezoelectric scanning stage consists of three piezo-crystals (P_x , P_y , P_z), usually made of lead zirconate titanate polycrystalline ceramics, placed per pair in a vertical position so that they form a tripod (Figure 3.20 (b)) at the end of which a metallic tip is mounted. The position of the tip is controlled by the changes induced by the voltage applied to the two sides of the piezo-crystals. Then, the length of the piezo-tube is either compressed or extended resulting in changes to the tip position along the direction of the piezo-tube [226].

In our case, all STM measurements were performed with tips fabricated from electrochemical etching of thin wires of W. The etching is taking place under ambient conditions and hence it results in the formation of a surface oxide. To remove the oxide, additional steps of ion sputtering and thermal annealing were applied to the tip inside the UHV system, before mounting it onto the tripod [223].

3.3 Physical Properties Measurement System (PPMS)

The Physical Properties Measurement System is a commercial cryostat fabricated by Quantum Design which can perform diverse measurements in a precisely controlled temperature range and under a magnetic field. The PPMS configuration used at Néel Institute measures the resistivity, Hall effect and specific heat. The cooling system of the cryostat as well as measurements are fully automated and optimised.

The temperature range accessible with the PPMS system is 1.9 K to 400 K with a ^4He cooling system. A full sweep option allows to vary the temperature with rates ranging from 0.01 K/min to 12 K/min. A magnetic field up to 9 Tesla can also be applied to the sample.

In the following, the main set-up and the working principle of the resistivity option that was used in our measurements will be briefly presented. Additional

information and further description of the PPMS system operation can be found in reference [227].

3.3.1 PPMS set-up and the option of resistivity measurements

The system consists of a cryostat (dewar and probe) and the electronics controller (Figure 3.22). The PPMS probe is inserted from the top hole of the dewar and it is immersed in the liquid helium reservoir.



Figure 3.22 PPMS set-up at Néel Institute (Grenoble).

The probe is composed of two major components regarding their position on the dewar. The top part of the probe is called probe head and it protrudes on the top of the dewar. The head probe connects electrically the sample chamber with the PPMS controller through cables and additionally it controls the vacuum in the sample chamber and the ^4He level in the dewar. The lower part of the probe is immersed into the liquid helium tank. This part is composed of the sample

chamber which allows the introduction of the measurement platform (called puck) containing the sample to be characterized. The sample chamber is equipped with a heating resistor and thermometers in order to accurately regulate its temperature and it is surrounded by the superconducting magnet.

As it was mentioned before the PPMS set-up was used to perform resistivity measurements with our MAXene devices and hence the pucks used for mounting the samples were customised to resistivity option (Figure 3.23). This characterization is based on the four-wires resistance measurement method. To get the sample's resistance, two separate pairs of wires are used to apply an electrical current "I" and to measure the voltage "V" across the sample. Using the dimensions of the MAXene device (sample thickness and the surface of the sample between the contacts) we can deduce the resistivity value by measuring the resistance from the Ohm's law.

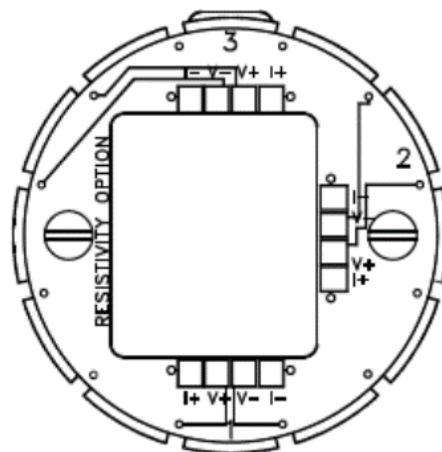


Figure 3.23 Resistivity option PPMS puck consisting of three channels with four negatively and positively labeled I, V contact pads each. Figure adapted from Ref. [227].

3.4 Conclusion

The description of the AFM tip-sample interaction in our system's configurations, MAM and MADM, was based on two models owing to the acceptable approximations of the AFM tip geometry that they provide. The sphere-

plane model proposed by Sadeghi et al. can describe both MAM and MADM configurations, however, the lack of computing the AFM cone contribution in the case of MADM, renders the model less accurate at large tip-sample distances. On the contrary, the sphere-cone model of Hudlet et al. demonstrates excellent accuracy with the experimental measurements in the MAM configuration, at all distances, but it cannot be used in the absence of flake. Both models however, converge at small distances. Considering the prediction of an appreciable contrast between our system configurations, the prevailing model in our case could not be other than the sphere-plane even if it lacks accuracy at large interaction distances.

Chapter 4

Topography of cleaved MAX phase single crystals and MAXenes electrical characterization

In this chapter, we present the results obtained from the surface characterization of bulk single crystal cleaved in UHV and electrical characterization of several MAXene flakes.

First, we demonstrate the process we applied to cleave a Cr_2AlC crystal in UHV and then, we show the surface topography images scanned at the nanoscale by STM. Next, we refer to the electrical behavior of mechanically exfoliated MAXene flakes with various thickness probed by EFM and KPFM techniques. We explain all results derived from the analysis of the scanned images through the implementation of the sphere-plane model described in chapter 3. Finally, we detail the device fabrication process applied to various thickness MAXene flakes while measurements with four-point probes method are shown for thin flakes of the four phases studied in this thesis. Resistivity measurements as a function of temperature and flake thickness are also presented.

4.1. STM characterization of mechanically cleaved Cr_2AlC single crystals in UHV

4.1.1. Preparation of the Cr_2AlC samples

The large and irregular size of Cr_2AlC single crystals obtained after the growth flux etching in HCl, made impossible direct mechanical cleavage and besides, the sample holder (plate) presented in 3.2.3 could not support them. Therefore, to reduce their size and render them suitable for uniform cleavage, we cut the crystals in squares of $5 \times 5 \text{ mm}^2$ using a diamond wire saw. A conducting epoxy glue was used to stick the square crystal on the plate while ensuring a closed electrical path from STM tip to ground (the sample-holder served as the back-electrode in the STM measurements). To ensure a uniform cleavage of Cr_2AlC inside the UHV system described in Figure 3.18 of the third chapter, we used a stainless steel rod (pin) with a disk attached to its end (Figure 4.1 (a)). The disk diameter was around 6 mm covering thus completely the crystal's surface (Figure 4.1 (b)) thereby suited for a uniform cleavage. In practice, to glue the pin and the crystal's back-surface, the amount of conducting epoxy was low-enough to avoid its spreading away from the interface that would be detrimental to cleavage, creating so a “sandwich” structure of the plate- Cr_2AlC -pin system (Figure 4.1 (b)). To enhance the epoxy efficiency, an annealing step in ambient conditions at 80°C in the oven for one hour was needed. Lastly, the sample was cooled down for half an hour in air.



Figure 4.1 (a) Stainless steel rod (pin) having a disk shape terminated side and (b) the plate- Cr_2AlC -pin system after mild annealing at 80°C .

4.1.2. Cleavage of Cr_2AlC crystals in UHV conditions

The sample, mounted on its plate, was placed on a molybdenum block (Figure 4.2 (a)) that can be manipulated within the UHV system via magnetic transfer rods (Figure 3.18). The molybdenum block is introduced via a fast load-lock (SAS) chamber,

which is purged from air down to a 10^{-8} mbar residual pressure. Next, the molybdenum block is moved into the UHV tunnel (pressure in the 10^{-10} mbar range). There, the molybdenum block with its pin is translated against the end of the magnetic transfer rod (Figure 3.18), which thereby exerts a mechanical moment onto the pin that leads to a uniform cleavage of the Cr_2AlC single crystal. One part of the cleaved surface remains on top of the plate (Figure 4.2 (b)) and the other on the pin, which was collected in a small receptacle placed below the molybdenum block, inside the tunnel.

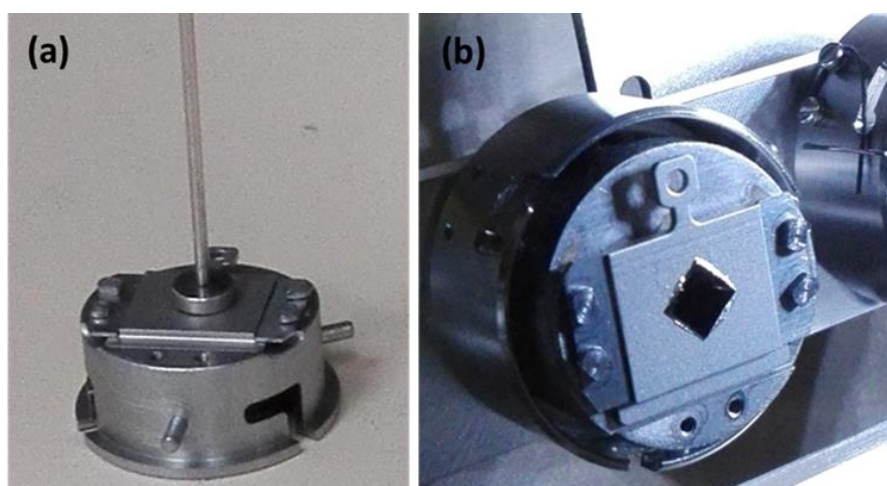


Figure 4.2 (a) The plate- Cr_2AlC -pin system placed on a molybdenum block. (b) The cleaved surface of Cr_2AlC crystal remained on the plate after the cleaving process inside the UHV system.

The molybdenum block with the freshly cleaved Cr_2AlC surface was directly transferred to the STM chamber for in situ analysis of the surface topography at about 10^{-11} mbar.

4.1.3. Surface topography characterization of the cleaved Cr_2AlC crystals

STM imaging was performed in the constant-current mode. Various freshly prepared W tips, prolonged STM tip conditioning including dipping it into a good surface, high tunneling current / high tip-sample voltage pulses, a broad range of imaging conditions (tunneling current, tip-sample voltage, scan rate) were explored to seek for optimal high resolution imaging. Although the STM tips were

found suited to achieve on a routine basis, atomic resolution imaging onto graphene surfaces (in the framework of research projects not relevant here), stable high-resolution imaging proved especially challenging onto the cleaved surface of the MAX samples. Nevertheless, we managed to reproducibly obtain topography images of the cleaved surface of Cr_2AlC single crystals in diverse scanning scales which, as far as we are aware, were the first of their kind.

At a rather large scale, as seen on $150 \times 150 \text{ nm}^2$ images (Figure 4.3 (a)), surface segregation into two nested or interpenetrating domains of different apparent heights is observed. We attribute this peculiar mottled structure on the cleaved surface to an uneven distribution of the Al atoms of the cleaved atomic planes. Since it is reasonable to assume that the Al atoms are distributed roughly equally on each face of the fractured surfaces, surface reconstruction or Al clustering could then lead to the formation of the two distinct kinds of regions we observed. Herein, we note that the Al atoms are in fact more strongly bonded to the M atoms than in their in-plane neighbors [18], which in principle favors their equal repartition between both fractured faces. When exfoliation occurs in air, the Al atoms are expected to promptly react with oxygen to form Al-O clusters.

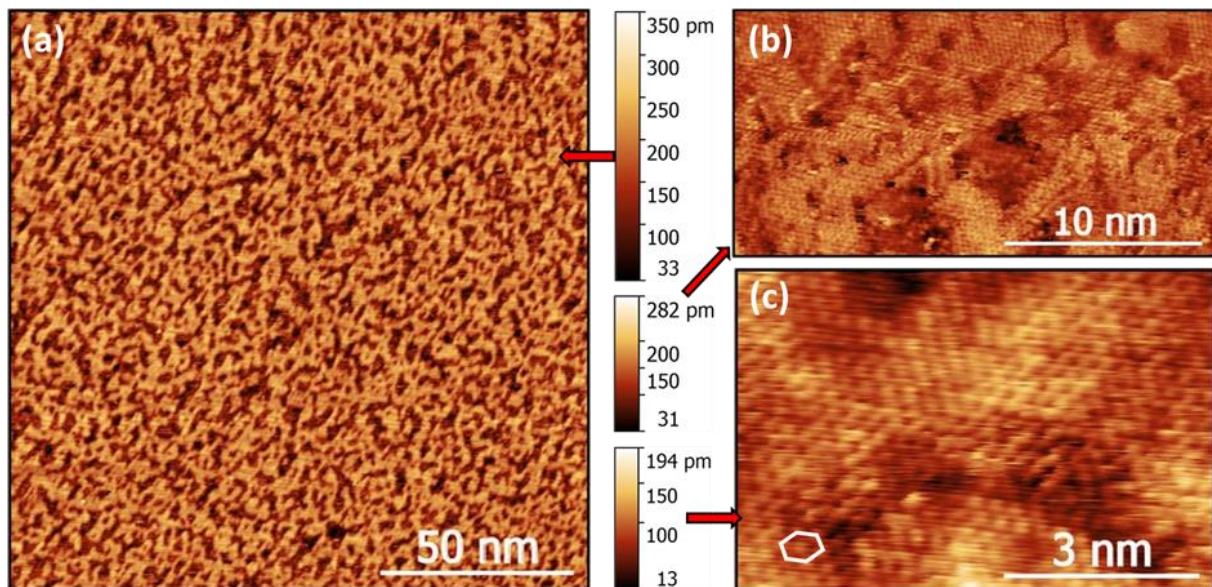


Figure 4.3 (a)-(c) STM topographic images of Cr_2AlC single crystals cleaved in UHV and measured in situ at 300 K. (a) Tunneling current $I = 1 \text{ nA}$, bias $V = -1 \text{ V}$, (b) $I = 3.35 \text{ nA}$, $V = -0.45 \text{ V}$ and (c) $I = 10.2 \text{ nA}$, $V = -0.48 \text{ V}$ [228].

In MAX phases, the largest contribution to the density of states (DOS) at the Fermi level (E_F) is that of the d -orbitals of the “M” – Cr in this case – atoms [229], [230]. It follows that the Al-free surfaces should appear closer to the tip than the Al-covered regions. Said otherwise, the tunneling current setpoint value is obtained at a larger distance when the DOS is higher. Therefore, we tentatively attribute the existence of the darker domains to disordered Al or Al-O clusters and the brighter ones to the Cr-rich surfaces. Hence, one should be able to distinguish a regular hcp atomic lattice in the latter areas, as it is indeed observed in the atomic resolution images (Figure 4.3 (c)) which highlight that the hexagonal, closed-packed lattice is preserved on the Cr atoms regions (hexagon on lower left side of the figure) [228].

4.2. Probing MAXenes electrical behavior using EFM and KPFM methods

A quantitative characterization of the electrical properties of a MAXene surface can be performed by EFM and KPFM, which allow for the detection of charges or surface potentials with high sensitivity [214], [231], [232]. As described in the previous chapter, in the MAM and MADM configurations, when the AFM tip approaches a flake-SiO₂ interface, a surface potential-induced contrast between the flake and the bare SiO₂ surface is expected only when there is a surface potential difference between the top and the bottom of the flake ($\Delta\phi_s \neq 0$). In the case of graphene, the low DOS renders thin flakes non-ideal conductors, so that very few-layered flakes differ from their thicker counterparts. This is not observed in our case. When the tip is positioned above a bare SiO₂ surface two changes are expected. Initially, a surface potential contrast is expected between the flake and the SiO₂. This is the main contribution to the phase contrast (3.28) and helped us determine the electrical behavior of MAXenes. A second contribution, the capacitance contrast, which is defined by the second derivative of the capacitance

in equation (3.28), was essential to assess the electrical character of MAXene flakes down to the thinnest layers.

Figure 4.4 (a) shows an AFM surface topography image in which a staircase of small terraces with different thickness was created on a mechanically exfoliated flake Cr_2AlC . In the corresponding EFM image (Figure 4.4 (b)) two main features are observed. First, a comparison of both images makes it amply clear that there is no apparent dependence of the EFM signal on the flake thickness [228].

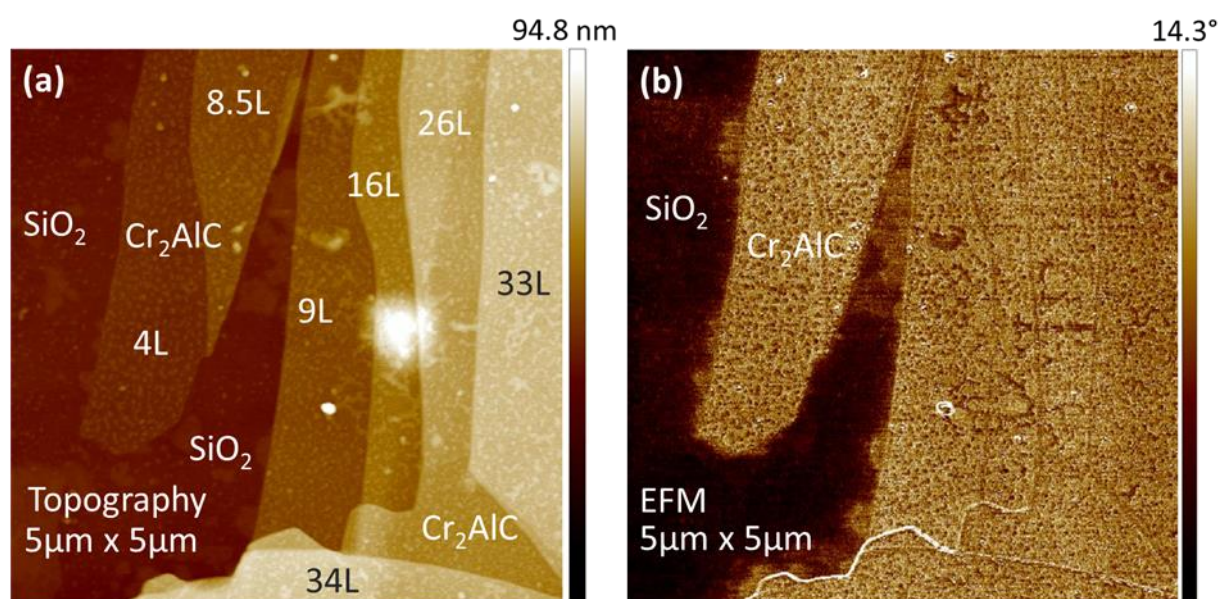


Figure 4.4 (a) Topographic image of a Cr_2AlC MAXene flake having different thickness terraces and covered by a substantial amount of glue residues. (b) Corresponding EFM phase image measured at a lift height of 150 nm and a tip voltage of -8 V [228].

The second feature is the presence of glue residues, which can be clearly distinguished on the surface topography image (Figure 4.4 (a)) and which lead to a local variation of the EFM signal (Figure 4.4 (b)). This contrast difference arises because either the regions of glue residues are electrically charged, or they modify the surface potential of the flakes [228].

Similar results were also obtained for V_2AlC phase where the EFM signal was measured on very thin flakes down to a single layer (1L, Figure 4.5 (a)).

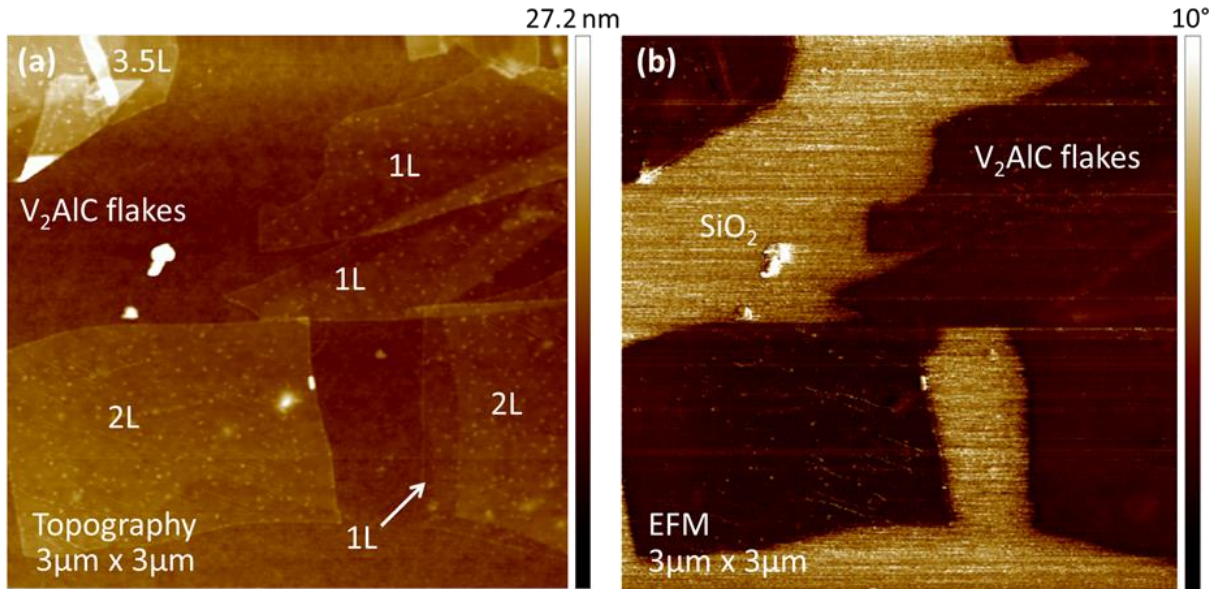


Figure 4.5 (a) Topographic image of very thin V₂AlC flakes and (b) the corresponding EFM phase image measured at a lift height of 600 nm for a tip voltage of 7 V [228].

Figure 4.5 (b) reveals no contrast variation on 3.5L, 2L and 1L V₂AlC flakes, explicitly affirming the preservation of MAXenes metallic behavior. KPFM measurements on the surface of V₂AlC flakes further confirmed the qualitative results derived from EFM (Figure 4.6 (b)).

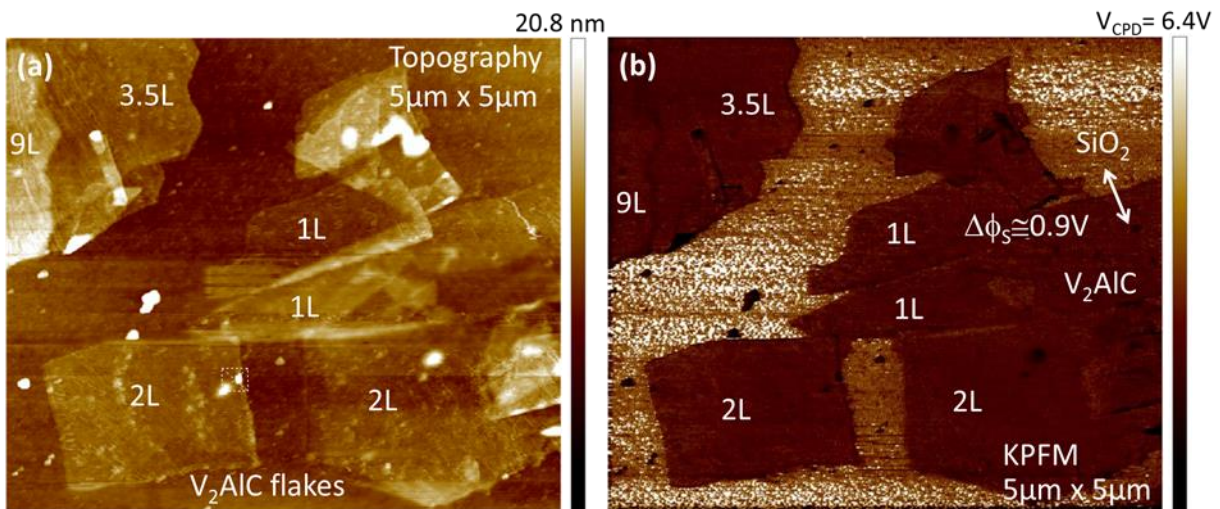


Figure 4.6 (a) Topographic image of very thin V₂AlC flakes (larger scale than for Figure 4.5 (a)) and (b) the corresponding KPFM image measured at a lift height of 40 nm.

The KPFM image presents the same V_2AlC flakes as in Figure 4.5 but at a larger scanning range. A surface potential difference of 0.9 V is found between the bottom and the top of the flakes which corroborated the induced contrast between the oxide and the V_2AlC phase. Any conversion of flakes to insulating oxide would have resulted to a different contrast with the thicker conductive flakes. Overall, in the KPFM map, the MAXene flakes' electrical signal is a weak function of their thickness and since the thicker flakes are metallic, the monolayer ones should also be. Also, the KPFM signal indicated that parts of the insulating oxide were exhibiting a saturated signal during the scan, a phenomenon most probably due to charge accumulation on the oxide from the tip, owing to the multiple scan.

For all studied surfaces, we systematically measured phase parabolas as a function of z in both MAM and MADM configurations [228]. A typical measurement on a Cr_2AlC flake at a given lift height of 75 nm (Figure 4.7 (a)) shows the phase shift as a function of the tip voltage recorded on top of the flake and oxide surfaces. Figure 4.7 (b) presents plots of ΔV_{CPD} for various z values, where sample-to-sample variability is obvious.

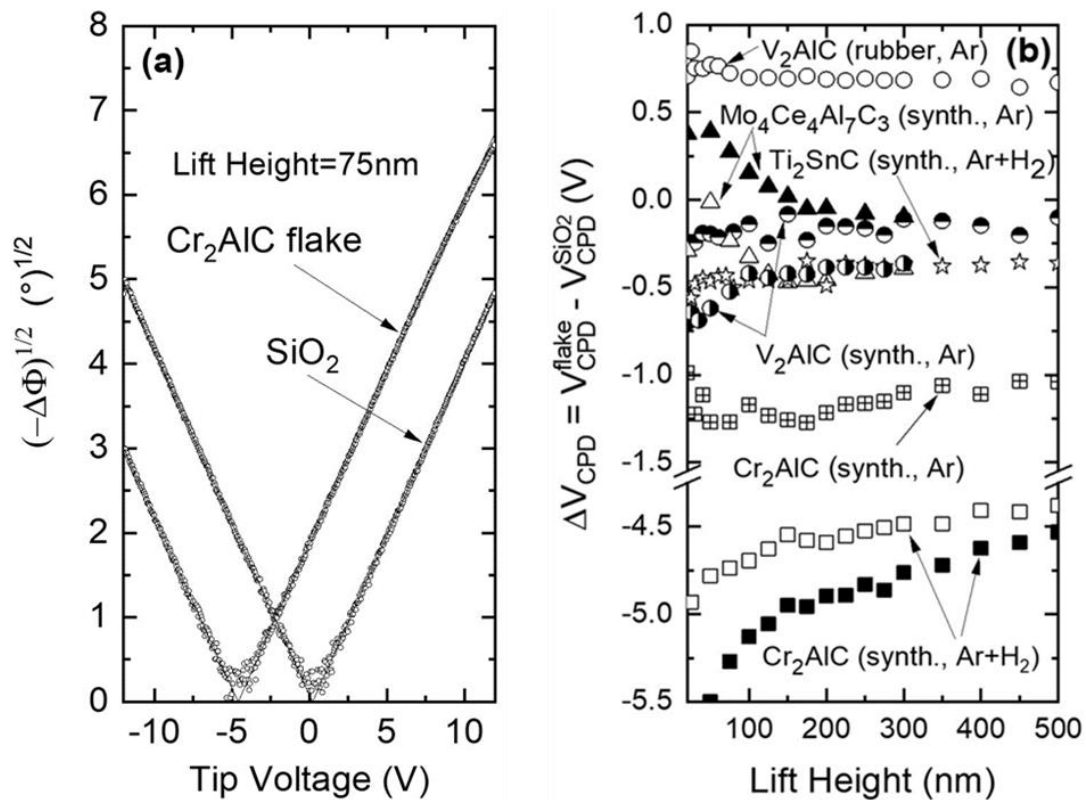


Figure 4.7 (a) Typical experimental plot of the square root of the phase shift versus tip voltage, measured at a given lift height and a given position. (b) Experimental

plot of the contact potential difference between MAXene flakes and the nearby SiO₂ surface, measured for different phases, prepared or annealed under various conditions. Every point in the plot was computed by plots shown in (a) at given lift heights [228].

The scatter can be traced to several factors, such as flake annealing conditions used for removing the glue residues, MAX chemistry, SiO₂ surface preparation prior to flake transfer, residual glue on top of the flakes, relative humidity (RH) during the EFM experiments. For instance, if different amounts of glue are present on the bottom or top of the flakes then, in principle, a surface potential contrast should be observed. Annealing conditions can also contribute to an asymmetry between top and bottom because the glue reactivity on top is not necessarily similar to that on the flake's bottom. Therefore, no useful information can be extracted from the plots in Figure 4.7 (b) except from the variation of the apparent MAXenes-SiO₂ surface potential difference at diverse lift heights.

In order to prove that flakes are metallic, we measured and compared phase parabolas at various z values, between a V₂AlC flake and a bare SiO₂ surface (Figure 4.8 (a)) [228]. For each of the measured parabolas we extracted the curvature and V_{CPD} by least-squares fitting. We quantified the contrast extracted from the parabolas' fits by the ratio α between the parabola curvatures of the two surfaces (Figure 4.8 (b)), down to the shortest attainable distances without, however, getting in a repulsive interaction regime with the sample surface.

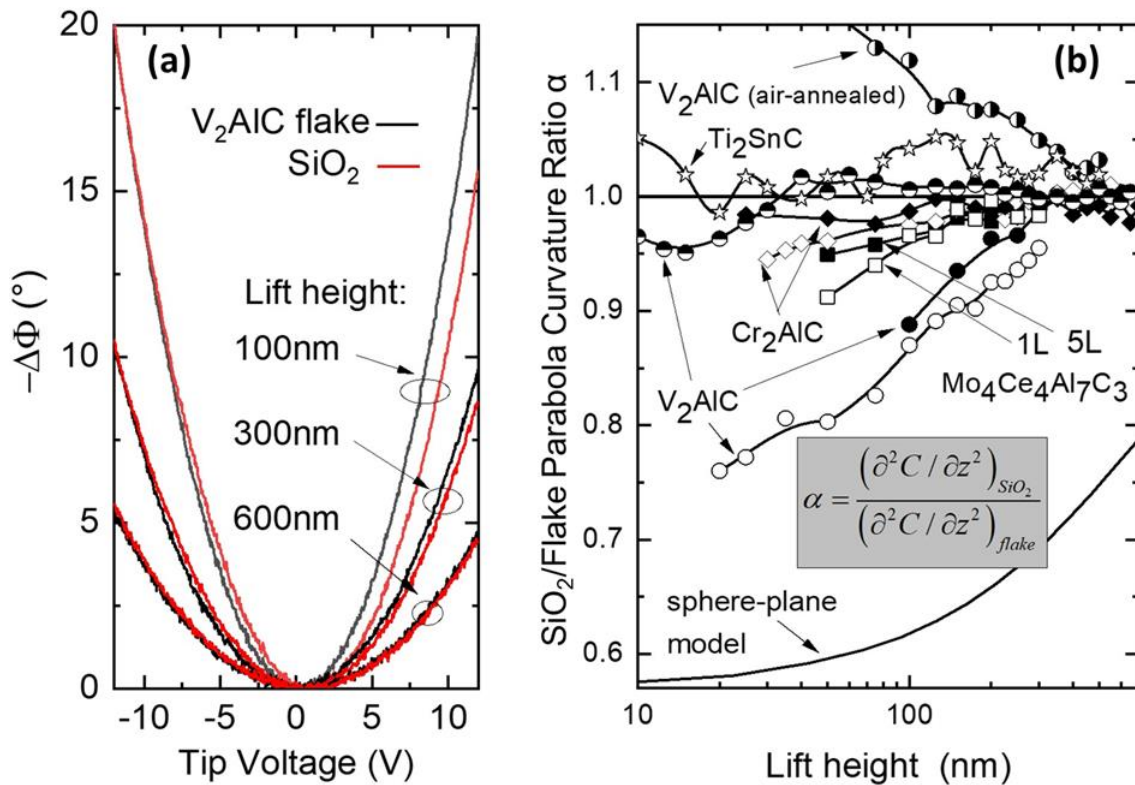


Figure 4.8 (a) Typical experimental plots of the parabolas versus tip voltage at various lift heights, showing marked differences in curvature between flakes and SiO_2 with decreasing lift height. (b) Experimental plot of capacitance contrast between MAXene flakes and SiO_2 versus lift height, expressed in the form of the ratio α among the electrostatic force parabola's curvatures measured on both surfaces [228].

As seen in Figure 4.8 (b) there is a strong variability from sample to sample. Nevertheless, three main responses on the curvature ratio seemed to prevail. In some cases, α remained close to unity for any distance indicating no contrast difference between MAM and MADM configurations. In others, $\alpha > 1$ and increases with decreasing z values, which is incompatible with the sphere-plane model we used. In a third set of measurements, a considerable decrease in α with decreasing z was observed, being thus in qualitative agreement with the model. Within these responses, we also observed various gradations (Figure 4.8 (b)) which could not be explained solely by changes in MAX phase composition and/or annealing conditions. Nonetheless, a common trend for all samples is that α always tended to 1 for large z values, meaning that at large tip-sample distances no contrast differences between bare and covered surfaces were visible.

4.2.1. EFM and KPFM signal probed on hydrophilic and hydrophobic surfaces

The frequent lack of contrast ($\alpha = 1$) and particularly the “inverted” contrast, ($\alpha > 1$), sometimes observed in Figure 4.8 (b), drove us to the hypothesis that the main cause of the change in the recorded signal was the presence of adsorbed water molecules on the SiO₂ surfaces in case they were hydrophilic and the RH was high [215]. It is worth noting that even a 15% RH results in two monolayer-thick adsorbed water layers [215] and the hydrophilic/hydrophobic character may substantially vary with time [233].

To test this inference, we prepared two SiO₂ surfaces: one hydrophilic and the other hydrophobic. In the latter case, we dipped the SiO₂/Si substrates in Piranha solution (sulfuric acid and hydrogen peroxide with a ratio of 3:1) for 1 h to remove all organic residues of the substrates and render the SiO₂ surface hydrophilic. In the former case, Piranha-cleaned SiO₂/Si substrates were dipped in a 10 mM octadecyl-methyl dichlorosilane (97%, abcr GmbH) solution in toluene for 3 h and then the substrates were baked at 120°C for 0.3 h on a hot plate for silanization. Afterwards, they were sonicated in toluene for 0.3 h to remove any unreacted silane and then dried in vacuum. Substrates were stored in vacuum before further measurements. Hydrophobicity and hydrophilicity could easily be checked by depositing a water droplet on a substrate and by inspecting the contact angle. Then, MAXene flakes were transferred on hydrophilic/hydrophobic substrates following the same recipe as the one described in detail in chapter 2.

Both substrates were measured the same day where RH was ranging between 45% and 47%. From these values, we presume that the hydrophilic substrates were covered by substantial water adlayers [215]. Experimental values of the parabola curvature ratio, for V₂AlC flakes on both surfaces versus the lift height, are presented in Figure 4.9. As it was expected, a drop in α values at the shortest distances appeared only in the case of hydrophobic SiO₂ surfaces for all measured samples, and once again, for larger z values, all curves converged around a value of 1.

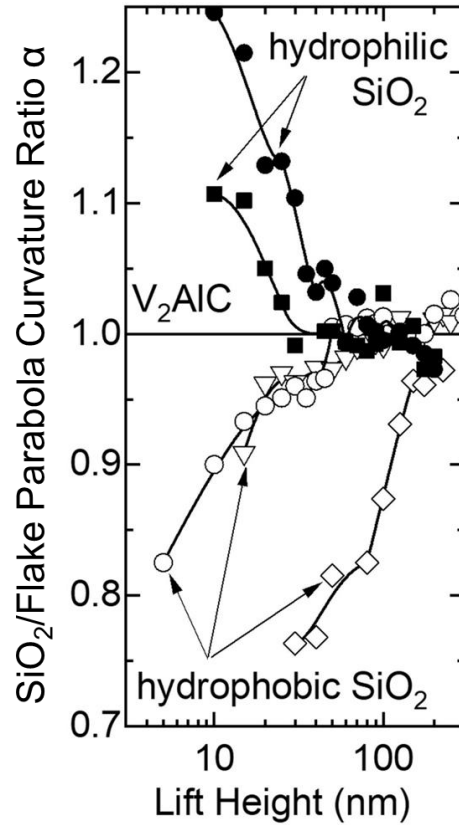


Figure 4.9 Electrostatic force parabola curvature ratio calculated from phase parabolas EFM capacitance contrast versus lift height for V_2AlC flakes prepared under the same conditions, on the same day, on hydrophobic and hydrophilic SiO_2 surfaces and measured the same day in air with RH around 45% - 47% [228].

The results for the parabola curvature ratio were further confirmed by the electrostatic force parabolas ($\Delta\Phi$) measurements on a V_2AlC flake and a hydrophobic SiO_2 surface, as a function of the applied tip voltage (Figure 4.10 (a)). A phase shift was clearly demonstrated at closer tip-sample distances. Furthermore, extracting the contrast $\Delta V_{CPD} = V_{CPD}^{FLAKE} - V_{CPD}^{SiO_2}$ from the parabola fits showed that values obtained from the hydrophobic substrates were always larger than those of the hydrophilic ones (Figure 4.10 (b)). This is in accordance with the experimental observation that the surface potential of SiO_2 surface increases when the thickness of adsorbed water layers increases [215].

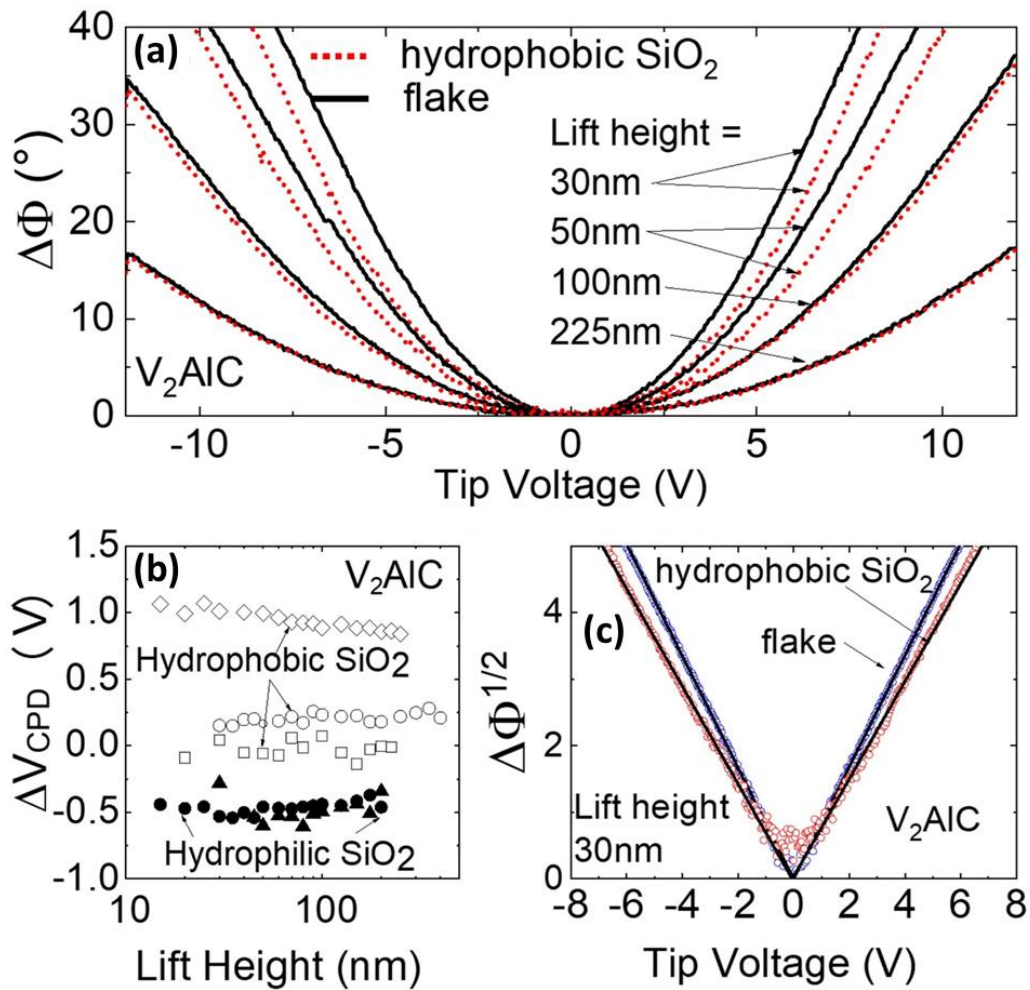


Figure 4.10 (a) Electrostatic force parabolas measured at V₂AlC flake and SiO₂ surfaces at various z , and which were used to calculate α values in Figure 4.9. (b) Experimental plot of contact potential difference for V₂AlC flakes on hydrophobic and hydrophilic SiO₂ substrates versus the lift height. (c) Typical square root of the phase shift used to determine the curvature in (a) and ΔV_{CPD} in (b) [228].

The aforementioned results are remarkable, since the capacitance contrast between the SiO₂ and the flake surface, when $\alpha > 1$ and decreases with decreasing z , hints to a metallic nature of MAXenes, even for the thinnest ones. Consequently, EFM and KPFM methods can efficiently probe the conducting nature of the MAXene flakes.

4.3 Resistivity measurements on MAXene devices

To obtain a quantitative estimation of MAXene flakes conductivity the device processing of flakes is mandatory. For this purpose, several flakes of various thickness and lateral dimensions were used to fabricate four- or five-contact devices.

4.3.1 MAXene device fabrication process

In this subsection, we present in detail the fabrication process through a number of steps we implemented to our MAXene flakes to create top surface electrical contacts for resistivity measurements.

Once bulk MAX phase single crystals have been mechanically exfoliated into their 2D counterparts, MAXenes, and the flakes height profiles have been obtained using AFM, those flakes with uniform height, are then processed to fabricate devices. The fabrication took place in the clean room (NANOFAB) located at the Néel Institute where the relative humidity is low (~45%) and air pressure and temperature (20°C) are stable.

Several steps are required to obtain the metal contacts onto the surface of the selected flakes:

- i. The lithography marks are drawn based on the coordinates (x, y) of the flakes (which have been determined by optical microscope, see chapter 2). For flakes localization and their alignment with the electrodes design, a number of marks are initially designed by using the KLayout software. A field area of $500 \mu\text{m}^2$, with the flake located at its center, is covered with $10 \mu\text{m}^2$ -size marks in parallel rows (apart from the flake area) separated by gaps of $50 \mu\text{m}$ horizontally and $100 \mu\text{m}$ vertically. The scale ratio between the sample and the design in the software is 1:1.

- ii. The sample is covered by a layer (~260 nm) of poly-methyl-methacrylate (PMMA), which is a positive electron-sensitive resin, using a spin coater (4000 rpm, 4000 rpm/s, 60s) and a hot plate where the sample is annealed at 180°C for 5 min. The process is applied inside a fume hood.
- iii. A LEO 1530 SEM equipped with a mechanically controlled stage and the Raith Elphy Plus software to control the electron beam, was used to perform the electron beam lithography (EBL). A series of image correction (wobble, astigmatism, focus) and calibration of the e-beam relative position are prerequisites of the lithography step in order to improve the writing precision of the beam. A 30 keV electron energy for 10 μm lens aperture with the dose at 250 $\mu\text{C}/\text{cm}^2$ was used to perform the lithography after having the marks drawing uploaded to the Elphy software.
- iv. After e-beam lithography the sample was developed in a solution of MIBK/IPA with 1:3 ratio for 45 seconds and then it was immersed directly in IPA for 1 minute. After the IPA bath it was dried out by nitrogen flow.
- v. The KLayout software was used again to design the pattern of electrodes on the flake, on the same file where the marks were previously designed. The optical microscopy image of the marks after the development was imported to the software and used for precisely drawing the electrodes onto the flake by aligning and rotating the image to coincide with the marks drawing. Then, depending on the lateral dimensions of the flake, usually four to five electrodes were drawn with 150 μm^2 -size pads.
- vi. The sample with the same PMMA layer as for the first lithography step was mounted on the SEM and the electrodes pattern was

uploaded to the Elphy software. Once the preparatory step of image correction and position calibration of the beam was completed, two lithography procedures were performed to the PMMA layer. The first one exposed the area covered with PMMA within a writing field area of $500 \mu\text{m}^2$ at the location of the narrow layout electrodes, using $10 \mu\text{m}$ lens aperture and electron energy of 30 keV with the dose at $250 \mu\text{C}/\text{cm}^2$. The second procedure focused on patterning the path between the narrow electrodes and their pads, as well as the pads, within a larger writing field area of $1000 \mu\text{m}^2$ using $30 \mu\text{m}$ aperture and electron energy of 60 keV with the same dose. By reducing the lens aperture in the former step, a higher resolution pattern needed for the electrodes contact with the flake surface was obtained, while the exposure time was increased. On the contrary, by increasing the aperture the resolution was degraded but less time consuming lithography steps were achieved.

- vii. After the EBL process, another development step was performed in the same conditions as in the step (iv).
- viii. Metal deposition on the sample surface was performed at room temperature using an electron beam metal evaporator (Plassys). The sample was loaded in the load-lock chamber of the evaporator which works in high vacuum conditions ($\sim 5 \cdot 10^{-7} \text{ mbar}$). A thin layer (4-5 nm) of Ti or Cr was first deposited as an adhesion layer. Then a Au layer at 40 nm was deposited. The average deposition rate for both metal layers was 0.6-0.7 nm/min.
- ix. For the lift off process, the sample was immersed in a beaker containing N-Methyl-2-Pyrrolidone (NMP) solvent and it was heated at 80°C onto a hot plate for 1 hour. Then, the sample-NMP beaker was subjected to ultrasounds for a very short time (5-10 s in the ultrasonic bath) to completely remove any remaining Ti (or Cr) - Au

parts. Finally, the sample was rinsed with IPA and dried out with a nitrogen flow.

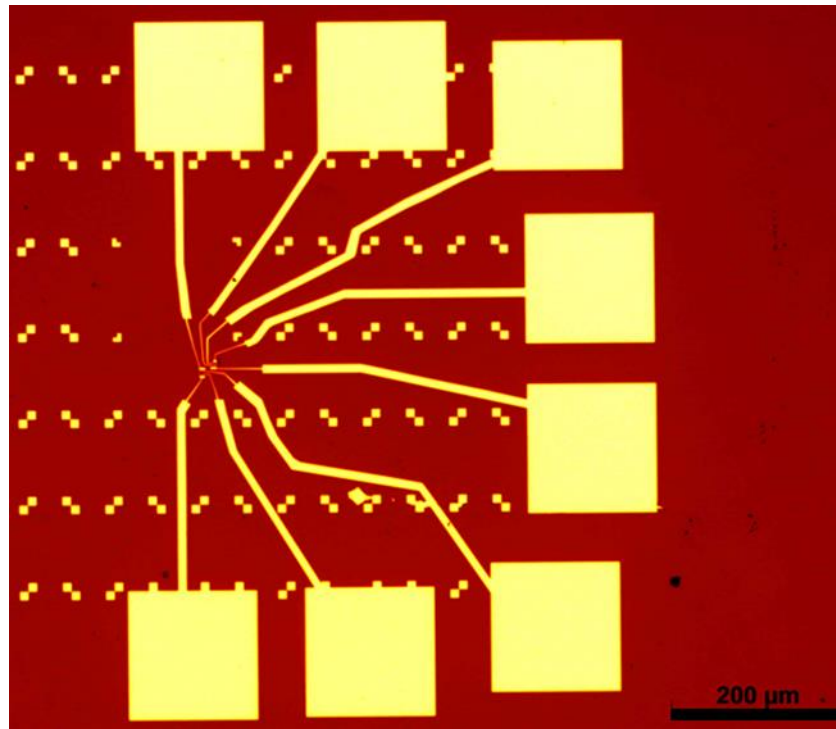


Figure 4.11 Optical microscopy image of two Cr₂AlC flakes after device processing. Each device includes four contacts.

Figure 4.11 shows the device pattern for two Cr₂AlC flakes located in close proximity to one another onto a SiO₂/Si substrate, once the device fabrication process has been completed successfully.

4.3.2 MAXene resistivity using four-point probes method

The four-point probes set-ups at Néel institute (MPS 150 mm manual open probe station) and IMEP (PM5 EMI-shielded manual probe station) were used for measuring the resistance of MAXene devices. The basic working principle of four-point probes is the current injection at the side contacts and the detection of the voltage drop in the middle electrodes. To avoid any device degradation through a possible burnout of the flake, the maximum value of the injected current did not exceed 0.5 μA. To improve the signal-to-noise ratio, a dual-phase SR830 digital signal processing (DSP) lock-in amplifier was used, which was connected through

the BNC (coaxial) cables to the four probes. A resistor of $10\text{ M}\Omega$ was connected in series between the lock-in amplifier and the flake device to obtain a low injected current. All MAXene devices were measured in ambient conditions in both set-ups with the frequency of the lock-in sine signal set at 13 Hz.

Herein, we only discuss the results obtained from a limited number of the many MAXene devices, that were fabricated for the four crystal phases we studied. In Table 4.1, we present selected samples for which the contact resistance made possible the measurement of their conductivity. In the following, one representative MAXene device for each phase is discussed, and problems that occurred during measurements are mentioned at the end of the subsection.

4.3.2.1 Cr_2AlC flake device

The thinnest Cr_2AlC flake (8.5 nm) measured with four-point probes was first submitted to various annealing steps in Ar and HV conditions for 35 h in total to reduce the glue residues on its surface and thus to improve the fabrication of ohmic contacts. The partial reduction of the residues and the probed metallic behavior of MAXenes sparked expectations for obtaining a low contact (R_c) and four probes resistance (R_{4pr}) on the flake. As the injected current (electrodes 1-4) increased from $0.1\ \mu\text{A}$ to $0.4\ \mu\text{A}$, the detected voltage increased linearly proving the ohmic behavior of the contacts (Figure 4.12 (b)).

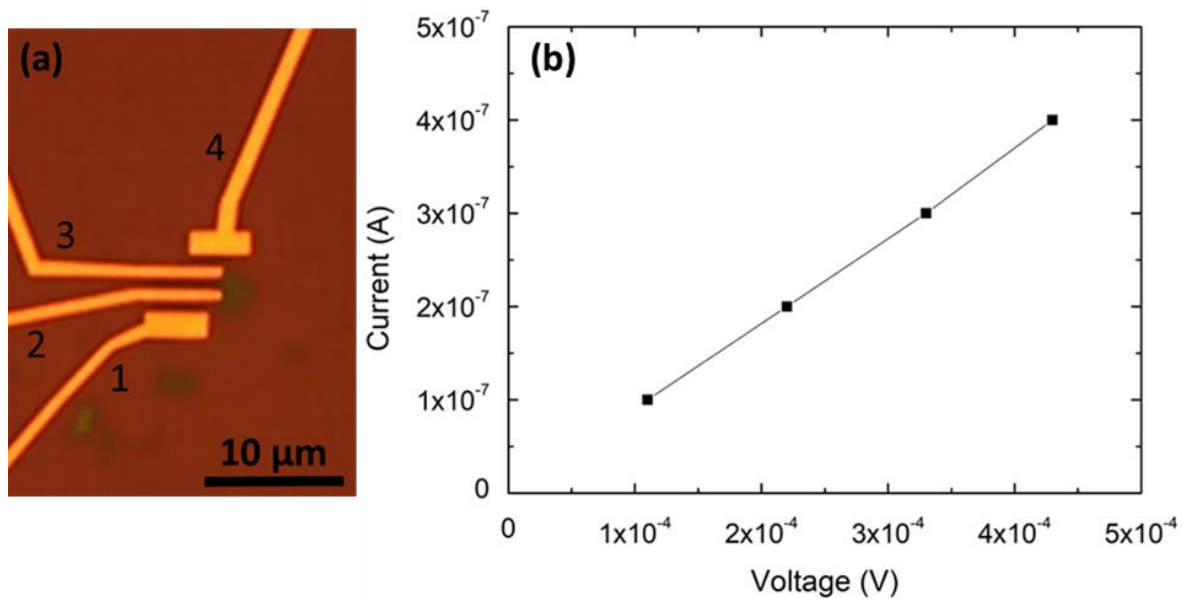


Figure 4.12 (a) Optical micrograph of a four-contact configuration on a Cr_2AlC flake with thickness of 8.5 nm and (b) the plot of the measured I-V curve at the four-point probes set-up.

The R_{4pr} of the above I-V curve is 1.1 k Ω while the R_c exceeded a few tens of k Ω . The flake resistivity, ρ , extracted by the R_{4pr} value using the average length, width and thickness of the flake, is equal to $2.69 \cdot 10^{-6} \Omega \cdot \text{m}$. Owing to the irregular lateral dimensions (flake edges are never straight and parallel) some uncertainty is expected to the resistivity values. The contact resistance in the range of k Ω indicated the restricted influence of thermal annealing on the glue residues and probably a native oxide layer formation mainly on the flake's edges.

4.3.2.2 V_2AlC flake device

One potential way to avoid the oxide layer formation and eliminate glue residues on the flake's surface and edges seemed to be dry etching in Ar plasma. This process was expected to reduce mainly the contact resistance. An e-beam evaporator equipped with an Ar plasma source (CIME) was used to initially etch few V_2AlC flakes in the regions where metal contacts were to be fabricated. Thus, before the metal evaporation the flakes were etched in-situ for 90s in vacuum

conditions (10^{-5} - 10^{-4} Torr). Among the etched V_2AlC flakes that were measured in four-point probes set-up, the thinnest one (6.4 nm) is shown in Figure 4.13.

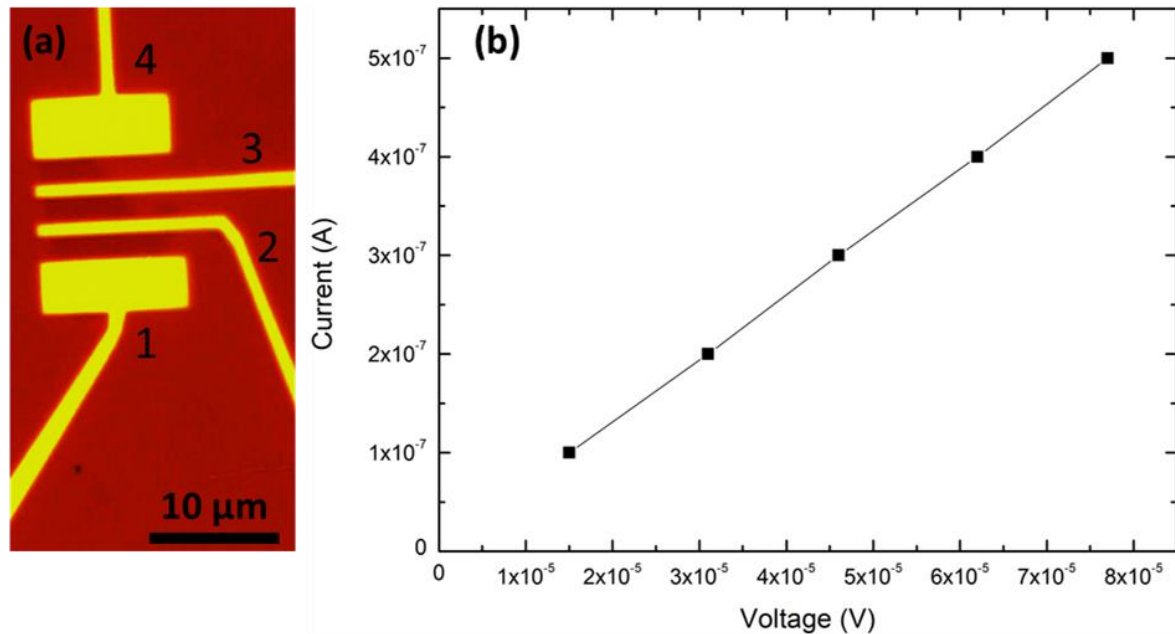


Figure 4.13 (a) Micrograph of a four-contact device with a thin (6.4 nm) V_2AlC flake etched in Ar plasma before metal evaporation. (b) Corresponding I-V plot measured with four probes.

The etching step in Ar plasma seemed to retain contacts with ohmic behavior and furthermore resulted in one of the lowest R_{4pr} values ($150\ \Omega$) measured for V_2AlC flakes in our study. Subsequently, the flake's resistivity found equal to $2.8 \cdot 10^{-7}\ \Omega \cdot \text{m}$ which is comparable to the in-plane resistivity of V_2AlC polycrystals [234]. However, the R_c maintained in the order of tens of $\text{k}\Omega$ indicating that etching in Ar plasma did not eventually improve the contacts.

4.3.2.3 Ti_2SnC flake device

The replacement of the Ti adhesion layer with Cr before Au layer deposition in metal evaporation process favors the inter-diffusion of Cr atoms to the upper deposited Au layer, and despite the partial chromium oxidation, it leads to a Cr-Au alloy formation. This alloy seemed to enhance the electrical contact with the material beneath as supported in Ref. [235].

We used a thin (9.1 nm) Ti_2SnC flake and we replaced the Ti with a Cr adhesion layer during the metal evaporation process. Prior to metals deposition, the flake was etched in-situ in Ar plasma for 60s, in the same vacuum conditions as those previously mentioned; next a Cr adhesion layer of 4 nm was firstly deposited, then a 40 nm Au layer. The four-probes I-V measurement indicates that contacts are ohmic with R_{4pr} and the flake's ρ equal to 129 $\text{k}\Omega$ and $3.67 \cdot 10^{-4} \Omega\cdot\text{m}$, respectively. The R_c values did not exceed 100 $\text{k}\Omega$.

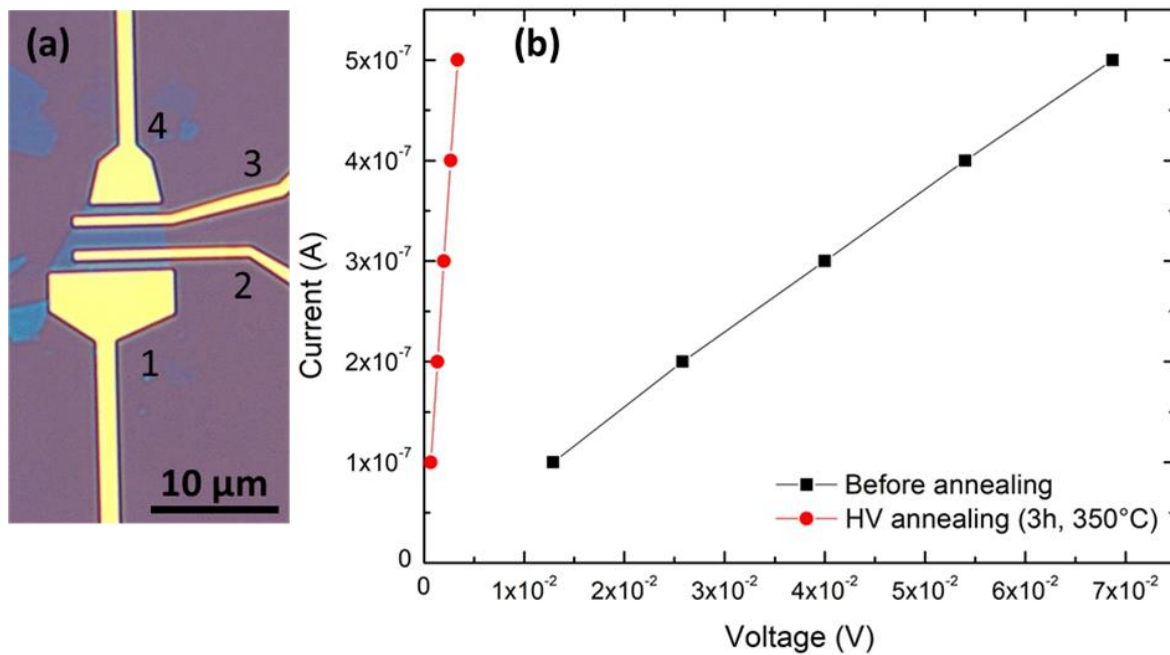


Figure 4.14 (a) Micrograph of the four-contact device with a thin (9.1 nm) Ti_2SnC flake initially etched in Ar plasma before metal evaporation. A Cr adhesion layer was used instead of Ti. (b) Corresponding four-probes I-V curves, before and after HV annealing at 350°C for 3 h.

Considering the possibility that metal deposition could not be uniform in the electrodes positions, which were previously etched, and thus, only the top layers of the flake are finally contacted then, large resistivity and R_{4pr} values are expected. Assuming that annealing could ensures ohmic contacts to the bottom layers so that the overall flake thickness contributes to resistance, we annealed the flake at 350°C for 3 h in HV conditions. It is evident that the R_{4pr} and flake's ρ decreased more than an order of magnitude to 6.7 $\text{k}\Omega$ and $1.9 \cdot 10^{-5} \Omega\cdot\text{m}$, respectively while the R_c found equal to 40 $\text{k}\Omega$.

4.3.2.4 $\text{Mo}_4\text{Ce}_4\text{Al}_7\text{C}_3$ flake device

Several flakes were exfoliated using a natural rubber based adhesive tape, a different approach towards elimination of the remaining glue residues as it was described in chapter 2. Such a flake of $\text{Mo}_4\text{Ce}_4\text{Al}_7\text{C}_3$ phase with thickness of 12.8 nm is presented herein. After exfoliation, the flake was dipped in warm acetone (50°C) for 15 h to reduce the amount of surface glue residues. The I-V curve (Figure 4.15 (b)) reveals ohmic behavior of the contacts. A R_{4pr} value of 13.8 k Ω is derived. The flake's resistivity was found equal to $5.3 \cdot 10^{-4} \Omega \cdot \text{m}$ and R_c below 40 k Ω .

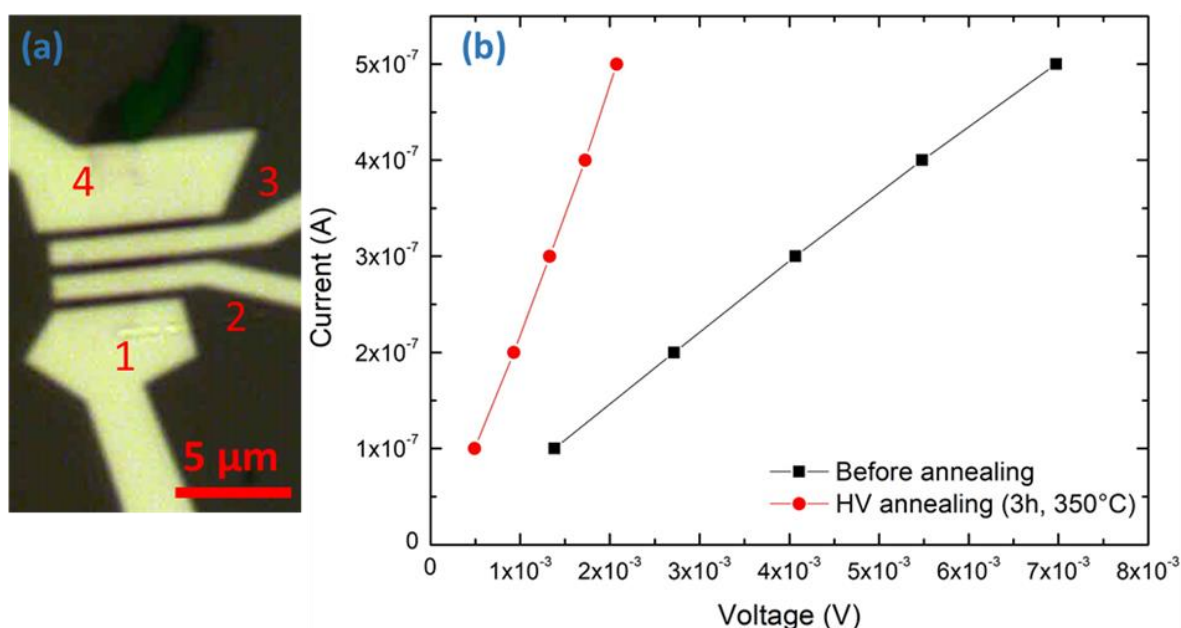


Figure 4.15 (a) Micrograph of the four-contact device with a $\text{Mo}_4\text{Ce}_4\text{Al}_7\text{C}_3$ flake of 12.8 nm thickness. (b) Corresponding I-V curves, measured before and after HV annealing at 350°C for 3 h.

Similarly to the Ti_2SnC case, the $\text{Mo}_4\text{Ce}_4\text{Al}_7\text{C}_3$ flake was also annealed for 3 h in HV at 350°C in order to improve the quality of the metal contacts. As observed from the curve, the R_{4pr} and thus ρ were reduced to 4.8 k Ω and $1.84 \cdot 10^{-4} \Omega \cdot \text{m}$, respectively. An unexpected increase of R_c with values in the range of 40-100 k Ω was found. A possible explanation could be the contraction of remaining glue on

the flake's edges due to HV annealing (§2.2.1.5) forming thus agglomerates that restrict electrons penetration.

The following table presents the resistance and resistivity values for a selected number of MAXene flakes and additionally provides details of their device processing steps (Ar plasma etching before metal evaporation, sputtering deposition of metals) and/or their exfoliation process (different tapes, annealing or warm acetone treatment for glue residues).

Table 4.1 R_{4pr} , R_c and resistivity values measured herein for several fabricated MAXene devices.

	Phase	Sample details	Thickness (nm)	R_{4pr} (k Ω)	R_c (k Ω)	Resistivity ($\Omega \cdot m$)	
						1 st measur.	2 nd measur.
UV tape	Cr ₂ AlC	Ar annealing (3 h, 400°C)	17	7.6	≤ 200	$5.46 \cdot 10^{-5}$	-
			12	8.2	≤ 145	$2.81 \cdot 10^{-5}$	-
Synthetic adhesive tape	V ₂ AlC	Annealing in H ₂ + Ar flux (2 h, 400°C) – sputtering deposition of metal contacts	7.7	44	≤ 100	$9.06 \cdot 10^{-5}$	$2.57 \cdot 10^{-5}$ (HV annealing: 3.5 h, 350°C)
				12.5 (HV annealing: 3.5 h, 350°C)	28 (HV annealing: 3.5 h, 350°C)		
	V ₂ AlC	Annealing in H ₂ + Ar flux (2 h, 400°C) – 90s Ar plasma etching before metal evaporation	8	0.65	≤ 200	$6.2 \cdot 10^{-7}$	-
16			0.05	≤ 500	$2.4 \cdot 10^{-7}$	-	
	Mo ₄ Ce ₄ Al ₇ C ₃	Annealing at 400°C: 2 h in Ar & 5 h in HV	10.9	3	< 90	$8.18 \cdot 10^{-5}$	-

Chapter 4: Topography of cleaved MAX phase single crystals and MAXenes electrical characterization

Natural rubber based tape	Mo ₄ Ce ₄ Al ₇ C ₃	Dipped in warm (50°C) acetone (15 h)	30.4	16.4	≥1000	1.35 · 10 ⁻³	5.34 · 10 ⁻⁴ (HV annealing: 3 h, 350°C)
				6.5 (HV annealing: 3 h, 350°C)	≤ 300 (HV annealing: 3 h, 350°C)		
	Ti ₂ SnC		12	9.9	≤ 120	4.04 · 10 ⁻⁴	8.16 · 10 ⁻⁵ (HV annealing: 3 h, 350°C)
				2 (HV annealing: 3 h, 350°C)	< 65 (HV annealing: 3 h, 350°C)		
			24	2.6	≤ 60		

4.3.3 MAXene resistivity as a function of temperature

Resistivity measurements as a function of temperature down to 4 K were performed with few flakes. For that purpose, a resistivity option PPMS puck (Figure 3.23) was used to mount the sample by sticking it with a varnish and then solder it. An ultrasound microbonding 7400E set-up with Au wire was used to connect the pads of one of the total three channels of the puck with those on MAXene device. One of the samples measured down to 4 K was the Cr_2AlC flake mentioned above (§4.3.2.1). The injected current was $10\ \mu\text{A}$ and starting from 300 K the temperature was decreasing with a rate of 3 K/min. Using the flake's average length, width and thickness the resistivity values were extracted as a function of temperature.

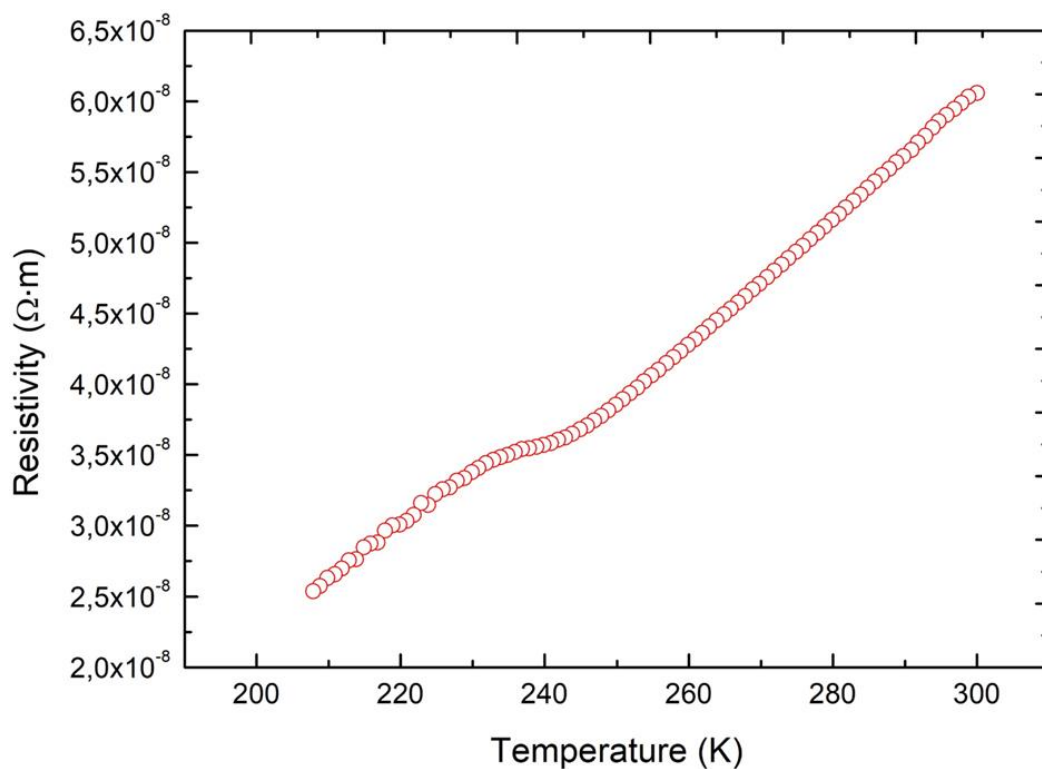


Figure 4.16 Resistivity plot as a function of temperature from 300 K to 208 K, for a Cr_2AlC device.

In Figure 4.16, resistivity was plotted down to 208 K. Below this temperature the contacts are not ohmic probably due to the presence of glue residues on the flake's surface. The maximum ρ value was measured at 300 K, $6,06 \cdot 10^{-8}\ \Omega\cdot\text{m}$ and

the minimum at 208 K, $2.54 \cdot 10^{-8} \Omega \cdot \text{m}$. It is evident that ohmic behavior is maintained. The reason of the small gradient change observed around 240 K is not clear at this time. The linear increase of the resistivity with T is a clear indication of the metallic character of the flake.

4.3.4 MAXene resistivity as a function of flake thickness

The influence of the thickness on the flakes resistivity and their conducting nature established previously with EFM, prompted us to measure the MAXene resistivity as a function of flake thickness for various flakes of all four phases studied herein (Figure 4.17).

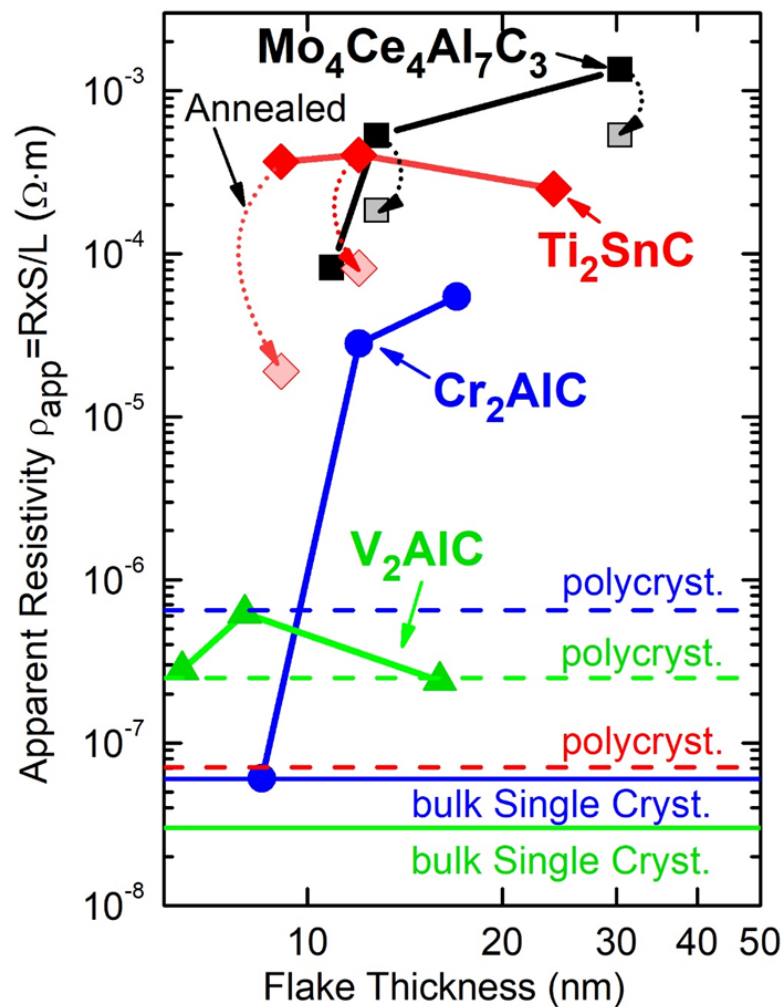


Figure 4.17 Log-log plot of four-contact apparent resistivity as a function of flake thickness, for the three MAX phases and $\text{Mo}_4\text{Ce}_4\text{Al}_7\text{C}_3$. Annealing some samples in high vacuum at 350°C for 3 h lead to a noticeable improvement in resistivity (light

color squares). Solid and dashed lines represent measured resistivity values of the three MAX phases reported to date in the literature for single crystalline and polycrystalline forms.

Apart from V_2AlC , all other compositions in the plot exhibit an abnormal increase of the apparent ρ with the thickness. The reason of the V_2AlC exception is not completely clear. The extracted ρ values can also be increasingly underestimated with increasing flake thickness if interlayer defects, most likely delaminations between layers, are present. Then, for the true thickness ρ is also lower than the one assumed, which in turns leads to an overestimation in resistivity. This scenario may be consistent with the fabrication of our side contacts because i) flakes are more prone to oxide formation at the edges than on top (a recurrent problem with 2D flakes) and/or ii) depending on the flake edge angle, metal deposition is not conformal. Then, in both cases, current is just injected at the top. Possible explanations of the increase of apparent resistivity with thickness are i) partial delamination of intermediate layers and/or ii) high transport anisotropy of some phases, as has been evidenced in bulk materials [236], [237]. Taking these considerations into account, it follows that the lowest ρ values are more representative of the true ρ values.

A comparison of the resistivity values between the bulk V_2AlC , Ti_2SnC and Cr_2AlC phases and their 2D derivatives indicated that in the case of V_2AlC , the flake resistivity values measured herein are of the same order as in-plane resistivity of the polycrystalline samples [234]. However, they are notably higher than those measured on macroscopic single crystal samples [236]. The exact reason for this discrepancy is still unknown. A possible reason could be the quality of crystals as the values measured herein could derive from defective ones. Another reason could be the decrease of the dimension along c -axis that leads to electron scattering. For Ti_2SnC phase, the resistivity values measured on flakes highly diverge from the in-plane value of bulk polycrystals [48] with the aforementioned reasons appear as a possible explanation. In the case of Cr_2AlC , the measured flake resistivity is one and two orders of magnitude higher than the bulk polycrystal [229] and single crystal [236] in-plane values, respectively. Exception is the thinnest measured Cr_2AlC flake whose resistivity is similar to that of the bulk

single crystal. Notwithstanding the discrepancy between the values of bulk and thicker flakes (more than 10 nm) that can be explained by the same possible reasons mentioned in the V_2AlC and Ti_2SnC case, the reason of the accordance in resistivity values between the bulk single crystal and thinner flake remains unspecified. Here it is needed to elucidate that the aforementioned flake resistivity which was measured in PPMS set-up converges with the resistivity of bulk single crystal. However, a great discrepancy in resistivity is observed between the values measured at room temperature on PPMS and on four-point probes set-up, for the same flake (§4.3.2.1). This discrepancy could be attributed to a possible oxidation of the tip-apex of the four-point probes set-up. Therefore, all resistivity values plotted in Figure 4.17 can be underestimated.

4.4 Conclusion

In conclusion, STM observations shown that the cleaved surface of a Cr_2AlC crystal consists of two nested areas with different apparent heights where the dark regions are attributed to the disordered Al or Al-O clusters while brighter ones to the Cr-rich surfaces. Additionally, the EFM and KPFM methods using the capacitance contrast ($\frac{\partial^2 C}{\partial z^2}$) and the surface potential difference (ΔV_{CPD}) between SiO_2 and flakes indicated the metallic behavior of MAXene flakes down to monolayer thickness. The metallic nature of MAXene flakes was also verified by resistivity measurements at room temperature as well as down to 208 K. In the range of low injected current we demonstrated the ohmic behavior of contacts, even if R_c remains in the range of $k\Omega$. Annealing in HV conditions proved that improves R_c . A possible oxidation mainly on the flakes edges, perhaps hinders a proper estimation of the conductivity, which could be avoided by using a more complex process for fabricating “edge” contacts and thus to ensure a contribution from all layers [238]. Determining accurate values of thin flake resistivity is important because DFT calculations by Sankaran et al. have suggested that MAX phases in general and V_2AlC in particular, can be good candidate materials for the next generation interconnects, beyond Cu and even Ru [239].

Chapter 5

Elementary processes governing V_2AlC chemical etching in HF

The last chapter presents in detail our kinetics study on the MAX-to-MXene transformation starting from a well-defined single crystalline structure. Focusing on the V_2AlC phase and based on the recipe we developed in the lab, we firstly describe, step-by-step, the fabrication of well-defined square-size V_2AlC pillars. Next, the etching process of the pillars structure in HF is presented. The V_2AlC pillars were submitted to several etching steps as a function of time. Finally, using various characterization techniques, we identify some key aspects ruling the MAX phase to MXene conversion in chemical exfoliation.

5.1 Chemical etching and well-defined V_2AlC pillar structures

Our interest in the present thesis is not restricted to the mechanical exfoliation of MAXenes from their parent MAX phases but it also concerns chemical etching processes of MXenes from their Al-based 3D counterparts. The latter kind of etching is focused on the weak M-A bonds and the ease with which Al can react with HF, as it was mentioned in the first chapter. Although literature on MAX phases chemical etching is abundant [90], well-defined structures with definite crystal orientations are lacking, which has so far hindered our capability to observe some key aspects and define the limitations of the etching process. This restriction derives from the fact that MXenes are mainly produced from MAX powders with a

statistical distribution in size and defects – typical grain sizes can range from a very few μm to a few tens of μm .

A few kinetics studies of MAX-to-MXene conversion have been reported to date with the earliest one being that of Mashtalir et al. who studied the conversion of Ti_3AlC_2 powders in HF [240]. However, to select the most appropriate etching conditions, to determine up-to-now unknown key aspects such as etching anisotropy and secondary phase production, or to set some bounds on the maximum convertible size, it is essential to start from well-defined, well-oriented structures of controlled dimensions.

In our kinetics study [241] we focused on V_2AlC , one of the studied MAX phases that forms the strongest M-Al bond [242] and requires extreme etching conditions for a full transformation of V_2AlC into V_2CT_z [124] that can lead to partial carbonization. The latter is liable to affect the conductivity in applications like fuel cells and biosensors [243]. As it will be described in details, we fabricated various well-defined square-size V_2AlC pillars using photo-lithography and plasma-assisted etching techniques starting from centimeter-sized V_2AlC single crystals synthesized in our lab [70]. The purpose of our study was to apply chemical etching steps in HF to the pillar structure for various time intervals so as to observe the chemical composition, the crystal structure and the morphology of the pillars at the local scale after each step by using optical microscopy (OM) in the Nomarski mode, scanning electron microscopy (SEM), energy dispersive X-ray spectroscopy (EDS) and Raman spectroscopy [241]. Characterization with the aforementioned techniques allowed us to extract the time dependence of etching, to obtain qualitative insights into the influence of defects and residual stresses, and in the case of defect-free pillars, to quantify the conversion into MXene and competing phase kinetics. Besides, we managed to determine a maximum limit to the convertible size that can be reasonably obtained when no sonication or elevated temperatures are used.

5.2 Fabrication of V_2AlC pillars

The prerequisite of the fabrication of the pillars structure was the availability of V_2AlC single crystals with large lateral size and a few hundreds of μm thickness

that in our case were produced abundantly thanks to the high temperature solution growth technique [70] we developed and which was discussed in the first chapter. The selected centimeter-sized single crystals were first cut into 5 x 5 mm² using a diamond wire saw. To ensure the good uniformity of the crystal surface we cleaved them once or twice using a stronger adhesive tape than that in our mechanical exfoliation process (adhesion strength \gg 4.8 N/m) by peeling off abruptly.

5.2.1. Pattern of square size array

The square size arrays were created via a new recipe we developed in the lab using the appropriate photoresist and photo-lithography conditions. Owing to the strong intra- and inter-layer bonding of the V₂AlC single crystals (compared to van der Waals structures) and the deep trench we target (depth \geq 5 μ m), we chose a photoresist that could withstand the harsh dry etching conditions of the plasma-assisted etching technique. Before the photoresist deposition, the V₂AlC crystal was heated on a hot plate at 150°C for 4 min, to improve the photoresist adhesion (Figure 5.2 (a)). One drop of SPR220 positive (the exposed part to light is removed) photoresist onto the crystal's surface, was enough to form a 10-12 μ m thick covering layer after spin coating (Figure 5.2 (b)) with a speed of 3000 rounds/s, 3000 rounds/s² acceleration and spin coating time of 30 s. Subsequently, the resist was baked for 90 s at 115°C on a hot plate (Figure 5.2 (c)) after which the crystal-resist system was allowed to relax for one hour inside the hood. To create the various square size array patterns, a chromium oxide mask was prepared with a pattern (Figure 5.1) of dimensions matching those of V₂AlC single crystals (5 x 5 mm²). The design was composed of horizontal lines with squares whose sides ranged from 4 μ m to 500 μ m whilst the distance between their rows was 12 μ m.

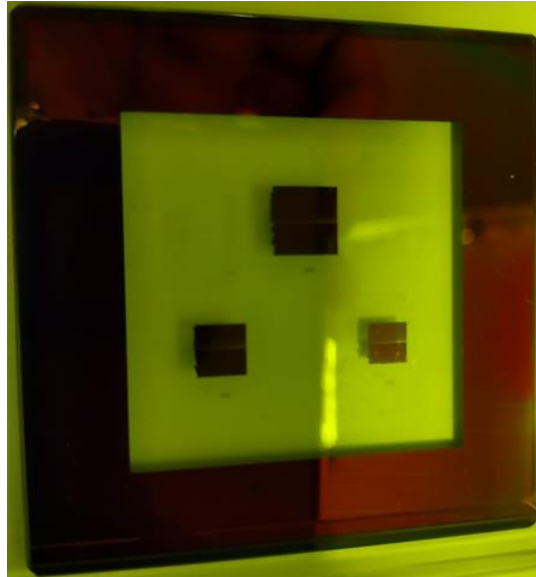


Figure 5.1 Lithography mask with $5 \times 5 \text{ mm}^2$ (right), $6 \times 6 \text{ mm}^2$ (left) and $8 \times 8 \text{ mm}^2$ (top) patterns of various square size array. The $5 \times 5 \text{ mm}^2$ pattern was compatible with our V_2AlC crystals size and was used in our experiments. The colored area on the mask corresponds to the chromium oxide.

The lithography step was carried out in a deep UV MJB3 Contact Mask Aligner where the crystal-photoresist system was placed on the top of the apparatus holder and then the mask was manually adjusted onto the resist by three knobs (x, y, z) without however sticking on it (Figure 5.2 (d)). A 365 nm wavelength UV light of 0.22 mW/cm^2 power and a dose of 900 mJ/cm^2 was applied to the resist for a total duration of $\approx 70 \text{ min}$. Once the lithography step was completed, a relaxation step of $3/4 \text{ h}$ inside the hood was needed to permit the water, which is necessary to complete the photo-reaction, to diffuse back into the photoresist film. For pattern development, the V_2AlC crystal was dipped into MF-26A microposit developer for 8 min (Figure 5.2 (e)). The small size of $4 \times 4 \text{ }\mu\text{m}^2$ and $5 \times 5 \text{ }\mu\text{m}^2$ squares and the high exposure dose applied to the pattern, reduced the resist adhesion on the crystal's surface such that the lines of the array with $4 \times 4 \text{ }\mu\text{m}^2$ and $5 \times 5 \text{ }\mu\text{m}^2$ squares were completely removed after development. Therefore, the minimum starting size of the array pattern was $7 \times 7 \text{ }\mu\text{m}^2$ instead of the $4 \times 4 \text{ }\mu\text{m}^2$. A final step of hard bake at 100°C for 4 min (Figure 5.2 (f)) was needed to improve the photoresist adhesion for the next process of dry etching.

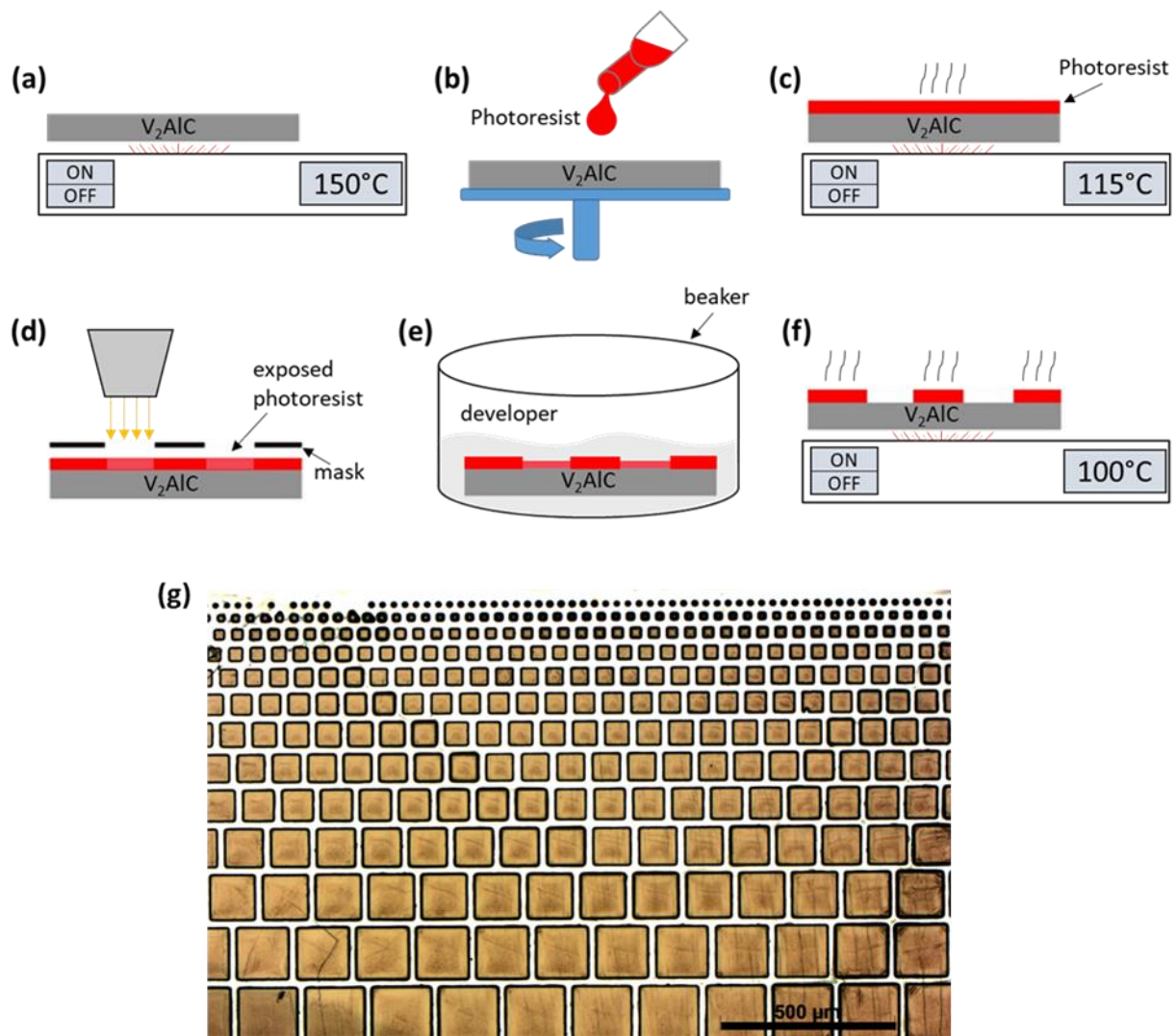


Figure 5.2 (a)-(f) Schematics of the steps followed to create the V_2AlC pillar structure. (g) Optical microscopy image showing the pattern of various square size array after the hard bake at $100^{\circ}C$ for 4 min.

5.2.2. Formation of V_2AlC pillars using Inductively Coupled Plasma (ICP) etching

To obtain the final form of the pillars, the single crystals were processed with inductively coupled plasma (ICP) etching. Compared to other dry etching techniques we tested, physical ones like ion beam etching (IBE) and chemical ones such as reactive ion etching (RIE), ICP proved to have higher efficiency as it resulted in higher etching rates, at lower etching time.

ICP uses two independent radio frequency (RF) sources that allow to independently control the plasma density (ion flux) and the energy of the ions. The

cylindrical chamber, where etching takes place, has a coil that is wrapped externally and around the chamber walls (Figure 5.3). One of the RF sources (ICP generator) is connected to the coil where a RF voltage is applied and generates a RF current. The flux of the oscillating magnetic field that is thereby induced in the coil generates an electric field in the chamber that thermally activates the electrons of the gas molecules and atoms favoring thus their ionization and the plasma creation. The chamber walls are made from insulating material to hinder any electrical interaction with the charged particles. The second RF source is connected to the cathode where a lower power RF bias voltage is applied to the sample holder to attract and accelerate electrons and ions from the plasma to the sample's surface so as to increase the etching yield [244].

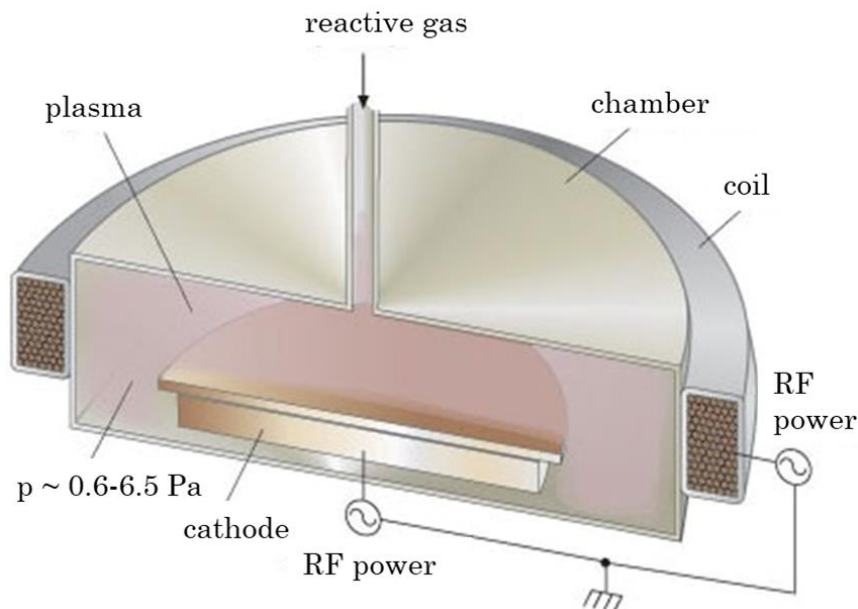


Figure 5.3 Cross section sketch of the reaction chamber of ICP. Figure adapted from Ref. [245].

The ICP etching apparatus we used was the Oxford plasmalab 100 installed at the Upstream Technological Platform (PTA) in French Alternative Energies and Atomic Energy Commission (CEA). Both RF power sources of the apparatus work at 13.56 MHz. Our small size single crystals ($5 \times 5 \text{ mm}^2$) needed a wafer carrier in order to be loaded in the plasma chamber. Therefore, we used a Si wafer with $1 \mu\text{m}$ -thick top SiO_2 layer and we stuck the crystal with a residue-free glue on a hot plate at 65°C . Then, the wafer was loaded into the ICP chamber and a combination

of Cl₂ (40 sccm) with BCl₃ (10 sccm) gases was used to etch the crystal for 4-5 min using a plasma RF power of 1500 W and 150 W for generating the bias voltage (cathode RF power). These etching conditions were optimized through various trials that besides all proved the great etching efficiency of Cl₂ and BCl₃ gases against metal surfaces like V₂AlC, compared to Ar, O₂ and SF₆ gases that were also tested. After etching, the V₂AlC crystal was removed from the wafer by heating it on a hot plate to 65°C and then it was washed with deionized (DI) water. In order to completely remove the remaining photoresist on top of the crystal, as soon as the etching was completed, we immersed it in a N-methyl-2-pyrrolidone (NMP) bath for 1 h at 80°C. The final height of pillars was around 5 μm with areas ranging from 7 x 7 μm² to 500 x 500 μm² (Figure 5.4 (a)) and their edges having an angle instead of being sharp (Figure 5.4 (b)) as it seems that resist was etched faster along the sidewalls of squares than on top of their surface. Attempts to etch deeper trenches resulted in unwanted etching of the protective layer of the photoresist.

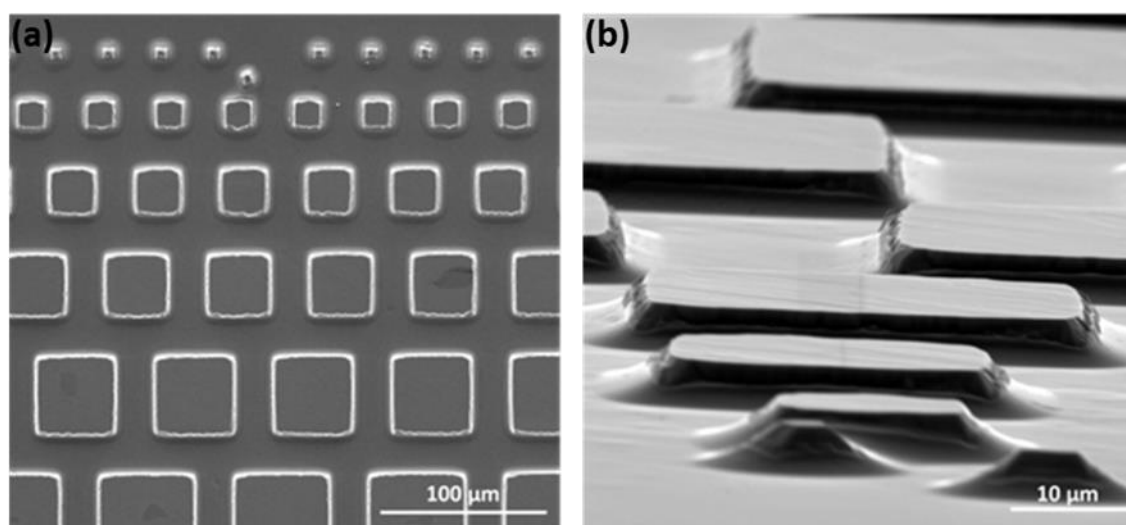


Figure 5.4 SEM images of the V₂AlC pillars in (a) top view and (b) tilted at 82° [241].

5.3 Hydrofluoric etching of V₂AlC pillars and MXene conversion kinetics

Once the fabrication of the well-oriented V₂AlC pillar structure was completed, the last processing step was chemical etching. As etchant we used a 20 mL solution

of 49% HF acid in which we immersed the V_2AlC crystal with the pillar structure at room temperature (25°C). To homogeneously etch the pillars an orbital shaker was used to rotate the sample during the process (Figure 5.5). The pillars etching was carried out for different time intervals with measurements made after each etching step. When the desired etching time was reached, the V_2AlC pillars were washed with DI water several times until the pH value reached 6.

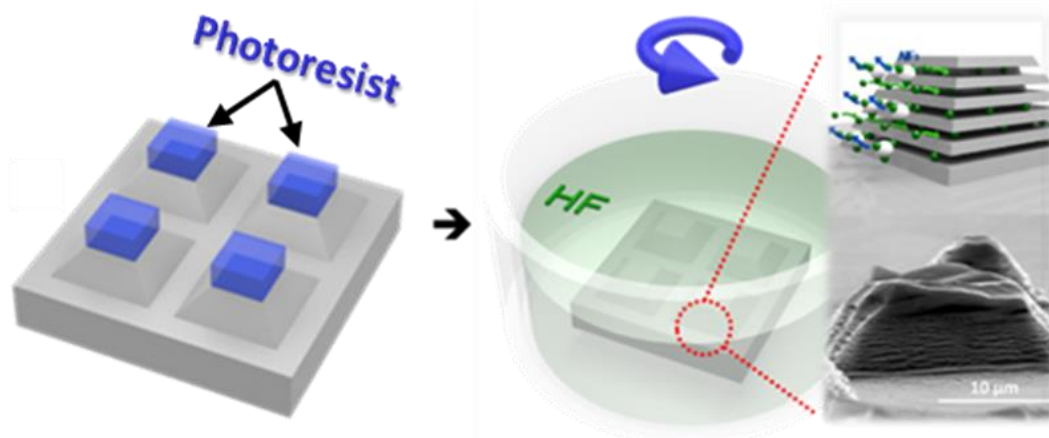


Figure 5.5 Schematics of the pillar structure directly after the etching step (left) followed by the HF etching into the orbital shaker (right). Before submerge the sample into HF, the remaining photoresist after the ICP etching was firstly removed. In magnification a drawing of the HF penetration through the pillar's side, above a SEM image of a pillar after the etching process [241].

5.3.1 HF etching of defective V_2AlC pillars

During our study we realised that all pillars were not etched equally or uniformly but that etching was accelerated by the presence of defects and/or stresses into pillars. In Figure 5.6 the same sample was etched for 6, 15, 24, 33 and 40 h in 49% HF and the influence on pillars morphology was observed using a FEI QUANTA 250 scanning electron microscope (SEM) after washing (Figure 5.6 (a), (b)). A back-scattered electron detector was used to reveal contrast between the unaffected and the HF-etched part of the pillars (Figure 5.6 (c)), whereas a Bruker AXS-30 mm^2 SDD detector with a 15 kV acceleration voltage was used for EDS measurements, specifically to map the Al loss in the etched areas (Figure 5.6 (d)).

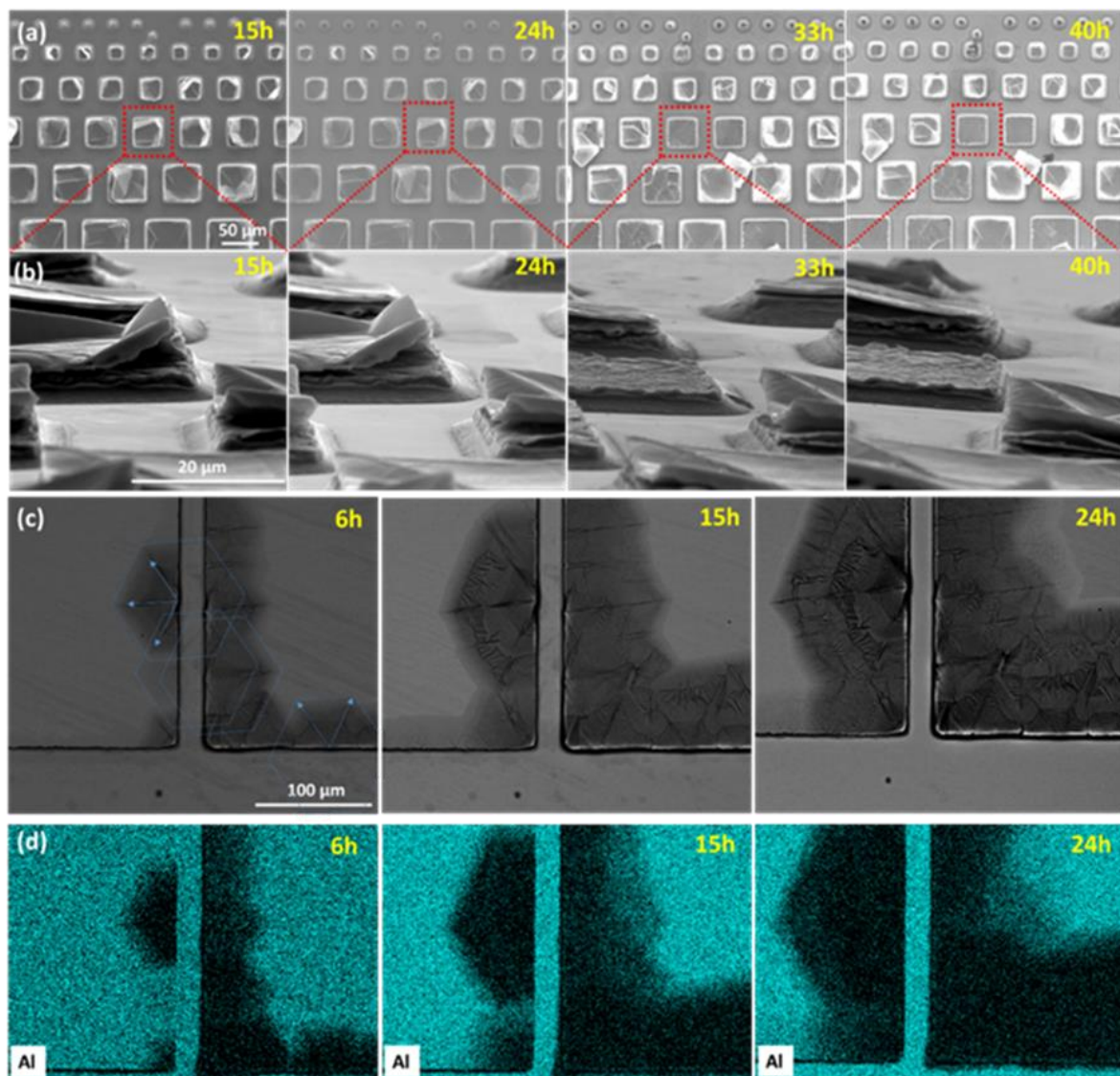


Figure 5.6 Top view of SEM images (a) of various size V_2AlC pillars and 82° tilted views (b) of the red framed region in (a) images, as a function of HF etching time. SEM images (c) and EDS maps (d) revealing the loss of Al in a 500 μm-sized pillar versus HF etching time. Blue arrows in (c) indicate preferred etching directions (hexagon-like shape) [241].

Owing to the fact that the single crystals remain in the growth flux during the final cooling stage, large mechanical stresses can develop. Stress does not only favor chemical etching but also a preferential etching of some particular layers. The expansion of any small etching fluctuation in the various “A” layers seems favored by the high stress and results in a macroscopic opening of the pillar well before conversion of all other layers. Said differently, highly stressed pillars tend to open and they do so preferentially at particular regions. In addition to Figure 5.6 (b), Figure 5.7 highlights the morphology of diverse size stressed pillars versus the HF

etching time. As it can be clearly seen in both figures, those pillars have been detached from the bulk crystal surface well before the full conversion to MXene was completed.

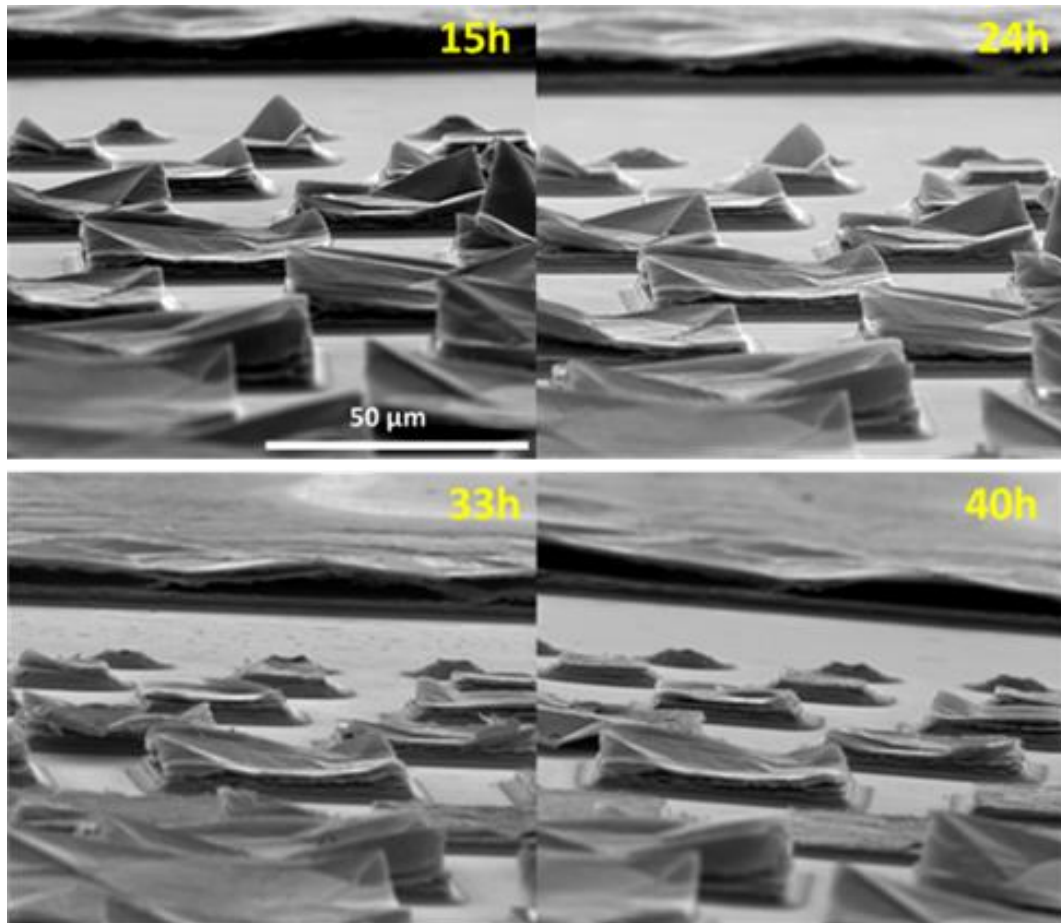


Figure 5.7 82° tilted SEM images of stressed V₂AlC pillars morphology as a function of HF etching time [241].

Chemical exfoliation can be accelerated by localised defects that are located at, or close, to the pillar edges (Figure 5.6 (c)). Starting from the initial defect location, large ripples were observed forming a star-shaped pattern centered on the initial defect with directions separated by angles of $\pi/3$, progressively extend with time over the surface of a 500 μm -sized pillar. Each main ripple gives in turn birth to a set of smaller, lateral ripples. The darker color, observed in the hexagonal patterns in the backscattered electron (BSE) mode in the SEM images, is indicative of Al removal, as confirmed by the EDS maps (Figure 5.6 (d)), and thus conversion into MXene.

The growth direction of V_2AlC is highly anisotropic, resulting in a very low crystal aspect ratio [70] and most of the V_2AlC single crystals have the lateral size of around 1 cm^2 and thickness less than a few $100\text{ }\mu\text{m}$. Hence, the top surface of the pillars is always parallel to an ab plane, and perpendicular to the c axis. In this respect, the hexagonal patterns are clearly crystallographic, since all patterns have the same orientations, regardless of their initial positions. The SEM micrographs prove that in the presence of a local stress field, chemical conversion is anisotropic in the ab plane. A tempting and plausible explanation is that in the regions of high strain, the F ions penetrate more easily along directions that are less dense in Al atoms [241].

The lateral etching distance for a defective V_2AlC pillar could exceed $100\text{ }\mu\text{m}$ after 24 h of chemical etching. After 6 h only, Al atoms have been removed from the pillar structure at a lateral distance around $50\text{ }\mu\text{m}$, in the case of both the larger size pillars (Figure 5.6 (c)) and those having smaller lateral dimensions (Figure 5.8 (a), (c)).

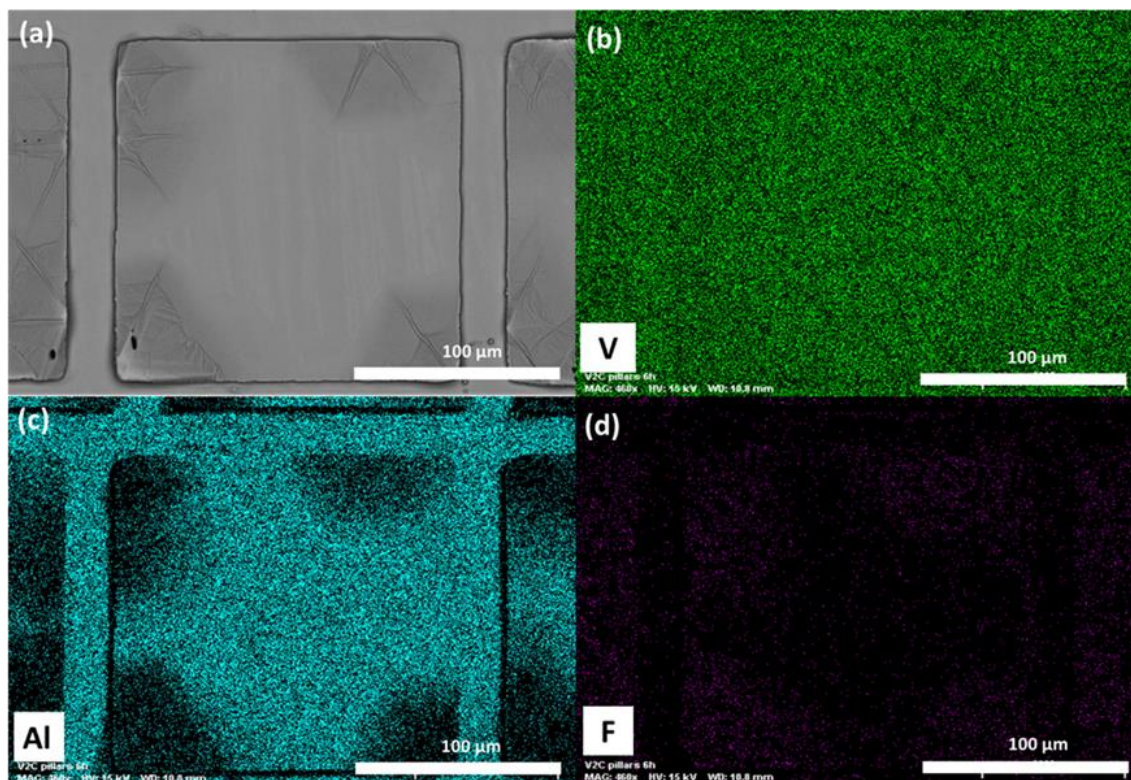


Figure 5.8 Surface morphology and elemental maps of a $160 \times 160\text{ }\mu\text{m}^2$ pillar after 6 h etching in 49% HF. (a) Top view SEM image, (b) V, (c) Al and (d) F elemental EDS maps [241].

In pillars having even smaller lateral size, e.g. $90 \times 90 \mu\text{m}^2$ pillars, delamination of the structure was complete after 24 h of HF etching (Figure 5.9). The OM images (Figure 5.9 (b)) clearly show a contrast change close to the pillar edges after 6 h of etching that progressively expanded towards the center as the etching process was evolving. This contrast difference refers to Al loss from the pillar structure as it can be seen in Al elemental EDS map (Figure 5.9 (d)).

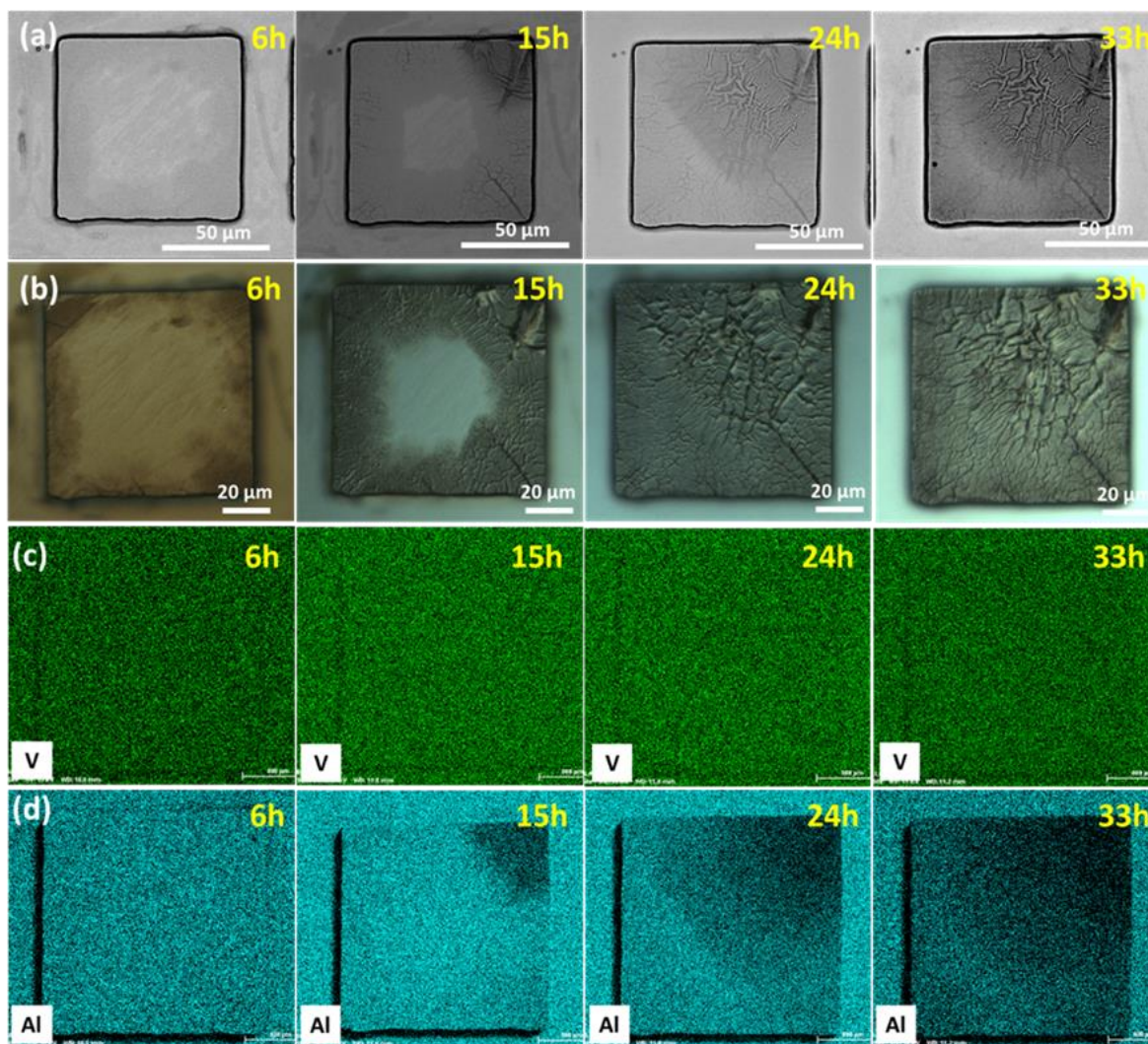


Figure 5.9 Surface morphology and elemental maps of a $90 \times 90 \mu\text{m}^2$ pillar as a function of etching time in 49% HF. (a) Top view SEM images, (b) OM images, (c) V and (d) Al EDS maps [241].

Similar patterns were also observed with $60 \mu\text{m}$ -lateral size pillars. Measurements shown that such pillars can be fully etched even after 6 h into 49% of HF (Figure 5.10).

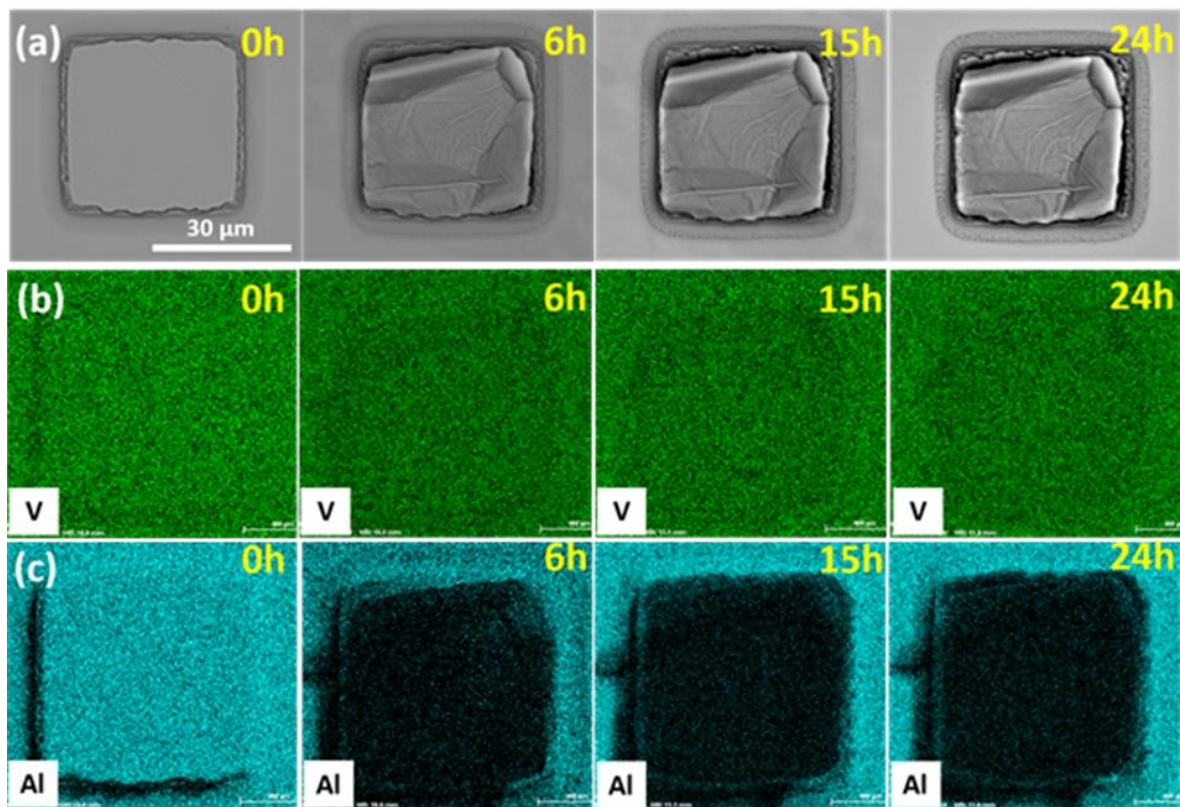


Figure 5.10 (a) Top view SEM images of the surface morphology of a $40 \times 40 \mu\text{m}^2$ pillar and (b) V and (c) Al EDS maps as a function of etching time in HF [241].

Finding such patterns is not only interesting by itself but it is also quite useful for determining crystal orientations. As seen in Figure 5.6 (c), one pillar side is almost parallel (within very few degrees) to the side of the etched hexagonal patterns. This implies that the “horizontal” square sides and the “vertical” ones, in the figure, respectively correspond to the two extremal possible in-plane crystal orientations.

5.3.2. HF etching of defect-free V_2AlC pillars

Defects and/or internal stress in the pillars structure proved to accelerate their chemical etching in HF. For defect-free pillars the MXene conversion kinetics is expected to be different. Herein, we observed the etching kinetics for the above-mentioned “horizontal” and “vertical” square sides, each corresponding to a high-symmetry crystallographic direction, of defect-free pillars.

A striking observation is that the square shape of the defect-free V_2AlC pillars is retained even after 96 h of etching in 49% HF (Figure 5.11), while for most defective pillars the structure was delaminated after 33 h of etching (Figure 5.7).

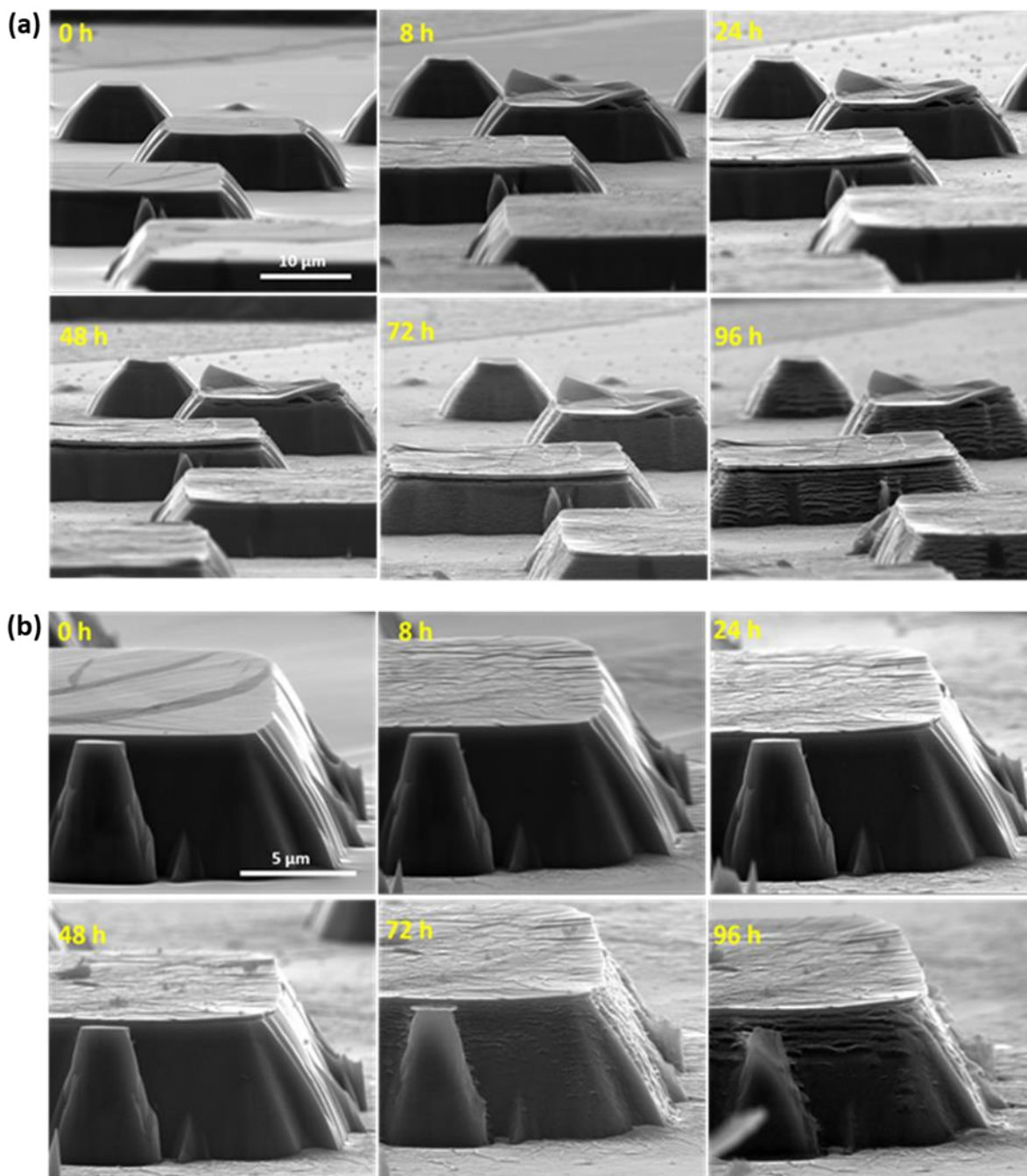


Figure 5.11 82° tilted SEM images of defect-free V_2AlC pillars, in the array (a) and individually in higher magnification (b), as a function of etching time in 49% HF [241].

Generally, except from very few layers on the top surface of some pillars, the penetration of F ions into the Al layers of defect-free pillars was observed between

72 to 96 h of etching. The partial delamination of layers and the formation of the penetration “channels” was easily observed in tilted SEM images (Figure 5.11 (a), (b)). A detailed observation of the defect-free pillars etching was made by top view SEM images in combination with elemental EDS maps and line profiles. OM images and SEM views in BSE mode was taken for a $110 \times 110 \mu\text{m}^2$ pillar with Al EDS maps and elemental line profiles showing the variation of V, Al and F atomic concentrations at different etching time (Figure 5.12 (a)-(f)).

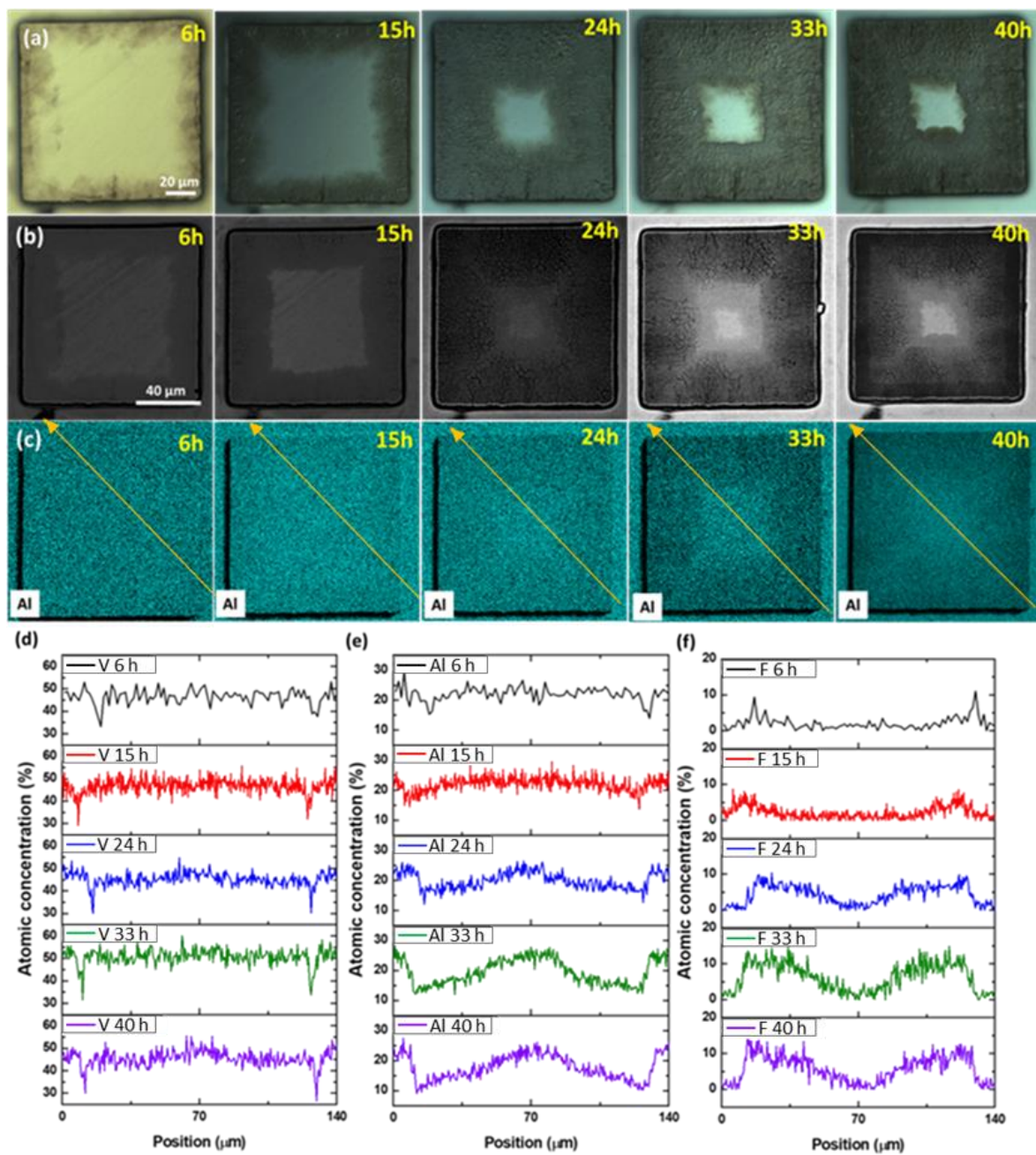


Figure 5.12 (a) OM images, (b) top view SEM images in BSE mode, (c) Al EDS maps of $110 \times 110 \mu\text{m}^2$, defect-free V_2AlC pillar and EDS line profiles of (d) V, (e) Al and (f)

F atomic concentrations at different etching time (yellow arrows in (c) represent the line profiles direction) [241].

Similar to the surface morphology of the 90 x 90 μm² defective pillar (Figure 5.9), the OM views reveal a contrast change, characteristic of Al removal, close to the edges of the pillar that extends towards its center with etching time (Figure 5.12 (a)). Al removal in these regions is confirmed by the BSE SEM images (Figure 5.12 (b)) and Al EDS maps (Figure 5.12 (c)). Hence, like defective pillars, the conversion of MAX phases to MXenes starts from the edges and moves inwards. Nevertheless, the center of the defect-free pillar seemed almost unaffected by the etching process even after 40 h in HF. This partial MXene conversion (Figure 5.12 (a), (b), (c)) is in contrast with the full conversion of defective pillar, observed after 24 h of etching in HF (Figure 5.9 (a), (b), (d)).

Besides the time-dependent quenching of the Al atomic concentration, a progressive depletion of V along the pillar edges has also been observed (Figure 5.12 (d)). In contrast, a substantial increase of the F atomic concentration at the pillar's edges, expanding towards the center with time, was measured (Figure 5.12 (e)). This confirms that chemical etching starts from the edges. Quantifying the presence of oxygen at the chemically converted regions is unfortunately impossible, due to the inevitable adsorbed oxygen-containing layer or native surface oxide formed upon mere exposure to air, as well as to oxygen's small atomic weight and low Kα₁ energy. It is worth noting that all locations, on the pillar surface, where elemental line profiles of V, Al and F were measured, were selected in order to avoid shadowing effects.

Measurements of elemental line profiles on smaller square-size, defect-free pillars indicated a total loss of the Al signal after 15 h of etching, whereas the F atomic concentration reached a homogeneous level throughout the pillar surface (Figure 5.13 (c), (d)). This result suggests that the etched regions are slowly functionalised by F atoms and further confirms that MXene conversion prevalently occurs by edge exposition and not normal to the basal planes [241].

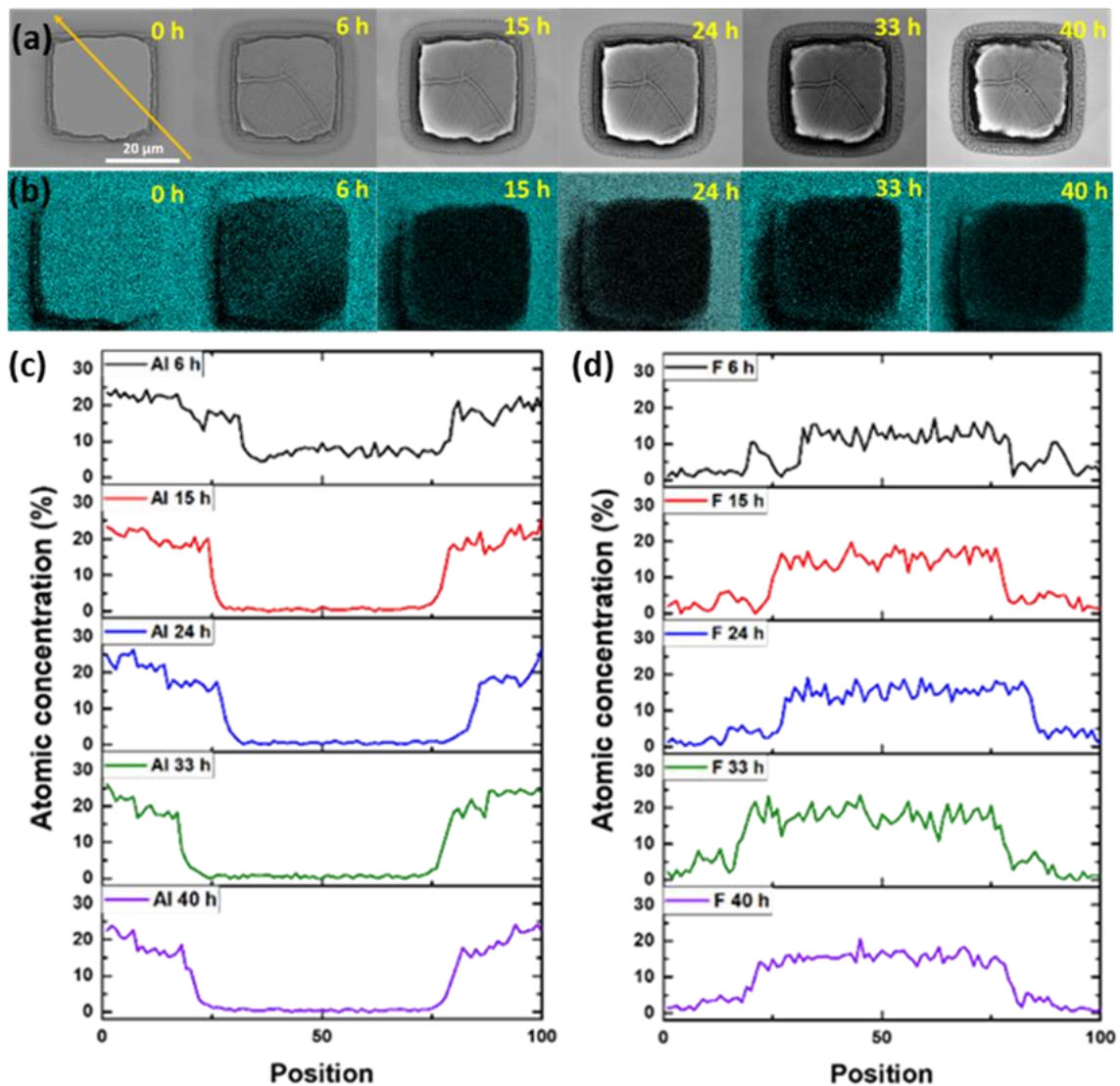


Figure 5.13 (a) Top view SEM images of the surface morphology of a $30 \times 30 \mu\text{m}^2$ pillar as a function of etching time in HF. (b) Al EDS maps with the corresponding elemental concentration (c) and the F concentration (d) measured by EDS line profiles at different etching time (the orange arrow in (a) show the measured profile direction) [241].

Consequently, the defect-free pillars present no substantial inhomogeneities in their etching fronts and no appreciable dependence of the etching rate on the in-plane orientation. As shown in Figure 5.12 and described in the previous section, the perpendicular edges do not exhibit appreciable differences although they were almost aligned to the two extreme possible orientations in the ab plane.

5.3.3 Raman characterization of V₂AlC pillars and etching kinetics quantification

The influence of HF etching in both defective and defect-free pillars as it was assessed through SEM and EDS observations was incomplete. Issues such as the nature of the phase in the etched pillars, the partial or complete conversion of the MAX phase to MXene as well as the occurrence of etching either exclusively along the *ab* planes or partly perpendicular to them, required to use an additional technique. Therefore, to obtain a quantitative analysis of our results, we combined the SEM and EDS observations with micro-Raman spectroscopy.

Using a Jobin Yvon/Horiba Labram spectrometer equipped with a liquid nitrogen cooled CCD detector and an Ar⁺ laser of 488 nm excitation line, power close to 2.5mW and spot size less than 1 μm , we conducted all measurements in the micro-Raman mode in a backscattering geometry and at room temperature. All the Raman modes we observed during our measurements were reported in Table 5.1 where the calculated mode wavenumber positions for V₂AlC and V₂C with all kinds of terminations were also reported.

Table 5.1 Raman wavenumber positions in cm⁻¹ of V₂AlC (experimental and calculated), V₂C-V₂CF₂-V₂C(OH)₂-V₂CF(OH) (calculated) and of 6 h-, 40 h- and 72 h-etched V₂AlC (experimental) [241].

V₂AlC mode symmetry (SG <i>P6₃/mmc</i>)	E_{2g}	E_{1g}	E_{2g}	A_{1g}	
V ₂ AlC exp [this work]	157.5	239	258	~365	
V ₂ AlC exp [246]	158	239	258	360	
V ₂ AlC exp [70]	158	239	259	362	
V ₂ AlC exp [247]	157.4	239.1	257.3	364.2	
V ₂ AlC calc [247]	157	254	255	345	
V₂C mode symmetry (SG <i>P-3m1</i>)		E_g		A_{1g}	
V ₂ C calc [246]		224		359	
V₂CF₂ mode symmetry (SG <i>P-3m1</i>)		E_g	A_{1g}	E_g	A_{1g}
V ₂ CF ₂ calc [246]		198	290	282	526

V₂C(OH)₂ mode symmetry (SG <i>P-3m1</i>)	E_g		A_{1g}	E_g	E_g	A_{1g}			A_{1g}	
V ₂ C(OH) ₂ calc [246]	214		301	297	443	530			3613	
V₂CF(OH) mode symmetry (SG <i>P3m1</i>)	E	E	A₁	E	E	A₁	A₁	A₁	E	A₁
V ₂ CF(OH) calc [246]	196	240	293	297	434	459	534	632	759	3617
6 h etched V₂AlC [this work]	~170	~226	~256	277	~321	~422	~533	~616	~700	
40 h etched V₂AlC [this work]	178	~226	-	287	-	~422	~526	~655	~700	
72 h etched V₂AlC [246]	~170	~230	~270		~430	~540	~650		~3600	

Initially we compared the Raman spectra at two positions on an un-etched pillar (Figure 5.14), at the top of its surface (black curve) and in the trenches between the pillars (red curve). All the Raman modes of V₂AlC [70], [247], [248] are detected on top of the un-etched V₂AlC pillar (E_{2g} modes at 157.5 and 258 cm⁻¹, E_{1g} at 239 cm⁻¹ and A_{1g} at 365 cm⁻¹).

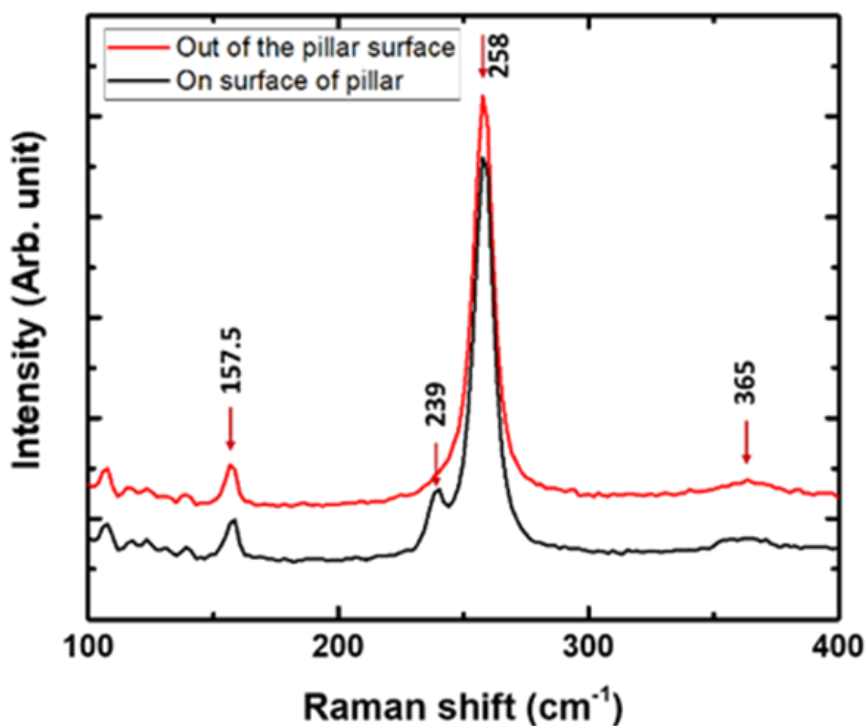


Figure 5.14 Raman spectra measured at the top surface of an un-etched V₂AlC pillar and in the trench area exposed to ICP etching with Cl₂ and BCl₃ reactive gases [241].

In the trenches, where the V₂AlC crystal was exposed to ICP etching, the Raman peak located at 239 cm⁻¹ has almost disappeared, probably due to some minor surface modification of V₂AlC which lead to a decrease of the E_{1g} mode intensity and also produced a small shift in the E_{2g} Raman modes.

Measurements on the converted areas of the pillars as a function of the etching time in HF (6 h, 15 h, 24 h, 33 h and 40 h) showed broad V₂CT_z Raman peaks that were not all affected by the etching time in a similar way (Figure 5.15). Especially, with increasing etching time from 6 h to 40 h, some of the V₂CT_z peaks were shifted (178 to 188 cm⁻¹, 277 to 287 cm⁻¹, 533 to 526 cm⁻¹, 651 to 655 cm⁻¹), others remained unchanged (226, 422, 700 cm⁻¹) while others disappeared or merged (256, 321, 616, 710 cm⁻¹). After 40 h of etching, the spectra are quite similar to those previously reported for V₂CT_z [246] and most of the peaks match well with the calculated Raman modes of terminated V₂CT_z (T = F, OH) MXenes (Table 5.1).

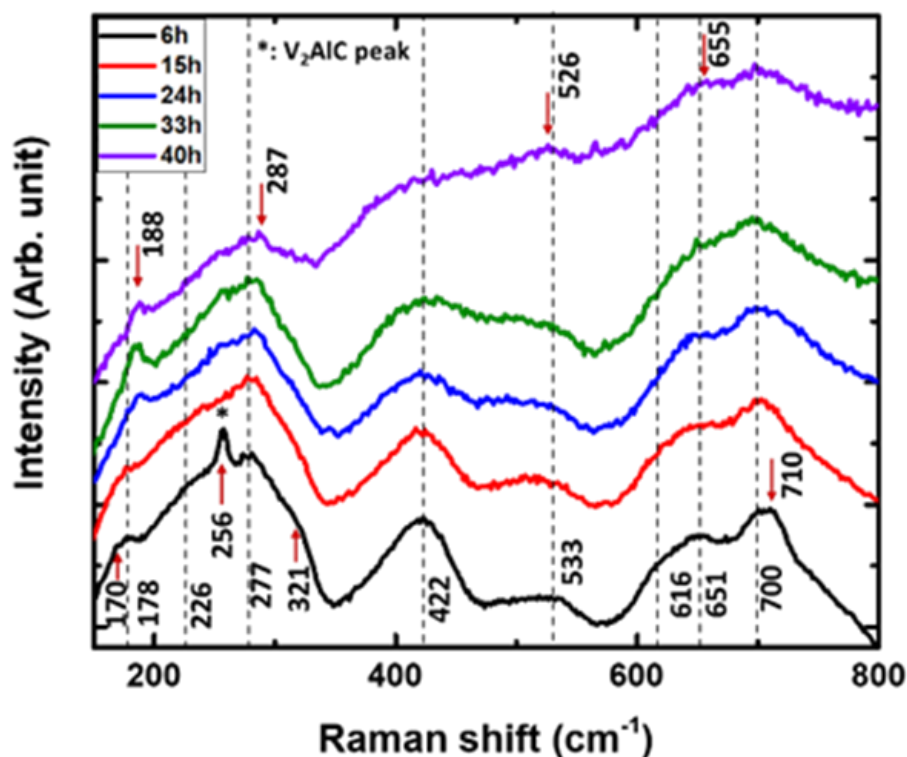


Figure 5.15 Raman spectra measured on a converted V₂CT_z area at different HF etching time (6 h, 15 h, 24 h, 33 h and 40 h) [241].

Here, it should be mentioned that the V₂C surface can accommodate different types of functional groups, which are presumably randomly distributed and can influence the existence and position of the various peaks [246], [249]. Particularly,

the peaks at 188, 655 and 700 cm^{-1} can only be explained by the formation of $V_2CF(OH)$, with F on one side and OH on the other side of the sheets [246]. As seen in Table 5.1 and calculated in Ref. 33, those peaks do not exist in the calculated spectra of V_2C , $V_2C(OH)_2$ or V_2CF_2 . Moreover, the Raman peak located at 256 cm^{-1} could be assigned to a partially un-etched V_2AlC area. This confirms the conversion into MXene and allows us to monitor the Raman signature at a given location as a function of etching time.

Four specific locations on a $110 \times 110 \mu m^2$ defect-free pillar and particularly at its center, in the trench close to the pillar, on the pillar's top surface but around 30 μm from the edge and on the pillar's surface but close to an edge, were used to measure the evolution of the Raman spectra with HF etching time (Figure 5.16 (a)-(d)).

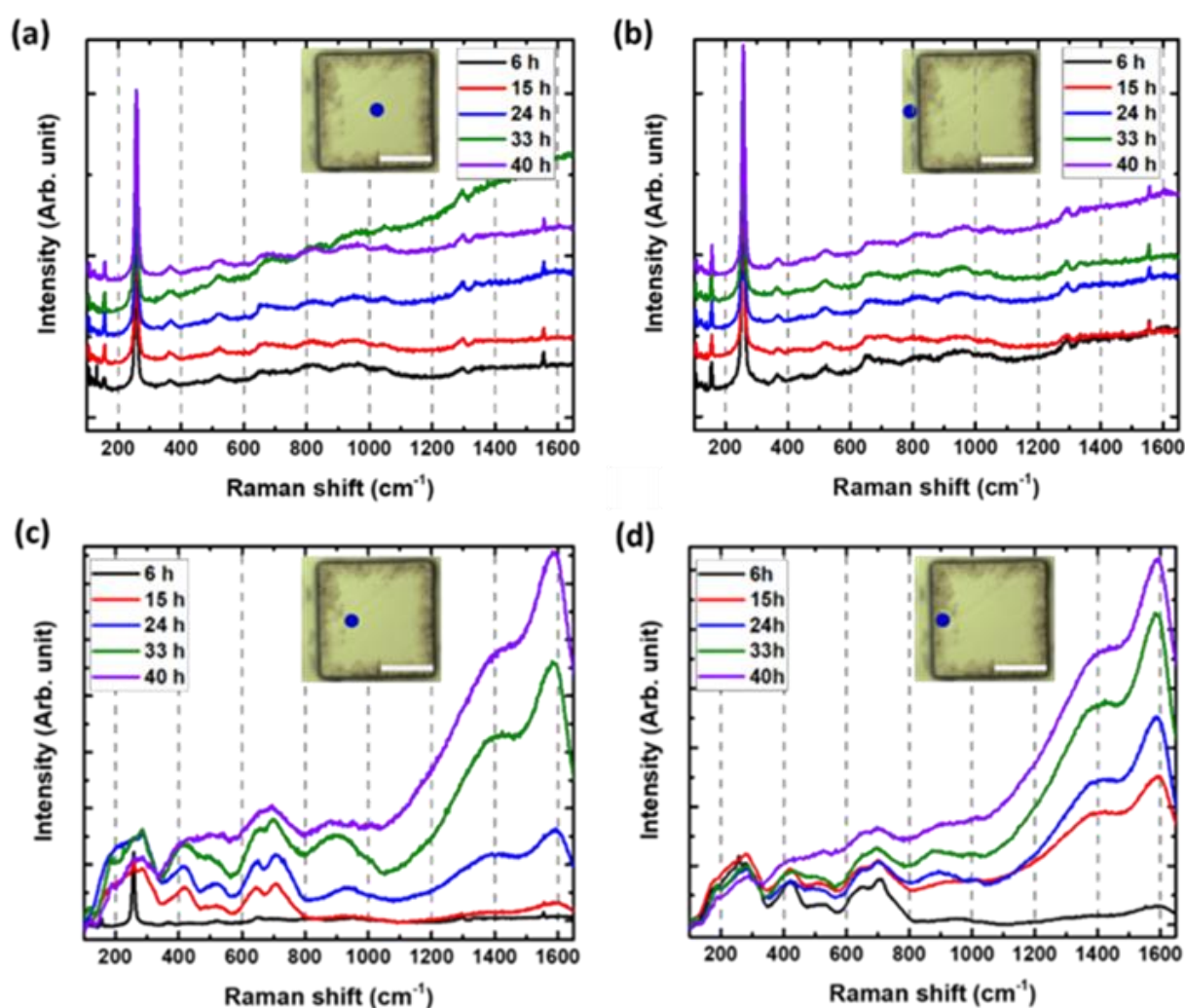
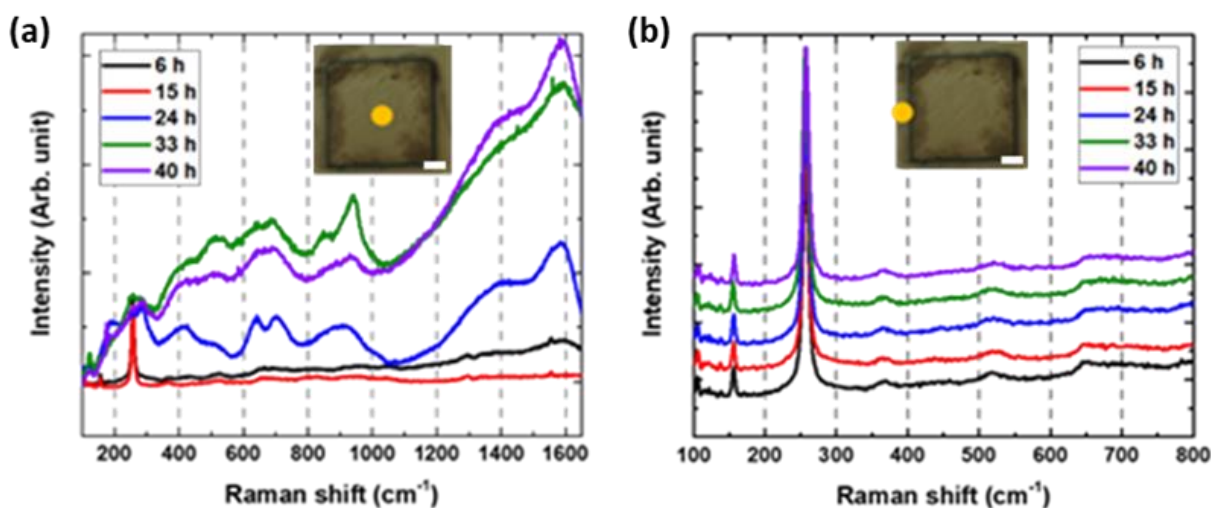


Figure 5.16 Evolution with HF etching time of the Raman spectra of a $110 \times 110 \mu m^2$ defect-free V_2AlC pillar measured (a) at the center of its surface, (b) in the trench

close to the pillar, (c) on the pillar's surface but around 30 μm from the edge and (d) on the pillar's surface very close to the edge. The blue dots in the insets indicate the measurement positions (scale bar = 50 μm) [241].

The spectra in the trench area and the pillar center were identical to those of the original V₂AlC even after 40 h of etching (Figure 5.16 (a), (b)). This is a remarkable finding, since it demonstrated that the HF did not penetrate normal to the *ab* (basal) planes verifying that the pillar's edges should be exposed to the acid for etching to occur. Of great importance is also the evolution of the spectra measured at 30 μm from the edge of the pillar that clearly illustrated the conversion into MXene after 6 h to 15 h of etching (Figure 5.16 (c)). Very close to the edge, the transformation occurs during the first 6 h of etching (Figure 5.16 (d)) indicating thus, an important aspect of V₂CT_z synthesis, especially if purity is key for targeted applications.

Raman measurements as a function of time were also taken for a 90 x 90 μm^2 defective V₂AlC pillar at locations similar to those marked in Figure 5.16. No measurement was taken 30 μm from the edge of the pillar (unlike for larger pillar in Figure 5.16 (c)); instead measurements were performed at the corner of the pillar (Figure 5.17 (c)).



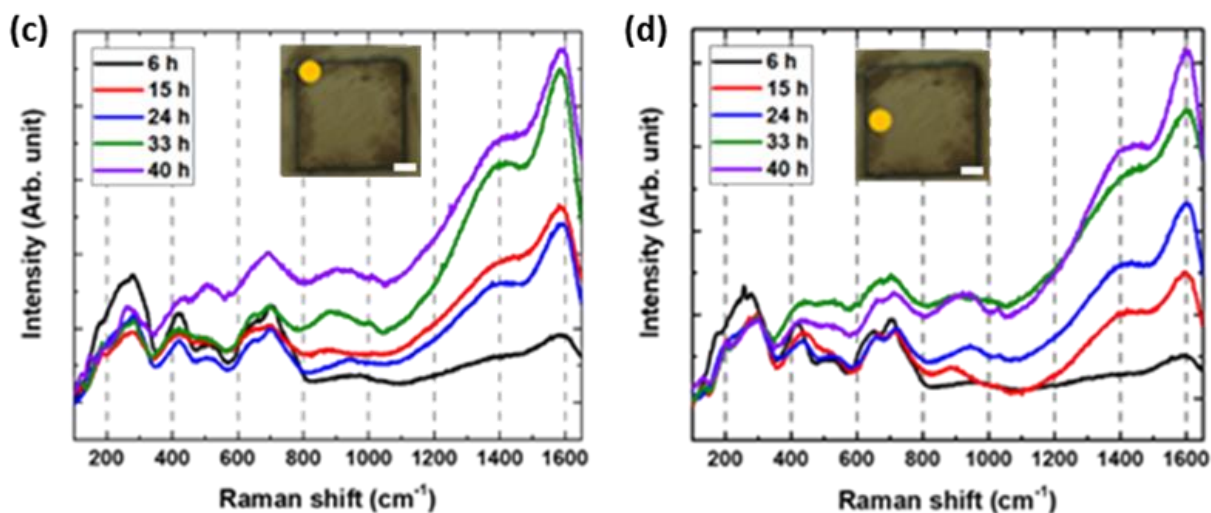


Figure 5.17 Evolution of Raman spectra with HF etching time for a $90 \times 90 \mu\text{m}^2$ defective V₂AlC pillar measured (a) at the center of its surface, (b) in the trench close to the pillar, (c) on the corner of the pillar's surface and (d) on the pillar's surface close to the edge. The orange dots in the insets indicate the measurement positions (scale bar = $20 \mu\text{m}$) [241].

As expected, the spectra in the trench (Figure 5.17 (b)) are similar to those observed in the same location for a defect-free pillar case and identical to that of V₂AlC phase, regardless of the etching time. In accordance to the spectra measured at the edges of a defect-free pillar (Figure 5.16 (d)), those measured both at the edges and the corners of a defective pillar corroborated that independently of the pillar type the MAX-to-MXene conversion occurs at the pillar's edges in the first 6 h of etching (Figure 5.17 (c), (d)). A complete transformation was observed at the center of the defective pillar after 24 h (Figure 5.17 (a)), confirming the SEM, OM and EDS measurements (Figure 5.9 (a), (b), (d)), contrary to the defect-free pillar where not even a partial conversion into MXene was detected after 40 h of etching (Figure 5.16 (a)). Defects and/or internal stresses on the pillar structure hence seem to accelerate chemical etching.

In a $30 \times 30 \mu\text{m}^2$ defect-free pillar, the Raman spectra measured at the trench close to the pillar and the center of its surface (Figure 5.18 (a), (b)) confirmed the aforementioned conclusion that outside of the pillar's surface no MXene conversion occurred while on the pillar's surface the transformation happened between 6 h to 15 h (Figure 5.18 (b)). Once more, the spectra at the center of the pillar's surface

confirmed the initial SEM observations and elemental atomic concentrations deduced from EDS line profiles taken on the same pillar (Figure 5.13).

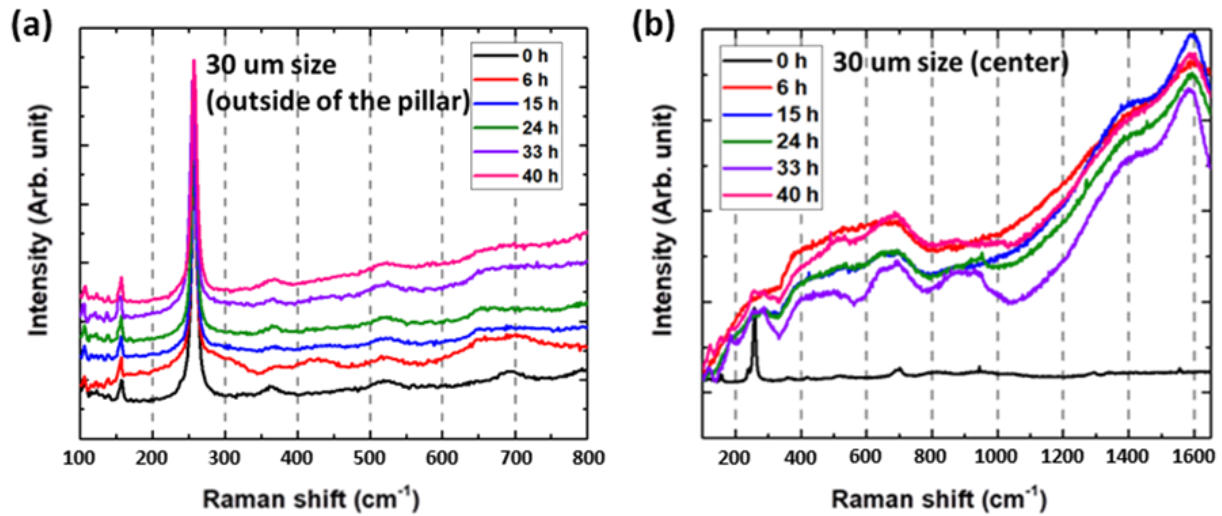


Figure 5.18 Effect of HF etching time on Raman spectra measured (a) in the trench and (b) the center of the surface of the same 30 μm -size defect-free V_2AlC pillar reported to Figure 5.13 [241].

Similar results were obtained from the Raman measurements on a 40 x 40 μm^2 defective V_2AlC pillar made at the same positions versus etching time, as for the defect-free pillar, with the difference that for the defective pillar, total MXene conversion during the first 6 h of HF etching was found (Figure 5.19 (b)). Again, this agrees with the SEM and EDS observations on the same pillar (Figure 5.10).

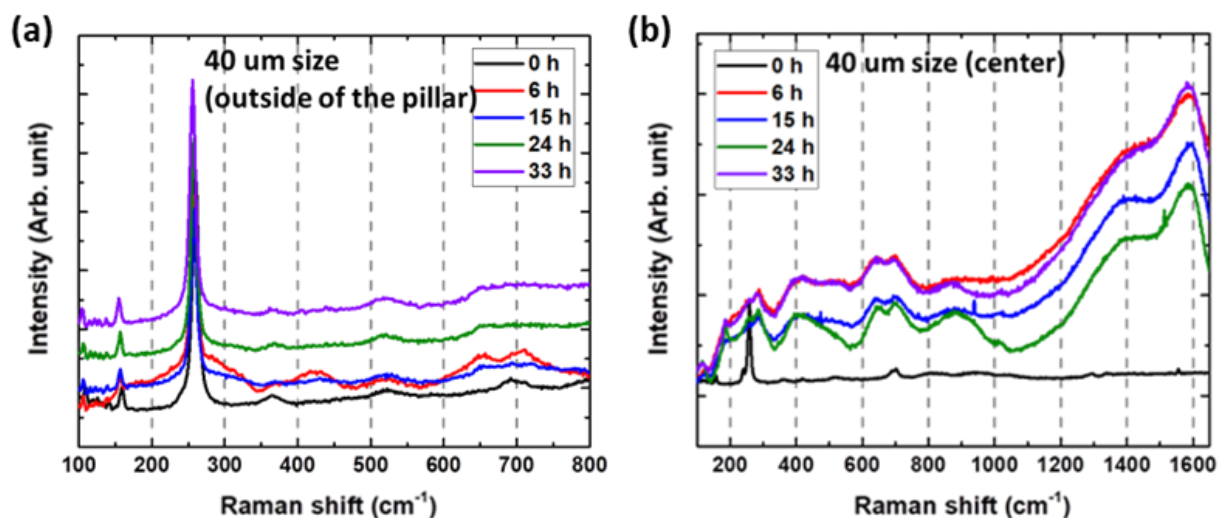


Figure 5.19 Evolution of the Raman spectra with HF etching time measured (a) in the trench and (b) the center of the surface of the 40 μm -size defective V₂AlC pillar also addressed in Figure 5.10 [241].

In all the aforementioned Raman spectra, (defect-free and defective pillars), broad peaks appeared during the MXene transformation on the pillar's surface. Specifically, the carbon peak around 1600 cm^{-1} showed a much higher intensity than the other peaks, for almost all the spectra corresponding to MXene-converted regions. To quantitatively analyse the possible presence of C (non-pure MXene), we compared the Raman intensities of the MXene peak at 287 cm^{-1} and of the carbon peak at 1600 cm^{-1} . The ratio of the two intensities, plotted as a function of etching time at various locations (Figure 5.20 (a)), reveals that partial carbonization takes place at the edge even after etching for 6 h; 10 μm away from the edge, it takes 15 h. After 24 h, the carbon signal largely prevails over that of the MXene in all observed converted parts (Figure 5.20 (b)). In a linear scale, the ratio seems to saturate to negligible values after 15 h (edge) and 24 h (10 μm far from the edge), but a log-log scale shows a continuous decrease (Figure 5.20 (b)) due to the carbonization effect that seems to continuously increase the carbon concentration versus etching time, although at a lower rate. The carbonization results from the dissolution of some V atoms into the etching solution, as it was highlighted by the EDS atomic concentration measurements for V in the case of $110 \times 110\ \mu\text{m}^2$ V₂AlC pillar (Figure 5.12 (d)).

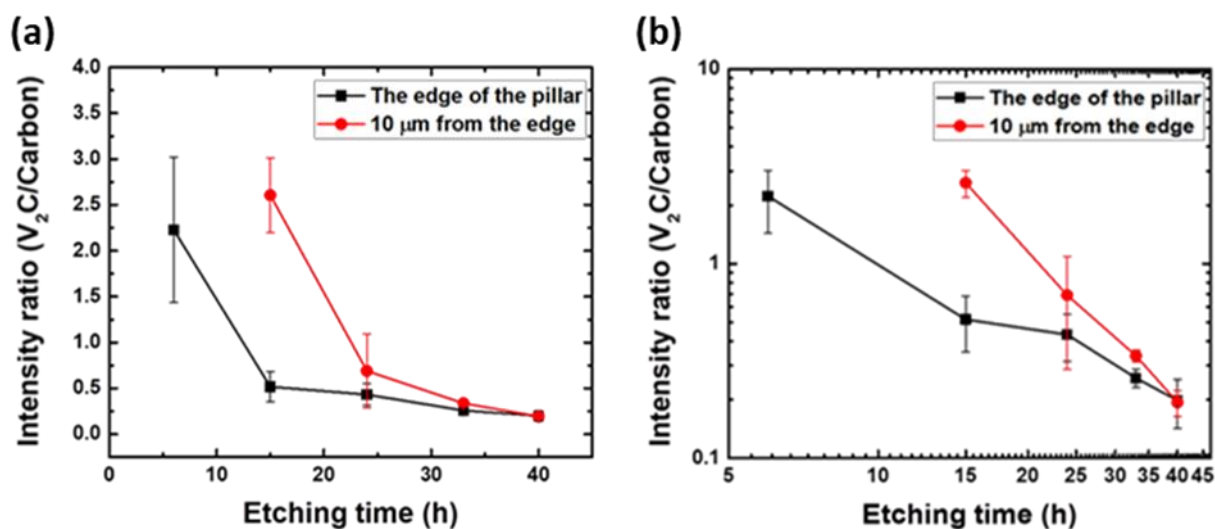


Figure 5.20 (a) Intensity ratio of V₂CT_z (~287 cm⁻¹) to C (~1600 cm⁻¹) Raman peaks after HF etching of defect-free V₂AlC pillars as a function of HF etching time. Each square or circle represents the average of 5 points on a given pillar and error bars represent the standard deviation of many pillars. (b) same graph as in (a) but in a log-log scale [241].

All Raman measurements indicated that the V₂AlC regions that have been converted or transformed by HF etching exhibit the characteristic MXene Raman signature. Therefore, we can safely use Raman spectra to monitor the evolution of the boundary between the converted and non-converted areas. As we have just seen, after etching V₂AlC powders in HF, it is important to measure their Raman spectra and try to quantify any fraction of the material that is carbonized [241].

Our efforts to quantify the HF etching kinetics were focused on observing and recording the progression of the etching front into the pillar as a function of time (Figure 5.21).

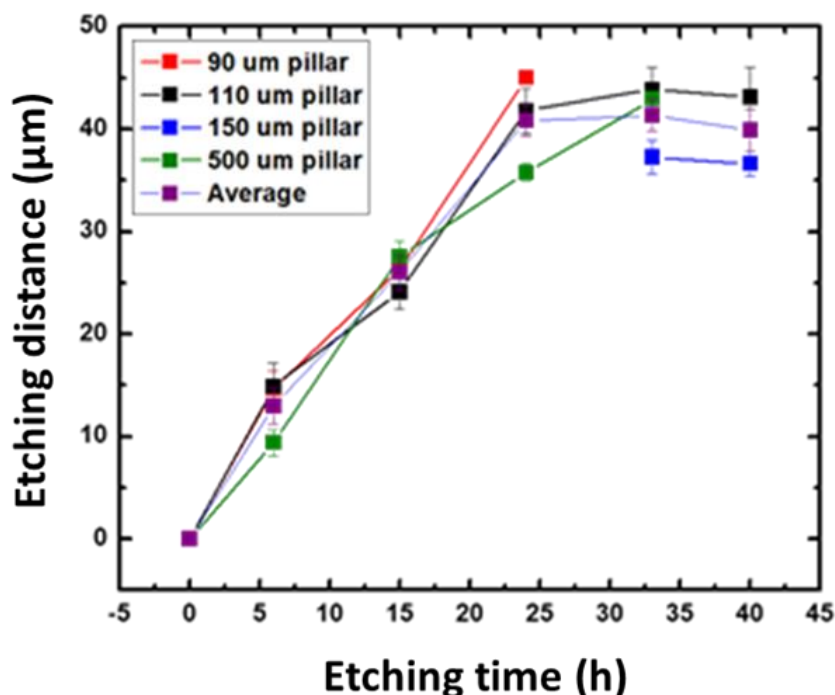


Figure 5.21 Range of etching penetration as a function of HF etching time for 4 defect-free pillars with different sizes. Each square represents an average of 20 points and error bars correspond to the standard deviation. The curve in purple refers to the average etching distance obtained from the values for the different sizes of pillars [241].

As shown in the plot, after a roughly linear increase, a saturation is clearly observed. Especially, up to a penetration depth of around 25 μm , it is reasonable to assume that the reaction rate is controlled by the interface. It is a remarkable conclusion since it implies that diffusional limitations should not play much of a role for powders with particle sizes less than 10 μm . However, this is in contrast with typical etching protocols where etching time for 400 mesh powders ($< 38 \mu\text{m}$) at room temperature is about three days. This can be related to the saturation observed after one day (Figure 5.21), even if the etching progress remains unclear after the linear regime, e.g. whether the process becomes controlled by the diffusion rate or stops totally for unknown reasons. Unfortunately, our data did not allow us to discriminate between the various possible out- and in- diffusion processes, or to identify the diffusing species limiting the chemical conversion process. According to the plot above, the maximum etched distance is obtained after 24 h of etching and is around 40 μm , setting thus an upper bound to the size of a defect-free V₂AlC crystal that can be etched, at around 100 μm . In the linear part at the early stage, the etching rate is around $2.2 \pm 0.3 \mu\text{m/h}$ at 25°C.

We next decided to assess the possibility to etch small, as-grown V₂AlC single crystals and detect their conversion to MXenes through XRD measurements (Figure 5.22). Firstly, we etched a solidified flux in hydrochloric acid (HCl), we properly filtered the crystals and using a sieve shaker of 100, 200, 300 and 500 μm grid sizes we selected various sizes single crystals. For crystals selected by sieve shaking, a lateral crystal size is very frequently smaller than another and if the larger dimension prohibits the crystal separation through the sieve, its smaller dimension makes crystal conversion easier. For instance, a narrow and long crystal is etched as easily as a much smaller crystal having all dimensions similar to the width of the former, larger crystal. Once the crystals selected, they were etched in 49% HF for seven days at room temperature and then tetrabutylammonium hydroxide (TBAOH) was used to complete the delamination process in the centrifugator. Repeated centrifugation steps successfully delaminated the crystals, nonetheless, those steps led to a loss of a large part of the fully converted MXenes while the non-converted crystals with a larger mass remained at the bottom of the container. At the end of the process, the liquid is filtered and the

segregated part is mostly eliminated. The selected samples i.e. non-converted crystals and MXenes are dried and tend to self-organize without however, having exactly the same orientation way.

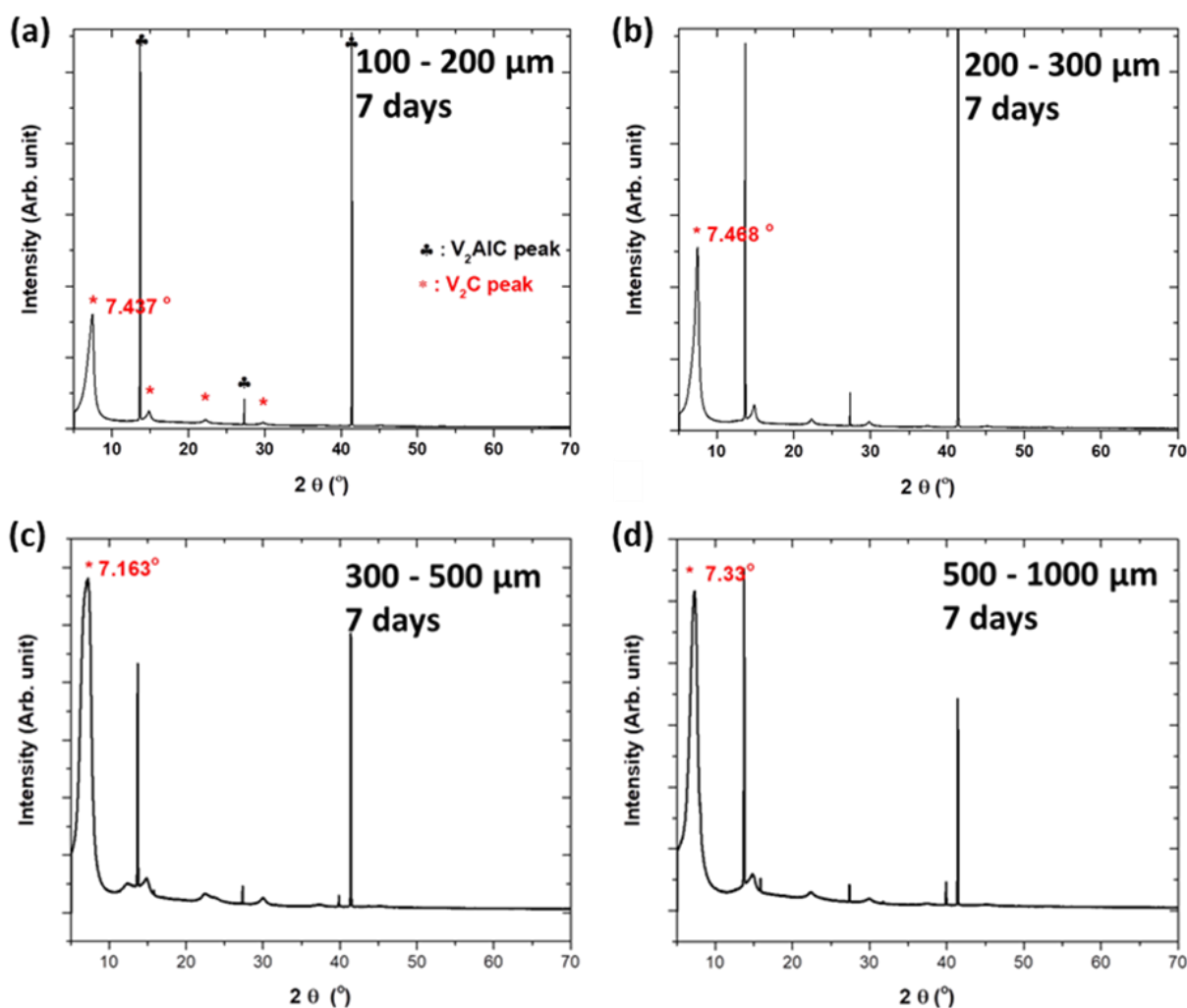


Figure 5.22 XRD patterns of single crystalline V_2AlC powders after etching in 49% HF at room temperature for seven days, sieved by (a) 100 μm , (b) 200 μm , (c) 300 μm and (d) 500 μm size meshes [241].

The powder XRD patterns were measured for ensembles of V_2AlC crystals with a distribution of sizes, e.g. 100 to 200 μm , due to the sieving process implying vertical stacks of sieves of different grid size. In other words, to sort the crystals by size, a 1000 μm grid was placed on top and all other sieves were placed beneath it in a decreasing grid size. Thus, the sieve of 100 μm grid selects crystal sizes from 100 to 200 μm if the sieve above has 200 μm grid size.

XRD spectra indicate a substantial but nevertheless incomplete conversion into MXenes, whatever the etching time duration (up to seven days). Since all crystal sizes ($\geq 100 \mu\text{m}$) were more than twice the maximum etching distance determined in Figure 5.21, it seems to confirm the saturation of the chemical conversion as that observed in the same plot. It is worth mentioning that several factors before and during HF etching can modify the statistics of the finally converted MXenes and thus, the obtained XRD results. First, the irregular size of crystals selected by sieve shaking can easily result in full MXene conversion owing to a small lateral dimension. Another factor is the centrifugation steps which tend to increase the amount of non-fully converted samples as a large amount of fully converted MXenes is lost during centrifugation. Additionally, the liquid filtration at the end of HF etching, where the larger and possibly non-fully converted crystals are eliminated and the drying step in which the self-organization of the selected samples increase the intensity of some XRD peaks, should also be considered. The above factors could be very useful to select a crystal size distribution that would remain colloidal after all centrifugation steps. This may well eliminate not only the larger crystals but also the smaller fully converted ones, to induce more homogeneous results on the different size crystals, as long as their average sizes remain reasonably close to one another [241].

5.4 Conclusion

As a conclusion, the fabrication of V₂AlC single crystalline pillars in various square size array pattern and our study on the MAX-to-MXene transformation, by using chemical etching in 49% HF, as a function of position and time, indicated that etching and thus HF penetration essentially takes place through facets oriented perpendicular to the basal planes, the latter ones being mostly immune to HF penetration. Furthermore, we observed that the etching rate is initially linear, measured at about $2.2 \pm 0.3 \mu\text{m/h}$, but slows down considerably at distances $> 40 \mu\text{m}$ while the HF penetration gradually leads to a partial carbonization of the converted layers that is a major concern once the convertible crystal size needs to be maximized.

Conclusions and prospects

The mechanical exfoliation process based on adhesive (or “scotch”) tape, which was initially applied to graphene, was found to be applicable to other lamellar structures, herein single crystals of MAX and Ce 4473 phases, with stronger inter-layer (metallic) bonds than van der Waals. We exfoliated mechanically, for the first time, Cr_2AlC , V_2AlC , Ti_2SnC and $\text{Mo}_4\text{Ce}_4\text{Al}_7\text{C}_3$ single crystals producing flakes with homogeneous thickness of a few layers to (half-)monolayer (0.5L), achieving thus, the main objective of the thesis. A distinction in the layer sequence between chemically and mechanically exfoliated flakes is that the latter retain either in total or partly the “A” layers in case of the MAX phases, or the Al_7Ce_2 layers in the $\text{Mo}_4\text{Ce}_4\text{Al}_7\text{C}_3$ case. Thus, we refer to our flakes as MAXenes instead of MXenes. Although the yield of mechanically exfoliated flakes was lower than that of chemical exfoliation, the lateral size of few layer thickness flakes was larger, reaching few tens of μm (Chapter 2).

The isolation of very thin flakes paved the way for the characterization of their O-terminated surface and their pristine electrical properties owing to the lack of solvents. The latter are responsible for several surface terminations and structural defects that are induced during chemical etching.

EFM and KPFM probe methods were applied to quantitatively assess the electrical properties of the flakes’ surface based on the tip-flake interactions. The measured phase shift of the mechanically excited oscillation of the cantilever that derived from the tip-sample electrostatic interaction depends on the capacitance contrast probed by EFM and on the contrast due to the contact potential difference detected by KPFM. EFM and KPFM methods probed changes in capacitance contrast and surface potential, respectively, between hydrophobic SiO_2 and MAXenes. The contrast differences between the two surfaces are attributed to a value of parabola curvature ratio (α) of less than unity. The low value of the α ratio that further decreases with reducing the tip-sample distance demonstrated the

metallic nature of the MAXene flakes, which is retained to the thinnest ones (Chapter 4).

STM technique was necessary to obtain detailed insights into the influence of mechanical exfoliation on the structure of cleaved MAX phases. Large scale areas of the cleaved Cr_2AlC surface scanned in UHV revealed two segregated regions with different apparent heights. Considering that the largest contribution to the density of states at the Fermi level derives from the d -orbitals of Cr atoms, we attributed the regions of large apparent height to Cr-rich surfaces and the lower ones to disordered Al or Al-O clusters. Atomic resolution images highlighted the preservation of the hcp lattice in the former areas (Chapter 4).

Al clusters on the surface of mechanically exfoliated MAXene flakes are prone to oxidation. This occurs directly after the exfoliation process, an unavoidable drawback to the fabrication of ohmic contacts. Notwithstanding the flake oxidation, MAXenes from all phases studied in this thesis were processed into devices and their electrical characteristics were measured with four-point probes method (Chapter 4). The linearity of plotted I-V curves for MAXene devices presented in this thesis demonstrated the ohmic behavior of their contacts. However, despite an improvement of the contact resistance owing to high vacuum annealing at 350°C for a few hours, both the contact and four-probes resistance remained in the range of $\text{k}\Omega$.

The linear increase of resistivity as a function of the temperature is an evidence of the metallic character of the flake that is maintained down to 208 K. Below this temperature the measurements indicated contacts without ohmic behavior with the presence of glue residues on the flake's surface being a possible explanation. The resistivity value at 300 K was in excellent agreement with that of the bulk phase. Furthermore, an abnormal increase of the apparent resistivity was also recorded versus the flake thickness for all studied phases except for V_2AlC . Such an increase is possibly explained by the partial delamination of intermediate layers and/or high transport anisotropy of some phases, from which it can be deduced that the measured resistivity value of the thinnest flake is more representative of the true resistivity value (Chapter 4).

Al layers can be fully separated from "M" layers in MAX phases using chemical etching in e.g. an HF solution. Our kinetics study of MAX-to-MXene conversion on

a well-defined crystallographic structure and orientation shed light on some key aspects of chemical exfoliation which had not been explained so far in the analysis of MXenes produced from MAX powders, whose structure is much less well-defined.

The fabrication of various square-size V_2AlC pillars was based on a recipe we developed in our lab, starting from centimeter-sized V_2AlC single crystals (Chapter 5). The etching of pillars in a solution of 49% HF was found to occur following a preferred direction of HF penetration through the pillars' facets that are perpendicularly oriented with respect to their basal planes. A roughly linear increase of the etching rate as a function of time was observed for the first 24 h, which led to an approximate penetration depth of 40 μm , and then a saturation level was reached. Additionally, it was evidenced that HF etching affected the V-C bonds mainly at the pillars' edges favoring partial dissolution of V atoms into the acid solution and thus resulting in partial carbonization, even after few hours of etching (Chapter 5).

The partial carbonization of MXenes remains a major problem in chemical exfoliation of MAX phases that needs to be solved in order to maximize the convertible crystal size of the latter. An increase on the size of etched crystals, could yield chemically exfoliated MXene flakes of large lateral dimensions.

In the case of mechanical exfoliation, the glue residues left by the adhesive tape on the flakes' surface after their transfer on substrates is one of the main issues that has to be handled to improve ohmic contacts. In spite of our various efforts (Chapter 2), only part of them was eventually removed from flakes.

Besides, the presence of Al onto the surface of mechanically exfoliated flakes renders them vulnerable to oxidation. Additionally, the conservation of Al layers in the structure of MAXenes probably renders the edges of the flakes also prone to oxidation, intensifying thus the problem, as both top and side "bad" contacts of a MAXene device can prevent from measuring high conductivity.

Further work on the aforementioned problems is required to overcome them. A possible route to eliminate the influence of flakes oxidation and glue residues on the flakes' resistivity is the fabrication of "edge" contacts. A more complex process including additional steps, such as Ar plasma etching and metal deposition at an angle in UHV, could be applied to form contacts only at the edges of flakes [238],

thus ensuring a contribution to conductivity from the overall thickness of the flake. This approach could improve electronic transport in MAXene devices rendering them possible good candidates for the next generation interconnects [239].

The presence of Al layers in the structure of the rare earth based phases, as in the case of $\text{Mo}_4\text{Ce}_4\text{Al}_7\text{C}_3$ single crystals, opens a discussion on magnetic applications. This quaternary phase is ferromagnetic at $T < 10$ K [74] which is attributed to the ordered honeycomb sublattice of the interleaved Ce plane between two Al layers in the crystal structure. Specifically, it has been demonstrated that the ferromagnetism of the $\text{Mo}_4\text{Ce}_4\text{Al}_7\text{C}_3$ phase derives from the $4f^1$ electronic configuration of the Ce atoms [250]. Therefore, mechanical exfoliation, which retains the Al layers could be well-suited to investigate ferromagnetism of the Ce 4473 phase as a function of flake thickness.

Last but not least, MAXene flakes could exhibit controllable and desirable surface terminations. Contrary to MXenes that derive from chemical exfoliation where interactions with chemical etchants render the flakes' surface prone to termination with species imposed by the most electronegative element of the used acid e.g. -F, -Cl, in combination with O and/or OH, most MAXenes are O-terminated mainly due to Al oxidation. Using a dry etching process to remove any unwanted oxidation layer and an atomic layer deposition (ALD) set-up to control the thickness of the deposited layer, both processes in HV/UHV conditions, various terminations could be formed on the surface of the flakes that could tune the electrical properties of MAXene devices. In addition, this prospect favors the formation of surface terminations on flakes' surface that derive from MAX phases, which either cannot be chemically etched, such as Ti_2SnC or their "M" element dissolves during chemical etching e.g. Cr_2AlC .

Bibliography

- [1] V. H. Nowotny, 'Strukturchemie einiger Verbindungen der Übergangsmetalle mit den elementen C, Si, Ge, Sn', *Prog. Solid State Chem.*, vol. 5, no. C, pp. 27–70, 1971, doi: 10.1016/0079-6786(71)90016-1.
- [2] J. C. Schuster and V. H. NOWOTNY, 'INVESTIGATIONS OF THE TERNARY SYSTEMS (ZR, HF, NB, TA)-AL-C AND STUDIES ON COMPLEX CARBIDES', *Z.METALLKD*, vol. 71, pp. 341–346, 1980.
- [3] C. J. Rawn, M. W. Barsoum, T. El-raghy, and A. Procipio, 'Structure of Ti_4AlN_3 —a layered M', vol. 35, no. 2000, pp. 1785–1796, 2008.
- [4] B. Manoun, S. K. Saxena, T. El-Raghy, and M. W. Barsoum, 'High-pressure x-ray diffraction study of Ta_4AlC_3 ', *Appl. Phys. Lett.*, vol. 88, no. 20, pp. 2004–2007, 2006, doi: 10.1063/1.2202387.
- [5] C. Hu, F. Li, J. Zhang, J. Wang, J. Wang, and Y. Zhou, 'Nb $_4$ AlC $_3$: A new compound belonging to the MAX phases', *Scr. Mater.*, vol. 57, no. 10, pp. 893–896, 2007, doi: 10.1016/j.scriptamat.2007.07.038.
- [6] J. Etzkorn, M. Ade, D. Kotzott, M. Kleczek, and H. Hillebrecht, 'Ti $_2$ GaC, Ti $_4$ GaC $_3$ and Cr $_2$ GaC-Synthesis, crystal growth and structure analysis of Ga-containing MAX-phases $M_{n+1}GaC_n$ with M=Ti, Cr and n=1, 3', *J. Solid State Chem.*, vol. 182, no. 5, pp. 995–1002, 2009, doi: 10.1016/j.jssc.2009.01.003.
- [7] J. P. Palmquist *et al.*, 'Mn $_{n+1}$ AX $_n$ phases in the Ti-Si-C system studied by thin-film synthesis and ab initio calculations [74]', *Phys. Rev. B - Condens. Matter Mater. Phys.*, vol. 70, no. 16, pp. 1–13, 2004, doi: 10.1103/PhysRevB.70.165401.
- [8] N. J. Lane, M. Naguib, J. Lu, L. Hultman, and M. W. Barsoum, 'Structure of a new bulk Ti $_5$ Al $_2$ C $_3$ MAX phase produced by the topotactic transformation of Ti $_2$ AlC', *J. Eur. Ceram. Soc.*, vol. 32, no. 12, pp. 3485–3491, 2012, doi: 10.1016/j.jeurceramsoc.2012.03.035.
- [9] T. Lapauw *et al.*, 'Synthesis of the new MAX phase Zr $_2$ AlC', *J. Eur. Ceram. Soc.*, vol. 36, no. 8, pp. 1847–1853, 2016, doi: 10.1016/j.jeurceramsoc.2016.02.044.

- [10] M. A. Pietzka and J. C. Schuster, 'Summary of constitutional data on the Aluminum-Carbon-Titanium system', *J. Phase Equilibria*, vol. 15, no. 4, pp. 392–400, 1994, doi: 10.1007/BF02647559.
- [11] Z. Lin, M. Zhuo, Y. Zhou, M. Li, and J. Wang, 'Microstructures and theoretical bulk modulus of layered ternary tantalum aluminum carbides', *J. Am. Ceram. Soc.*, vol. 89, no. 12, pp. 3765–3769, 2006, doi: 10.1111/j.1551-2916.2006.01303.x.
- [12] T. Lapauw *et al.*, 'Synthesis of the novel Zr₃AlC₂ MAX phase', *J. Eur. Ceram. Soc.*, vol. 36, no. 3, pp. 943–947, 2016, doi: 10.1016/j.jeurceramsoc.2015.10.011.
- [13] T. Lapauw *et al.*, 'Synthesis of MAX Phases in the Hf-Al-C System', *Inorg. Chem.*, vol. 55, no. 21, pp. 10922–10927, 2016, doi: 10.1021/acs.inorgchem.6b01398.
- [14] C. Hu, J. Zhang, J. Wang, F. Li, J. Wang, and Y. Zhou, 'Crystal structure of V₄AlC₃: A new layered ternary carbide', *J. Am. Ceram. Soc.*, vol. 91, no. 2, pp. 636–639, 2008, doi: 10.1111/j.1551-2916.2007.02136.x.
- [15] J. Etzkorn, M. Ade, and H. Hillebrecht, 'V₂AlC, V₄AlC_{3-x} (x ≈ 0.31), and V₁₂Al₃C₈: Synthesis, crystal growth, structure, and superstructure', *Inorg. Chem.*, vol. 46, no. 18, pp. 7646–7653, 2007, doi: 10.1021/ic700382y.
- [16] X. Wang *et al.*, 'Ti₅Al₂C₃: A new ternary carbide belonging to MAX phases in the Ti - Al - C system', *J. Am. Ceram. Soc.*, vol. 95, no. 5, pp. 1508–1510, 2012, doi: 10.1111/j.1551-2916.2012.05158.x.
- [17] A. S. Ingason *et al.*, 'A nanolaminated magnetic phase: Mn₂GaC', *Mater. Res. Lett.*, vol. 2, no. 2, pp. 89–93, 2017, doi: 10.1080/21663831.2013.865105.
- [18] M. W. Barsoum, 'The MN_nAX_n phases: A new class of solids', *Prog. Solid State Chem.*, vol. 28, no. 1–4, pp. 201–281, 2000, doi: 10.1016/s0079-6786(00)00006-6.
- [19] D. T. Cuskelly, E. R. Richards, E. H. Kisi, and V. J. Keast, 'Ti₃GaC₂ and Ti₃InC₂: First bulk synthesis, DFT stability calculations and structural systematics', *J. Solid State Chem.*, vol. 230, pp. 418–425, 2015, doi: 10.1016/j.jssc.2015.07.028.
- [20] P. Eklund *et al.*, 'Discovery of the ternary nanolaminated compound Nb₂GeC by a systematic theoretical-experimental approach', *Phys. Rev. Lett.*, vol. 109, no. 3, 2012, doi: 10.1103/PhysRevLett.109.035502.
- [21] H. Högberg, P. Eklund, J. Emmerlich, J. Birch, and L. Hultman, 'Epitaxial Ti₂GeC, Ti₃GeC₂, and Ti₄GeC₃ MAX-phase thin films grown by magnetron

- sputtering', *J. Mater. Res.*, vol. 20, no. 4, pp. 779–782, 2005, doi: 10.1557/JMR.2005.0105.
- [22] M. A. Hadi, N. Kelaidis, S. H. Naqib, A. Chroneos, and A. K. M. A. Islam, 'Mechanical behaviors, lattice thermal conductivity and vibrational properties of a new MAX phase Lu₂SnC', *J. Phys. Chem. Solids*, vol. 129, no. December 2018, pp. 162–171, 2019, doi: 10.1016/j.jpcs.2019.01.009.
- [23] M. Barsoum and T. El-Raghy, 'The MAX Phases: Unique New Carbide and Nitride Materials', *Am. Sci.*, vol. 89, no. 4, p. 334, 2001, doi: 10.1511/2001.4.334.
- [24] M. Li *et al.*, 'Element Replacement Approach by Reaction with Lewis Acidic Molten Salts to Synthesize Nanolaminated MAX Phases and MXenes', *J. Am. Chem. Soc.*, vol. 141, no. 11, pp. 4730–4737, 2019, doi: 10.1021/jacs.9b00574.
- [25] T. Lapauw, B. Tunca, T. Cabioc'h, J. Vleugels, and K. Lambrinou, 'Reactive spark plasma sintering of Ti₃SnC₂, Zr₃SnC₂ and Hf₃SnC₂ using Fe, Co or Ni additives', *J. Eur. Ceram. Soc.*, vol. 37, no. 15, pp. 4539–4545, 2017, doi: 10.1016/j.jeurceramsoc.2017.06.041.
- [26] J. Zhang, B. Liu, J. Y. Wang, and Y. C. Zhou, 'Low-temperature instability of Ti₂SnC: A combined transmission electron microscopy, differential scanning calorimetry, and x-ray diffraction investigations', *J. Mater. Res.*, vol. 24, no. 1, pp. 39–49, 2009, doi: 10.1557/jmr.2009.0012.
- [27] M. W. Barsoum, J. Golczewski, H. J. Seifert, and F. Aldinger, 'Fabrication and electrical and thermal properties of Ti₂InC, Hf₂InC and (Ti,Hf)₂InC', *J. Alloys Compd.*, vol. 340, no. 1–2, pp. 173–179, 2002, doi: 10.1016/S0925-8388(02)00107-X.
- [28] C. C. Lai *et al.*, 'Phase formation of nanolaminated Mo₂AuC and Mo₂(Au_{1-x}Ga_x)₂C by a substitutional reaction within Au-capped Mo₂GaC and Mo₂Ga₂C thin films', *Nanoscale*, vol. 9, no. 45, pp. 17681–17687, 2017, doi: 10.1039/c7nr03663a.
- [29] H. Fashandi *et al.*, 'Synthesis of Ti₃AuC₂, Ti₃Au₂C₂ and Ti₃IrC₂ by noble metal substitution reaction in Ti₃SiC₂ for high-temperature-stable Ohmic contacts to SiC', *Nat. Mater.*, vol. 16, no. 8, pp. 814–818, 2017, doi: 10.1038/nmat4896.
- [30] M. W. Barsoum, *MAX Phases: Properties of Machinable Ternary Carbides and Nitrides*. 2013.

- [31] M. Sokol, V. Natu, S. Kota, and M. W. Barsoum, 'On the Chemical Diversity of the MAX Phases', *Trends in Chemistry*, vol. 1, no. 2. pp. 210–223, 2019, doi: 10.1016/j.trechm.2019.02.016.
- [32] M. Magnuson and M. Mattesini, 'Chemical bonding and electronic-structure in MAX phases as viewed by X-ray spectroscopy and density functional theory', *Thin Solid Films*, vol. 621, no. November, pp. 108–130, 2017, doi: 10.1016/j.tsf.2016.11.005.
- [33] M. Łopaciński, J. Puszynski, and J. Lis, 'Synthesis of Ternary Titanium Aluminum Carbides Using Self-Propagating High-Temperature Synthesis Technique', *J. Am. Ceram. Soc.*, vol. 84, no. 12, pp. 3051–3053, 2001, doi: 10.1111/j.1151-2916.2001.tb01138.x.
- [34] C. L. Yeh and Y. G. Shen, 'Effects of TiC and Al₄C₃ addition on combustion synthesis of Ti₂AlC', *J. Alloys Compd.*, vol. 470, no. 1–2, pp. 424–428, 2009, doi: 10.1016/j.jallcom.2008.02.086.
- [35] S. Zhimei, Z. Yi, and Z. Yanchun, 'SYNTHESIS OF Ti₃SiC₂ POWDERS BY A SOLID-LIQUID', *Scr. Mater.*, vol. 41, no. 1, pp. 61–66, 1999.
- [36] H. Y. Dong, C. K. Yan, S. Q. Chen, and Y. C. Zhou, 'Solid-liquid reaction synthesis and thermal stability of Ti₂SnC powders', *J. Mater. Chem.*, vol. 11, no. 5, pp. 1402–1407, 2001, doi: 10.1039/b008973g.
- [37] J. F. Li, T. Matsuki, and R. Watanabe, 'Fabrication of highly dense Ti₃SiC₂ ceramics by pressureless sintering of mechanically alloyed elemental powders', *J. Mater. Sci.*, vol. 38, no. 12, pp. 2661–2666, 2003, doi: 10.1023/A:1024490720287.
- [38] S. B. Li, H. X. Zhai, G. P. Bei, Y. Zhou, and Z. L. Zhang, 'Synthesis and microstructure of Ti₃AlC₂ by mechanically activated sintering of elemental powders', *Ceram. Int.*, vol. 33, no. 2, pp. 169–173, 2007, doi: 10.1016/j.ceramint.2005.07.024.
- [39] S. B. Li, G. P. Bei, H. X. Zhai, and Y. Zhou, 'Synthesis of Ti₂SnC from Ti/Sn/TiC powder mixtures by pressureless sintering technique', *Mater. Lett.*, vol. 60, no. 29–30, pp. 3530–3532, 2006, doi: 10.1016/j.matlet.2006.03.045.
- [40] S. B. Li, G. P. Bei, H. X. Zhai, and Y. Zhou, 'Bimodal microstructure and reaction mechanism of Ti₂SnC synthesized by a high-temperature reaction using Ti/Sn/C and Ti/Sn/TiC powder compacts', *J. Am. Ceram. Soc.*, vol. 89, no. 12, pp. 3617–

- 3623, 2006, doi: 10.1111/j.1551-2916.2006.01275.x.
- [41] B. B. Panigrahi, M. C. Chu, A. Balakrishnan, and S. J. Cho, 'Synthesis and pressureless sintering of Ti₃SiC₂ powder', *J. Mater. Res.*, vol. 24, no. 2, pp. 487–492, 2009, doi: 10.1557/jmr.2009.0063.
- [42] S. Yang, Z. M. Sun, H. Hashimoto, and T. Abe, 'Synthesis of single-phase Ti₃SiC₂ powder', *J. Eur. Ceram. Soc.*, vol. 23, no. 16, pp. 3147–3152, 2003, doi: 10.1016/S0955-2219(03)00096-7.
- [43] M. W. Barsoum and T. El-Raghy, 'Synthesis and characterization of a remarkable ceramic: Ti₃SiC₂', *Journal of the American Ceramic Society*, vol. 79, no. 7. pp. 1953–1956, 1996, doi: 10.1111/j.1151-2916.1996.tb08018.x.
- [44] W. Zhang, N. Travitzky, C. Hu, Y. Zhou, and P. Greil, 'Reactive hot pressing and properties of Nb₂AlC', *J. Am. Ceram. Soc.*, vol. 92, no. 10, pp. 2396–2399, 2009, doi: 10.1111/j.1551-2916.2009.03187.x.
- [45] Y. Zhou, H. Dong, X. Wang, and C. Yan, 'Preparation of Ti₂SnC by solid-liquid reaction synthesis and simultaneous densification method', *Mater. Res. Innov.*, vol. 6, no. 5–6, pp. 219–225, 2002, doi: 10.1007/s10019-002-0200-8.
- [46] Y. Zhou, Z. Sun, S. Chen, and Y. Zhang, 'In-situ hot pressing/solid-liquid reaction synthesis of dense titanium silicon carbide bulk ceramics', *Mater. Res. Innov.*, vol. 2, no. 3, pp. 142–146, 1998, doi: 10.1007/s100190050076.
- [47] W. Tian, P. Wang, G. Zhang, Y. Kan, Y. Li, and D. Yan, 'Synthesis and thermal and electrical properties of bulk Cr₂AlC', *Scr. Mater.*, vol. 54, no. 5, pp. 841–846, 2006, doi: 10.1016/j.scriptamat.2005.11.009.
- [48] M. W. Barsoum, G. Yaroshuk, and S. Tyagi, 'Fabrication and characterization of M₂SnC (M = Ti, Zr, Hf and Nb)', *Scr. Mater.*, vol. 37, no. 10, pp. 1583–1591, 1997, doi: 10.1016/S1359-6462(97)00288-1.
- [49] S. Dubois, T. Cabioch, P. Chartier, V. Gauthier, and M. Jaouen, 'A new ternary nanolaminate carbide: Ti₃SnC₂', *J. Am. Ceram. Soc.*, vol. 90, no. 8, pp. 2642–2644, 2007, doi: 10.1111/j.1551-2916.2007.01766.x.
- [50] T. El-Raghy, S. Chakraborty, and M. W. Barsoum, 'Synthesis and characterization of Hf₂PbC, Zr₂PbC and M₂SnC (M = Ti, Hf, Nb or Zr)', *J. Eur. Ceram. Soc.*, vol. 20, no. 14–15, pp. 2619–2625, 2000, doi: 10.1016/S0955-2219(00)00127-8.

- [51] T. El-Raghy and M. W. Barsoum, 'Processing and Mechanical Properties of Ti₃SiC₂: I, Reaction Path and Microstructure Evolution', *J. Am. Ceram. Soc.*, vol. 82, no. 10, pp. 2849–2854, 2004, doi: 10.1111/j.1151-2916.1999.tb02166.x.
- [52] Z. Sun, H. Hashimoto, W. Tian, and Y. Zou, 'Synthesis of the MAX phases by pulse discharge sintering', *Int. J. Appl. Ceram. Technol.*, vol. 7, no. 6, pp. 704–718, 2010, doi: 10.1111/j.1744-7402.2010.02555.x.
- [53] D. M. Hulbert, A. Anders, J. Andersson, E. J. Lavernia, and A. K. Mukherjee, 'A discussion on the absence of plasma in spark plasma sintering', *Scr. Mater.*, vol. 60, no. 10, pp. 835–838, 2009, doi: 10.1016/j.scriptamat.2008.12.059.
- [54] W. Tian *et al.*, 'Synthesis and characterization of Cr₂AlC ceramics prepared by spark plasma sintering', *Mater. Lett.*, vol. 61, no. 22, pp. 4442–4445, 2007, doi: 10.1016/j.matlet.2007.02.023.
- [55] S. Jacques, H. Di-Murro, M. P. Berthet, and H. Vincent, 'Pulsed reactive chemical vapor deposition in the C-Ti-Si system from H₂/TiCl₄/SiCl₄', *Thin Solid Films*, vol. 478, no. 1–2, pp. 13–20, 2005, doi: 10.1016/j.tsf.2004.09.043.
- [56] J. P. Palmquist *et al.*, 'Magnetron sputtered epitaxial single-phase Ti₃SiC₂ thin films', *Appl. Phys. Lett.*, vol. 81, no. 5, pp. 835–837, 2002, doi: 10.1063/1.1494865.
- [57] P. Eklund, M. Beckers, J. Frodelius, H. Högberg, and L. Hultman, 'Magnetron sputtering of Ti₃SiC₂ thin films from a compound target', *J. Vac. Sci. Technol. A Vacuum, Surfaces, Film.*, vol. 25, no. 5, p. 1381, 2007, doi: 10.1116/1.2757178.
- [58] P. Eklund *et al.*, 'Homoepitaxial growth of Ti-Si-C MAX-phase thin films on bulk Ti₃SiC₂ substrates', *J. Cryst. Growth*, vol. 304, no. 1, pp. 264–269, 2007, doi: 10.1016/j.jcrysgro.2007.02.014.
- [59] J. Rośn, L. Ryves, P. O. Persson, and M. M. M. Bilek, 'Deposition of epitaxial Ti₂AlC thin films by pulsed cathodic arc', *J. Appl. Phys.*, vol. 101, no. 5, pp. 2006–2007, 2007, doi: 10.1063/1.2709571.
- [60] J. J. Hu, J. E. Bultman, S. Patton, J. S. Zabinski, and T. Ti, 'Pulsed laser deposition and properties of M', *Tribol. Lett.*, vol. 16, no. 1–2, pp. 113–122, 2004.
- [61] C. Höglund, M. Beckers, N. Schell, J. V. Borany, J. Birch, and L. Hultman, 'Topotaxial growth of Ti₂AlN by solid state reaction in AlNTi (0001) multilayer

- thin films', *Appl. Phys. Lett.*, vol. 90, no. 17, pp. 1–4, 2007, doi: 10.1063/1.2731520.
- [62] J. Frodelius *et al.*, 'Ti₂AlC coatings deposited by High Velocity Oxy-Fuel spraying', *Surf. Coatings Technol.*, vol. 202, no. 24, pp. 5976–5981, 2008, doi: 10.1016/j.surfcoat.2008.06.184.
- [63] P. Eklund, M. Beckers, U. Jansson, H. Högberg, and L. Hultman, 'The Mn + 1AX_n phases: Materials science and thin-film processing', *Thin Solid Films*, vol. 518, no. 8, pp. 1851–1878, 2010, doi: 10.1016/j.tsf.2009.07.184.
- [64] J. Emmerlich *et al.*, 'Growth of Ti₃SiC₂ thin films by elemental target magnetron sputtering', *J. Appl. Phys.*, vol. 96, no. 9, pp. 4817–4826, 2004, doi: 10.1063/1.1790571.
- [65] J. Etzkorn, M. Ade, and H. Hillebrecht, 'Ta₃AlC₂ and Ta₄AlC₃ - Single-crystal investigations of two new ternary carbides of tantalum synthesized by the molten metal technique', *Inorg. Chem.*, vol. 46, no. 4, pp. 1410–1418, 2007, doi: 10.1021/ic062231y.
- [66] L. Shi, L. Shi, and F. Max, 'From MAX to MXenes : synthesis , characterization and electronic properties To cite this version : HAL Id : tel-01762172 UNIVERSITÉ CATHOLIQUE DE LOUVAIN Ecole Polytechnique de Louvain Institut de la Matière Condensée et des Nanosciences FROM MAX PHASES T', 2018.
- [67] F. Mercier, T. Ouisse, and D. Chaussende, 'Morphological instabilities induced by foreign particles and Ehrlich-Schwoebel effect during the two-dimensional growth of crystalline Ti₃SiC₂', *Phys. Rev. B - Condens. Matter Mater. Phys.*, vol. 83, no. 7, pp. 1–11, 2011, doi: 10.1103/PhysRevB.83.075411.
- [68] T. Ouisse, E. Sarigiannidou, O. Chaix-Pluchery, H. Roussel, B. Doisneau, and D. Chaussende, 'High temperature solution growth and characterization of Cr₂AlC single crystals', *J. Cryst. Growth*, vol. 384, pp. 88–95, 2013, doi: 10.1016/j.jcrysgro.2013.09.021.
- [69] F. Mercier, J. M. Dedulle, D. Chaussende, and M. Pons, 'Coupled heat transfer and fluid dynamics modeling of high-temperature SiC solution growth', *J. Cryst. Growth*, vol. 312, no. 2, pp. 155–163, 2010, doi: 10.1016/j.jcrysgro.2009.10.007.
- [70] L. Shi *et al.*, 'Synthesis of single crystals of V₂AlC phase by high-temperature

- solution growth and slow cooling technique', *Acta Mater.*, vol. 83, pp. 304–309, 2015, doi: 10.1016/j.actamat.2014.10.018.
- [71] Q. Tao *et al.*, 'Atomically Layered and Ordered Rare-Earth i-MAX Phases: A New Class of Magnetic Quaternary Compounds', *Chem. Mater.*, vol. 31, no. 7, pp. 2476–2485, 2019, doi: 10.1021/acs.chemmater.8b05298.
- [72] M. Dahlqvist, J. Lu, R. Meshkian, Q. Tao, L. Hultman, and J. Rosen, 'Prediction and synthesis of a family of atomic laminate phases with Kagomé-like and in-plane chemical ordering', *Sci. Adv.*, vol. 3, no. 7, pp. 1–10, 2017, doi: 10.1126/sciadv.1700642.
- [73] Q. Tao *et al.*, 'Two-dimensional Mo_{1.33}C MXene with divacancy ordering prepared from parent 3D laminate with in-plane chemical ordering', *Nat. Commun.*, vol. 8, pp. 1–7, 2017, doi: 10.1038/ncomms14949.
- [74] Q. Tao *et al.*, 'Rare-earth (RE) nanolaminates Mo₄RE₄Al₇ C₃ featuring ferromagnetism and mixed-valence states', *Phys. Rev. Mater.*, vol. 2, no. 11, pp. 1–12, 2018, doi: 10.1103/PhysRevMaterials.2.114401.
- [75] K. S. Novoselov, A. Mishchenko, A. Carvalho, and A. H. Castro Neto, '2D materials and van der Waals heterostructures', *Science (80-.)*, vol. 353, no. 6298, pp. 1–25, 2016, doi: 10.1126/science.aac9439.
- [76] K. S. Novoselov *et al.*, 'Electric Field Effect in Atomically Thin Carbon Films', *Science (80-.)*, vol. 306, pp. 666–669, 2004, doi: 10.1126/science.1102896.
- [77] and C. Z. Dmitri Golberg,* Yoshio Bando, Yang Huang, Takeshi Terao, Masanori Mitome, Chengchun Tang, 'Boron nitride nanotubes and nanosheets', vol. 4, no. 6, pp. 2979–2993, 2002.
- [78] Q. H. Wang, K. Kalantar-Zadeh, A. Kis, J. N. Coleman, and M. S. Strano, 'Electronics and optoelectronics of two-dimensional transition metal dichalcogenides', *Nat. Nanotechnol.*, vol. 7, no. 11, pp. 699–712, 2012, doi: 10.1038/nnano.2012.193.
- [79] R. Ma and T. Sasaki, 'Nanosheets of oxides and hydroxides: Ultimate 2D charge-bearing functional crystallites', *Adv. Mater.*, vol. 22, no. 45, pp. 5082–5104, 2010, doi: 10.1002/adma.201001722.
- [80] C. C. Coleman, H. Goldwhite, and W. Tikkanen, 'A Review of Intercalation in

- Heavy Metal Iodides', *Chem. Mater.*, vol. 10, no. 10, pp. 2794–2800, 1998, doi: 10.1021/cm980211r.
- [81] Y. Gogotsi and B. Anasori, 'The Rise of MXenes', *ACS Nano*, vol. 13, no. 8, pp. 8491–8494, 2019, doi: 10.1021/acsnano.9b06394.
- [82] M. Naguib *et al.*, 'Two-dimensional nanocrystals produced by exfoliation of Ti₃AlC₂', *Adv. Mater.*, vol. 23, no. 37, pp. 4248–4253, 2011, doi: 10.1002/adma.201102306.
- [83] B. Zhang, J. Zhou, Z. Guo, Q. Peng, and Z. Sun, 'Two-dimensional chromium boride MBenes with high HER catalytic activity', *Appl. Surf. Sci.*, vol. 500, no. September 2019, p. 144248, 2020, doi: 10.1016/j.apsusc.2019.144248.
- [84] Z. Guo, J. Zhou, and Z. Sun, 'New two-dimensional transition metal borides for Li ion batteries and electrocatalysis', *J. Mater. Chem. A*, vol. 5, no. 45, pp. 23530–23535, 2017, doi: 10.1039/c7ta08665b.
- [85] B. Anasori, M. R. Lukatskaya, and Y. Gogotsi, '2D metal carbides and nitrides (MXenes) for energy storage', *Nat. Rev. Mater.*, vol. 2, no. 2, 2017, doi: 10.1038/natrevmats.2016.98.
- [86] B. Anasori *et al.*, 'Two-Dimensional, Ordered, Double Transition Metals Carbides (MXenes)', *ACS Nano*, vol. 9, no. 10, pp. 9507–9516, 2015, doi: 10.1021/acsnano.5b03591.
- [87] M. Khazaei, A. Mishra, N. S. Venkataramanan, A. K. Singh, and S. Yunoki, 'Recent advances in MXenes: From fundamentals to applications', *Curr. Opin. Solid State Mater. Sci.*, vol. 23, no. 3, pp. 164–178, 2019, doi: 10.1016/j.cossms.2019.01.002.
- [88] J. Halim *et al.*, 'Synthesis of two-dimensional Nb_{1.33}C (mxene) with randomly distributed vacancies by etching of the quaternary solid solution (Nb₂/3Sc₁/3)2AlC_{max} phase', *ACS Appl. Nano Mater.*, vol. 1, no. 6, pp. 2455–2460, 2018, doi: 10.1021/acsanm.8b00332.
- [89] R. Meshkian *et al.*, 'W-Based Atomic Laminates and Their 2D Derivative W_{1.33}C MXene with Vacancy Ordering', *Adv. Mater.*, vol. 30, no. 21, pp. 1–8, 2018, doi: 10.1002/adma.201706409.
- [90] L. Verger, V. Natu, M. Carey, and M. W. Barsoum, 'MXenes: An Introduction of Their Synthesis, Select Properties, and Applications', *Trends Chem.*, vol. 1, no. 7,

- pp. 656–669, 2019, doi: 10.1016/j.trechm.2019.04.006.
- [91] J. Halim *et al.*, ‘X-ray photoelectron spectroscopy of select multi-layered transition metal carbides (MXenes)’, *Appl. Surf. Sci.*, vol. 362, pp. 406–417, 2016, doi: 10.1016/j.apsusc.2015.11.089.
- [92] M. Khazaei *et al.*, ‘Novel electronic and magnetic properties of two-dimensional transition metal carbides and nitrides’, *Adv. Funct. Mater.*, vol. 23, no. 17, pp. 2185–2192, 2013, doi: 10.1002/adfm.201202502.
- [93] M. Khazaei, M. Arai, T. Sasaki, A. Ranjbar, Y. Liang, and S. Yunoki, ‘OH-terminated two-dimensional transition metal carbides and nitrides as ultralow work function materials’, *Phys. Rev. B - Condens. Matter Mater. Phys.*, vol. 92, no. 7, pp. 1–28, 2015, doi: 10.1103/PhysRevB.92.075411.
- [94] T. Hu, J. Wang, H. Zhang, Z. Li, M. Hu, and X. Wang, ‘Vibrational properties of Ti₃C₂ and Ti₃C₂T₂ (T = O, F, OH) monosheets by first-principles calculations: A comparative study’, *Phys. Chem. Chem. Phys.*, vol. 17, no. 15, pp. 9997–10003, 2015, doi: 10.1039/c4cp05666c.
- [95] K. Hantanasirisakul and Y. Gogotsi, ‘Electronic and Optical Properties of 2D Transition Metal Carbides and Nitrides (MXenes)’, *Adv. Mater.*, vol. 30, no. 52, 2018, doi: 10.1002/adma.201804779.
- [96] A. N. Enyashin and A. L. Ivanovskii, ‘Two-dimensional titanium carbonitrides and their hydroxylated derivatives: Structural, electronic properties and stability of MXenes Ti₃C_{2-x}N_x(OH)₂ from DFTB calculations’, *J. Solid State Chem.*, vol. 207, pp. 42–48, 2013, doi: 10.1016/j.jssc.2013.09.010.
- [97] M. Khazaei, A. Ranjbar, M. Arai, T. Sasaki, and S. Yunoki, ‘Electronic properties and applications of MXenes: a theoretical review’, *J. Mater. Chem. C*, vol. 5, no. 10, pp. 2488–2503, 2017, doi: 10.1039/c7tc00140a.
- [98] S. Lai *et al.*, ‘Surface group modification and carrier transport properties of layered transition metal carbides (Ti₂CT_x, T: -OH, -F and -O)’, *Nanoscale*, vol. 7, no. 46, pp. 19390–19396, 2015, doi: 10.1039/c5nr06513e.
- [99] X. H. Zha *et al.*, ‘Role of the surface effect on the structural, electronic and mechanical properties of the carbide MXenes’, *Epl*, vol. 111, no. 2, 2015, doi: 10.1209/0295-5075/111/26007.

- [100] J. L. Hart *et al.*, ‘Control of MXenes’ electronic properties through termination and intercalation’, *Nat. Commun.*, vol. 10, no. 1, 2019, doi: 10.1038/s41467-018-08169-8.
- [101] S. Kajiyama *et al.*, ‘Enhanced Li-Ion Accessibility in MXene Titanium Carbide by Steric Chloride Termination’, *Adv. Energy Mater.*, vol. 7, no. 9, pp. 1–8, 2017, doi: 10.1002/aenm.201601873.
- [102] M. Naguib, R. R. Unocic, B. L. Armstrong, and J. Nanda, ‘Large-scale delamination of multi-layers transition metal carbides and carbonitrides “mXenes”’, *Dalt. Trans.*, vol. 44, no. 20, pp. 9353–9358, 2015, doi: 10.1039/c5dt01247c.
- [103] I. Persson *et al.*, ‘On the organization and thermal behavior of functional groups on Ti₃C₂ MXene surfaces in vacuum’, *2D Mater.*, vol. 5, no. 1, 2018, doi: 10.1088/2053-1583/aa89cd.
- [104] P. Lian *et al.*, ‘Alkalized Ti₃C₂ MXene nanoribbons with expanded interlayer spacing for high-capacity sodium and potassium ion batteries’, *Nano Energy*, vol. 40, no. April, pp. 1–8, 2017, doi: 10.1016/j.nanoen.2017.08.002.
- [105] L. Verger, C. Xu, V. Natu, H. M. Cheng, W. Ren, and M. W. Barsoum, ‘Overview of the synthesis of MXenes and other ultrathin 2D transition metal carbides and nitrides’, *Curr. Opin. Solid State Mater. Sci.*, vol. 23, no. 3, pp. 149–163, 2019, doi: 10.1016/j.cossms.2019.02.001.
- [106] C. Xu *et al.*, ‘Large-area high-quality 2D ultrathin Mo₂C superconducting crystals’, *Nat. Mater.*, vol. 14, no. 11, pp. 1135–1141, 2015, doi: 10.1038/nmat4374.
- [107] Z. Zhang, F. Zhang, H. Wang, C. Ho Chan, W. Lu, and J. Y. Dai, ‘Substrate orientation-induced epitaxial growth of face centered cubic Mo₂C superconductive thin film’, *J. Mater. Chem. C*, vol. 5, no. 41, pp. 10822–10827, 2017, doi: 10.1039/c7tc03652c.
- [108] D. R. Dreyer, S. Park, C. W. Bielawski, and R. S. Ruoff, ‘The chemistry of graphene oxide’, *Chem. Soc. Rev.*, vol. 39, no. 1, pp. 228–240, 2010, doi: 10.1039/b917103g.
- [109] P. Joensen, R. F. Frindt, and S. R. Morrison, ‘Single-layer MoS₂’, *Mater. Res. Bull.*, vol. 21, no. 4, pp. 457–461, 1986, doi: 10.1016/0025-5408(86)90011-5.

- [110] Z. H. Liu, K. Ooi, H. Kanoh, W. P. Tang, and T. Tomida, 'Swelling and delamination behaviors of birnessite-type manganese oxide by intercalation of tetraalkylammonium ions', *Langmuir*, vol. 16, no. 9, pp. 4154–4164, 2000, doi: 10.1021/la9913755.
- [111] Y. Hernandez *et al.*, 'High-yield production of graphene by liquid-phase exfoliation of graphite', *Nat. Nanotechnol.*, vol. 3, no. 9, pp. 563–568, 2008, doi: 10.1038/nnano.2008.215.
- [112] M. Naguib *et al.*, 'Two-dimensional transition metal carbides', *ACS Nano*, vol. 6, no. 2, pp. 1322–1331, 2012, doi: 10.1021/nn204153h.
- [113] J. Halim *et al.*, 'Synthesis and Characterization of 2D Molybdenum Carbide (MXene)', *Adv. Funct. Mater.*, vol. 26, no. 18, pp. 3118–3127, 2016, doi: 10.1002/adfm.201505328.
- [114] J. Zhou *et al.*, 'A Two-Dimensional Zirconium Carbide by Selective Etching of Al₃C₃ from Nanolaminated Zr₃Al₃C₅', *Angew. Chemie - Int. Ed.*, vol. 55, no. 16, pp. 5008–5013, 2016, doi: 10.1002/anie.201510432.
- [115] J. Zhou *et al.*, 'Synthesis and Electrochemical Properties of Two-Dimensional Hafnium Carbide', *ACS Nano*, vol. 11, no. 4, pp. 3841–3850, 2017, doi: 10.1021/acsnano.7b00030.
- [116] M. Naguib *et al.*, 'New two-dimensional niobium and vanadium carbides as promising materials for li-ion batteries', *J. Am. Chem. Soc.*, vol. 135, no. 43, pp. 15966–15969, 2013, doi: 10.1021/ja405735d.
- [117] I. Persson *et al.*, 'Tailoring Structure, Composition, and Energy Storage Properties of MXenes from Selective Etching of In-Plane, Chemically Ordered MAX Phases', *Small*, vol. 14, no. 17, pp. 1–7, 2018, doi: 10.1002/sml.201703676.
- [118] M. H. Tran *et al.*, 'Adding a New Member to the MXene Family: Synthesis, Structure, and Electrocatalytic Activity for the Hydrogen Evolution Reaction of V₄C₃T_x', *ACS Appl. Energy Mater.*, vol. 1, no. 8, pp. 3908–3914, 2018, doi: 10.1021/acsaem.8b00652.
- [119] M. Ghidui *et al.*, 'Synthesis and characterization of two-dimensional Nb₄C₃ (MXene)', *Chem. Commun.*, vol. 50, no. 67, pp. 9517–9520, 2014, doi: 10.1039/c4cc03366c.

- [120] J. Yang *et al.*, ‘Two-Dimensional Nb-Based M₄C₃ Solid Solutions (MXenes)’, *J. Am. Ceram. Soc.*, vol. 99, no. 2, pp. 660–666, 2016, doi: 10.1111/jace.13922.
- [121] M. Alhabeab *et al.*, ‘Selective Etching of Silicon from Ti₃SiC₂ (MAX) To Obtain 2D Titanium Carbide (MXene)’, *Angew. Chemie - Int. Ed.*, vol. 57, no. 19, pp. 5444–5448, 2018, doi: 10.1002/anie.201802232.
- [122] M. Ghidui, M. R. Lukatskaya, M. Q. Zhao, Y. Gogotsi, and M. W. Barsoum, ‘Conductive two-dimensional titanium carbide “clay” with high volumetric capacitance’, *Nature*, vol. 516, no. 7529, pp. 78–81, 2015, doi: 10.1038/nature13970.
- [123] F. Liu *et al.*, ‘Preparation of Ti₃C₂ and Ti₂C MXenes by fluoride salts etching and methane adsorptive properties’, *Appl. Surf. Sci.*, vol. 416, pp. 781–789, 2017, doi: 10.1016/j.apsusc.2017.04.239.
- [124] F. Liu *et al.*, ‘Preparation of High-Purity V₂C MXene and Electrochemical Properties as Li-Ion Batteries’, *J. Electrochem. Soc.*, vol. 164, no. 4, pp. A709–A713, 2017, doi: 10.1149/2.0641704jes.
- [125] A. F. Cooper and R. Thakur, ‘The group of twenty (G20)’, *Gr. Twenty*, pp. 1–194, 2013, doi: 10.4324/9780203071236.
- [126] T. Li *et al.*, ‘Fluorine-Free Synthesis of High-Purity Ti₃C₂T_x (T=OH, O) via Alkali Treatment’, *Angew. Chemie - Int. Ed.*, vol. 57, no. 21, pp. 6115–6119, 2018, doi: 10.1002/anie.201800887.
- [127] S. Yang *et al.*, ‘Fluoride-Free Synthesis of Two-Dimensional Titanium Carbide (MXene) Using A Binary Aqueous System’, *Angew. Chemie*, vol. 130, no. 47, pp. 15717–15721, 2018, doi: 10.1002/ange.201809662.
- [128] B. Soundiraraju and B. K. George, ‘Two-Dimensional Titanium Nitride (Ti₂N) MXene: Synthesis, Characterization, and Potential Application as Surface-Enhanced Raman Scattering Substrate’, *ACS Nano*, vol. 11, no. 9, pp. 8892–8900, 2017, doi: 10.1021/acsnano.7b03129.
- [129] I. R. Shein and A. L. Ivanovskii, ‘Graphene-like titanium carbides and nitrides Ti_{n+1}C_n, Ti_{n+1}N_n (n = 1, 2, and 3) from de-intercalated MAX phases: First-principles probing of their structural, electronic properties and relative stability’, *Comput. Mater. Sci.*, vol. 65, pp. 104–114, 2012, doi:

- 10.1016/j.commat.2012.07.011.
- [130] P. Urbankowski *et al.*, ‘2D molybdenum and vanadium nitrides synthesized by ammoniation of 2D transition metal carbides (MXenes)’, *Nanoscale*, vol. 9, no. 45, pp. 17722–17730, 2017, doi: 10.1039/c7nr06721f.
- [131] T. Hu *et al.*, ‘Interlayer coupling in two-dimensional titanium carbide MXenes’, *Phys. Chem. Chem. Phys.*, vol. 18, no. 30, pp. 20256–20260, 2016, doi: 10.1039/c6cp01699e.
- [132] M. Ghidui, J. Halim, S. Kota, D. Bish, Y. Gogotsi, and M. W. Barsoum, ‘Ion-Exchange and Cation Solvation Reactions in Ti₃C₂ MXene’, *Chem. Mater.*, vol. 28, no. 10, pp. 3507–3514, 2016, doi: 10.1021/acs.chemmater.6b01275.
- [133] P. Urbankowski *et al.*, ‘Synthesis of two-dimensional titanium nitride Ti₄N₃ (MXene)’, *Nanoscale*, vol. 8, no. 22, pp. 11385–11391, 2016, doi: 10.1039/c6nr02253g.
- [134] O. Mashtalir *et al.*, ‘Intercalation and delamination of layered carbides and carbonitrides’, *Nat. Commun.*, vol. 4, pp. 1–7, 2013, doi: 10.1038/ncomms2664.
- [135] M. Alhabeab *et al.*, ‘Guidelines for Synthesis and Processing of Two-Dimensional Titanium Carbide (Ti₃C₂T_x MXene)’, *Chem. Mater.*, vol. 29, no. 18, pp. 7633–7644, 2017, doi: 10.1021/acs.chemmater.7b02847.
- [136] A. Lipatov, M. Alhabeab, M. R. Lukatskaya, A. Boson, Y. Gogotsi, and A. Sinitskii, ‘Effect of Synthesis on Quality, Electronic Properties and Environmental Stability of Individual Monolayer Ti₃C₂ MXene Flakes’, *Adv. Electron. Mater.*, vol. 2, no. 12, 2016, doi: 10.1002/aelm.201600255.
- [137] C. J. Zhang *et al.*, ‘Oxidation Stability of Colloidal Two-Dimensional Titanium Carbides (MXenes)’, *Chem. Mater.*, vol. 29, no. 11, pp. 4848–4856, 2017, doi: 10.1021/acs.chemmater.7b00745.
- [138] M. Khazaei, A. Ranjbar, M. Arai, and S. Yunoki, ‘Topological insulators in the ordered double transition metals M₂' M'' C₂ MXenes (M' = Mo, W; M'' = Ti, Zr, Hf)’, *Phys. Rev. B*, vol. 94, no. 12, 2016, doi: 10.1103/PhysRevB.94.125152.
- [139] H. Kim, B. Anasori, Y. Gogotsi, and H. N. Alshareef, ‘Thermoelectric Properties of Two-Dimensional Molybdenum-Based MXenes’, *Chem. Mater.*, vol. 29, no. 15, pp. 6472–6479, 2017, doi: 10.1021/acs.chemmater.7b02056.

- [140] J. Halim, E. J. Moon, P. Eklund, J. Rosen, M. W. Barsoum, and T. Ouisse, 'Variable range hopping and thermally activated transport in molybdenum-based MXenes', *Phys. Rev. B*, vol. 98, no. 10, pp. 1–11, 2018, doi: 10.1103/PhysRevB.98.104202.
- [141] B. Anasori *et al.*, 'Control of electronic properties of 2D carbides (MXenes) by manipulating their transition metal layers', *Nanoscale Horizons*, vol. 1, no. 3, pp. 227–234, 2016, doi: 10.1039/c5nh00125k.
- [142] A. Miranda, J. Halim, M. W. Barsoum, and A. Lorke, 'Electronic properties of freestanding Ti₃C₂T_x MXene monolayers', *Appl. Phys. Lett.*, vol. 108, no. 3, 2016, doi: 10.1063/1.4939971.
- [143] V. N. Borysiuk, V. N. Mochalin, and Y. Gogotsi, 'Molecular dynamic study of the mechanical properties of two-dimensional titanium carbides Ti_n+1C_n (MXenes)', *Nanotechnology*, vol. 26, no. 26, pp. 1–10, 2015, doi: 10.1088/0957-4484/26/26/265705.
- [144] M. Kurtoglu, M. Naguib, Y. Gogotsi, and M. W. Barsoum, 'First principles study of two-dimensional early transition metal carbides', *MRS Commun.*, vol. 2, no. 4, pp. 133–137, 2012, doi: 10.1557/mrc.2012.25.
- [145] A. Lipatov *et al.*, 'Elastic properties of 2D Ti₃C₂T_x MXene monolayers and bilayers', *Sci. Adv.*, vol. 4, no. 6, pp. 1–8, 2018, doi: 10.1126/sciadv.aat0491.
- [146] Z. Ling *et al.*, 'Flexible and conductive MXene films and nanocomposites with high capacitance', *Proc. Natl. Acad. Sci. U. S. A.*, vol. 111, no. 47, pp. 16676–16681, 2014, doi: 10.1073/pnas.1414215111.
- [147] A. D. Dillon *et al.*, 'Highly Conductive Optical Quality Solution-Processed Films of 2D Titanium Carbide', *Adv. Funct. Mater.*, vol. 26, no. 23, pp. 4162–4168, 2016, doi: 10.1002/adfm.201600357.
- [148] R. R. Nair *et al.*, 'Fine structure constant defines visual transparency of graphene', *Science (80-.)*, vol. 320, no. 5881, p. 1308, 2008, doi: 10.1126/science.1156965.
- [149] G. Ying, A. D. Dillon, A. T. Fafarman, and M. W. Barsoum, 'Transparent, conductive solution processed spincoated 2D Ti₂CT_x (MXene) films', *Mater. Res. Lett.*, vol. 5, no. 6, pp. 391–398, 2017, doi: 10.1080/21663831.2017.1296043.
- [150] G. Ying, S. Kota, A. D. Dillon, A. T. Fafarman, and M. W. Barsoum, 'Conductive

- transparent V₂CT_x (MXene) films', *FlatChem*, vol. 8, no. March, pp. 25–30, 2018, doi: 10.1016/j.flatc.2018.03.001.
- [151] K. Hantanasirisakul *et al.*, 'Fabrication of Ti₃C₂T_x MXene Transparent Thin Films with Tunable Optoelectronic Properties', *Adv. Electron. Mater.*, vol. 2, no. 6, pp. 1–7, 2016, doi: 10.1002/aelm.201600050.
- [152] M. R. Lukatskaya *et al.*, 'Cation intercalation and high volumetric capacitance of two-dimensional titanium carbide', *Science (80-.)*, vol. 341, no. 6153, pp. 1502–1505, 2013, doi: 10.1126/science.1241488.
- [153] Y. Xie *et al.*, 'Prediction and characterization of mxene nanosheet anodes for non-lithium-ion batteries', *ACS Nano*, vol. 8, no. 9, pp. 9606–9615, 2014, doi: 10.1021/nn503921j.
- [154] Y. Xie *et al.*, 'Role of surface structure on li-ion energy storage capacity of two-dimensional transition-metal carbides', *J. Am. Chem. Soc.*, vol. 136, no. 17, pp. 6385–6394, 2014, doi: 10.1021/ja501520b.
- [155] G. Choi *et al.*, 'Enhanced Terahertz Shielding of MXenes with Nano-Metamaterials', *Adv. Opt. Mater.*, vol. 6, no. 5, pp. 1–6, 2018, doi: 10.1002/adom.201701076.
- [156] F. Shahzad *et al.*, 'Electromagnetic interference shielding with 2D transition metal carbides (MXenes)', *Science (80-.)*, vol. 353, no. 6304, pp. 1137–1140, 2016, doi: 10.1126/science.aag2421.
- [157] H. Liu, C. Duan, C. Yang, W. Shen, F. Wang, and Z. Zhu, *A novel nitrite biosensor based on the direct electrochemistry of hemoglobin immobilized on MXene-Ti₃C₂*, vol. 218. Elsevier B.V., 2015.
- [158] X. F. Yu *et al.*, 'Monolayer Ti₂CO₂: A Promising Candidate for NH₃ Sensor or Capturer with High Sensitivity and Selectivity', *ACS Appl. Mater. Interfaces*, vol. 7, no. 24, pp. 13707–13713, 2015, doi: 10.1021/acsami.5b03737.
- [159] X. Xie, S. Chen, W. Ding, Y. Nie, and Z. Wei, 'An extraordinarily stable catalyst: Pt NPs supported on two-dimensional Ti₃C₂X₂ (X = OH, F) nanosheets for oxygen reduction reaction', *Chem. Commun.*, vol. 49, no. 86, pp. 10112–10114, 2013, doi: 10.1039/c3cc44428g.
- [160] Q. Hu *et al.*, 'MXene: A new family of promising hydrogen storage medium', *J.*

- Phys. Chem. A*, vol. 117, no. 51, pp. 14253–14260, 2013, doi: 10.1021/jp409585v.
- [161] H. Zhang *et al.*, ‘Preparation, mechanical and anti-friction performance of MXene/polymer composites’, *Mater. Des.*, vol. 92, pp. 682–689, 2016, doi: 10.1016/j.matdes.2015.12.084.
- [162] H. Lin, S. Gao, C. Dai, Y. Chen, and J. Shi, ‘A Two-Dimensional Biodegradable Niobium Carbide (MXene) for Photothermal Tumor Eradication in NIR-I and NIR-II Biowindows’, *J. Am. Chem. Soc.*, vol. 139, no. 45, pp. 16235–16247, 2017, doi: 10.1021/jacs.7b07818.
- [163] C. E. Ren *et al.*, ‘Porous Two-Dimensional Transition Metal Carbide (MXene) Flakes for High-Performance Li-Ion Storage’, *ChemElectroChem*, vol. 3, no. 5, pp. 689–693, 2016, doi: 10.1002/celec.201600059.
- [164] S. Kajiyama *et al.*, ‘Sodium-Ion Intercalation Mechanism in MXene Nanosheets’, *ACS Nano*, vol. 10, no. 3, pp. 3334–3341, 2016, doi: 10.1021/acsnano.5b06958.
- [165] M. Naguib *et al.*, ‘Electrochemical performance of MXenes as K-ion battery anodes’, *Chem. Commun.*, vol. 53, no. 51, pp. 6883–6886, 2017, doi: 10.1039/c7cc02026k.
- [166] A. Vahidmohammadi, A. Hadjikhani, S. Shahbazmohamadi, and M. Beidaghi, ‘Two-Dimensional Vanadium Carbide (MXene) as a High-Capacity Cathode Material for Rechargeable Aluminum Batteries’, *ACS Nano*, vol. 11, no. 11, pp. 11135–11144, 2017, doi: 10.1021/acsnano.7b05350.
- [167] Q. Tang, Z. Zhou, and P. Shen, ‘Are MXenes promising anode materials for Li ion batteries? Computational studies on electronic properties and Li storage capability of Ti₃C₂ and Ti₃C₂X₂ (X = F, OH) monolayer’, *J. Am. Chem. Soc.*, vol. 134, no. 40, pp. 16909–16916, 2012, doi: 10.1021/ja308463r.
- [168] M. Naguib *et al.*, ‘MXene: A promising transition metal carbide anode for lithium-ion batteries’, *Electrochem. commun.*, vol. 16, no. 1, pp. 61–64, 2012, doi: 10.1016/j.elecom.2012.01.002.
- [169] Y. Wang, Y. Song, and Y. Xia, ‘Electrochemical capacitors: Mechanism, materials, systems, characterization and applications’, *Chem. Soc. Rev.*, vol. 45, no. 21, pp. 5925–5950, 2016, doi: 10.1039/c5cs00580a.
- [170] M. R. Lukatskaya *et al.*, ‘Ultra-high-rate pseudocapacitive energy storage in two-

- dimensional transition metal carbides', *Nat. Energy*, vol. 6, no. July, pp. 1–6, 2017, doi: 10.1038/nenergy.2017.105.
- [171] Y. Dall'Agnese, M. R. Lukatskaya, K. M. Cook, P. L. Taberna, Y. Gogotsi, and P. Simon, 'High capacitance of surface-modified 2D titanium carbide in acidic electrolyte', *Electrochem. commun.*, vol. 48, pp. 118–122, 2014, doi: 10.1016/j.elecom.2014.09.002.
- [172] O. Mashtalir *et al.*, 'The effect of hydrazine intercalation on the structure and capacitance of 2D titanium carbide (MXene)', *Nanoscale*, vol. 8, no. 17, pp. 9128–9133, 2016, doi: 10.1039/c6nr01462c.
- [173] J. Come *et al.*, 'Controlling the actuation properties of MXene paper electrodes upon cation intercalation', *Nano Energy*, vol. 17, pp. 27–35, 2015, doi: 10.1016/j.nanoen.2015.07.028.
- [174] Z. Chen, C. Xu, C. Ma, W. Ren, and H. M. Cheng, 'Lightweight and flexible graphene foam composites for high-performance electromagnetic interference shielding', *Adv. Mater.*, vol. 25, no. 9, pp. 1296–1300, 2013, doi: 10.1002/adma.201204196.
- [175] M. Han *et al.*, 'Ti₃C₂ MXenes with Modified Surface for High-Performance Electromagnetic Absorption and Shielding in the X-Band', *ACS Appl. Mater. Interfaces*, vol. 8, no. 32, pp. 21011–21019, 2016, doi: 10.1021/acsami.6b06455.
- [176] J. Xu, J. Shim, J. H. Park, and S. Lee, 'MXene Electrode for the Integration of WSe₂ and MoS₂ Field Effect Transistors', *Adv. Funct. Mater.*, vol. 26, no. 29, pp. 5328–5334, 2016, doi: 10.1002/adfm.201600771.
- [177] K. S. Novoselov *et al.*, 'Electric field in atomically thin carbon films', *Science (80-.)*, vol. 306, no. 5696, pp. 666–669, 2004, doi: 10.1126/science.1102896.
- [178] Y. Huang *et al.*, 'Reliable Exfoliation of Large-Area High-Quality Flakes of Graphene and Other Two-Dimensional Materials', *ACS Nano*, vol. 9, no. 11, pp. 10612–10620, 2015, doi: 10.1021/acsnano.5b04258.
- [179] K. S. Novoselov *et al.*, 'Two-dimensional atomic crystals', *Proc. Natl. Acad. Sci. U. S. A.*, vol. 102, no. 30, pp. 10451–10453, 2005, doi: 10.1073/pnas.0502848102.
- [180] M. Yi and Z. Shen, 'A review on mechanical exfoliation for the scalable production of graphene', *J. Mater. Chem. A*, vol. 3, no. 22, pp. 11700–11715, 2015, doi:

10.1039/c5ta00252d.

- [181] H. Li *et al.*, ‘Fabrication of single- and multilayer MoS₂ film-based field-effect transistors for sensing NO at room temperature’, *Small*, vol. 8, no. 1, pp. 63–67, 2012, doi: 10.1002/sml.201101016.
- [182] R. V. Gorbachev *et al.*, ‘Hunting for monolayer boron nitride: Optical and raman signatures’, *Small*, vol. 7, no. 4, pp. 465–468, 2011, doi: 10.1002/sml.201001628.
- [183] A. Ayari, E. Cobas, O. Ogundadegbe, and M. S. Fuhrer, ‘Realization and electrical characterization of ultrathin crystals of layered transition-metal dichalcogenides’, *J. Appl. Phys.*, vol. 101, no. 1, pp. 1–6, 2007, doi: 10.1063/1.2407388.
- [184] X.-Y. Wang, A. Narita, and K. Müllen, ‘Precision synthesis versus bulk-scale fabrication of graphenes’, *Nat. Rev. Chem.*, vol. 2, no. 1, pp. 1–10, 2018, doi: 10.1038/s41570-017-0100.
- [185] C. Reeves, ‘Graphene : Characterization After Mechanical Exfoliation’, pp. 1–23, 2010.
- [186] W. Xueshen, L. Jinjin, Z. Qing, Z. Yuan, and Z. Mengke, ‘Thermal annealing of exfoliated graphene’, *J. Nanomater.*, vol. 2013, 2013, doi: 10.1155/2013/101765.
- [187] R. Kadowaki, N. Sano, and T. Abukawa, ‘PEEM and micro-UPS studies of cleaved and exfoliated molybdenum disulfide surfaces’, *e-Journal Surf. Sci. Nanotechnol.*, vol. 15, no. November, pp. 115–120, 2017, doi: 10.1380/ejsnt.2017.115.
- [188] A. Jain *et al.*, ‘Minimizing residues and strain in 2D materials transferred from PDMS’, *Nanotechnology*, vol. 29, no. 26, 2018, doi: 10.1088/1361-6528/aabd90.
- [189] A. E. Mag-Isa, J. H. Kim, H. J. Lee, and C. S. Oh, ‘A systematic exfoliation technique for isolating large and pristine samples of 2D materials’, *2D Mater.*, vol. 2, no. 3, p. 34017, 2015, doi: 10.1088/2053-1583/2/3/034017.
- [190] M. M. Benameur, B. Radisavljevic, J. S. Héron, S. Sahoo, H. Berger, and A. Kis, ‘Visibility of dichalcogenide nanolayers’, *Nanotechnology*, vol. 22, no. 12, 2011, doi: 10.1088/0957-4484/22/12/125706.
- [191] P. Blake *et al.*, ‘Making graphene visible’, *Appl. Phys. Lett.*, vol. 91, no. 6, pp. 9–12, 2007, doi: 10.1063/1.2768624.
- [192] A. Miranda, J. Halim, A. Lorke, and M. W. Barsoum, ‘Rendering Ti₃C₂T_x(

- MXene) Monolayers Visible', pp. 1–16.
- [193] A. Obrosov *et al.*, 'Chemical and morphological characterization of magnetron sputtered at different bias voltages Cr-Al-C coatings', *Materials (Basel)*, vol. 10, no. 2, pp. 1–16, 2017, doi: 10.3390/ma10020156.
- [194] M. Nath, P. Kumar, S. Song, Y. Li, and H. S. Tripathi, 'Thermo-mechanical stability of bulk $(Al_{1-x}Cr_x)_2O_3$ solid solution', *Ceram. Int.*, vol. 45, no. 9, pp. 12411–12416, 2019, doi: 10.1016/j.ceramint.2019.03.172.
- [195] 'Dimension of the AFM head configuration'. [Online]. Available: [http://nanophys.kth.se/nanophys/facilities/nfl/afm/icon/bruker-help/Content/System Overview/SPM Head.htm](http://nanophys.kth.se/nanophys/facilities/nfl/afm/icon/bruker-help/Content/System%20Overview/SPM%20Head.htm).
- [196] J. E. Sader and S. P. Jarvis, 'Interpretation of frequency modulation atomic force microscopy in terms of fractional calculus', *Phys. Rev. B - Condens. Matter Mater. Phys.*, vol. 70, no. 1, pp. 8–10, 2004, doi: 10.1103/PhysRevB.70.012303.
- [197] F. J. Giessibl, 'Advances in atomic force microscopy', *Rev. Mod. Phys.*, vol. 75, no. 3, pp. 949–983, 2003, doi: 10.1103/RevModPhys.75.949.
- [198] A. Morelli, 'Piezoresponse Force Microscopy of ferroelectric thin films', Groningen, 2009.
- [199] Y. Martin, D. W. Abraham, and H. K. Wickramasinghe, 'High-resolution capacitance measurement and potentiometry by force microscopy', *Appl. Phys. Lett.*, vol. 52, no. 13, pp. 1103–1105, Mar. 1988, doi: 10.1063/1.99224.
- [200] D. El Khoury, 'Towards the use of Electrostatic Force Microscopy to study interphases in nanodielectric materials Présentée par Diana EL KHOURY', 2018.
- [201] P. Girard, 'Electrostatic force microscopy: Principles and some applications to semiconductors', *Nanotechnology*, vol. 12, no. 4, pp. 485–490, 2001, doi: 10.1088/0957-4484/12/4/321.
- [202] R. Hiesgen and K. A. Friedrich, *Atomic force microscopy*. Elsevier Inc., 2011.
- [204] Lord Kelvin, 'V. Contact electricity of metals', *London, Edinburgh, Dublin Philos. Mag. J. Sci.*, vol. 46, no. 278, pp. 82–120, 1898, doi: 10.1080/14786449808621172.
- [205] M. Nonnenmacher, M. P. O'Boyle, and H. K. Wickramasinghe, 'Kelvin probe force microscopy', *Appl. Phys. Lett.*, vol. 58, no. 25, pp. 2921–2923, 1991, doi:

10.1063/1.105227.

- [206] J. M. R. Weaver, ‘High resolution atomic force microscopy potentiometry’, *J. Vac. Sci. Technol. B Microelectron. Nanom. Struct.*, vol. 9, no. 3, p. 1559, 1991, doi: 10.1116/1.585423.
- [207] S. Sadewasser and C. Barth, ‘Electrostatic Force Microscopy And Kelvin Probe Force Microscopy’, in *Characterization of Materials*, Hoboken, NJ, USA: John Wiley & Sons, Inc., 2012.
- [208] W. Melitz, J. Shen, A. C. Kummel, and S. Lee, ‘Kelvin probe force microscopy and its application’, *Surf. Sci. Rep.*, vol. 66, no. 1, pp. 1–27, 2011, doi: 10.1016/j.surfrep.2010.10.001.
- [209] T. Hochwitz, ‘Capacitive effects on quantitative dopant profiling with scanned electrostatic force microscopes’, *J. Vac. Sci. Technol. B Microelectron. Nanom. Struct.*, vol. 14, no. 1, p. 457, 1996, doi: 10.1116/1.588494.
- [210] Spectrum Instruments (NT-MDT), ‘2.3 Cantilever linear oscillations’, 2014. [Online]. Available: <http://www.ntmdt.com/spm-basics/view/linear-oscillations>.
- [211] S. William, ‘Application Note # 140 PeakForce Kelvin Probe Force Microscopy’, *Bruker*, pp. 1–14, 1898.
- [212] R. García and R. Pérez, *Dynamic atomic force microscopy methods*, vol. 47, no. 6–8. 2002.
- [213] A. Singh, P. Guha, A. K. Panwar, and P. K. Tyagi, ‘Estimation of intrinsic work function of multilayer graphene by probing with electrostatic force microscopy’, *Appl. Surf. Sci.*, vol. 402, pp. 271–276, 2017, doi: 10.1016/j.apsusc.2017.01.047.
- [214] T. Ouisse, M. Stark, F. Rodrigues-Martins, B. Bercu, S. Huant, and J. Chevrier, ‘Theory of electric force microscopy in the parametric amplification regime’, *Phys. Rev. B - Condens. Matter Mater. Phys.*, vol. 71, no. 20, pp. 1–12, 2005, doi: 10.1103/PhysRevB.71.205404.
- [215] A. Verdaguer, C. Weis, G. Oncins, G. Ketteler, H. Bluhm, and M. Salmero, ‘Growth and structure of water on SiO₂ films on Si investigated by kelvin probe microscopy and in situ X-ray spectroscopies’, *Langmuir*, vol. 23, no. 19, pp. 9699–9703, 2007, doi: 10.1021/la700893w.
- [216] C. K. Oliveira, M. J. S. Matos, M. S. C. Mazzoni, H. Chacham, and B. R. A. Neves,

- ‘Anomalous response of supported few-layer hexagonal boron nitride to DC electric fields: A confined water effect?’, *Nanotechnology*, vol. 23, no. 17, 2012, doi: 10.1088/0957-4484/23/17/175703.
- [217] J. Moser, A. Verdaguer, D. Jiménez, A. Barreiro, and A. Bachtold, ‘The environment of graphene probed by electrostatic force microscopy’, *Appl. Phys. Lett.*, vol. 92, no. 12, 2008, doi: 10.1063/1.2898501.
- [218] A. Sadeghi, A. Baratoff, and S. Goedecker, ‘Electrostatic interactions with dielectric samples in scanning probe microscopies’, *Phys. Rev. B - Condens. Matter Mater. Phys.*, vol. 88, no. 3, pp. 1–8, 2013, doi: 10.1103/PhysRevB.88.035436.
- [219] S. Hudlet, M. Saint Jean, C. Guthmann, and J. Berger, ‘Evaluation of the capacitive force between an atomic force microscopy tip and a metallic surface’, *Eur. Phys. J. B*, vol. 2, no. 1, pp. 5–10, 1998, doi: 10.1007/s100510050219.
- [220] W. R. Smythe, ‘Chapter 5 : Three-dimensional potential distributions’, in *Static and Dynamic Electricity*, 2nd ed., McGraw-Hill, Ed. New York, 1950.
- [221] G. Binnig, H. Rohrer, C. Gerber, and E. Weibel, ‘Surface Studies by Scanning Tunneling Microscopy’, *Phys. Rev. Lett.*, vol. 49, no. 1, pp. 57–61, Jul. 1982, doi: 10.1103/PhysRevLett.49.57.
- [222] E. DM and S. EK, ‘Positioning single atoms with scanning tunnelling microscope’, *Nature*, vol. 344, no. April, p. 524, 1990.
- [223] A. Della Pia and G. Costantini, ‘Scanning Tunneling Microscopy’, in *Springer Series in Surface Sciences*, vol. 51, no. 1, G. Bracco and B. Holst, Eds. 2013, pp. 565–597.
- [224] A. Artaud, ‘Quasi-long-range order and topological defects in graphene on rhenium studied by scanning tunneling microscopy’, Université Grenoble Alpes, 2017.
- [225] C. Manfredotti, ‘Imaging at the Nanoscale: Scanning Probe Microscopies Applied to Semiconductors’, in *Characterization of Semiconductor Heterostructures and Nanostructures: Second Edition*, Second Edi., Elsevier B.V., 2013, pp. 467–507.
- [226] W. N. Unertl and M. E. Kordesch, ‘Chapter 8 Direct imaging and geometrical methods’, in *Handbook of Surface Science*, vol. 1, 1996, pp. 361–421.
- [227] Q. Design, ‘Physical Property Measurement System, Hardware Manual’, *Design*, no. 1070. p. 150, 2004.

- [228] A. Gkountaras *et al.*, ‘Mechanical Exfoliation of Select MAX Phases and Mo₄Ce₄Al₇C₃ Single Crystals to Produce MAXenes’, *Small*, vol. 16, no. 4, pp. 1–8, 2020, doi: 10.1002/sml.201905784.
- [229] M. W. Barsoum, *MAX Phases: Properties of Machinable Ternary Carbides and Nitrides*. 2013.
- [230] T. Ito *et al.*, ‘Electronic structure of Cr₂AlC as observed by angle-resolved photoemission spectroscopy’, *Phys. Rev. B*, vol. 96, no. 19, 2017, doi: 10.1103/PhysRevB.96.195168.
- [231] T. Mélin, D. Deresmes, and D. Stiévenard, ‘Charge injection in individual silicon nanoparticles deposited on a conductive substrate’, *Appl. Phys. Lett.*, vol. 81, no. 26, pp. 5054–5056, 2002, doi: 10.1063/1.1532110.
- [232] T. Ouisse, F. Martins, M. Stark, S. Huant, and J. Chevrier, ‘Signal amplitude and sensitivity of the Kelvin probe force microscopy’, *Appl. Phys. Lett.*, vol. 88, no. 4, pp. 1–3, 2006, doi: 10.1063/1.2168251.
- [233] A. Kurokawa, K. Odaka, Y. Azuma, T. Fujimoto, and I. Kojima, ‘Diagnosis and Cleaning of Carbon Contamination on SiO₂ Thin Film’, *J. Surf. Anal.*, vol. 15, no. 3, pp. 337–340, 2009, doi: 10.1384/jsa.15.337.
- [234] J. D. Hettinger *et al.*, ‘Electrical transport, thermal transport, and elastic properties of M₂AlC (M=Ti, Cr, Nb, and V)’, *Phys. Rev. B - Condens. Matter Mater. Phys.*, vol. 72, no. 11, pp. 2–7, 2005, doi: 10.1103/PhysRevB.72.115120.
- [235] M. Todeschini, A. Bastos Da Silva Fanta, F. Jensen, J. B. Wagner, and A. Han, ‘Influence of Ti and Cr Adhesion Layers on Ultrathin Au Films’, *ACS Appl. Mater. Interfaces*, vol. 9, no. 42, pp. 37374–37385, 2017, doi: 10.1021/acsami.7b10136.
- [236] T. Ouisse, L. Shi, B. A. Piot, B. Hackens, V. Mauchamp, and D. Chaussende, ‘Magnetotransport properties of nearly-free electrons in two-dimensional hexagonal metals and application to the Mn_{n+1}AX_n phases’, *Phys. Rev. B - Condens. Matter Mater. Phys.*, vol. 92, no. 4, pp. 1–12, 2015, doi: 10.1103/PhysRevB.92.045133.
- [237] T. Flatten *et al.*, ‘Direct measurement of anisotropic conductivity in a nanolaminated (Mn_{0.5}Cr_{0.5})₂GaC thin film’, *Appl. Phys. Lett.*, vol. 115, no. 9, pp. 0–5, 2019, doi: 10.1063/1.5115347.

- [238] L. Wang, ‘One-Dimensional Electrical Contact to’, *Sci. (New York, N.Y.)* **432**, vol. 342, no. November, pp. 614–617, 2013, doi: 10.1126/science.1244358.
- [239] G. Sankaran, K. Moors, K. Dutta, S. Adelman, C., Tokei, Z., Pourtois, ‘Metallic ceramics for low resistivity interconnects: an ab initio insight’, in *IEEE International Interconnect Technology Conference*, 2018, p. p.160.
- [240] O. Mashtalir, M. Naguib, B. Dyatkin, Y. Gogotsi, and M. W. Barsoum, ‘Kinetics of aluminum extraction from Ti₃AlC₂ in hydrofluoric acid’, vol. 139, pp. 147–152, 2013.
- [241] Y. Kim *et al.*, ‘Elementary processes governing V₂AlC chemical etching in HF’, *RSC Adv.*, vol. 10, no. 42, pp. 25266–25274, 2020, doi: 10.1039/d0ra00842g.
- [242] M. Khazaei, A. Ranjbar, K. Esfarjani, D. Bogdanovski, R. Dronskowski, and S. Yunoki, ‘Insights into exfoliation possibility of MAX phases to MXenes’, *Phys. Chem. Chem. Phys.*, vol. 20, no. 13, pp. 8579–8592, 2018, doi: 10.1039/c7cp08645h.
- [243] R. Thakur *et al.*, ‘Insights into the thermal and chemical stability of multilayered V₂CT: X MXene’, *Nanoscale*, vol. 11, no. 22, pp. 10716–10726, 2019, doi: 10.1039/c9nr03020d.
- [244] P. Verdonck, ‘Plasma etching’, in *Oficina de Microfabricacao: Projeto e Construcao de CIs MOS*, Sao Paolo, 2006, p. 11.
- [245] The Open University, ‘Alternative plasma chamber designs: MERIE and ICP’, 2019. [Online]. Available: <https://www.open.edu/openlearn/science-maths-technology/engineering-technology/structural-devices/content-section-8.3.5>.
- [246] A. Champagne, L. Shi, T. Ouisse, B. Hackens, and J. C. Charlier, ‘Electronic and vibrational properties of V₂C-based MXenes: From experiments to first-principles modeling’, *Phys. Rev. B*, vol. 97, no. 11, pp. 1–23, 2018, doi: 10.1103/PhysRevB.97.115439.
- [247] V. Presser, M. Naguib, L. Chaput, A. Togo, G. Hug, and M. W. Barsoum, ‘First-order Raman scattering of the MAX phases: Ti₂AlN, Ti₂AlC_{0.5}N_{0.5}, Ti₂AlC, (Ti_{0.5}V_{0.5})₂AlC, V₂AlC, Ti₃AlC₂, and Ti₃GeC₂’, *J. Raman Spectrosc.*, vol. 43, no. 1, pp. 168–172, 2012, doi: 10.1002/jrs.3036.
- [248] J. E. Spanier, S. Gupta, M. Amer, and M. W. Barsoum, ‘Vibrational behavior of the M_{n+1}AX_n phases from first-order Raman scattering (M=Ti, V, Cr, A=Si, X=C,

- N)', *Phys. Rev. B - Condens. Matter Mater. Phys.*, vol. 71, no. 1, pp. 2–5, 2005, doi: 10.1103/PhysRevB.71.012103.
- [249] K. J. Harris, M. Bugnet, M. Naguib, M. W. Barsoum, and G. R. Goward, 'Direct measurement of surface termination groups and their connectivity in the 2D MXene V₂CT_x using NMR spectroscopy', *J. Phys. Chem. C*, vol. 119, no. 24, pp. 13713–13720, 2015, doi: 10.1021/acs.jpcc.5b03038.
- [250] M. Barbier *et al.*, 'Mo₄Ce₄Al₇C₃: A nanolamellar ferromagnetic Kondo lattice', *Phys. Rev. B*, vol. 102, no. 15, p. 155121, 2020, doi: 10.1103/PhysRevB.102.155121.
- [251] P. Eklund, J. Rosen, and P. O. Å. Persson, 'Layered ternary Mn_{n+1}AX_n phases and their 2D derivative MXene: An overview from a thin-film perspective', *J. Phys. D. Appl. Phys.*, vol. 50, no. 11, 2017, doi: 10.1088/1361-6463/aa57bc.

Publications

2019

- Athanasios Gkoutaras, Youngsoo Kim, Johann Coraux, Vincent Bouchiat, Simone Lisi, et al.. Mechanical Exfoliation of Select MAX Phases and Mo₄Ce₄Al₇C₃ Single Crystals to Produce MAXenes. *Small*, Wiley-VCH Verlag, 2020, 16 (4), pp.1905784. ([10.1002/sml.201905784](https://doi.org/10.1002/sml.201905784))

2020

- Youngsoo Kim, Athanasios Gkoutaras, Odette Chaix-Pluchery, Isabelle Gélard, Johann Coraux, et al.. Elementary processes governing V₂AlC chemical etching in HF. *RSC Advances*, Royal Society of Chemistry, 2020, 10 (42), pp.25266-25274. ([10.1039/D0RA00842G](https://doi.org/10.1039/D0RA00842G))